# Section D
# Interdisciplinary and Multidisciplinary Problems

# FERTILISATION AS A BIOMECHANICAL OSCILLATORY PHENOMENON IN MAMALS

**Andjelka Hedrih[1], Mihailo Lazarević[2], Ana Mitrović-Jovanović[3]**

[1] State University of Novi Pazar, Department for Bio-medical science, Novi Pazar, Vuka Karadzica bb, 36 300 Novi Pazar, Serbia
e-mail: handjelka@hm.co.rs
[2] Faculty of Mechanical Engineering,
The University of Belgrade, Kraljice Marije 16, 11120 Belgrade, Serbia
e-mail: idemlazarevic@mas.bg.ac.rs
[3] School of Medicine, The University of Belgrade, Dr Subotica 8, 11 000, Belgrade, Serbia
e-mail: anamitrovicjov@googlemail.com

**Abstract.** Fertilization, the process of reunion of genetic material of oocyte and one sperm cell is well described on the biochemical level. In this paper we consider fertilization as a biomechanical oscillatory phenomenon. Using an oscillatory spherical net model of mouse ZP [4] we consider the resonance between forced oscillations of mouse Zona pelucida and impact of sperm cells as necessary condition for successful fertilization. To restate the resonance condition the numerical analysis were done.
**Keywords**: Zona Pelucida spherical net model, fertilization, sperm impact, resonance.

## 1. Introduction

Fertilization in mammals is the process of reunion of genetic material of oocyte and one sperm cell. The fertilization process requires healthy mature oocyte and certain amount of morphologically normal sperm cells with effective velocity that passed trough the process of capacitation. From the biochemical point of view fertilization passes trough several steps: recognition and specific receptor binding of sperm cell to the zona pelucida (ZP), acrozome reaction, penetration of a sperm head trough zona pelucida and cortical reaction [1] Penetration of the sperm cell through ZP induces cortical reaction - oocyte releases the cortical granules with enzymes in perivitelin space. Released enzymes change the structural and mechanical properties of ZP. It becomes "harder". The consequence is polyspermy block and is important for maintaining the quantity of genetic material [2].
After capacitation sperm cells are hyperactivated, which is characterized by pronounced flagellar movements, marked lateral excursion of the sperm head and a non-linear trajectory [1, 3].
The aim of our study was to explain the fertilization process in mammals using an oscillatory spherical net model of mouse ZP.

## 2. Fertilization as a biomechanical oscillatory phenomenon –basic settings

We considered the oocyte with ZP as a biomechanical oscillator that could oscillate in the free and forced regime. We considered that forced regime is induced by sperm cells that are "attacking" the outer surface layer of the oocyte- the ZP. We were focus on the events that

are happening on the ZP, induced by the impact of the sperm cells. Inspired by the Wassermans' model of m*ZP* (mouse *ZP*) [4] and 3D structural changes of *ZP* on atomic force microscopy [5] and scanning electron microscopy analysis [6] we developed a mechanical oscillatory model of *ZP* [7,8].

*Free oscillations.* We consider that the system of ZP oscillatory net oscillates in a free regime after ovulation without presence of spermatozoa. If there is only an initial perturbation by kinetic and potential energy given to oscillatory structures, only free vibration regimes of vibration discrete structure appear. In this case material particles at the initial moment obtain the initial displacement measured from their equilibrium positions and initial velocities. In order for free oscillations to appear, it is enough that only one mass particle position is perturbed from its equilibrium position, or that only one mass particle at its equilibrium position obtains initial velocity.

*Forced vibrations.* It is argued that vibro-impacts of sperm cells on *ZP* cause ZP oscillatory net to oscillate in a forced regime. The application of one or multi-frequency external excitation forces to a *ZP* discrete net that oscillates in a free regime results in multi-frequency forced regime oscillations.

According to the oscillatory spherical surface net model of mZP [7,8], m*ZP* is modeled as a non-linear net that envelops the oocyte in one layer (see Figure 1 a* and b*). Spherical net consists of orthogonal chains in meridian and circular directions with cross-sections with knot mass particles. The net has the same structure in circular and meridian directions and lies in the sphere concentric to the oocyte that we suppose is rigid. Each oscillatory mechanical chain has a finite number of material particles with a finite number of degrees of freedom. Chains are composed of material particles of different masses interconnected with massless non-linear elastic elements on a specific manner. See Fig 1. a and b. For modeling this oscillatory spherical net ZP model, the method of discrete continuum was used [9]. Each material particle has three degrees of freedom and is connected to the sphere surface with a standard light non-linear-elastic element (Fig 2a*) in the radial direction and can oscillate in the radial direction as well as in the circular and meridional directions.

We suppose that from the mechanical point of view fertilization occurs in the moment of forced regime of oscillations of mZP induced by sperm cells, when the spermatozoid that oscillate in a resonance with the *ZP* net, penetrates the *ZP*.

We want to determine the resonant frequencies for a certain theoretical initial conditions.

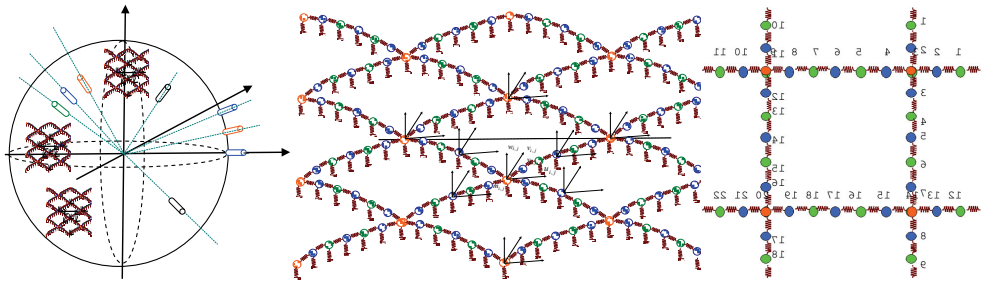

a* b* c*

Figure 1. **a*** Model of *ZP* spherical surface that shows a radial direction of axis of constructive elements of the model - *ZP* proteins. **b*** Part of the *ZP* network on a part of the sphere (oocyte). Orange (*ZP*1), blue (*ZP*2) and green (*ZP*3) represent *ZP* proteins. The network is identical in both circular and meridional direction. Axis shows

directions of movements of *ZP* proteins. Each *ZP* protein is connected to the sphere with elastic springs that can oscillate in radial direction. ***c**** segment of spherical surface net model of *mZP*.

**3. Determination of the resonant frequencies**

The resonance will occur if one sperm cell oscillates with one of the eigen circular frequencies of ZP. The first step is to determine the eigen circular frequencies of mZP.
Using the smallest part of the mZP oscillatory spherical surface model that still preserves the molar ratio of the mZP glycoproteins (*ZP*1: *ZP*2- *ZP*3 is 1:5 [4]) (See Fig 1c.), we made a frequency equation that describes the oscillations of the mZP glycoproteins in the form of chain with eleven material particles. The frequency equation is eleven degree function and is in the form:

$$f\left(\omega^2\right)=\left|\mathbf{C}-\omega^2\mathbf{A}\right|=0 \tag{1}$$

$\mathbf{C}$ is matrix of coefficient of elasticity, and $\mathbf{A}$ is matrix of coefficient of inertia. For obtaining eigen circular frequencies we used graphical method and Matcad software. Relative molecular masses of the three mZP glycoproteins: (*M*r*ZP*1): (200 000 Da, Mr*ZP*2): 120 000 Da and (Mr*ZP*3): 83,000 Da [4] transformed in kg were used. The zeros in the frequency equations are squares of eigen circular frequencies. For considered non-homogenous chains there are 11 squares of eigen circular frequencies: $\omega_s^2$, $s = 1,2,3,4,5,6,7,8,9,10,11$. For determine the amplitude of forced vibrations $C_k\left(\Omega_3^2\right)$ and frequency $\Omega_3$, of each material particle in the chain when external periodical force- $F_3 = F_{03}\cos\Omega_3 t$ (trough the impact of one sperm cell) is applied to the knot material particle (third material particle in the chain), the required condition is:

$$\Delta\left(\Omega_3^2\right)\neq 0 \tag{2}$$

If

$$\Delta\left(\Omega_3^2\right)=\left|\mathbf{C}-\Omega_3^2\mathbf{A}\right|=0 \tag{3}$$

than amplitudes :

$$C_k\left(\Omega_3^2\right)=\frac{\Delta_k\left(\Omega_3^2\right)}{\Delta\left(\Omega_3^2\right)},\ k = 1,2,3,4,5,6,7,8,9,10,11 \tag{4}$$

tending to infinity. In this case resonance stage of forced vibrations of material particles in the chain appears.
Combining frequency equation (1) and resonance condition in forced oscillatory regime (2) we can conclude that resonance could occur under following conditions:

$$\Omega_{3res,s}=\omega_s,\ s = 1,2,3,4,5,6,7,8,9,10,11 \tag{5}$$

Frequency of external force component preformed on the knot material particle in the direction of the chain is equal to one of the eigen circular frequencies of free oscillations.

Zeros of the function present square values of possible resonant frequencies of external force.

According to our knowledge, there are no experimental data of ZP rigidity on stretching in radial, circular or meridian direction. There are experimental data of applied forces on the ZP and indentation of the ZP membrane and calculate values of Young modulus of elasticity according to the different theoretical models of ZP membrane [10,11].

Using the available experimental data we could use different formula to calculate the rigidity of mZP on banding and stretching in radial, circular or meridian direction. For our numerical experiment we approximate that coefficient of elasticity is equal for all material particles and calculated it from the experimental data of Sun et al [10] according to the formula (6):

$$c_m = \frac{E\left(R^2 - r^2\right)\pi}{2R} \tag{6}$$

E-Young module of elasticity, R is half diameter of the mouse oocyte, r-is half diameter of the oocyte minus approximate thickness of mZP

E=17.5kPa, 2R=56.2μm-average diameter of the oocyte from [10], δ=4.8μm-approximate thickness of the oocyte, c=246.75N/m. For obtaining eigen/resonance circular frequencies we used graphical method and Matcad software and correction factor $10^6$. The obtained eigen/resonance circular frequencies are: $\omega_1 = 7.3\text{x}10^{10}$ rad/s $\omega_2 = 1.0712\text{x}10^{11}$ rad/s $\omega_3 = 3.1\text{x}10^{11}$ rad/s $\omega_4 = 8.1\text{x}10^{11}$ rad/s $\omega_5 = 1.569\text{x}10^{12}$ rad/s $\omega_6 = 2.61\text{x}10^{12}$ rad/s $\omega_7 = 2.79\text{x}10^{12}$ rad/s $\omega_8 = 3.26\text{x}10^{12}$ rad/s $\omega_9 = 4.6508\text{x}10^{12}$ rad/s $\omega_{10} = 4.7924\text{x}10^{12}$ rad/s $\omega_{11} = 5.6988\text{x}10^{12}$ rad/s.

*3.2.Conditions for dynamical absorption and resonance for some cases*

Graphs of amplitude-frequency stationary forced regimes for forced vibration of $C_1\left(\Omega_3^2\right)$first, $C_3\left(\Omega_3^2\right)$third and $C_9\left(\Omega_3^2\right)$ ninth material particle in chain excited by external excitation $F_3 = F_{03}\cos\Omega_3 t$ force with amplitude $F_{03}$ and frequency $\Omega_3$ applied to third mass particle in chain are given in the Fig.2, Fig.3, Fig.4, respectively. When external excitation $F_3 = F_{03}\cos\Omega_3 t$ force with amplitude $F_{03}$ and frequency $\Omega_3$ is applied to third mass particle in chain, frequencies under which dynamical absorption occurs for the firs material particle in the chain are $5.65\text{x}10^{11}$ rad/s, $3.8\text{x}10^{11}$ rad/s, 1.2x1012 rad/s, $1.44\text{x}10^{12}$ rad/s, and $1.679\text{x}10^{12}$rad/s.

When external excitation $F_3 = F_{03}\cos\Omega_3 t$ force with amplitude $F_{03}$ and frequency $\Omega_3$ is applied to third mass particle in chain, frequencies under which dynamical absorption occurs for the third material particle in the chain are $1.48\text{x}10^{11}$ rad/s, 6.04x1011 rad/s, and $2.824\text{x}10^{12}$ rad/s. Under these conditions there no dynamical absorption on the ninth material particle in the chain.

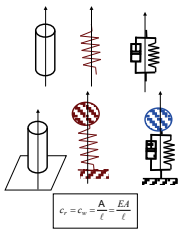

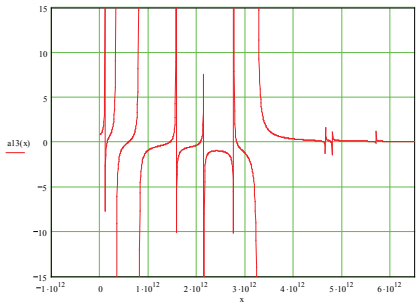

$$\Omega_{res,s} = \omega_s \,, \quad s = 1,2,3,4,5,6,7,8,9,10,11$$

a* b*

Figure 2. a* Model for obtaining rigidity in radial direction. b* Amplitude-frequency stationary forced regimes for forced vibration of $C_1\left(\Omega_3^2\right)$ first material particle in chain excited by external excitation $F_3 = F_{03}\cos\Omega_3 t$ force with amplitude $F_{03}$ and frequency $\Omega_3$ applied to third mass particle in chain; x=$\Omega^2$.

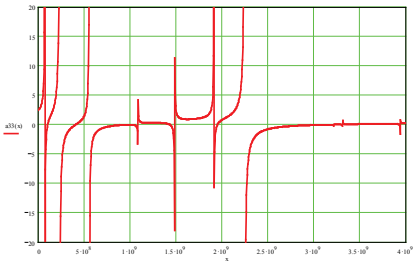

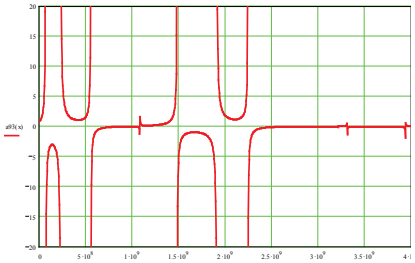

a* b*

Fig 3. Amplitude-frequency stationary forced regimes for forced vibration of $C_3\left(\Omega_3^2\right)$ third a* and ninth b* material particle in chain excited by external excitation $F_3 = F_{03}\cos\Omega_3 t$ force with amplitude $F_{03}$ and frequency $\Omega_3$ applied to third mass particle in chain; x=$\Omega^2$.

## 5. Conclusion

On amplitude-frequency graphs positions with asymptotes corresponds to resonant frequencies and there at the same time eigen circular frequencies. In these positions amplitudes tend to infinity. On these frequencies vertical asymptotes appear for all material particles in the chain.

Dynamical absorption is present in the systems with multiply degree of freedom (in our case 11 degree of freedom) when external periodical force is applied to the system. Depending on the parameters of the system (coefficient of elasticity, amplitudes, frequencies) it is possible that under influence of periodical external force one or more material particles don't oscillate. In the theory of oscillation this phenomenon is known as dynamical absorption.

On amplitude-frequency graphs zeros corresponds to dynamical absorptions in forced oscillatory regime. On these frequencies certain material particle is not oscillating and external force has no effect on it. In general case, for each material particle, there are

different frequencies on which dynamical absorption occurs. For example on amplitude-frequency graph of third material particle Fig 3 on which external force is applied there are three frequencies on which dynamical absorption occurs; on amplitude-frequency graph of ninth material particle Fig 4, (force is applied on the third material particle), there no frequencies on which dynamical absorption occurs. This means that under these conditions ninth material particle will always oscillate in forced regime. Under same conditions first material particle has also possibilities for dynamical absorption to occur.

*Acknowledgement.* The authors would like to thank to Prof. Katica (Stevanović) Hedrih from the Mathematical Institute of SASA, Belgrade, Serbia for help with useful consultations. Parts of this research were supported by the Ministry of Education, Science and Technological Development of Republic of Serbia through Grant ON174001 (State Universitz of Novi Pazar) and Project No.35006.

References

[1] Tipalski-Fišteš N. Fiziologija menstrualnog ciklusa i oplodnja (2005) u Milašinović Lj. i saradnici. *Fitiologija Trudnoće.*IP SKK Kosmos, Beograd, pp.41-59.
[2] R.Fraser R.L**.** **(**1998) Sperm capacitation and the acrosome reaction**.** *Human Reproduction* 13 Supp 1, pp 9-19.
[3] LItscher ES, Williams Z, and Wassarman P.M, (2009) Zona Pellucida Glycoprotein *ZP*3 and Fertilization in Mammals, *Mol Reprod Dev* 76pp. 933–941.
[4] [4] Green DPL, (1997) Three-dimensional structure of the zona pellucida**,** *Rev Reprod* 2pp. 147–156.
[5] Michelmann HW, Rath D, Topfer-Petersen E, Schwartz P, (2007) Structural and Functional Events on the Porcine Zona Pellucida During Maturation, Fertilization and Embryonic Development: a Scanning Electron Microscopy Analysis, *Reprod Dom Anim* 42pp/ 594–602.
[6] Familiari G, Relucenti M, Heyn R, Micara G, and Correr S, (2006) Three-Dimensional Structure of the Zona Pellucida at Ovulation. *Microsc Res Techniq* 69 pp.415–426.
[7] Hedrih A. (2011) Modeling oscillations of zona pelucida before and after fertilization. ENOC Young Scientist Prize Paper. *EUROMECH Newsletter 40,* Europian Mechanics Society, 40, pp. 6-14.
[8] Hedrih A. (2012) Frequency analysis of knot mass particles in oscillatory spherical net model of mouse *zona pellucida. Lecture Session, Short Paper, Abstract book of 23rd International Congress of Theoretical and Applied Mechanics*, (IUTAM ICTAM Beijing 2012), 19-24 August 2012, Beijing, China, SM01-049, pp. 209. ISBN 978-988-16022-3-7.
[9] Hedrih (Stevanović) K, (2002) Discrete Continuum Method, Symposium, Recent Advances in Analytical Dynamics Control, Stability and Differential Geometry, Proceedings Mathematical institute SANU Edited by Vladan Djordjević, p.151, pp.30-57, 2002, ISBN 86-80593-32-X. http://www.mi.sanu.ac.yu/publications.htm
[10] Sun Y*,* Wan KT, Roberts KP, Bischof JS, Nelson BJ**,** **(**2003) Mechanical Property Characterization of Mouse Zona Pellucida, *IEEE T Nanobiosci*, 2(4), pp. 279-286.
[11] Khalilian M, Navidbakhsh M, Valojerdi MR, Chizari M, Yazdi PE, (2010) Estimating Young's modulus of zona pellucida by micropipette aspiration in combination with theoretical models of ovum, *R. Soc. Interfac,*. 7(45), pp.687-94.

# FURTHER RESULTS ON FINITE-TIME STABILITY OF SINGULAR TIME-DELAY SYSTEMS: DELAY-DEPENDENT CONDITIONS

**Sreten B. Stojanović[1], Dragutin Lj. Debeljković[2], Goran V. Simeunović[3], Nebojša J. Dimitrijević[4]**

[1] Faculty of Technology,
The University of Nis, Bulevar oslobodjenja 124, 16000 Leskovac, Serbia
e-mail: ssreten@ptt.rs
[2] Faculty of Mechanical Engineering,
The University of Belgrade, Kraljice Marije 16, 11120 Belgrade 35
e-mail: ddebeljkovic@mas.bg.ac.rs
[3] Innovation Center, Faculty of Mechanical Engineering,
The University of Belgrade, Kraljice Marije 16, 11120 Belgrade 35
e-mail: g_simeunovic@yahoo.com
[4] School of Higher Applied Professional Education, 17500 Vranje, Serbia
e-mail: nebojsa.j.dimitrijevic@gmail.com

**Abstract.** This paper provides sufficient conditions for finite-time stability of linear singular continuous time-delay systems. Considering a finite-time stability concept, new delay dependent conditions have been derived using the approach based on the Lyapunov-like functions and their properties on the subspace of consistent initial conditions. These functions do not need to have the properties of positivity in the whole state space and negative derivatives along the system trajectories. Moreover an LMI approach has been applied in order to get less conservative conditions.

## 1. Introduction

Singular systems, which are also referred to as descriptor systems, generalized state-space systems or semi-state systems, have been extensively studied in the last few decades since singular systems can describe better practical dynamical systems than standard state-space systems and due to the comprehensive applications in economics, electrical and mechanical engineering, etc. [1-2]. In general, the singular representation consists of differential and algebraic equations, and hence it is a generalized representation of the state-space system. Some particular properties of singular systems and their significance in chemical engineering are illustrated by [3-5]. Numerical solution of singular systems is more difficult as compared to regular models due to the existence of linear and non-linear algebraic equations and due to discontinuities in the algebraic variables over the independent variable space.
It has been observed that variety of singular systems is characterized by the phenomena of time delay. Such systems are called singular systems with time delay. In general, the dynamic behavior of continuous-time singular systems with delays is more complicated than that of system without any time-delay because the continuous time-delay system is infinite dimensional.

For this reason, over the past decades, there has been increasing interest in the stability analysis for singular time-delay systems and many results have been reported in the literature [6–11].
In practice one is not only interested in the system stability, but also in the bounds of system trajectories. A system could be stable but completely useless because it possesses undesirable transient performances. A system is said to be finite-time stable (FTS) if, once a time interval is fixed, its state does not exceed some bounds during this time interval. A little work has been done for the finite-time stability and stabilization of singular time-delay systems. Some results on FTS and practical stability can be found in [12-22] (singular systems) and [23-24] (singular time-delay systems).
In this article, we consider the problem of finite-time stability for a class of linear singular time-delay systems. First, we present delay-dependent criteria which provide sufficient conditions for a singular time-delay system to be regular, impulse free and finite-time stable. Then, using LMI approach novel sufficient condition for the finite-time stability is derived. Numerical example is given to show the effectiveness of the proposed approaches.

## 2. Notation and preliminaries

Consider a linear continuous singular system with state delay, described by

$$\hat{E}\dot{\hat{x}}(t) = \hat{A}\hat{x}(t) + \hat{A}_d\hat{x}(t-\tau) \tag{1}$$

with a known compatible vector valued function of the initial conditions

$$\hat{x}(t) = \hat{\varphi}(t), \quad -\tau \le t \le 0 \tag{2}$$

where $\hat{x}(t) \in \Re^n$ is the state vector, $\tau$ is constant time delay, $\hat{A} \in \Re^{n\times n}$ and $\hat{A}_d \in \Re^{n\times n}$ are known constant matrices. It is assumed that $rank(\hat{E}) = r \le n$.
It is known ([12]) that there exist invertible matrices *M* and *N* such that

$$E = M\hat{E}N = \begin{bmatrix} I_r & 0 \\ 0 & 0 \end{bmatrix}, \quad A = M\hat{A}N = \begin{bmatrix} A_{11} & A_{12} \\ A_{21} & A_{22} \end{bmatrix}, \quad A_d = M\hat{A}_d N = \begin{bmatrix} A_d^{11} & A_d^{12} \\ A_d^{21} & A_d^{22} \end{bmatrix} \tag{3}$$

Then, by the nonsingular transformation

$$x = N^{-1}\hat{x} \tag{4}$$

the system (1) can be described by the following system:

$$\begin{aligned} &E\dot{x}(t) = Ax(t) + A_d x(t-\tau) \\ &x(t) = \varphi(t), \quad \varphi(t) = N^{-1}\hat{\varphi}(t), \quad t \in [-\tau, 0] \end{aligned} \tag{5}$$

The following definition will be used in the proof of the main results.
*Definition 1.* Matrix pair $(E, A)$ is said to be regular if $\det(sE - A) \equiv 0$ [6].
*Definition 2.* The matrix pair $(E, A)$ is said to be impulse-free if $deg\det(sE - A) = rank\, E$ [6].
*Lemma 1.* Suppose that the matrix pair $(E, A)$ ($(\hat{E}, \hat{A})$) is regular and impulsive free, then the solution to (5) ((1)) exists and is impulse-free and unique on [0, ∞) [6].
*Definition 3.* The singular continuous system with state delay (5) ((1)) is said to be regular and impulse-free, if the matrix pair $(E, A)$ ($(\hat{E}, \hat{A})$) is regular and impulse-free [6].

*Lemma 2.* Continuous singular time-delay systems (1) and (5) are regular and impulse-free if matrix $A_{22}$, which is defined by (3), is invertible.

*Lemma 3.* For any symmetric, positive definite matrix $\Gamma = \Gamma^T > 0$ the following condition is satisfied:

$$2u^T(t)v(t) \le u^T(t)\Gamma^{-1}u(t) + v^T(t)\Gamma v(t) \tag{6}$$

*Definition 4.* Singular time delayed *s*ystem (5) is finite-time stable with respect to $\{\alpha, \beta, T\}$, $\alpha < \beta$, if

$$\sup_{t\in[-\tau,\,0]} \varphi^T(t)\varphi(t) \le \alpha \tag{7}$$

implies

$$x^T(t)E^T E\,x(t) < \beta, \quad \forall t \in [0,T] \tag{8}$$

## 3. Main results

**Theorem 1.** Consider a singular time-delay *s*ystem (5). If the matrix $A_{22}$, which is defined by (3), is invertible and if there exists a positive scalar $\wp$, matrix $P$ and positive define symmetric matrix $Q$, such that the following conditions hold:

$$PE = E^T P^T \ge 0\ , \quad PE = E^T RE \tag{9}$$

$$\beta e^{-(\Xi_m+\Sigma_m)T}\lambda_{\min}(R) - \alpha\left[\lambda_{\max}(PE) + \tau\,\lambda_{\max}(Q)\right] < 0 \tag{10}$$

where:

$$\Xi_{\mathrm{m}} = \max\left[x^T(t)\Xi x(t):\ \ x^T(t)PE\,x(t) = 1\right], \Xi = A^T P^T + PA + Q + PA_d\wp^{-1}A_d^T P^T \tag{11}$$

$$\Sigma_{\mathrm{m}} = \max\left[x^T(t-\tau)\Sigma x(t-\tau):\ \ x^T(t)PE\,x(t) = 1\right], \quad \Sigma = \wp I - Q \tag{12}$$

then system (5) is regular, impulse free and finite-time stable with respect to $\{\alpha, \beta, T\}$, $\alpha < \beta$ for all $T > 0$.

**Proof.** Based on Lemma 2, the condition $A_{22} \ne 0$ provides that the system (5) is regular and impulse free. Next, we show the stability.

Let us consider the following Lyapunov-like function:

$$V(x(t)) = x^T(t)PE\,x(t) + \int_{t-\tau}^{t} x^T(s)Qx(s)ds \tag{13}$$

Based on Lemma 3, for total derivative $\dot{V}(t,x(t))$ along the trajectories of the system (5) we get:

$$\dot{V}(x(t)) \le x^T(t)\left[A^T P^T + PA + Q + PA_d\wp^{-1}A_d^T P^T\right]x(t) + x^T(t-\tau)\left[\wp I - Q\right]x(t-\tau) \tag{14}$$

Further:

$$\frac{dV(x(t))}{V(x(t))} \le \frac{x^T(t)\Xi x(t) + x^T(t-\tau)\Sigma x(t-\tau)}{V(x(t))}dt = \left(\Xi_{\mathrm{m}} + \Sigma_m\right)dt \tag{15}$$

After integrating the previous inequality we get:

$$V(x(t)) < V(x(0))e^{(\Xi_m+\Sigma_m)t} \tag{16}$$

Furthermore:

$$V\left(x(0)\right) = x^T(0)PEx(0) + \int_{-\tau}^{0} x^T(s)Qx(s)ds \le \alpha\left[\lambda_{\max}(PE) + \tau\lambda_{\max}(Q)\right] \tag{17}$$

$$V\left(x(t)\right) = x^T(t)PEx(t) + \int_{t-\tau}^{t} x^T(s)Qx(s)ds \ge x^T(t)E^T REx(t) > \lambda_{\min}(R)x^T(t)E^T E^T x(t) \tag{18}$$

If the condition (10) is satisfied, then $x^T(t)E^T Ex(t) < \beta$, for all. This completes the proof.

*Theorem 2.* Singular time delayed *s*ystem (5) is regular, impulse free and finite-time stable with respect to $\{\alpha, \beta, T\}$, $\alpha < \beta$, if there exist positive definite matrix $P$, $Q$, matrices $S_0$, $S_1$, nonnegative constant $\gamma$, and positive constants $\lambda_1$, $\lambda_2$ and $\lambda_3$ such that the following LMIs are satisfied:

$$\begin{bmatrix} A^T PE + E^T PA + Q + S_0 R^T A + A^T RS_0^T - \gamma E^T PE & E^T PA_d + S_0 R^T A_d + A^T RS_1^T \\ * & -Q + S_1 R^T A_d + A_d^T RS_1^T \end{bmatrix} < 0 \tag{19}$$

$$\lambda_1 I < P, \quad E^T PE < \lambda_2 I, \quad Q < \lambda_3 I \tag{20}$$

$$\begin{bmatrix} -\beta e^{-\gamma T}\lambda_1 & \sqrt{\alpha}\lambda_2 & \sqrt{\alpha\tau}\lambda_3 \\ * & -\lambda_2 & 0 \\ * & * & -\lambda_3 \end{bmatrix} < 0 \tag{21}$$

where $R$ is any matrix with full column rank and satisfies $E^T R = 0$.

*Proof.* The proof of the regularity and impulse free is proved similarly as Theorem 1 and it is omitted here. Next, we show the finite-time stability. Let us consider the following Lyapunov-like function:

$$V\left(x(t)\right) = x^T(t)E^T PEx(t) + \int_{t-\tau}^{t} x^T(\vartheta)Qx(\vartheta)d\vartheta \tag{22}$$

If we adopt $R^T E = 0$, then:

$$\dot{V}\left(t, x(t)\right) \le \xi^T(t)\bar{\Omega}\xi(t), \quad \xi(t) == \left[x^T(t) \quad x^T(t-\tau)\right]^T \tag{23}$$

where

$$\bar{\Omega} = \begin{bmatrix} A^T PE + E^T PA + Q + S_0 R^T A + A^T RS_0^T & E^T PA_d + S_0 R^T A_d + A^T RS_1^T \\ * & S_1 R^T A_d + A_d^T RS_1^T - Q \end{bmatrix} \tag{24}$$

From (19) and (23), one can have:

$$\dot{V}\left(x(t)\right) < \gamma V\left(x(t)\right) \tag{25}$$

Integrating (25) from 0 to $t \le T$, follows:

$$V\left(x(t)\right) < e^{\gamma t} V\left(x(0)\right) \tag{26}$$

From Definition 4, follows:

$$V\left(x(0)\right) \le \alpha\left[\lambda_{\max}\left(E^T PE\right) + \tau \cdot \lambda_{\max}\left(Q\right)\right] \tag{27}$$

On the other hand, we have:

$$V\left(x(t)\right) > \lambda_{\min}\left(P\right) x^T\left(t\right) E^T E x(t) \tag{28}$$

So combining (26), (27) and (28) we get:

$$x^T\left(t\right) E^T E x(t) < \alpha\, e^{\gamma t}\, \frac{\lambda_{\max}\left(E^T P E\right) + \tau \cdot \lambda_{\max}\left(Q\right)}{\lambda_{\min}\left(P\right)} \tag{29}$$

If

$$\alpha e^{\gamma T}\, \frac{\lambda_{\max}\left(E^T P E\right) + \tau \cdot \lambda_{\max}\left(Q\right)}{\lambda_{\min}\left(P\right)} < \beta \tag{30}$$

then the system (5) is finite-time stable with respect to $\{\alpha,\ \beta,\ T\}$.

If

$$0 < \lambda_1 < \lambda_{\min}\left(P\right), \quad 0 \le \lambda_{\max}\left(E^T P E\right) < \lambda_2, \quad 0 < \lambda_{\max}\left(Q\right) < \lambda_3 \tag{31}$$

then the matrix inequality (20) is satisfied, and

$$-\beta e^{-\alpha T} \lambda_1 + \alpha\lambda_2 + \alpha\tau\lambda_3 < 0 \tag{32}$$

Using Schur complement we get (21).
This completes the proof.

## 4. Numerical examples

The effectiveness of the results presented in the previous section is now shown by means of numerical examples.
*Example 1.* Consider following unstable singular continuous time-delay system:

$$E\dot{x}(t) = Ax(t) + A_d x(t-\tau)$$

$$E = \begin{bmatrix} 1 & 0 & 0 \\ 0 & 1 & 0 \\ 0 & 0 & 0 \end{bmatrix}, \quad A_0 = \begin{bmatrix} -2 & 1 & 0 \\ 0 & -2 & 0 \\ -1 & 0 & -2 \end{bmatrix}, \quad A_1 = \begin{bmatrix} 0.5 & 1 & 0 \\ 1 & 0.5 & 1 \\ 1 & 1 & 0 \end{bmatrix}, \quad \tau = 1 \tag{33}$$

$$\varphi(t) = \begin{bmatrix} 2 & 1 & 0.5 \end{bmatrix}, \quad t \in [-\tau, 0]$$

Let $R = \begin{bmatrix} 0 & 0 & 1 \end{bmatrix}^T$. One should investigate finite-time stability of the system (33) with respect to $\alpha = 3,\ \beta = 26,\ T = 5$. Based on Theorem 2, for fixed $\gamma = 1 \cdot 10^{-2}$, follows that the LMI conditions (19)-(21) are feasible. Therefore, the system (33) is regular, impulse free and finite-time stable with respect to $(3, 26, 5)$.

## 5. Conclusion

Generally, this paper extends some of the basic results in the area of the non-Lyapunov stability to the particular class of linear singular time-delay systems. The finite-time stability problems of linear singular time-delay systems are studied. Using classical and LMI approaches novel sufficient conditions for finite-time stability are presented. The obtained LMI conditions can be checked by using the standard numerical optimization methods. Finally, a numerical example is given to show the effectiveness of the proposed approaches.

**Acknowledgement.** This work has been supported by The Ministry of Science and Technological Development of Serbia under the Project ON 174001.

## References

[1] Campbell S L (1980) *Singular Systems of Differential Equations*, Pitman, London.

[2] Müller P C (1993) Stability of Linear Mechanical Systems with Holonomic Constraints, *Appl. Mech. Rev*., 46 (11) 60–164.

[3] Pantelides C C, Gridsis D, Morison K R, Sargent R W H (1988) The mathematical modeling of transient systems using differential-algebraic equations, *Comp. & Chem. Eng*., 12 449–454.

[4] Kumar A, Daoutidis P (1997) Control of nonlinear differential algebraic equation systems: an overview, *Proc. NATO Advanced Study Institute on Nonlinear Model Based Process Control*, Antalya, Turkey, August 10-20, 311-344.

[5] Rehm A, Allgower F (2004) H-Infinity Control of Descriptor Systems: An Application from Binary Distillation Control, *Proc. 7 International Symposium on Advanced Control of Chemical Processes*, Hong Kong, 11-14 January.

[6] Xu S, Dooren P V, Stefan R, Lam J (2002) Robust stability and stabilization for singular systems with state delay and parameter uncertainty, *IEEE Trans. Autom. Control*, 47(7) 1122–1128.

[7] Xu S, Lam J, Yang C (2003) H∞ control for uncertain singular systems with state delay, *Int. J. Robust Nonlinear Control*, 13 (13) 1213–1223.

[8] Fridman E (2002) Stability of linear descriptor systems with delay: a Lyapunov-based approach, *J. Math. Anal. Appl*., 273 24–44.

[9] Yue D, Han Q L (2005) Delay-dependent robust H∞ controller design for uncertain descriptor systems with time-varying discrete and distributed delays, *IEE Proc. Control Theory Appl*., 152(6) 628–638.

[10] Zhu S, Zhang C, Cheng Z, Feng J (2007) Delay-dependent robust stability criteria for two classes of uncertain singular time-delay systems, *IEEE Trans. Autom. Control*, 52(5) 880–885.

[11] Xu S, Lam J, Zou Y (2008) An improved characterization of bounded realness for singular delay systems and its applications, *Int. J. Robust Nonlinear Control*, 18(3) 263–277.

[12] Dai L (1981) Singular Control Systems, Springer, Berlin.

[13] Debeljkovic D Lj, Lazarevic M P, Koruga Dj, Tomasevic S (1997) Finite time stability of singular systems operating under perturbing forces: Matrix measure approach, *Proc. AMSE Conference*, Melbourne Australia, October 29 – 31 447–450.

[14] Kablar N A, Debeljkovic D Lj (1998) Non-Lyapunov stability of linear singular systems: Matrix measure approach, *Proc. Mathematical Theory of Networks and Systems*, Padova, Italy, July 6-10.

[15] Kablar N A, Debeljkovic D Lj (1998) Non-Lyapunov stability of linear singular systems: Matrix measure approach, *Proc. 5th IFAC Symposium on Low Cost Automation*, Shenyang, China, September 8-10 16 – 20.

[16] Kablar N A, Debeljkovic D Lj (1998) Finite time stability of time varying singular systems, *Proc IEEE Decision and Control*, Florida, USA, December 10-12 3831-3836.

[17] Debeljkovic D Lj, Kablar N A (1998) On necessary and sufficient conditions of linear singular systems stability operating on finite time interval, *Proc. XII CBA* , Uberlandia, Brazil Sep. 14 -18 Vol. IV, 1241-1246.

[18] Kablar N A, Debeljkovic D Lj (1999) Finite time instability of time varying linear singular systems, *Proc. IEEE ACC 99*, San Diego, USA, June 2-4 1796-1800.

[19] D.Lj. Debeljkovic, N.A. Kablar (1999) Finite time stability of linear singular systems: Bellman-Gronwall approach, *Proc. IEEE ACC 99*, San Diego, USA, June 2-4, 1803-1806.

[20] Yangy C., Zhang Y Q, Linz Y, Zhouy L (2006) Practical stability of closed-loop descriptor systems, *Int. J. Syst. Sci.*, 37(14) 1059–1067.

[21] Jun-E F, Zhen W, Jia-Bing S (2005) Finite-time control of linear singular systems subject to parametric uncertain and disturbances, *Acta Autom. Sin*., 31(4) 634-637.

[22] Yang C Y, Jing X, Zhang Q L, Zhou L N (2008) Practical stability analysis and synthesis of linear descriptor systems with disturbances, *Int. J. Autom. Comput*., 5(2) 138–144.

[23] Yang C, Zhang Q, Zhou L (2006) Practical stability of descriptor systems with time delays in terms of two measurements, *J. Franklin Inst*., 343 635–646.

[24] Su M, Wang S, Zhang X (2012) Finite-Time Stabilization for Singular Linear Time-delay Systems with Time-varying Exogenous Disturbance, *Adv. Mater. Res*., 490-495 2459-2463.

[25] Owens D H, Debeljkovic D Lj (1985) Consistency and Lyapunov Stability of Linear Descriptor Systems: a Geometric Analysis, *IMA J. Math. Control Inf*., 2 139-151.

[26] Hale J K (1977) *Theory of Functional Differential Equations*, Springer-Verlag, New York.

# MECHANICAL PROPERTIES INVESTIGATION OF COMMERCIAL AND NANOPHOTONICS SOFT CONTACT LENSES

**Vladimir Veljić[1], Aleksandra Debeljković[1], Đuro Koruga[2]**

[1] Innovation Center of Faculty of Mechanical Engineering,
The University of Belgrade, Kraljice Marije 16, 11120 Belgrade 35
e-mail: veljicvladimir@yahoo.com
e-mail: aleksandra.debeljkovic@gmail.com
[2] Faculty of Mechanical Engineering,
The University of Belgrade, Kraljice Marije 16, 11120 Belgrade 35
e-mail: djkoruga@mas.bg.ac.rs

**Abstract.** The contact lens industry and market have displayed a high level of dynamism in the past few decades, and have evolved into a rapidly changing field in which science and everyday practice constantly interact [1]. This work presents comparative research of characteristics of basic-commercial material and nanophotonic materials which were obtained by incorporation of fullerene nanoparticles in base material for soft contact lenses. Basic contact lens material was sintetized of monomer pHEMA, and fullerene was used due to his good transmission characteristics in ultra-violet, visible and near infra-red spectrum. Topography of soft contact lenses surfaces was obtained by atomic force microscope (AFM). AFM is a very powerful method of the characterization of complex polymer systems and it can measure sample surface roughness with high precision (less than $10^{-9}$m ≈ 1nm). Topography of lens surface is important for determining the connection between surface topography and corresponding optomechanical properties.[2,3]

## 1.Introduction

The technology of materials used in contact lenses production has improved vastly in the past decades starting from glass and moving to polymer based materials [3]. Since its first application for biological use in 1960, poly 2-hydroxyethyl methacrylate, pHEMA, has been used in many biomedical fields. Due to these reasons, the material properties of pHEMA have been extensively studied in many aspects such as swelling behavior in aqueous solutions, the nature of the absorbed water, gas permeation, and mechanical properties [1,2,4]. One of the main applications of these pHEMA hydrogels is in the manufacturing of basic contact lenses. Nanophotonic material was obtained by incorporating nanoparticles of fullerene and its derivates in the basic material for soft contact lenses. In order to improve a fundamental understanding, more information about its surface properties at the molecular level needs to be generated. To this end, we have studied the surfaces of soft contact lenses made of basic and nanophotonic material with atomic force microscopy (AFM).

## 2.Method of AFM

AFM is a scanning probe microscopy technique based on point-to-point examination of the specimen made by a sharpened tip probe. AFM probe is a micro-cantilever with sharpened conical or pyramidal tip whose radius can range from 2 – 90 nm, depending on the application. The principle of operation of AFM is shown in figure 1. In AFM, the probe (cantilever tip) is vibrated at near-resonant frequency and brought into interaction with the sample by the mechanism of intermolecular attractive/repulsive forces that are distance-dependent. The cantilever is maintained in the close proximity from the sample so that probe tip is within reach of attractive/repulsive forces. A typical AFM system is able to detect intermolecular forces in the order of $10^{-11} - 10^{-13}$ N which makes it an extremely sensitive device. The intermolecular interactions belong to the class of Van der Waals type forces, usually modeled by Lennard-Jones potentials. These forces cause the cantilever to deflect from the initial equilibrium position making it possible to derive the distance from the sample on the basis of force field gradient change that modulates the vibration of the cantilever.

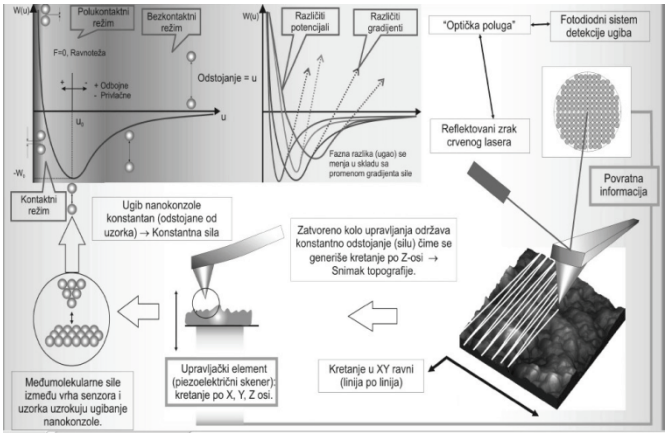


**Figure 1.** Principle of operation of atomic force microscope [3]

Many interesting studies have been performed on contact lenses using AFM [2,3,4,] in which the surface morphology has been investigated under various conditions. AFM technique gives image topography, precisely information about surface shape and relative positions and dimensions of particles. AFM image on the other side differentiates between different force gradients which in turn point to different conformational states of polymers, under the assumption that material constituents are homogenously distributed throughout the sample [6].

## 3.Experimental

All studies were performed in NanoLab at the Faculty of Mechanical Engineering of the University of Belgrade. In this research the new types of contact lense with incorporated nanoparticles (fullerene) was used. These nanomaterial was added during the polymerization process in the basic material, poly hydroxyethyl methacrylate. All samples were imaged in tapping mode and in ambient air. The AFM system used in this study was JSPM-5200, JEOL, Japan. Topography measurements were done using uniform scanning surface of 10 × 10μm for the basic material and 7 × 7μm for the nanophotonic material. It is used cantilever NSC35/AlBS produced by MicroMasch. The most important characteristics of this cantilever are shown in table 1.

| **Cantilever** | **A** | **B** | **C** |
|---|---|---|---|
| Length | 110 μm | 90 μm | 130 μm |
| Force constant | 8.9 N/m | 16 N/m | 5.4 N/m |
| Resonance frequency | 205 kHz | 300 kHz | 150 kHz |

**Table 1.** AFM Probe with 3 Different Tapping Mode Cantilevers NSC35/AlBS

All measurements were performed at room temperature and air humidity of 53% in space measuring device that is protected with glass bell.
The surface roughness is described by three different parameters: $R_z$ the root-mean-square roughness, i.e., the standard deviation of the z-axis values within a given area; $R_a$: the mean roughness, i.e., the arithmetic average of the deviations from the central plane; $R_q$: the difference between the highest and lowest points on the surface [5].

## 4.Results

Topography measurements were done using uniform scanning surface of 10 × 10μm for the basic material and 7 × 7μm for the nanophotonic material. The soft contact lens inner surface has been examined as shown in figure 2. It is observed that topography of basic material has a fine structure in the majority part with the periodic high elevations (hills). Because of these jumps contour lines can be concluded that the surface is quite nonuniform namely that the roughness of the nanophotonic material is more inconvenient than is the basic material.

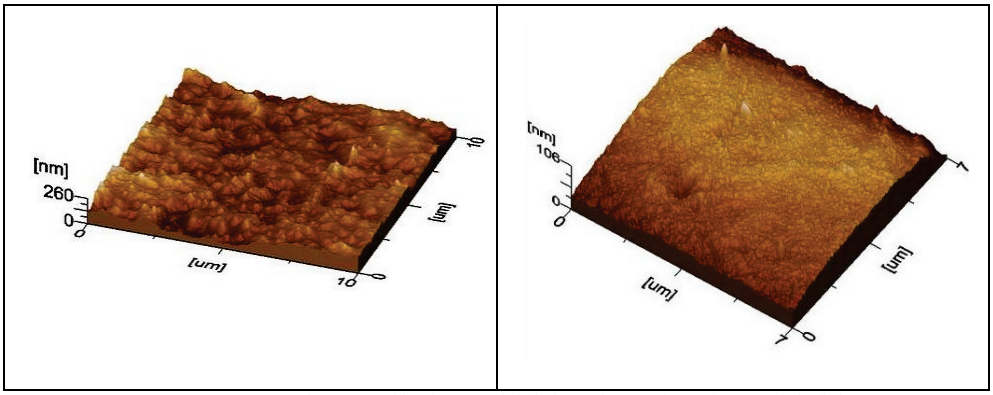


**Figure 2.** Topography (3D) of basic material (left) and nanophotonic material (right)

A comparison of surface roughness was based on the values obtained by AFM, such as $R_a$, $R_z$ and $R_q$. This three roughness parameters can adequately predict the surface character. Figure 3. shows the topography of surface of soft contact lens made of basic material. The relevant values of roughness are given, also.

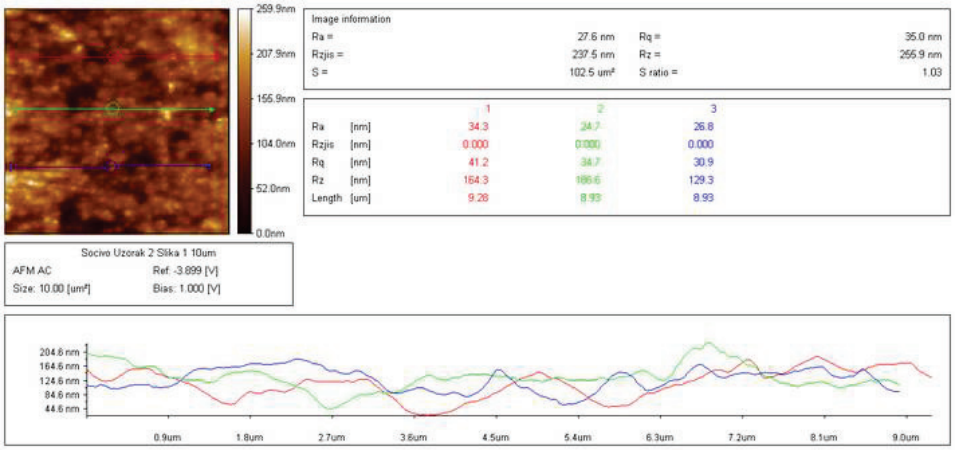


**Figure 3.** Topography of surface of basic soft contact lens

Figure 4. shows the topography of surface of soft contact lens made of basic material, three profile (blue, red, yellow), and also values of roughness.

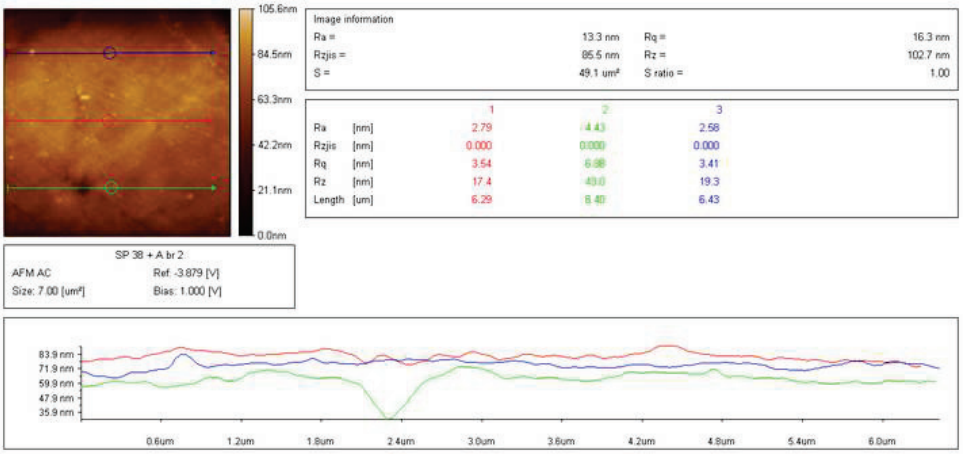


Figure 4. Topography of surface of nanophotonic soft contact lens

Comparing values of the mean roughness for soft contact lens made of basic ($R_a$ = 27.6 nm) and nanophotonic material ($R_a$ = 13.3 nm), it is easy to conclude that the surface of nanophotonic soft contact lens is less rough then the surface of basic soft contact lens. This is the mean roughness of the whole surface, so less rough surface means more regular and more uniform topography of the observed material. Analogously, this is true for parameters $R_q$ and $R_z$. For the basic soft contact lens $R_q$ = 35 nm and $R_z$ = 255.9 nm, and for the nanophotonic this values are smaller, $R_q$ = 16.3 nm and $R_z$ = 102.7 nm. Only reason for the roughness difference is incorporated fullerene. The surface roughness has a considerable influence on biocompatibility and generates important information about the material surface quality.

## 5.Conclusion

It is demonstrated that the application of AFM is a very useful method for detailed characterization of contact lenses surface. It is obvious that the fullerene has a considerable influence on the contact lens surface topography, as it is demonstrated by the values of roughness parameters. Nanophotonic material has a more uniform structure of the basic material. More uniform material structure provides greater comfort contact lenses for his patients as well as reducing the risk of irritation and eye infections.

***Acknowledgement.*** The authors acknowledge funding from the Ministry of Education and Science and Technology of the Republic of Serbia, Project No. III 45009. Also, parts of this research were supported by the Ministry of Education, Sciences and Technology of Republic of Serbia through Mathematical Institute SANU Belgrade Grant OI174001.

## References

[1] Lim H., Lee Y., Han S., Cho J., Kim K.J. (2001) Surface treatment and characterization of PMMA, PHEMA, and PHPMA, *Journal of Vacuum Science and Technology A*, Vol. 19, No. 4, pp. 1490–1496

[2] Bojović B., Miljković Z., Babić B. (2008) Fractal Analysis of AFM Images of Worn-Out Contact Lens Surface, *Faculty of Mechanical Engineering Transaction*, 36, 4, 175–180, ISSN 1451–2092

[3] Kojić D., Bojović B., Stamenković D., Jagodić N., Koruga Đ. (2012) Contact Lenses Characterization by AFM, MFM, and OMF, *Biomedical Science, Engineering and Technology InTech*, ISBN: 978-953-307-471-9.

[4] Kima S. H., Marmob C., Somorjaia, G. A. (2001) Friction studies of hydrogel contact lenses using AFM: non-crosslinked polymers of low friction at the surface, *Biomaterials*, Vol. 22, pp. 3285–3294

[5] Guryca V., Hobzova R., Pradny M., Širc J., Michalek J. (2007) Surface morphology of contact lenses probed with microscopy techniques, *Contact Lens & Anterior Eye* Vol. 30, pp. 215–222

[6] Stamenkovic D., Kojic D., Matija L., Miljkovic Z., Babic B., (2010) Physical Properties of contact lenses characterized by scanning probe microscopy and optomagnetic fingerprint, *International Journal of Modern Physics B*, Vol. 24, pp. 825–834

# COMPUTATION OF ACOUSTIC SOURCES FOR THE LANDING GEAR DURING THE TAKE-OFF AND LANDING

**Vladimir Jazarević, Boško Rašuo**

[1] Institute of Aeronautics
Faculty of Mechanical Engineering
The University of Belgrade, Kraljice Marije 16, 11120 Belgrade 35
e-mail: vlada.jazarevic@gmail.com
[2] Faculty of Mechanical Engineering,
The University of Belgrade, Kraljice Marije 16, 11120 Belgrade 35
e-mail: brasuo@mas.bg.ac.rs

**Abstract.** The sound which is generated from aircraft during the take-off and landing is one of the main problems for the peoples who lives in areas near the airport. It is very important to allocate and accurately calculate acoustic sources generated from turbulent flow produced by the aerodynamics components of aircraft in order to calculate inhomogeneous term of Helmholtz equation which leads to better prediction of sound propagation in domain. It is used subgrid-scale stabilized finite element method for solving incompressible Navier-Stokes equation for simulation of turbulent flow and double divergence of Litghill's tensor in order to calculate acoustics sources, further the transformation from time domain to frequency domain is used with Direct Fourier Transform which leads to smaller computational cost. It is shown that this method lead to better and richer representation of spectrum of frequencies which will give better inhomogeneous term of Helmholtz equation. Better prediction and calculation of acoustics sources will lead to reduction of sound through design of aerodynamics components on aircraft.

**Keywords**: Aeroacoustics,turbulent flow, subgrid-scale stabilized finite element method, Litghill's analogy, Direct Fourier transform, LES method

## 1. Introduction

With the constant need to travel faster, better and safer through air, the industry of aeronautics become one of industry with the highest progression in last century. As always progression lead to some problems that has to be overcome. One of the biggest problem for civil aviation and for people who are living near the airports is sound generated from aircrafts. In one period of aviation history scientists and engineers thought that sound is coming from aircraft engine, but during 1960 Lighthill notice that flow around aircrafts (aerodynamics) produce significant part of sound. In this period emerged a new field Aeroacoustics. This field investigate sound generated by unsteady and/or turbulent flow and also by their interaction with solid boundaries [1]. With constant growth of capabilities of personal computers also new field of computational mechanics emerged Computational Aeroacoustics (CAA). The aim of this field is to simulate and predict aerodynamically generated noise. Nowadays CAA has become an active area of research field due to its applications in the aeronautics, railway, automotive and underwater industry.
The objective of this work is to present stabilized finite element method for the approximation of incompressible Navier-Stokes equation and calculation of Lighthill's tensor which arise in Aeroacoustics for calculation of low speed CAA predictions acoustics sources. These sources are the source for the inhomogeneous Helmholtz equation which calculate distribution of pressure field in order to predict sound in domain. This work will show how different methods of stabilization for the Navier-Stokes equation gives different

solution of calculation of Lighthill's tensor. The natural way to predict turbulent flow is LES (Large Eddy Simulation) [2] which would be presented shortly and compared with proposed method of Orthogonal Subgrid-scale method (Variational multiscale method) proposed by Hughes [3]. The goal is to show how the small scales eddies has to be modelled and how they affect simulation of turbulent flow and latter calculation of aeroacoustics sources.

## 2. Subgrid scale stabilised finite element method with quasi static and dynamical subscales

To apply the SGS stabilised finite element method, we will decompose the velocity and velocity test function $\boldsymbol{u} = \boldsymbol{u}_h + \tilde{u}$, $\boldsymbol{v} = \boldsymbol{v}_h + \tilde{v}$ which correspond to the space splitting $V_0^d = V_{h,0}^d \oplus V_0^d$. The velocity time derivative can be split as $\partial_t \boldsymbol{u} = \partial_t \boldsymbol{u}_h + \partial_t \tilde{\mathrm{u}}$. The first term in previous equation would be the only one kept if the time derivative of the subscales is neglected. In this situation the subscales are termed as quasi-static [7].If the second term is kept, the subgrid scales are termed as dynamical subsales. We will decompose the pressure and the pressure test function as $p = p_h + \tilde{p}$, $q = q_h + \tilde{q}$ corresponding to the space splitting $Q_0 = Q_{h,0} \oplus Q_0$. where $\boldsymbol{u}_h$, $p_h$ belong to the finite element space and $\tilde{u}$ and $\tilde{p}$ are what we will call the subgrid scale. For simplicity, we will not consider pressure subscales, thus we consider $\boldsymbol{u}_* = \boldsymbol{u}_h + \tilde{u}$, $p \approx p_h$. Inserting this splitting in Galerkin formulation (multiplying with test function and integrate over hole domain) yield to:

$$\left(\partial_t \boldsymbol{u}_h, \boldsymbol{v}_h\right) + \left(\boldsymbol{u}_* \cdot \nabla \boldsymbol{u}_h, \boldsymbol{v}_h\right) + \upsilon\left(\nabla \boldsymbol{u}_h, \nabla \mathbf{v}_h\right) - (p_h, \nabla \cdot v_h) + (q_h, \nabla u_h).$$

$$+\left(\partial_t \tilde{u}, \boldsymbol{v}_h\right) - \sum_K \left\langle \tilde{u}, \boldsymbol{u}_* \cdot \nabla \boldsymbol{v}_h + \boldsymbol{\upsilon} \Delta \boldsymbol{v}_h + \nabla q_h \right\rangle_K + \sum_{\boldsymbol{K}} \left\langle \tilde{u}, \boldsymbol{\upsilon}\, \boldsymbol{n} \cdot \nabla \boldsymbol{v}_h + q_h\, n \right\rangle_{\partial k} = (\boldsymbol{f}, \boldsymbol{v}_h) \qquad (11)$$

$$\left(\partial_t \tilde{u}, \tilde{v}\right) + \sum_{\boldsymbol{K}} \left\langle u_* \cdot \nabla \tilde{u} - \boldsymbol{\upsilon} \Delta \tilde{u}, \tilde{v} \right\rangle_K + \sum_{\boldsymbol{K}} \left\langle \upsilon\, \boldsymbol{n} \cdot \nabla \tilde{u}, \tilde{v} \right\rangle + \sum_{\boldsymbol{K}} \left\langle \partial_t \boldsymbol{u}_h + \boldsymbol{u}_* \nabla \boldsymbol{u}_h - \boldsymbol{\upsilon} \Delta \boldsymbol{u}_h + \nabla p_h, \tilde{v} \right\rangle$$

$$+ \sum_{\kappa} \left\langle \upsilon\, \boldsymbol{n} \cdot \nabla \boldsymbol{u}_* - p_* \boldsymbol{n}, \tilde{v} \right\rangle. \qquad (12)$$

Where equation (11) correspond to the large scales and equation (12) correspond to the small scales. Assuming that the velocity subscales will be zero at the element boundaries as well as on $\partial\Omega$. This allows to understand the velocity subscales as bubble function vanishing on inter element boundaries. Applying these assumptions in equation (11) leads to equation for large scales

$$\begin{aligned}(\partial_t u_h, v_h) + \left\langle u_h \cdot \nabla u_h, v_h \right\rangle + \upsilon(\nabla u_h, \nabla v_h) - (p_h, \nabla \cdot v_h) + (q_h, \nabla \cdot u_h) \\ -\sum_{\Omega_e} \left\langle \tilde{u}, \upsilon \Delta v_h + u_h \cdot \nabla v_h + \nabla q_h \right\rangle_{\Omega_e} \\ +(\delta_t \tilde{u}, v_h) + \left\langle \tilde{u} \cdot \nabla u_h, v_h \right\rangle \\ -\left\langle \tilde{u} \cdot \nabla v_h \right\rangle = l(v) \end{aligned} \qquad (13)$$

The first line contains the Galerkin terms. The second line correspond to terms that are already obtained in stabilization of the linearized and stationary version of the Navier-Stokes equation. It is well known that the inclusion of these terms in the formulation allow to circumvent the convection instabilities and to use equal interpolation for the velocity and the pressure fields. The third and fourth lines contain terms arising from the effects of the velocity subscales $\tilde{u}$ n the material derivative of the equation. The first term in the third accounts for the time derivatives of the subscales and appearance of this term will distinguish method with dynamical subscales from method with quasi-static subscales, while we will justify that the second term provides global momentum conservation which is not satisfied in Galerkin finite element approach. The fourth line corresponds to a Reynolds stress for subscales. It would be explained that this term may be identified with the direct effects of the subscale turbulence onto the large scales. The key point of formulation in (13) that distinguish it from the standard SGS approach that resulted in the appearance of the additional third and fourth lines in (13) has been to keep all terms associated to the effectsof the velocity subscales ***u*** in the material derivative of the exact velocity field.

$$\frac{D}{Dt}u = \frac{D}{Dt}\left(u_h + \tilde{u}\right) = \partial u_h + \partial_t \tilde{u} + \tilde{u}\cdot\nabla u_h + u_h\cdot\nabla u_h + \tilde{u}\cdot\nabla\tilde{u} + u_h\cdot\nabla\tilde{u} \qquad 14)$$

Note that $\partial_t \boldsymbol{u}_h$ and $u_h\cdot\nabla u_h$ once discretized in time appear in the Galerkin formulation and the last term in (14), contributes to the standard SGS stabilisation in (13). The remaining terms $\partial_t\tilde{u}$ $\tilde{u}\cdot\nabla u_h$ and $\tilde{u}\cdot\nabla\tilde{u}$ re the hew terms respectively accounting for the time dependence of the velocity subscales, momentum conservation and the subscale Reynolds stresses. Our aim is to find now the solution in (13). Obviously to do so we first need a value for the subscales $\tilde{u}$ hat has to be obtained from the solution of the small subgrid scales equation of the problem. This equation can be written in differential form as

$$\delta_t\tilde{u} + \left(u_h + \tilde{u}\right)\cdot\nabla\tilde{u} - \upsilon\Delta\tilde{u} + \nabla\tilde{p} = r_{u,h} \qquad (15)$$

with $r_{u,h}$ epresenting residual of the finite element components $u_h$ given by

$$r_{u,h} = \mathcal{P}[\delta_t\tilde{u} + \left(u_h + \tilde{u}\right)\cdot\nabla\tilde{u} - \upsilon\Delta\tilde{u} + \nabla\tilde{p} - f] \qquad (16)$$

It would be refer to the case $\mathcal{P} = \mathcal{I}$ . (entity) [4] as the Algebraic Subgrid Scale (ASGS) method, whereas $\mathcal{P} = \mathbb{P}_h = \mathcal{I} - \mathbb{P}_h$, standing for the $L^2$ projection onto the appropriate velocity or pressure finite element space leads to the Orthogonal Subscale Stabilisation (OSS) approach. Using arguments based on a Fourier analysis for the subscale [8], the system of equation (15)-(16) can be approximated as

$$\partial_t\tilde{u} + \frac{1}{\tau_1}\tilde{u} = r_{u,h} \qquad (17)$$

where the stabilisation parameter $\tau_1$ have the expression

$$\tau_1 = (c_1\frac{\upsilon}{h^2} + c_2\frac{\left|u_h + \tilde{u}\right|}{h})^{-1} \qquad (18)$$

$c_1$ and $c_2$ in (18) are algorithmic parameters with recommended values of $c_1$=4 and $c_2$=2 for linear elements, while h stands for a characteristic mesh element size. From a physical point of view, the approximation (17) to problem (15) ensures that the kinetic energy of the modelled subscales resembles the kinetic energy of the exact subscales . Before we are writing final equation we will obtain essential approximation which state.

$$\sum_K \langle u_* \cdot \nabla \tilde{u} - \upsilon \Delta \tilde{u}, \tilde{v} \rangle_K \approx \sum_K \tau_1^{-1} \langle \tilde{u}, \tilde{v} \rangle_K \tag{20}$$

The approximations described allow us to formulate a method that can be effectively implemented and that is the formulation we propose. It consists in finding $u_h \in L^2(0,T;V_h)$ and $p_h \in D(0,T;Q_h)$ such that

$$(\partial_t \boldsymbol{u}_h, \boldsymbol{v}_h) + (\boldsymbol{u}_* \cdot \nabla \boldsymbol{u}_h, \boldsymbol{v}_h) + \upsilon (\nabla \boldsymbol{u}_h, \nabla \mathbf{v}_h) - (p_h, \nabla \cdot v_h) + (q_h, \nabla u_h) + \sum \langle \tilde{u}, u_* \cdot \nabla v_h + \upsilon \Delta v_h + \nabla p_h \rangle_{\Omega_e} = (f, v_h) \tag{21}$$

$$(\partial_t \tilde{u}, \tilde{v}) + \sum \tau_K^{-1} \langle \tilde{u}, \tilde{v} \rangle_{\Omega_e} \sum \langle u_* \cdot \nabla u_h - \upsilon \Delta u_h + \nabla p_h, \tilde{v} \rangle = (f, \tilde{v}) \tag{22}$$

### *2.4 CFD Simulation of simplified landing gear struts with horizontal angle α=0° using LES model and SGS method with dynamical subscales*

Here it would be presented the practical part of the article where it would be shown CFD simulation of generic landing gear struts shown in Figure 1. For sake of simplicity it would be simulated 2D version of simple 3D model shown in Figure 2. It is assumes as two struts are of infinite third dimension and emerged in an infinite uniform flow.

**Figure 1.** Landing gear

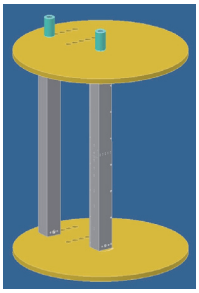

**Figure 2.** Simple 3D model of two struts

We will concentrate here in the case where the flow loses its steadiness as well as its up-and-down symmetry and a wake of altering vortices are formed behind the struts. The set of these shed vortices is known as the von Karman vortex street. Vortex shedding induces lift fluctuations on the body, which lead to the radiation of sound having dipole pattern. The configuration of struts consists of two in line square struts at centre to centre distance S=0.16m. Both struts have width D=0.04m. the distributed flow speed is $U_0$=70m/s which is imposed on the left side of rectangle domain and the fluid is air at atmospheric pressure and ambient temperature (say 20 °C). The mesh used to perform computation is shown in Figure 3.

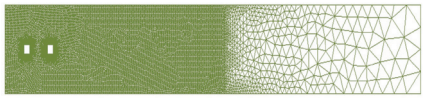

**Figure 3.**

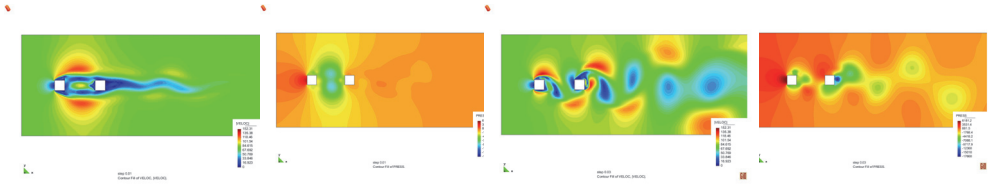

**Figure 4.** Velocity and pressure field using LES model

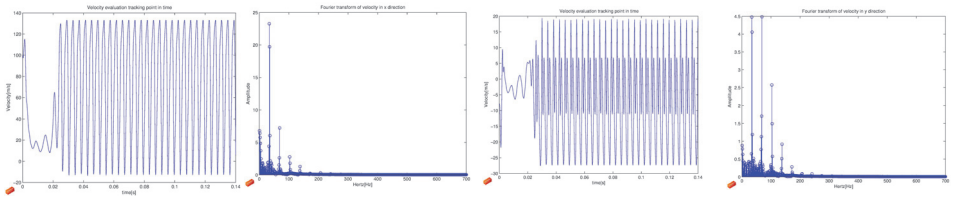

**Figure 5.** Velocity tracking (x and y component) in point between struts and spectral diagram of velocity obtained with LES model

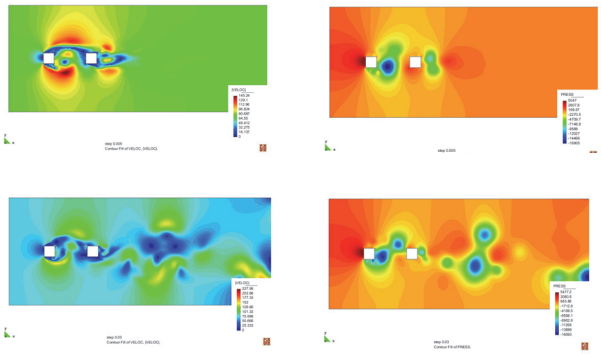

**Figure 6.** Velocity and pressure field using SGS with dynamical subscales

In figure 4-5. Is shown velocity and pressure field using LES model. As it is clear from figure 5. That LES model has a poor spectrum diagram of frequencies what means that this model is simulating only large scales and only small amount of small scales. Also what is obvious that this model is very dissipative because in this case the LES cannot capture real turbulent behaviour for this velocity and Reynolds number.

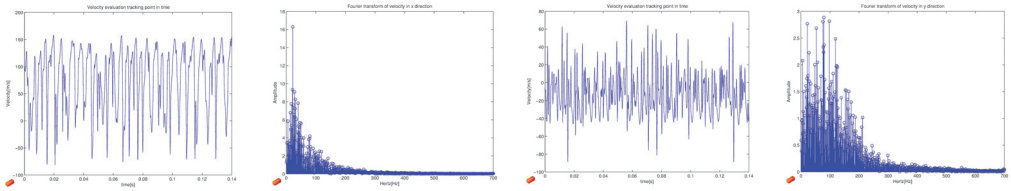

**Figure 7.** Velocity tracking (x and y component) in point between struts and spectral diagram of velocity obtained with SGS with dynamical subscales model

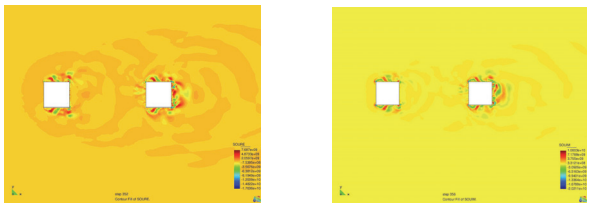

**Figure 8.** Dipole pattern of acoustics sources obtained from turbulent flow ( real and imaginary part) using SGS with dynamical subscales

In figure 6-7 is shown velocity and pressure field and also velocity tracking in point between struts. From the figure 7. Is obvious that SGS method with dynamical subscales is giving better representation of turbulent flow and also giving the richer spectral diagram recovering small fluctuations who are coming from small scales. In the end is shown figure 8. Where is shown acoustics sources for some particular frequency. Aeroacousitcs source is imaginary number and because of that is shown real and imaginary part. In the figure is recognized dipole pattern of aeroacoustics sources which is recognizable for von Karmen vortex shedding behaviour of turbulent flow.

## 3. **Conclusion**

The main objective of this article was to show the advantage of using new method of SGS with dynamical subscales. The advantage is in better representation of turbulent flow which is clearly shown in previous figures. This method is giving good representation of small scales which are somehow lost in LES modelling.
This better presentation of turbulent flow immediately is giving better representation of aeroacoustics sources, and in future is giving richer inhomogeneous term of Helmholtz equation which model the acoustic propagation in domain.

## **Preferences**

**[**1**]** J. Flowcs – Williams and D. Hawkings. Sound generated by turbulence and surfaces in arbitrary motion. Phil Trans Roy. Sec A, 264: 321-342,1969
[2] V. Canuto. Large Eddy simulation of turbulence: a subgrid scale model including shear, vortivity, rotation and buoyancy. Astrophysical J., 428: 729-758, 1994
[3] T.J.R. Hughes. Multiscale phenomena: Green's function, the Dirichlet-to-Neumann formulation, subgrid scale models, bubbles and the origins of stabilized formulations. *Computer Methods in Applied Mechanics and engineering, 127: 387-401,1995*
[4] S. Pope. Turbulent flows. 38,2000
**[**5**]** L. Berselli, T. Iliescu, and W. Layton, Mathematics of Large Eddy Simulation of turbulent flows. Springer – Verlag, 2006
[6] Germano. Differential filters for the large eddy simulation of turbulent flows. Phys. Fluids,, 29(6): 1755-1757,1986
[7] R.Codina. Stabilisation of incompressibility and convection through orthogonal sub-scales in finite element methods. *Computer Methods in Applied Mechanics and engineering, 190: 1579-1599, 1965*
[8] R. Codina. Stabilized finite element approximation of transient incompressible flows using orthogonal subscales. *Computer Methods in Applied Mechanics and engineering, 191: 4295-4321, 2002*

# MICROMECHANICS OF DILATANCY, CRITICAL STATE AND SHEAR BANDS IN GRANULAR MATTERIALS

**Siniša Đ. Mesarović[1], Jagan M. Padbidri[2], Balasingam Muhunthan[3]**

[1]School of Mechanical and Materials Engineering, Washington State University, Pullman, WA, USA, mesarovic@mme.wsu.edu
[2]George W. Woodruff School of Mechanical Engineering, Georgia Institute of Technology, Atlanta, GA, USA, jagan.padbidri@me.gatech.edu
[3]Department of Civil and Environmental Engineering, Washington State University, Pullman, WA, USA, muhuntha@wsu.edu

**Abstract.** By means of graph theory, we analyze the changes in topology of a granular assembly during deformation. The elementary mechanism of diffuse deformation consists of intermittent flips. We show that dilatancy is the direct result of: an increasing number of flips, and, elastic relaxation of particles upon flips. Both are dependent on particles' elastic potential energy prior to flip and after the flip. The latter is the result of nonuniform distribution of interparticle forces in force chains. Next, we consider shear bands in granular materials. Formation of shear bands is accompanied by accompanied by massive rolling of particle. Since rolling is constrained by neighbors, a characteristic rolling correlation length appears. The transmission of rotations in a particular direction depends on the strength of the force chain branches in the direction of propagation and across. The maximum propagation distance is comparable to observed widths of shear bands.

## 1. Introduction

Dilatancy in granular materials has been known since XIX century [1]. Despite of wealth of experimental observations [2-4] and phenomenological macroscopic models, the current understanding of dilatancy is purely empirical. The original Reynolds' rational for dilatancy, that nearly rigid particles must climb over each other to accommodate shear [5], only brings about other questions. Why materials particulate on the atomic level, such as crystals and simple fluids, don't dilate, as the rigid sphere model of densely packed atoms would predict? Moreover, the boundary between dilation and compaction behaviour, the *critical state*, depends on both porosity and pressure. Yet, the only existing rational for dilatancy, excludes pressure dependence.

Depending on the state of a particle assembly and boundary conditions, deformation may localize into a persistent shear band. Numerous experimental observations of shear bands of width 10-20 particle diameters [6] indicate that this width may be a universal length scale. The formation of a shear band is accompanied by massive rolling of particles within the band [7, 8]. Sliding engages frictional dissipation and thus requires more work for the same displacement than rolling, so that the latter is always the energetically preferred form of transverse relative motion. However, in a densely packed assembly, pure rolling motion is impossible, owing to the constraint posed by neighboring particles, as illustrated in Figure 1.

Since perfect rolling is impossible, sliding dissipates the energy so that only a part of the angular velocity of a rotating particle is transmitted to its neighbors. Therefore, the

information about rotation of a particle diminishes with distance from the particle through successive interparticle contacts. This implies the existence of a length scale, the *rotation transmission distance*, associated with the deformation process, which represents the distance from a particle beyond which the information about particle's rotation is not transmitted. For spherical particles, this length will depend on friction, pressure, particle size distribution, and the state of the assembly (e.g., the level of compaction). For non-spherical particles, additional parameters, such as the aspect ratio, will play a role.

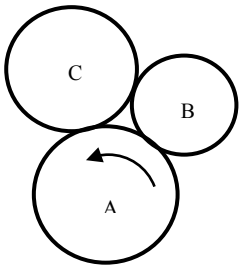


**Figure 1.** Necessity of sliding in a cluster of particles. The centers of three particles A, B and C are fixed and the particles are in contact with each other. Impose the counterclockwise rotation on particle A, as shown. Relative sliding is defined by non-zero relative velocities of the contact points. To avoid sliding with respect to A, both B and C must both rotate in the clockwise direction. But this will result in sliding on the B-C contact.

The rotation transmission is the result of frictional constraint and must depend on normal forces which are locally directionally dependent, following the pattern of force chains [9-11]. The localization mechanism based on buckling of force chains [12-14], although based on some phenomenological elements (such as confining forces and contact moments), does predict a characteristic buckling length.

## 2. Internittent Flips and Dilatancy

The mathematical description, endowed with information about connectivity of particles, is given by the Delaunay graph of the assembly for spheres [15], or its generalization for an assembly of convex particles, the *space cells* [16]. Delaunay or space cell graph provides a direct transition from discrete kinematics to the equivalent continuum. It allows unambiguous definition of strain, rotation, and their rates, at the level of individual cell. It also provides a mathematical distinction between two types of deformation of dense granular material. The *isotopologic* deformation is characterized by the deformed space cell graph which is topologically equivalent to the reference one, i.e., each particle must have the same nearest neighbors in reference and deformed configuration. The strains produced by such mechanism are of the order $10^{-4}$ [17], much smaller than the strains of interest here ($10^{-2} - 10^{-1}$). The *heterotopologic* deformation includes topological changes in the space cell graph. Since these are stochastic, the probability of any such change reversing itself upon unloading is vanishingly small.

The changes in topology of the space cell graph, characterizing the range of plastic deformation of interest, can only occur by a few generic mechanisms – *flips* [18]. Only one generic flip exists in 2D – the 2-2 flip, as illustrated in Figure 2. In 3D, with tetrahedra as cells, there are two such mechanisms – the 2-3 and 3-2 flips. (The numbers indicate the numbers of original and final cells in the generic flip.)

We performed a series of simulations on assemblies of cohesionless elastic particles with friction. Computational details are given in [19], while the details of the

analysis are given in [20]. The results demonstrate that the inelastic deformation of dense granular matter occurs by *intermittent flips*. At each deformation increment, only a small fraction of cells is undergoing a flip, and a completely different set of cells is flipping in the next increment. Such *diffuse deformation* mechanism governs the deformation regime where the dilatancy persists and the critical state is reached.

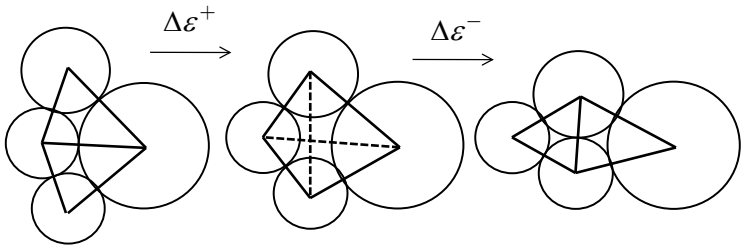


**Figure 2.** The generic 2-2 flip in 2D, after [18]. Left to right. As the cluster is compressed laterally, the nearest neighbors change. In the Delaunay graph, one diagonal is replaced by the other.

We find that about ¾ of the total volume change correspond to the increasing flipping fraction, while the remaining ¼ is the result of elastic relaxation of particles forming the flipping cells. This release of elastic energy is possible only because of the specific nonuniform organization of contact forces in force chains of different strength, which enables particles to flip from a strong force chain to a weaker one. Moreover, the nonuniform distribution of elastic energy is the underlying driving force for the increasing fraction of flipping cells. The role of elastic potential in inelastic deformation has been proposed on a phenomenological level [21, 22], but the results in [20] summarized here demonstrate its existence and give it a clear micromechanical meaning. The elastic potential energy of a particle prior to a flip depends on its history, particularly on maximum past pressure. After the flip, the particle has relaxed and its elastic energy corresponds to the current pressure. The flipping potential of a particle is the difference between the two elastic energies. Thus, the rate of dilation will depend on the current pressure.

## 3. Rotation Length Scale

To analyze the transmission of particle rotations through the contact network of an assembly, we perform numerical experiments on a 2D assembly of particles using the discrete element method [19]. A roughly circular assembly of particles (Figure 3) is subjected to confining pressure. Then, a disk on a strong force chain is forced to rotate with a prescribed angular velocity. Details are given in [23].

The non-dimensional parameters considered include: the friction coefficient $\mu$, the quasistatic coefficient [19], the non-dimensional standard deviation of the particle size distribution $\sigma/R$, the non-dimensional pressure coefficient $\varepsilon_0$, and the solid volume fraction.

The angular velocities diminish with distance from the forced particle. The distance from the forced particle at which the angular velocities decay to the level of noise associated with the simulation is the rotation transmission distance. This length scale is the

fundamental length scale exhibited by granular materials and should correlate with the shear band widths observed in experiments. The rotation transmission distance increases with increasing width of the particle size distribution. This corresponds well qualitatively with observations in numerical experiments [24], where the shear band width is lowest for the nearly monodisperse assembly. As the size distribution of particles narrows and approaches the monodisperse assembly, the kinematic constraints for particle rearrangement become more severe, yielding a shorter rotation transmission distance and thus – a narrower shear band.

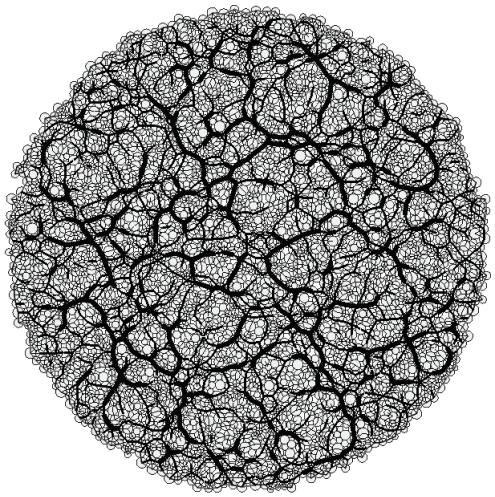

**Figure 3.** Force nework of a pressurized assembly of particles.

The propagation of rotation depends on the direction. The primary direction of transmission of rotations is along strong force chains. In [23], we have proposed a quantitative description, analogous to the fabric tensor and analyzed the spatial distribution of rotations in some detail. When the forced particle is crossed only by weak force chains, rotations propagate radially only up to the first transverse strong force chain. Such a force chain prevents propagation of rotations in the radial direction. Thus, strong force chains have a dual role in propagation of rotations: they improve the rotation propagation along the chain and impede the propagation across the chain.

## 4. Summary and Discussion

Consider a sample of high porosity, subjected to a constant pressure $p$ and continuous vibrations. The sample will compact until the porosity reaches its minimum value. For a given size distribution of particles and their shape, this minimum porosity will depend on the applied pressure. This state is called random dense packing (RDP) [25], originally an empirical concept that has only recently been subjected to a more rigorous rational treatment [26]. Numerical simulations of random packings of spheres under varying simulated gravity [27] (equivalent to varying pressure) confirm the pressure dependence of the RDP porosity.

The second stage of the flip mechanism in Figure 2 is dynamic; it sends waves through the assembly. If the sample is loose, flips act as a disturbance, similar to externally applied vibrations, albeit weaker and transient. Therefore, we expect that the critical state porosity is larger than the RDP porosity. Indeed, the experiments on identical steel beads (with friction) [28] indicate that the critical porosity is higher than the RDP value. In the absence of friction, the critical state could be as dense as the RDP, as simulations with frictionless spheres indicate [29].

Micromechanically, the critical state is defined as the state at which the compaction rate [caused by disturbances following flips] and dilation rate [caused elastic relaxation in flips] balance out, resulting in zero net volume change. For a given particle assembly, the critical state is a function of both pressure and porosity. The line in the pressure-porosity space delineating dilating and compacting states is the critical state line. Note that both, local dilation and compaction of flipping cell clusters occur on both sides of the critical state line, but their net sum is different.

As the mechanism of transverse relative motion of particles in a dense granular assembly, rolling is energetically preferred to frictional sliding. Owing to the geometrical constraints, pure rolling is impossible, so that dissipative frictional sliding is engaged. Consequently, the information about rotation of a particle diminishes with distance from the particle, resulting in an intrinsic length scale – rotation transmission distance. Our numerical simulations indicate that this distance increases with increasing width of particle size distribution, with increasing friction, and (weakly) with decreasing pressure.

Numerical simulations reveal that the structure of force chains greatly affects the transmission of rotations in a densely packed granular material. Rotations propagate easily along strong force chains but not across strong force chains. The rotation transmission through a particle is governed by the kinematic constraints imposed by the surrounding force network which consists of both favorably and unfavorably aligned force chains. The nonlocal force chain fabric tensor has been defined which describes directional distribution of contact force strengths in a neighborhood of a particle.

Our results of rotation transmission distance [23] correlate with existing observations of shear band widths in experiments and numerical simulations [38], as well as with the buckling force chain model [14]. The magnitude of angular velocity of particles decreases with distance from the center of the shear band [13, 31]. Interestingly, the nature of this distribution is preserved during the continuing deformation concentrated in the shear band [30]. This indicates that our rotation transmission distance corresponds to roughly half of the shear band width.

## 5. References

[1] Reynolds O (1885) On the dilatancy of media composed of rigid particles in contact. *Phil Mag* 20: 469-482.
[2] Thurairajah A (1961) Some properties of kaolin and of sand. *Dissertation*, Cambridge University.
[3] Wroth CP, Bassett RH (1965) A stress-strain relationship for the shearing behaviour of sand. Geotechnique 15(1): 32-56.
[4] Schofield AN, Wroth CP (1968) *Critical State Soil Mechanics*. McGraw-Hill, London.
[5] Goddard JD, Bashir JB (1990) On Reynolds dilatancy. In *Recent Developments in Structured Continua*, vol. 2: 23-35, Eds. D DeKee, PN Kaloni, Pitman Research Notes in Mathematics 229, Longman Scientific and Technical, John Wiley, New York.
[6] Rechenmacher, A.L. 2006 Grain-scale processes governing shear band initiation and evolution in sands. *J. Mech. Phys. Sol*ids 54, 22–45.
[7] Kuhn M.R & Bagi K. 2004 Contact rolling and deformation in granular media. *Int. J. Solids Struct.* 41, 5793–5820.

[8] Kuhn M.R. 1999 Structured deformation in granular materials. *Mech. Mater*. 31, 407– 429.
[9] Drescher, A. & DeJosselin DeJong, G. 1972 Photoelastic verification of a mechanical model for the flow of a granular material. *J. Mech. Phys. Sol*ids 20, 337-351.
[10] Hartley RR, Behringer RP (2003) Logarithmic rate dependence of force networks in sheared granular materials. *Nature* 421: 938-923.
[11] Ostojic S, Somfai E, Nienhius B (2006) Scale invariance and universality of force networks in static granular media. *Nature* 439: 828-830.
[12] Oda, M. & Kazama, H. 1998 Microstructure of shear bands and its relation to the mechanisms of dilatancy and failure of dense granular soils. *Geotechnique* 48, 465–481.
[13] Tordesillas A. 2007 Force chain buckling, unjamming transitions and shear banding in dense granular assemblies. *Phil. Mag*. 87(32), 4987–5016.
[14] Hunt, G.W., Tordesillas, A., Green, S.C. & Shi, J. 2010 Force-chain buckling in granular media: a structural mechanics perspective. *Phil. Trans. R. Soc.* A 368, 249–262.
[15] Satake M (1993) New formulation of graph-theoretical approach in the mechanics of granular materials. *Mech Mater* 16: 65-72.
[16] Bagi K (1996) Stress and strain in granular materials. *Mech Mater* 22: 165-177.
[17] Roux J-N, Combe G (2010) How granular materials deform in quasistatic conditions. *CP1227, IUTAM-ISIMM Symposium on Mathematical Modeling and Physical Instances of Granular Flow*, Eds. J Goddard, JT Jenkins, P Giovine, 260-270. American Institute of Physics.
[18] Edelsbrunner H (2000) Triangulations and meshes in computational geometry. *Acta Numerica* 9: 133-213.
[19] Padbidri J, Mesarovic SDj (2011) Acceleration of DEM algorithm for quasistatic processes. *Int J Numer Meth Engng* 86: 816–828.
[20] Mesarovic, S.Dj., Padbidri, J.M, & Muhunthan, B. 2012 Micromechanics of dilatancy and critical state in granular matter. *Geotechnique Letters* 2, 61-66.
[21] Jiang Y, Liu M (2009) Granular solid hydrodynamics. *Granular Matter* 11: 139–156.
[22] Collins IF, Muhunthan B, Qu B (2010) Thermomechanical "state parameter" model for sands. *Geotechnique* 60(8): 611-622.
[23] Padbidri JM, Hansen CM, Mesarovic SDj, Muhunthan B (2012) Length scale for transmission of rotations in dense granular materials. *J. Appl. Mech.* 79, 031011.
[24] Hu N. & Molinari J.F. 2004 Shear bands in dense metallic granular materials. *J. Mech. Phys. Solids* 52, 499 – 531.
[25] Bernal JD, Mason J (1960) Packing of Spheres: Co-ordination of randomly packed spheres. *Nature* 188: 910-911.
[26] Torquato S, Truskett TM, Debenedetti PG (2000) Is random close packing of spheres well defined? *Phys Rev Letters* 84(10): 2064-2067.
[27] Onoda GY, Liniger EG (1990) Random loose packings of uniform spheres and the dilatancy onset. *Phys Rev Letters* 64(22): 2727-2730.
[28] Roscoe KH, Schofield AN, Wroth CP (1958) On the yielding of soils. *Geotechnique* 8(1): 22-52.
[29] Peyneau P-E, Roux J-N (2008) Frictionless bead packs have macroscopic friction, but no dilatancy. *Phys Rev E* 78: 011307.
[30] Iwashita, K. & Oda, M. 2000 Micro-deformation mechanism of shear banding process based on modified distinct element method. *Powder Technology* 109, 192–205.
[31] Bardet, J.P. & Proubet, J. 1991 A numerical investigation of the structure of persistent shear bands in granular media. *Geotechnique* 41(4), 599-613.

# THERMAL BEHAVIOUR AND TRANSVERSAL JOINT DISTANCE COMPUTATION FOR GRAVITY RCC DAMS

**Vladan Kuzmanovic[1], Ljubodrag Savić[2], Nikola Mladenović[3]**

[1] Faculty of Civil Engineering,
The University of Belgrade, Bul. Kralja Aleksandra 73, 11000 Belgrade
e-mail: vladak@grf.bg.ac.rs
[2] Faculty of Civil Engineering,
The University of Belgrade, Bul. Kralja Aleksandra 73, 11000 Belgrade
e-mail: ljdsavic@grf.bg.ac.rs
[3] Faculty of Mechanical Engineering,
The University of Belgrade, Kraljice Marije 16, 11120 Belgrade
e-mail: nmladenovic@mas.bg.ac.rs

**Abstract.** Roller Compacted Concrete (RCC) is a special concrete mixture with low cement content, frequently used for concrete gravity dams. This paper deals with the 3D finite element model for unsteady phased thermal-stress analysis of RCC dams. Model calibration and verification has been done, based on the in-situ measurements of the Platanovryssi dam. The study has been done using the actual dam shape, RCC time schedule, and material properties. The results proves that the recommended 3D model enables a reliable thermal-stress prediction and transversal joint distance computation for an RCC gravity dam.

**Keywords**: RCC dam, thermal analysis, thermal stress, transversal joint distance

## 1. Introduction

Roller Compacted Concrete (RCC) is a special concrete mixture with low cement content, frequently used for concrete gravity dams. To reduce the thermal cracking, RCC dams are usually cut by transverse contraction joints into monoliths. The number and position of the joints should be determined based on the thermal-stress computations. The numerical model should consist of: (a) definition of the thermal and mechanical RCC properties, (b) computation of the temporal evolution of the thermal field, and (c) thermal-stress computation. Up to date models do not simulate accurately the long-term RCC behaviour ([1], [2]), due to simplifications. This research presents one of the first attempts to faithfully predict the RCC dams contraction joint distance, and to estimate it's influence on the thermal stress field. The developed model takes into account: the actual shape of the dam, different types of concrete, actual initial and boundary conditions, thermal and mechanical properties of RCC and construction technology, [3]. Calibration and verification are based on the in-situ measurements of the Platanovryssi dam, [4].

## 2. Theoretical background

The change of temperature (T) of a nonhomogeneous, isotropic body in time (t), due to the hydration heat, is described by the Fourier heat conductivity equation. If the thermal conductivity is independent of space and temperature:

$$\frac{\partial \mathrm{T}}{\partial \mathrm{t}} = \alpha_T \cdot \Delta \mathrm{T} + \frac{q}{\mathrm{c} \cdot \rho} \tag{1}$$

where: $\alpha_T = \lambda/(c \cdot \rho)$ – diffusivity, c – specific heat, ρ – density, λ – thermal conductivity, $\Delta T$ = div(grad T) – Laplace temperature operator and q – thermal source $= c \cdot \rho \cdot \frac{\partial T_{ad}}{\partial t}$, defined as a function of adiabatic temperature rise ($T_{ad}$).

RCC thermal behaviour greatly depends on the hydration processes of cementitious materials (cement and fly-ash). Hence, an adequate hydration-heat model must be defined and used. The presented model uses the degree of reaction method, [5]. The degree of reaction, r(t), ranges from 0 to 1, and is defined as a ratio between the heat released from the beginning of the reaction to the specified time, t, and the total amount of heat released due to the hydration. The amount of released heat is a function of a temperature time-history, and is mostly influenced by the temperature dependant increment of hydration heat, $q_T(T)$, defined as:

$$q_T(T) = e^{\frac{-C_A(r,T)}{T+273}}, \text{ where } C_A(r,T) \text{ – Arhenius constant.} \tag{2}$$

The differential FEM matrix formulation of thermal-stress analysis yields [5]:

$$\mathbf{C} \cdot \dot{\mathbf{u}} + \mathbf{K} \cdot \mathbf{u} + \mathbf{f} = 0 \ , \tag{3}$$

where: **C**–damping matrix, **K**–stiffness matrix, **f**–vector of nodal loads, $\dot{\mathbf{u}}$ –vector of unknown velocities, and **u**–vector of unknown nodal displacements. If conductivity, specific heat, and/or boundary conditions are temperature dependant, the problem becomes nonlinear, and the equation system (3) has to be solved iteratively. The dam body and foundation rock have been discretized by solid brick twenty-node isoparametric elements. The element is based on the quadratic interpolation and Gaussian integration.

In the phased thermal-stress analysis, used in this research, computational results from the previous construction phase are stored, and used as an initial condition for the following phase. From one phase to another, new parts of the model may show up (and some become inactive), therefore the active elements have to be defined at the beginning of the each phase. Within the each phase, the computation is performed in a given number of time steps, defined according to the observed concrete placement schedule, [6], [7], [8].

### 3. Numerical model

The numerical model is developed using the Finite Element Method based on the *Diana* package, [5]. The FEM formulation of the heat conductivity equation (1) yields:

$$\mathbf{K} \cdot \mathbf{T} + \mathbf{C} \cdot \dot{\mathbf{T}} = \mathbf{Q} \ , \tag{4}$$

where: **K** – the thermal conductivity matrix, **C** – the capacity matrix, **Q** – the nodal discharge. Since a nonlinear thermal problem is considered (properties and/or the boundary conditions depend on time), the incremental-iterative method is used for solving eq. (4).

The 3D model is applied to the non-overflow monolith, of the Platanovryssi dam. This dam is the highest to date RCC dam in Europe, 95 m high, with the crest length and width of

280 m and 7 m. The dam is built using 30 cm thick layers, and is divided into 13 monoliths by vertical contraction joints.

The initial conditions are defined by the temperatures at the finite element nodes, obtained from the observed mixture temperatures of each layer. The temperature boundary conditions include a constant temperature at the outside rock and the time variable temperature at the faces, galleries, or at the current top layer (during the construction), defined according to the available in-situ measurements [4]. The displacement boundary conditions are prescribed at the outer surfaces of the foundation rock.

## 4. Results of thermal field computation

The time evolution of the 3D thermal field of the representative dam monolith is presented in Fig. 1 and Fig. 2. During the initial phase of the construction, a "*hot core*" has formed some 10 m above the foundation line. The core has been gradually cooling for the following four months. By the summer, the air temperature rises, causing formation of another hot core (Fig. 1). After the completion of the dam, and the filling of the reservoir, only one hot core remains, at the centre of the dam (Fig. 2).

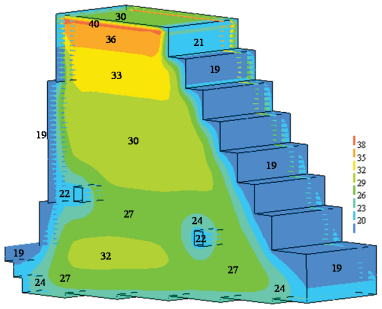

**Figure 1.** 3D Temperature field on 6.1.1996

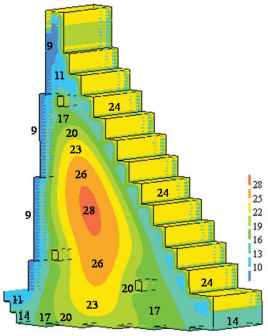

**Figure 2.** 3D Temperature field on 15.6.1999

## 5. Results of thermal-stress computation

The normal stresses in the dam-axes direction, $\sigma_z$, are considered. The stresses are primarily influenced by the temperature field, and to a less degree by the dead load, while the effect of other loads may be neglected, [8]. The tensile stresses are accepted to be positive, and the compressive stresses are negative.

Thermal-stress computation is performed for the 3 values of the monolith length: 16 m, 20 m, and 24 m. In this section, only the results for the 16 m monolith are presented.

At the Fig. 3, the stresses in the rock are equal to zero. Tensile stresses in the lower zone of the dam are less than 1.20 MPa (since the concrete have already reached its maximal temperature, and began to cool), while at the upper zone compressive stresses occur (as the temperature is still rising and the concrete is expanding). The stress concentration along the horizontal joints, between the successive layers are the consequence of the difference between the stiffness of the layers.

At the Fig. 4, 166 days after the commencement of concreting, the dam was 46 m high, with 153 RCC layers placed. The maximum tensile stress of 1.62 MPa occurred bellow the

ground level, at the vicinity of the upstream and downstream faces. The maximum compressive stress was -1.94 MPa.

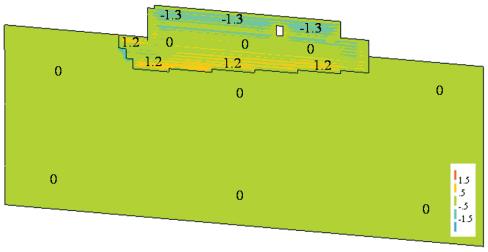


**Figure 4.** Middle plane stress-field, 1.4.1996

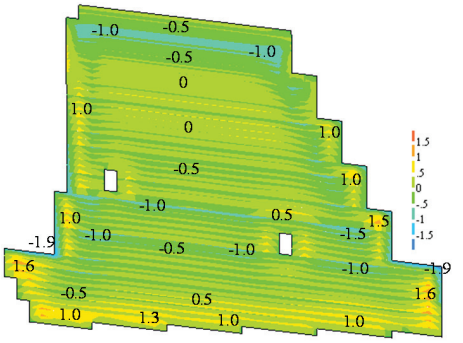


**Figure 3.** Middle plane stress-field, 9.1.1996

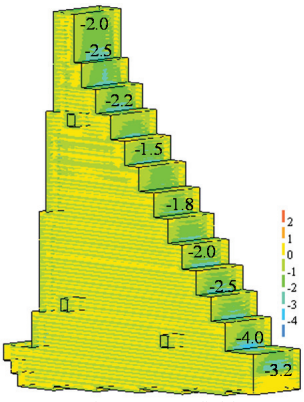


**Figure 5.** Surfaces Stress-field 1.9.1997

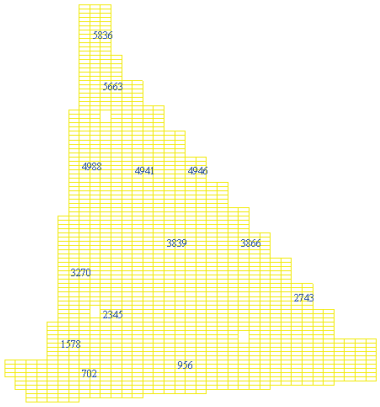


**Figure 6**. Characteristic elements at the middle plane

At Fig. 5, the dam was completed, but the filling of the reservoir has not begun. The maximum tensile stress of 2.21 MPa occurred in the middle plane, in the region of 10 m above the foundation line. The maximum compressive stress of -4.0 MPa occurred at the lower part of the dam, close to the downstream boundary.

The stress evolution in time is presented for the characteristic elements in the middle plain, Fig. 6. The results for the elements: 702, 2743, and 5836 are presented at Fig. 7.

One can observe that for all the elements, compressive stresses develop during the first 5 to 10 days after the placing, as a consequence of the hydration heat. The concrete tends to expand, and due to the restricted strains, the compressive stresses issue. When the concrete begin to cool, the shrinkage follows, and the tensile stresses result. The maximum tensile stresses depend on the temperature gradient, and the current stiffness of RCC.

The element 702 is within a massive structure, but relatively close to the upstream face, which influences the thermal-stress behaviour. After the initial compression, and tension phase, the stresses are mildly influenced by temperature boundary conditions. The element 2743 is strongly influenced by the downstream temperature boundary condition. Intensive

insulation causes high amplitude oscillations, together with the high tensile stresses (up to 0.8 MPa). The stress behaviour of element 5836 at the dam crest is governed by both, upstream and downstream boundary condition, with the less significant effect of insulation.

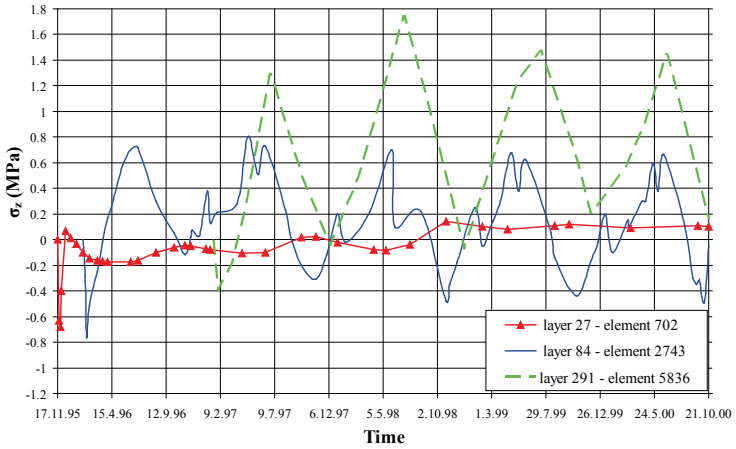


**Figure 7**. Stress evolution at the elements 702, 2743, and 5836

## 6. Evaluation of the transversal joint distance

The influence of temperature on the transversal joint distance is analysed, based on the results of the presented model, and the observed data. The length of the monolith of 16 m, 20 m, and 24 m is considered (models 3DL16, 3DL20, and 3DL24, respectively). At Fig. 8, the thermal stress evolution of the characteristic element in the middle plain is presented. One can observe that the stresses at the upstream face (the element 4988) follow the seasonal temperature oscillations. After the reservoir impounding, the stress oscillations dampen, due to the constant water temperature. The mean square deviation between 3DL24 and 3DL20 is negligible (0.07 MPa), comparing to the deviation of 0.16 MPa, between 3DL20 and 3DL16.

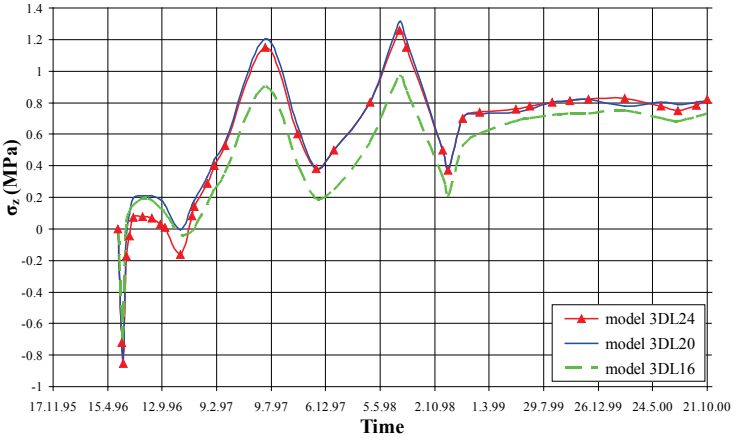


**Figure 8.** Stresses at element 4988 (layer No. 187), depending on the monolith length

Based on the maximum tensile stresses, their mean square deviation at characteristic elements, and the stress-field time evolution, it follows that the thermal stresses for RCC gravity dams depend on the monolith length. For the considered Platanovryssi dam, the mean square deviation of thermal stresses, between 3DL24 and 3DL20 is 0.11 MPa, and between 3DL20 and 3DL16 is 0.16 MPa. Increasing the monolith length from 20 m to 24 m, rises the maximal thermal stresses for about 0.33 MPa (12.2 %). Reducing the monolith length from 20 m to 16 m, decrease the maximal stresses for about 0.20 MPa (7.4 %).

Having in mind the computed maximal tensile stresses (depending on the monolith length), and the observed RCC tensile strength of 2.70 MPa [4], one may conclude that the maximal monolith length for the Platanovryssi dam should be 20 m. Bearing in mind that the constructed length of the particular monolith is 22 m, and with some cracking and leakage issuing at the downstream face (which implies exceeding of the tensile strength), it may be concluded that a somewhat shorter monolith should have been used.

## 7. Conclusions

- For the first time a comprehensive 3D numerical model for the phased thermal-stress analysis of the massive concrete structures has been developed, providing for a reliable evaluation of the transversal joint distance.
- Having in mind the maximum tensile stresses, their mean square deviation at characteristic elements, and the stress-field time evolution, it follows that the thermal stresses for RCC gravity dams depend on the transversal joint distance.
- The most important indicator of the thermal behaviour of RCC gravity dams, are the stresses in the direction of the dam axes.
- The shape of the diagram of the normal stresses time evolution, depends on the position in the middle plane, but it is almost independent on the monolith length
- It is not possible to formulate the universal suggestions for all RCC dams. Therefore, for each particular dam, the thermal-stress analyses should be performed to obtain the best estimate of the transversal joint distance.

*Acknowledgement.* This work was supported by the Ministry of Education and Science of the Republic of Serbia under project no. TR 37009 “Monitoring and Modeling of Rivers and Reservoirs – Physical, Chemical, Biological and Morphodynamic Parameters”.

## References

[1] Crichton A, Benzenati I, Qiu T, and Williams J (1999), Kinta RCC Dam – Are Oversimplified Thermal-Structural Analysis Valid?, *Proceedings of Australian National Committee on Large Dams Conference*. Jindabyne, pp. 446-457.
[2] Aniskin N A (2006) Temperature regime of a gravity dam from rolled concrete, Power Technology and Engineering, vol. **40**, pp. 23-27.
[3] Malcolm Dunstan & Associates Consulting Engineers (1996), *Platanovryssi Hydroelectric Project, Review of the Properties of the Concretes in Platanovryssi Dam*, Devon, England.
[4] Public Power Corporation (2004), *Platanovryssi Hydroelectric Project, Measurement Results*, Athens, Greece.
[5] TNO Building and Construction Research (2002), *Diana User’s Manual*, Delft, The Netherlands.
[6] Kuzmanović V (2007) Thermal-stress analysis of roller compacted concrete dams (in Serbian). *PhD thesis*, Department of Civil Engineering, The University of Belgrade, Serbia.
[7] Kuzmanovic V, Savic Lj and Stefanakos J (2010), Long-term thermal analysis of RCC dams using 2D and 3D models, *Canadian Journal of Civil Engineering*, vol. **37**, pp. 600–610.
[8] Kuzmanovic V, Savic Lj and Mladenovic N (2013), Computation of Thermal-Stresses and Contraction Joint Distance of RCC Dams, *Journal of Thermal Stresses*, **36**, pp. 112–134.

# WAVE PROPAGATION DUE TO A MOVING LOAD

**Mira Petronijević[1], Marko Radišić[1], Marija Nefovska Danilović[1]**

[1] Faculty of Civil Engineering
e-mail: pmira@grf.bg.ac.rs
University of Belgrade, Bulevar kralja Aleksandra 73, 11000 Belgrade
e-mail: mradisic@grf.bg.ac.rs
e-mail: marija@grf.bg.ac.rs

**Abstract.** The wave propagation on the surface of a half-space due to a moving load is analyzed using the Integral Transform Method. By using of the Helmholtz's decomposition and threefold Fourier transformation the body wave equation is transformed in the wave number-frequency domain and solved numerically. The obtained displacement field is transformed in time domain by the Inverse Fourier Transform. The analysis is carried out using computer program written in MATLAB program language. The load is vertical sinusoidal force P=1 MN moving along the line defined by x=0 with constant speed. The influence of source velocity on the displacements of the half-space and on the frequency content of the displacements at three locations at different distances from the load line is presented.

## 1. Introduction

Needs for easily accessible, available and mobile public transport have caused higher level of traffic induced vibrations in the urban zones. The rail/road - vehicle system imperfections, such as road and wheel roughness, are the main causes of ground vibrations. These vibrations induce waves that propagate through the soil and affect surrounding buildings. Different methods of analysis may be applied for evaluation of the ground response to moving sources. For simple geometry of the soil region analytical or semi-analytical solutions in the wavenumber–frequency domain are the most applicable, like Integral Transform Method (ITM), [1]. As an alternative to the semi-analytical solution, the thin-layer method can be employed, [2]. For the analysis of subsoil with complex geometry a numerical method, like Finite Element Method (FEM) with different type of transmitting boundaries, or Boundary Element Method (BEM) [3], are available in the time or frequency domain. The overview of the numerical methods for the analysis of ground vibrations due to the moving load is given by [4].

This paper presents the analysis of ground vibrations caused by a moving force with a constant speed in the *x*-direction along the surface of visco-elastic half-space. The force is half-cosine load, which represents the distribution of the moving wheel force. For this case the response is expressed in terms of a double integral with respect to $k_y$ and $\omega$. The solution is presented in the moving frame of reference. In that case it is the same as the solution for a stationary force. The dynamic responses at different load speed (subsonic, transonic and supersonic) are calculated using the ITM and presented. The results are compared with the results obtained by Chouw using the BEM [3].

## 2. Half-space solution according to ITM

The ITM was applied in the last years to several problems of halfspace dynamics [5] and soil structure interaction [6], in particular, to problems of road/track/soil interaction, [7]. Method is based on the Helmholz's decomposition of the Lamé's equations and their threefold Fourier transform from the time-space to the frequency-wavenumber domain. Therefore, it is restricted to linear systems and to the frequency domain analysis. The short description of this method will be presented in the following.
The Lamé's equations of motion of the continuum

$$\mu\nabla^2\mathbf{u}+(\lambda+\mu)\nabla\nabla\cdot\mathbf{u}=\rho\ddot{\mathbf{u}} \tag{1}$$

can be brought into the form of wave equations

$$\nabla^2\varphi=\frac{1}{c_p^2}\ddot{\varphi},\qquad \nabla^2\boldsymbol{\psi}=\frac{1}{c_s^2}\ddot{\boldsymbol{\psi}} \tag{2}$$

if the displacement vector is expressed by the scalar field $\varphi$ and the vector field $\psi$, according to Helmholtz's principle, as

$$\nabla u=\nabla\varphi+\nabla\times\boldsymbol{\psi}\ . \tag{3}$$

In Eqs. (2) $c_p$ and $c_s$ are the velocities of the dilatational and shear waves, respectively

$$c_p^2=\frac{\lambda+2\mu}{\rho},\qquad c_s^2=\frac{\mu}{\rho} \tag{4}$$

where $\rho$ is the mass density of the material and $\lambda$ and $\mu$ are the Lamé's constants.
If we assume that $\psi_z=0$, the displacement components can be obtained form Eq. (3) in the following form

$$\begin{aligned} u_x&=\varphi_{,x}-\psi_{y,z}\\ u_x&=\varphi_{,y}-\psi_{x,z}\\ u_z&=\varphi_{,z}-\psi_{x,y}+\psi_{y,x}\end{aligned}\ . \tag{5}$$

By a threefold Fourier transform

$$\hat{f}(k_x,k_y,\omega)=\int_{-\infty}^{+\infty}\int_{-\infty}^{+\infty}\int_{-\infty}^{+\infty}f(x,y,t)e^{-i(k_xx+k_yy+\omega t)}dxdydt\ , \tag{6}$$

Eqs. (2) can be transformed into a system of 3 decoupled ordinary differential equations in the frequency-wavenumber domain

$$\begin{aligned}-(k_x^2+k_y^2-k_p^2)\hat{\varphi}+\frac{\partial^2\hat{\varphi}}{\partial z^2}=0\\ -(k_x^2+k_y^2-k_s^2)\hat{\psi}_i+\frac{\partial^2\hat{\psi}_i}{\partial z^2}=0\end{aligned} \tag{7}$$

where

$$\lambda_1^2 = k_x^2 + k_y^2 - k_p^2, \quad k_p = \frac{\omega}{c_p}$$
$$\lambda_2^2 = k_x^2 + k_y^2 - k_s^2, \quad k_s = \frac{\omega}{c_s} \tag{8}$$

The solution of differential equations (7) in the transformed domain should satisfy the Sommerfield's radiation condition, which means that there is no propagation of waves from infinity toward the source. Therefore $A_1=B_{x1}=B_{y1}=0$, giving the solutions in the following form

$$\hat{\varphi} = A_2 e^{-\lambda_1 z}, \qquad \hat{\psi}_x = B_{x2} e^{-\lambda_2 z}, \qquad \hat{\psi}_y = B_{y2} e^{-\lambda_2 z} \quad . \tag{9}$$

Substituting Eq. (9) into the Eqs. (5) results in the following relation between the displacement vector $\hat{\mathbf{u}}$ and vector of unknown coefficients $\mathbf{C}$

$$\hat{\mathbf{u}} = \mathbf{A}^u \cdot \mathbf{C} \tag{10}$$

where

$$\hat{\mathbf{u}} = \begin{Bmatrix} \hat{u}_x \\ \hat{u}_y \\ \hat{u}_z \end{Bmatrix}, \quad \mathbf{A}^u = \begin{bmatrix} ik_x & 0 & \lambda_2 \\ ik_y & -\lambda_2 & 0 \\ -\lambda_1 & -ik_y & ik_x \end{bmatrix}, \quad \mathbf{C} = \begin{Bmatrix} A_2 \\ B_{2x} \\ B_{2y} \end{Bmatrix}. \tag{11}$$

The unknown coefficients $A_2$, $B_{x2}$ and $B_{y2}$ can be obtained from the boundary conditions at the surface of the half space, defined as

$$\begin{Bmatrix} \hat{\sigma}_{zx}(k_x, k_y, z=0, \omega) \\ \hat{\sigma}_{zy}(k_x, k_y, z=0, \omega) \\ \hat{\sigma}_z(k_x, k_y, z=0, \omega) \end{Bmatrix} = \begin{Bmatrix} 0 \\ 0 \\ \hat{p}_z(k_x, k_y, \omega) \end{Bmatrix} = \hat{\mathbf{p}}(k_x, k_y, \omega) \tag{12}$$

where $\hat{p}_z(k_x, k_y, \omega)$ is the Fourier's transform of the applied moving load $p_z(x,y,t)$

$$\hat{p}_z(k_x, k_y, \omega) = \int_{-\infty}^{+\infty} \int_{-\infty}^{+\infty} \int_{-\infty}^{+\infty} p_z(x, y, t) e^{-i(k_x x + k_y y + \omega t)} dx dy dt \, . \tag{13}$$

Using well known relations between stress and displacements, the stress in wavenumber domain can be written as

$$\boldsymbol{\sigma} = \mathbf{A}^\sigma \mathbf{C} \tag{14}$$

where

$$\mathbf{A}^\sigma = \mu \begin{bmatrix} -2ik_x\lambda_1 & k_x k_y & -\left(\lambda_2^2 + k_x^2\right) \\ -2ik_y\lambda_1 & \left(\lambda_2^2 + k_y^2\right) & -k_x k_y \\ 2k_r^2 - k_s^2 & 2ik_y\lambda_2 & -2ik_x\lambda_2 \end{bmatrix} \tag{15}$$

and $k_r^2 = k_x^2 + k_y^2$ .

Substituting solution for **C** obtained from the Eq. (14) into the Eq. (10), regarding the Eq. (12), gives the displacement vector in the frequency-wavenumber domain in the form

$$\hat{\mathbf{u}}(k_x,k_y,\omega)=\hat{\mathbf{H}}(k_x,k_y,\omega)\hat{\mathbf{p}}(k_x,k_y,\omega)\,, \tag{16}$$

where $\hat{\mathbf{H}}=\left[\mathbf{A}^u(\mathbf{A}^\sigma)^{-1}\right]$ is the transfer function matrix (compliance) of the half-space.

The response in the frequency-wavenumber domain requires the transformation in the space-time domain by usage of the inverse Fourier transform

$$f(x,y,t)=\frac{1}{8\pi^3}\int_{-\infty}^{+\infty}\int_{-\infty}^{+\infty}\int_{-\infty}^{+\infty}\hat{f}(k_x,k_y,\omega)e^{i(k_xx+k_yy+\omega t)}dk_xdk_yd\omega\,. \tag{17}$$

In these evaluations, damping is taken into account by using complex values for the Lamé's constants according to the principle of correspondence

$$\hat{E}=E\left(1+2i\xi\right),\qquad \hat{G}=G\left(1+2i\xi\right) \tag{18}$$

where ξ is the damping coefficient.

*2.1. Moving load*

Consider the vertical load that moves in *x*-direction along the surface of a half-space with a constant speed *v*, starting from the point $x_k$=0

$$p_z(x,y,t)=p_o\cdot p_1(x-v_it)p_2(y)\,. \tag{19}$$

By substituting Eq. (19) into Eq. (13) and applying the shifting theorem obtained is the moving force in the frequency-wavenumber domain as

$$\hat{p}_z(k_x,k_y,\omega)=2\pi p_o\delta(\omega+k_xv)\tilde{p}_1(x)\tilde{p}_2(y) \tag{20}$$

where $\tilde{p}_1(x)$ and $\tilde{p}_2(y)$ are wavenumber transform of $p_1(x)$ and $p_2(x)$.

The solution in the space domain is found by substituting Eq. (20) into Eq. (16) and applying inverse Fourier transform. Taking into account shifting theorem obtained is final result in the form

$$\mathbf{u}(x,y,t)=\frac{1}{(2\pi)^3}\int_{-\infty}^{+\infty}\int_{-\infty}^{+\infty}\int_{-\infty}^{+\infty}\hat{\mathbf{H}}(k_x,k_y,\tilde{\omega}-k_xv)\hat{\mathbf{p}}(k_x,k_y,\tilde{\omega})e^{ik_x\bar{x}}e^{ik_yy}e^{i\tilde{\omega}t}dk_xdk_ydt\,, \tag{21}$$

where

$$\bar{x}=x-vt,\qquad \tilde{\omega}=\omega+k_xv\quad, \tag{22}$$

represent the moving coordinate system $\bar{x}$ and frequency $\tilde{\omega}$ at the source, respectively.

From Eq. (20) follows that $\omega=-k_xv$ i.e $\tilde{\omega}=0$, which means that integral (21) is constant in time and the response of the half-space due to the moving load can be expressed in the moving frame of reference as

$$\mathbf{u}(\bar{x},y)=\frac{1}{(2\pi)^2}\int_{-\infty}^{+\infty}\int_{-\infty}^{+\infty}\hat{\mathbf{H}}(k_x,k_y,-k_xv)\hat{\mathbf{p}}(k_x,k_y)e^{ik_x\bar{x}}e^{ik_yy}dk_xdk_y\,. \tag{23}$$

The obtained integral is the same as in the case of stationary force. The only difference is that in the case of moving load the compliance of the soil has to be calculated with the shifted frequency $\omega = -k_x v$ [7].

### 3. Evaluation of numerical model

The response of the half-space is calculated using computer program using Matlab [8]. The characteristics of the half-space and the moving force distribution are taken as in [3]. The characteristics of the half-space are: $c_s=120$ *m/s*, $c_p=240$ *m/s*, $\rho=2000$ *kg/m*$^3$, $\xi=5\%$.

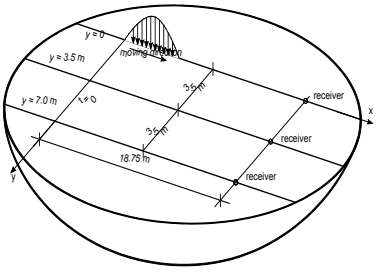


Figure 1.

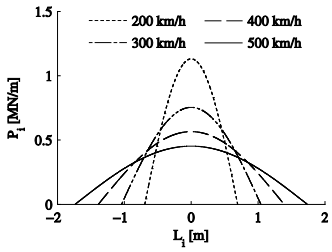


Figure 2.

The force is half-cosine load that moves in *x*-direction with a constant speed *v*, starting from the point $x_k$=0, Fig. 1. The force is half-cosine load

$$P_{z_i}(x,y,t) = P_i \cos\frac{\pi\bar{x}}{l_i}\delta(x - v_i t)\delta(y) \tag{24}$$

where $P_i=P_t\pi/l_i$ is the maximum, $P_t=1$ *MN* is the total load, $l_i$ is the length of half-cosine, Fig. 2. Load duration is *0.025 s*. The responses are obtained for the following velocities $v_i$ of the force: 200, 300, 400, and 500 *km/h*, respectively.
The displacements at the receiver *18.75 m* from the starting point, at a distance *y=0, 3.5* and *7 m*, respectively are displayed in Fig. 3. The higher the source speed the quicker response occurs. The displacement $u_y=0$, for $y=0$. The displacements decrease with increasing distances from the load path. The dependency of the displacements on the ratio between the source speed and the wave speed in the soil is obvious. The highest displacements $u_x$, $u_y$, $u_z$ occur when the force velocity is 400, 500 and 200 *km/h*, respectively.

### 4. Conclusion

In this paper presented is the application of the ITM to dynamic analysis of the half-space due to a moving load. The advantage of the ITM is based on the fact that in the wavenumber domain the displacement due to the moving force in the moving frame of reference is equal to the displacement due to the stationary force calculated with the shifting frequency.
The displacements due to the half-cosine force obtained by present approach are in a good agreement with those obtained by the Boundary element method [3] .

*Acknowledgement.* The authors are grateful to the Ministry of Science and Technology, Republic of Serbia, for the financial support of this research within the Project TR 36046.

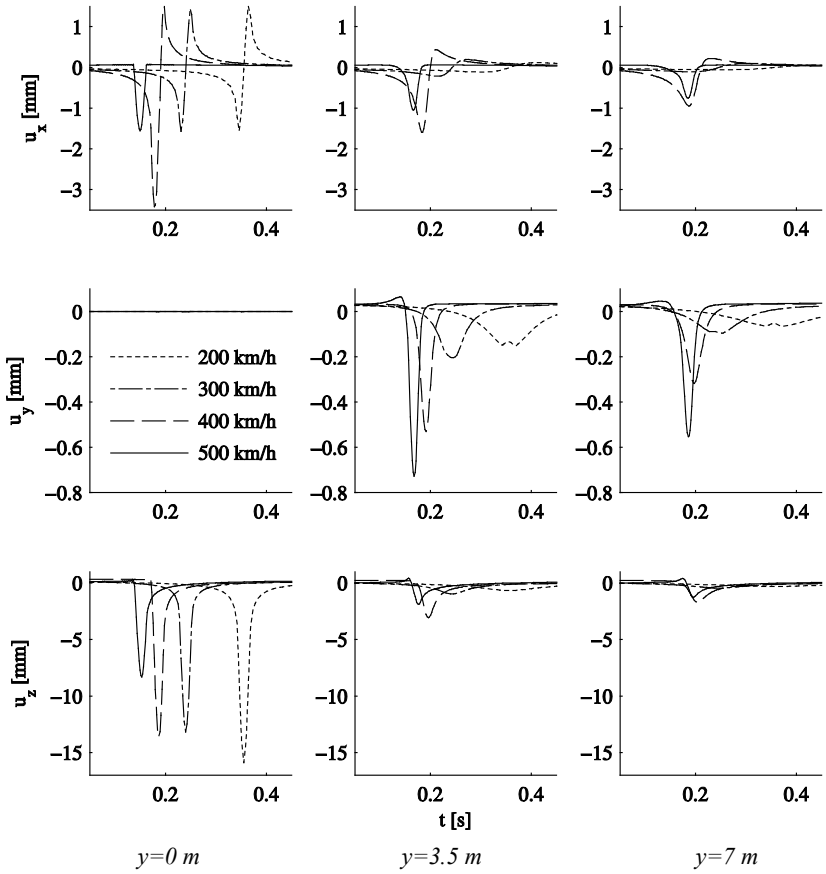


Figure 3. Influence of the moving force velocity on the displacements of the half-space surface at *x=18,5 m*

## References

[1] Grundmann H, Lieb M, Trommer E (1999) The response of a layered half-space to traffic loads moving along its surface, *Archive of Applied Mechanics*, **69**, pp. 55–67

[2] Pflanz G, Garcia J, Schmid G (2000) Vibrations due to loads moving with sub-critical and supercritical velocities on rigid track, *Proceedings of the International WorkshopWAVE 2000*, Bochum, Germany, 13-15 December 2000, Nawawi C, Schmid G (Eds.), pp.131-147, Balkema, Rotterdam, ISBN 90 5809 173 2

[3] Chouw N, Pflanz G, (2000) Reduction of structural vibrations due to moving load, *Proceedings of the International WorkshopWAVE 2000*, Bochum, Germany, 13-15 December 2000, Nawawi C, Schmid G (Eds.) pp. 251-286, Balkema, Rotterdam, pp. ISBN 90 5809 173 2

[4] Andersen L, Nielsen S R K, Krenk S (2007) Numerical methods for analysis of structure and ground vibration from moving loads, *Computers and Structures*, **85**, pp. 43-58

[5] Rastandi J I (2003) Modelization of Dynamic Soil-structure Interaction Using Integral Transform-finite Element Coupling, PhD Thesis, Lehrstuhl für Baumechanik, TU München

[6] Radišić M, Nefovska-Danilović M, Petronijević M, (2011) Application of Integral Transform Method to Calculate Impedance Functions, *Proceedings of the 3rd Serbian Congress Theoretical and Applied Mechanics*, Vlasina Lake, 5-8 July 2011, S. Maksimović and T. Igić (Eds.), pp 994-1006, ISBN 978-86-909973-3-6.

[7] Auerish L (2008) The effect of critically moving loads on the vibrations of soft soil and isolated railways tracks, *Journal of Sound and Vibration*, **310,** pp. 587-607

[8] Matlab (2011) MathWorks Inc. The Language of Technical Computing. MATLAB 2011b.

# FLIGHT PERFORMANCE DETERMINATON OF THE TURBOPROP AIRCRAFT

**Kosta Velimirović[1], Nemanja Velimirović[2]**

[1] Military Technical Institute, Žarkovo,
Ratka Resanovića bb, 11000 Belgrade , Serbia
e-mail: kolevelimirovic@yahoo.com
[2] Faculty of Mechanical Engineering,
The University of Belgrade, Kraljice Marije 16, 11120 Belgrade 35
e-mail: velimirovicnemanja@yahoo.com

**Abstract**. The method for the estimation of the turboprop, armed, long range and COIN (Counter Insurgency) aircraft performances is presented in this paper. Its primary role would be counter insurgency, intelligence, surveillance and reconnaissance. **"KOBACPERF"** computer program is used for the calculation of basic and special performances of the turboprop aircraft. Nonlinear model total energy which served as the computer program is basis for performance calculation. The computer program "**KOBACPERF**" consists of several modules: Module for determining the mass aircraft. Airport Module - based on current meteorological conditions determine the data of the airport. This module requests data: frontal wind speed, slop and quality of the runway. Atmosphere Module - data calculations are made for the altitude. It works for all conditions from polar to tropical. Aerodynamics Module - loaded aerodynamic characteristics of clean, takeoff and landing configurations. This module also presents data on the aerodynamic characteristics of the launcher and weapons under the wing. Engine Module - provides information on the performance and fuel consumption in function of the regime, the number of revolutions and the height of flight. Propeller Module - aerodynamic data of three blade propeller. Data from this module are used for the calculation of installed propeller thrust force. Performance Module - compute the minimum and maximum speed, climb and ceiling. Turn Module - turnaround data calculation. Takeoff and Landing Modules - presents all data related to the take-off or landing. The data refers to the characteristic length, velocity, and time and fuel consumption. Cruise Module - optimal parameters of cruising. Start, Taxi and Combat Modules - compute fuel consumption and other data. Range Module - the most complex module of the computer program "**KOBACPERF**". This module calls all the listed modules and determines the maximum length of the flight profile. The method and its results are illustrated by the numerical example. Used programming language is MATHCAD 14.

## 1. Introduction

During the proces of airplane design great attention is focused on the performance. For aircraft performance calculations it is necessary to have a "tool". **KOBACPERF** is "tool"-computer program for the calculation of turbo-prop aircraft flight characteristics. This paper presents a turbo-prop "COIN" aircraft performance calculation. A "COIN" aircraft will be a lightly armored, two-seat, turbo-prop aircraft capable of locating, tracking, identifying and engaging a variety of targets with suite of electro-optical/infrared sensors and laser-guided/unguided air-to-ground weapons/missiles. Aircraft is armed with gun, bombs and small gauge rockets. This airplane is not intended for heavy combat. Its primary role would be counter insurgency, intelligence, surveillance and reconnaissance. Aircraft belongs to the group COIN (Counter Insurgency) is armed aircraft designed for reconnaissance and

air escort of ground forces. Because of the current fight against global terrorism, need for "COIN" fleets now is greater then ever.

| | |
|---|---|
| Takeoff weight (2 Pilots) | 1525 kg |
| Max takeoff weight | 2025 kg |
| Fuel load | 156 kg |
| Fuel load tip tank | 190 kg |
| Weapon weight | 500 kg |
| Power plant | Turboprop 940 hp |
| Fuel type | Jet |
| Crew | 2 Pilots |

**Table 1.** Characteristics of the considered plane

**Figure 1.**A "COIN" aircraft (Military Technical Institute, UTVA, Serbia)

## 2. Turbo-prop propulsion

Turbo-prop consists of an intake, compressor, combustior, turbine and propelling nozzle. Air drawn into the intake and compressed by the compressor. Fuel is added to the compressed air where the fuel-air mixture combusts. The hot gasses expend through the turbine. Some of the turbine power is used to drive compressor. The rest of power is transmited to the propeller.

A turbo-prop engine is a tipe of turbine engine which drives an aircraftt using a reduction gear. Almost all of its output being used to drive the propeller. The engine exhaust gasses contain little energy and play only a minor role in the propulsion. The propeller is coupled to the turbine through a reduction gear that converts low torque output to high torque and high number of revolutions to low number of revolutions. The propeller is a constant speed, width variable pitch type. Turbo-prop engines are used on small subsonic aircraft such as a "COIN" aircraft.

Turbo-props are very efficient at flight speeds below 700 kph beacause the jet velocity of the propeller and exhaust is low.

Propellers are not efficient when the tips reach or exceed supersonic speeds. For this reason a reduction gearbox is placed between the power turbine and the propeller.Turbine operate at its most efficient speed while the propeller also operate at its most efficient speed. Propellers lose efficiency as aircraft speed increases so turboprops are normally not used on high-speed aircraft.

The TPE331 is a torque-producing engine [3]. It extracts power by converting heat energy into rotating mechanical energy (torque). Ambient air is drawn and compressed by a two-stage centrifugal compressor, shown in Fig. 2. Air is directed into the combustion chamber and mixed with fuel. The fuel/air mixture is ignited and a continuons combustion is maintained. Nozzle directed airflow impinges upon the first stage turbine rotor, causing it to rotate. The hot gases continue their flow through the turbine rotors and finally back to the atmosphere as exhaust.

Rotational turbine motion is transmited to the compressor and gearbox. 2/3 of the mechanical shaft power is used to rotate compressor. The gearbox converts the remaining low torque energy into high torque energy needed to drive the propeller and engine accessories.

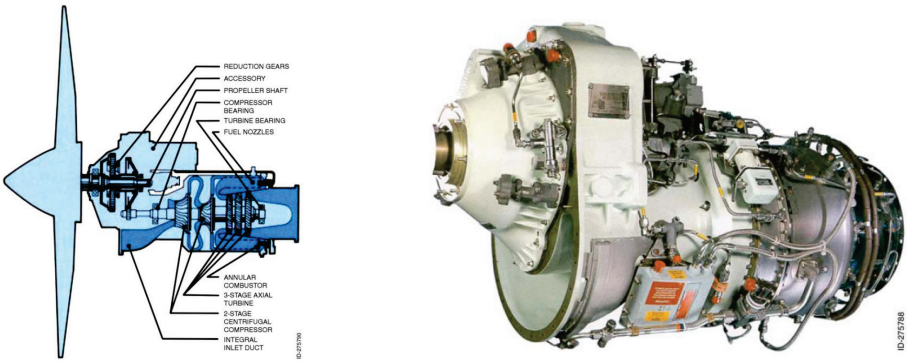


**Figure 2.** GARRETT' S TPE 331-10 Honeywell Turboprop engine

## 3. Computer program "KOBACPERF"

**"KOBACPERF"** computer program is used for the calculation of basic and special performances aircraft equipped with turbo-prop power plant. Nonlinear model total energy served as the computer program is basis for performance calculations [1]. Plane is considered as a material point. Used programming language is MATHCAD 14.

The program consists of several modules:

1. Module for determining the mass aircraft,
2. Airport Module - based on current meteorological conditions determine the data of the airport. This module requests data: frontal wind speed, slop and quality of the runway.
3. Atmosphere Module - data calculations are made for the altitude. It works for all conditions from polar to tropical.
4. Aerodynamics Module - loaded aerodynamic characteristics of clean, takeoff and landing configurations [2] [6]. This module also presents data on the aerodynamic characteristics of the launcher, missiles, bombs and gun under the wing.
5. Engine Module - provides information on the performance and fuel consumption in function of the regime, velocity and the height of flight.
6. Propeller Module - aerodynamic data of metal , three blade, propeller. Data from this module are used for the calculation of propeller thrust forces installed.
7. Performance Module - compute the minimum and maximum speed, climb and ceiling [7].
8. Turn Module - turnaround data calculation.
9. Takeoff and Landing Modules - presents all data related to the take-off or landing. The data refers to the characteristic length, velocity, time and fuel consumption.
10. Cruise Module - optimal parameters of cruising.
11. Start, Taxi and Combat Modules - compute fuel consumption and other data.
12. Planning module
13. Range Module - the most complex module of the computer program **"KOBACPERF"**. This module calls all the listed modules and determine the length and time of the flight profile [4][5].

## 4. Numerical example

Some aerodynamic characteristics, flight capability and other performances of the considered plane are presented in numerical example. Diagrams, Fig.3, showing the coeficients resistance and aerodynamic lift of clean, takeoff and landing configurations. Engine maximum (100%) shaft power for diferant heights (0.,3048.,6096.,9144.,10670.m) is presented in Fig.4. Fig.5 presents speed altitude envelope (maximum speed (kph), minimum speed (kph) and minimum speed with flaps (kph). Rates of climb w(m/s) for diferant heights (0.,500.,1000.,2000.,3000.,4000.,5000.,6000. m) are presented in Fig.6. Distances of take-off and landing are presented in Fig.7 and Fig.8 respectively. Flight profile is shown in Fig.9. Geometric characteristics of the flight profile are shown in the Table 2. Weather conditions and "altitude" airport (Standard Atmosphere, STA) are presented in Table 3. Some calculated data of flight profile are presented in Table 4.

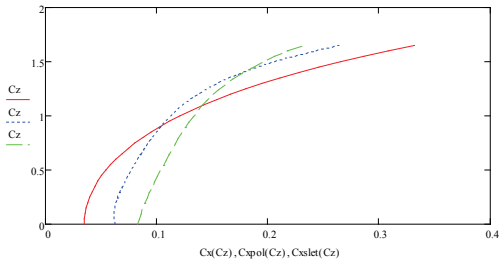


**Figure 3.** Speed altitude envelope

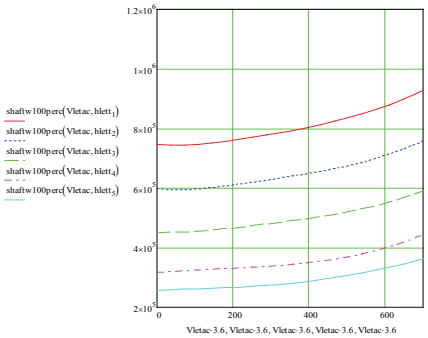


**Figure 4.** Maximum (100%) shaft power (W) for different heights (m)

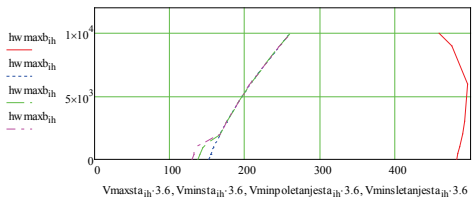


**Figure 5.** Speed altitude envelope

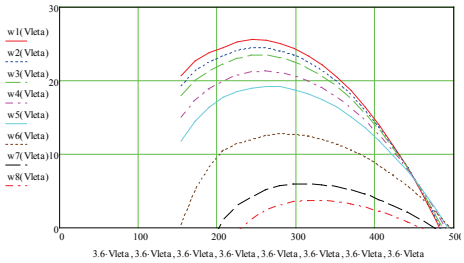


**Figure 6.** Rate of climb w (m/s) for different heights (m)

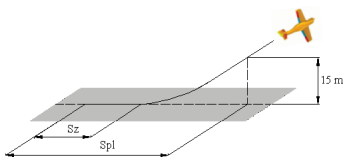


$S_z$=172m
$S_{pl}$=291m

**Figure 7.** Take-off

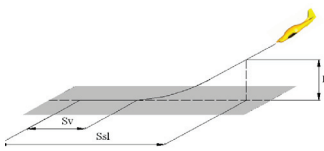


$S_{sl}$=655m
$S_v$=200m

**Figure 8.** Landing

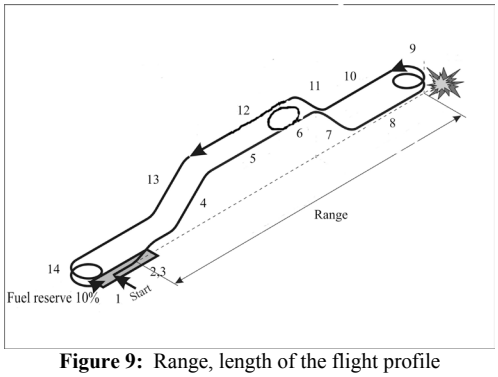


**Figure 9:** Range, length of the flight profile

| | |
|---|---|
| Height cruising 1 (5) | 5000 m |
| Height holding (6) | 5000 m |
| Height penetration 1 (8) | 1500 m |
| Height observation (9) | 1500 m |
| Height penetration 2 (10) | 1500 m |
| Height cruising 2 (12) | 3000 m |

**Table 2.** Data flight profile

| | |
|---|---|
| Temperature, airport (C°) | 15.0 |
| Air pressure, airport (Pa) | $1.013*10^5$ |
| Wind head, airport (m/s) | 0.0 |
| "Altitude" airport STA (m) | 5.096 |

**Table 3.** Meteo data airport

| | | Height (m) | Time (min) | Distance (km) | Speed (km/h) | Aircraft mass (kg) | Power rating (%) | Number of revolutions (o/min) |
|---|---|---|---|---|---|---|---|---|
| 1 | Start | 5. | 5. | - | - | 1525 | 98 | 1862 |
| 2 | Taxi | 5. | 5. | - | - | 1507 | 90 | 1710 |
| 3 | Takeoff | 5. | 0.156 | 0.282 | 162.41 | 1493 | 100 | 1900 |
| 4 | Climb 1 | 5.-5000. | 4.08 | 17.29 | 246.94 | 1492 | 100 | 1900 |
| 5 | Cruising 1 | 5000. | 29.49 | 227.32 | 462.34 | 1479 | 98 | 1862 |
| 6 | Holding | 5000. | 10.0 | - | - | 1399 | 96 | 1824 |
| 7 | Planning 1 | 5000.-1500. | 8.09 | 33.99 | 197.18 | 1373 | 70 | 1330 |
| 8 | Penetration 1 | 1500. | 6.79 | 50.0 | 410.0 | 1371 | 98 | 1862 |
| 9 | Observation | 1500. | 6. | - | 340.92 | 1351 | 98 | 1862 |
| 10 | Penetration 2 | 1500. | 5.57 | 40.0 | 400.0 | 1331 | 98 | 1862 |
| 11 | Climb 2 | 1500.-3000. | 1.00 | 4.05 | 234.21 | 1315 | 100 | 1900 |
| 12 | Cruising 2 | 3000. | 32.18 | 254.58 | 408.80 | 1311 | 97 | 1843 |
| 13 | Planning 2 | 3000.-5. | 8.09 | 28.44 | 186.72 | 1231 | 70 | 1330 |
| 14 | Landing | 5. | 0.289 | 0.567 | 144.88 | 1229 | 70 | 1330 |

**Range = 327.4 km Time=121.8 min**

**Table 5.** Calculated characteristics of the flight profile

## 5. Conclusion

Program **KOBACPERF** based on total energy method is used for turbo-prop power plant aircraft flight characteristics calculation. Program is very useful for: aircraft design, writing pilot instructions and planning combat missions. Program is enough fast and reliable. Accuracy of results depends on the loaded aerodynamic characteristics of the aircraft, launcher, missiles, bombs and gun under the wing. Method and its results are illustrated by numerical example for "COIN" aircraft in software MATHCAD 14.

## References

[1] Rendulić Z. (1987) *Mehanika leta*, Vojnoizdavački i Novinski Centar, Belgrade , Serbia.
[2] Smetana F. (2003) *Flight vehicle performance and aerodynamic,* AIAA Wright-Patterson Air Force Base, Ohio.
[3] *331 Turboprop engine - installation manual IM-5117-W*, (1987) Garrett Turbine Engine Company, Phoenix, Arizona.
[4] Velimirović K., Velimirović N., (2010) Određivanje maksimalnog taktičkog radijusa naoružanog klipno-elisnog aviona program, *SYM-OP-IS-2010,* Tara, Serbia 2010.
[5] Velimirović K., Velimirović N., (2011) Određivanje maksimalnog taktičkog radijusa klipno-elisne bespilotne letelice,program BELI ORAO, *SYM-OP-IS-2011,* Tara, Serbia 2011.
[6] Bajović, M., Velimirović K., Molović V., Velimirović, N., *(2009),* Analiza aerodinamčkih koeficijenata na osnovu aerotunelskih i letnih ispitivanja , *OTEH 2009,* Military Technical Institute, Belgrade , Serbia, 2009.
[7] Bajović, M., Velimirović, K., Molović V., Estimacija performansi klipno-elisnog aviona , *OTEH 2007* Military Technical Institute, Belgrade , Serbia, 2007.

# KINEMATIC AND DYNAMIC MODEL OF THE HUMAN CENTRIFUGE

**Jelena Vidaković[1], Vladimir Kvrgić[1], Goran Ferenc[1], Zorana Dančuo[1], Mihailo Lazarević[2],**

[1] Lola Institute
Kneza Višeslava 70a, Belgrade, Serbia
jelena.vidakovic@li.rs
[2] Faculty of Mechanical Engineering,
The University of Belgrade, Kraljice Marije 16, 11120 Belgrade 35

**Abstract.** Human centrifuge is dynamic flight simulator used to provide motion and forces cues of modern combat aircraft. It is mainly intended for safe and reliable generation of high G onset rates and high levels of sustained G for pilot trainings and research. In this paper, modeling of human centrifuge as a three DoF robot manipulator with revolute joints is presented. Pilots seat is controlled as end-effector. Here, Rodriguez formula is proposed for modeling kinematics and dynamics of the human centrifuge. Algorithms of direct and inverse kinematics are developed. Velocities and accelerations of CM's (centers of masses) of centrifuge links are determined and the results are compared with results obtained from developed Jacobian where singular positions are particularly discussed. Inverse dynamics algorithm based on covariant form of Lagrange equations of the second kind is given. Developed kinematic and dynamic models are implemented into control unit and simulated in offline part if control system.

## 1. Introduction

Combat aircrafts of the last generation are characterized by the feature of super maneuverability. Pilots are exposed to dangerous effects of high G-forces, impetuous angular movements, spatial disorientation, etc. In such conditions their ability to control aircraft is reduced and they may suffer from the loss of consciousness induced by the high G loads, so-called G-LOC. Human centrifuge is dynamic flight simulator used to provide motion and forces cues of modern combat aircraft [1].

Accelerations simulated in the cabin of centrifuge must be authentic to those that pilot experience during the flight at the most rotating maneuvers. This device can be modeled as a three DoF robot manipulator with revolute joints [2]. Main motion is rotation of the centrifuge arm about vertical, planetary axis. Arm carries gondola which is able to rotate about two axes, pitch and roll, as shown in Fig. 1 [3].

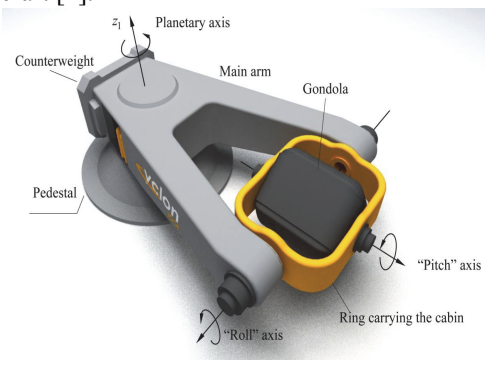


**Figure 1.** Human centrifuge-rotational axes

Control system intended for control of industrial robots have been previously

developed in Lola Institute [4]. System is set up in modules: kinematical, dynamical, servo, path interpolator etc. [5]. This system is used as control system for human centrifuge by implementing kinematical and dynamical model and by adding functionalities specific for human centrifuge.

## 2. Kinematic model

In this section algorithms of forward and inverse kinematics, as well as development of Jacobian and analysis of singular positions are presented. Centrifuge is modelled as tree-like multibody system which moves in uniform gravitational field. Its motion is described by Lagrange generalized internal coordinates [6].

### *2.1. Forward kinematics*

Local orthogonal Cartesian coordinate system $C_i\xi_i\eta_i\zeta_i$ which moves together with link $i$ is joined to links. Here $C_i$ is the center of mass of the link $i$. Based reference frame is denoted by $\xi_0\eta_0\zeta_0$. Rodriguez formula is used to obtain transformation matrices which define mutual position and orientation of centrifuge's links [6]:

$$\mathbf{A}^r = [I] + (1-\cos q)\left(\mathbf{e}^d\right)^2 + \sin q\,\mathbf{e}^d \tag{1}$$

where $q$ is angle of rotation about axis determined by unit vector $\mathbf{e}$ . $\mathbf{e}^d$ is skew symmetric matrix of vector $\mathbf{e}$ .Transformation matrices are given in (2a, 2b, 2c). Hereafter superscript 0 is used to denote that quantuty is given w.r.t. based reference frame.

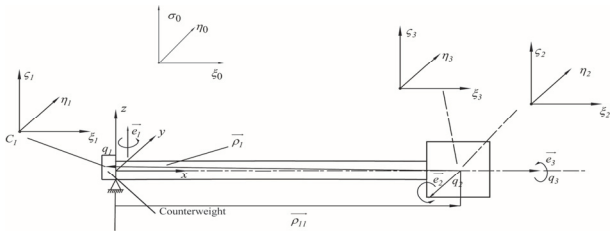


**Figure 2.** Coordinate frames in reference position

$$\boldsymbol{A}_{0,1} = \begin{bmatrix} c_1 & -s_1 & 0 \\ s_1 & c_1 & 0 \\ 0 & 0 & 1 \end{bmatrix}, \boldsymbol{A}_{1,2} = \begin{bmatrix} c_2 & 0 & -s_2 \\ 0 & 1 & 0 \\ s_2 & 0 & c_2 \end{bmatrix}, \boldsymbol{A}_{2,3} = \begin{bmatrix} 1 & 0 & 0 \\ 0 & c_3 & -s_3 \\ 0 & s_3 & c_3 \end{bmatrix} \tag{2a, 2b, 2c}$$

Pilot's seat is placed at the intersection of gondola axes. Its position w.r.t. to based frame is:

$$\boldsymbol{r}_E^0 = \sum_{k=1}^{n} \left[\boldsymbol{A}_{0,k}\right] \left\{ \left(\boldsymbol{\rho}_{kk} + q_k \boldsymbol{e}_k\right) \right\} = \left[a_1 c_1 \quad a_1 s_1 \quad 0\right]^T \tag{3}$$

Here $c_i, s_i$ are cosine and sine of the $q_i$ angle, $a_1$ is the length of the centrifuge arm. $c_{ij}$ is $c_i c_j$ , $s_{ij}$ is $s_i s_j$ , $s_{ijk=}s_i s_j s_k$ and $\boldsymbol{\rho}_{ii} = \overrightarrow{O_i O_{i+1}}$ . Vector $\overrightarrow{O_{i+1}C_i} = \boldsymbol{\rho}_i$ defines position of the $i+1$-th center of mass of the w.r.t. to frame $C_i\xi_i\eta_i\zeta_i$. These positions are obtained from

mechanical design performed in 3CAD design software CATIA. Position of the *i*-th center of mass of the w.r.t. to based frame is given by equation:

$$\overrightarrow{OC_i} = \vec{r}_{Ci} = \sum_{k=1}^{i} \left( \boldsymbol{\rho}_{kk} + \xi_k \mathbf{e}_k q_k \right) + \boldsymbol{\rho}_i \tag{4}$$

Here $\mathbf{e}_k$ represents unit vector along joint axis. Parameter $\xi_k$ has value 1 for rotation and 0 for translation.

Orientation of pilot seat is defined by classical Euler angles of precession $\psi$, nutation $\theta$, and intrinsic rotation $\varphi$:

$$\boldsymbol{A}_{0,3} = \begin{bmatrix} c_{12} & -s_1c_3 - c_1s_{23} & s_{13} - c_{13}s_2 \\ s_1c_2 & c_{13} - s_{123} & -c_1s_3 - s_{12}c_3 \\ s_2 & c_2s_3 & c_{23} \end{bmatrix} = \begin{bmatrix} c_\psi c_\varphi - s_\psi c_\theta s_\varphi & -c_\psi c_\varphi - s_\psi c_\theta c_\varphi & s_\psi s_\theta \\ c_\psi c_\varphi + c_\psi c_\theta s_\varphi & -s_\psi c_\varphi + c_\psi c_\theta c_\varphi & -c_\psi s_\theta \\ s_\theta s_\varphi & s_\theta c_\varphi & c_\theta \end{bmatrix} \tag{5}$$

$$\psi = arctg\left( -\frac{s_{13} - c_{13}s_2}{-c_1s_3 - s_{12}c_3} \right) + k\pi, \quad k = 0,\pm1,\pm2,... \quad \varphi = arctg\left( -\frac{s_2}{c_2s_3} \right) + k_2\pi, \quad k_2 = 0,\pm1,\pm2,... \tag{6a, 6b}$$

$$\theta = arctg\left( -\sqrt{\left(s_{13} - c_{13}s_2\right)^2 + \left(-c_1s_3 - s_{12}c_3\right)^2} \,/\, c_{23} \right) + k_1\pi, \quad k_1 = 0,\pm1,\pm2,... \tag{7}$$

Angular velocities and accelerations of the link *i* w.r.t. based frame are obtained from following expressions:

$$\boldsymbol{\omega}_i^0 = \sum_{\alpha=1}^{i} \mathbf{A}_{0,i} \left\{ \mathbf{e}_\alpha \right\} \dot{q}_\alpha \,, \boldsymbol{\varepsilon}_i^0 = \sum_{\alpha=1}^{i} \mathbf{A}_{0,\alpha} \left\{ \mathbf{e}_\alpha \right\} \ddot{q}_\alpha + \sum_{\alpha=1}^{i} \sum_{\beta=1}^{\alpha} \mathbf{A}_{0,\beta} \left\{ \mathbf{e}_\beta^d \right\} \mathbf{A}_{\beta,\alpha} \left\{ \mathbf{e}_\alpha \right\} \dot{q}_\alpha \dot{q}_\beta \tag{8a, 8b}$$

Linear velocities and accelerations of the link's center of masses are obtained from:

$$\mathbf{v}_{C_i} = \sum_{\alpha=1}^{i} \vec{T}_{\alpha(i)} \dot{q}_\alpha \quad \mathbf{a}_{C_i} = \sum_{\alpha=1}^{i} \vec{T}_{\alpha(i)} \ddot{q}_\alpha + \sum_{\alpha=1}^{i} \frac{d\vec{T}_{\alpha(i)}}{dt} \dot{q}_\alpha \tag{9a, 9b}$$

where $\vec{T}_{\alpha(i)} = \partial \vec{r}_{Ci} / \partial q_\alpha$ .

### *2.2. Inverse kinematics*

Inverse kinematics problem is to find the values of joint angles (internal coordinates) required to obtain the desired values of position and orientation of end-effector (in this case pilot's seat). Input (external coordinates) can have different forms, depending on purpose. In this paper, Euler angles are chosen as input. Joint angles obtained from (10) and by multiplying (10) with $\boldsymbol{A}_{1,0}$ are given in (11a, 11b, 11c):

$$\boldsymbol{A}_{0,3} = \begin{bmatrix} c_\psi c_\varphi - s_\psi c_\theta s_\varphi & -c_\psi c_\varphi - s_\psi c_\theta c_\varphi & s_\psi s_\theta \\ c_\psi c_\varphi + c_\psi c_\theta s_\varphi & -s_\psi c_\varphi + c_\psi c_\theta c_\varphi & -c_\psi s_\theta \\ s_\theta s_\varphi & s_\theta c_\varphi & c_\theta \end{bmatrix} = \begin{bmatrix} n_{x3} & o_{x3} & a_{x3} \\ n_{y3} & o_{y3} & a_{y3} \\ n_{z3} & o_{z3} & a_{z3} \end{bmatrix} = \begin{bmatrix} c_{12} & -s_1c_3 - c_1s_{23} & s_{13} - c_{13}s_2 \\ s_1c_2 & c_{13} - s_{12}s_3 & -c_1s_3 - s_{12}c_3 \\ s_2 & c_2s_3 & c_{23} \end{bmatrix} \tag{10}$$

$$q_1 = arctg\left( \frac{n_{y3}}{n_{x3}} \right), q_2 = a\tan 2\left( n_{z3}, c_1n_{x3} + s_1n_{y3} \right), q_3 = arctg\left( \frac{o_{z3}}{a_{y3}} \right) \tag{11a, 11b, 11c}$$

*2.3. Jacobian and singular positions*

For robot manipulators, Jacobian is defined as the matrix that transforms the joint rates in the actuator space to velocity state in end-effector space:

$$\dot{\bar{\mathbf{q}}} = \mathbf{J}\dot{\mathbf{q}}, \mathbf{J} = \begin{bmatrix} \mathbf{J}_I & \mathbf{J}_{II} \end{bmatrix}^T \tag{12}$$

Here, $\bar{\mathbf{q}}$ is vector of external coordinates, and $\mathbf{q}$ is vector of internal coordinates. If external coordinates describing position and orientation of the end-effector are given in the form of (3) and (6a,6b,7) $\mathbf{J}_I$ and $\mathbf{J}_{II}$ are given in following equations:

$$\mathbf{J}_I = \begin{bmatrix} -s_1 a_1 & 0 & 0 \\ c_1 a_1 & 0 & 0 \\ 0 & 0 & 0 \end{bmatrix}, \mathbf{J}_{II} = \begin{bmatrix} 1 & -s_\psi c_\theta / s_\theta s_1 - c_\psi c_\theta c_1 & -s_\psi c_\theta / s_\theta c_{12} + c_\psi c_\theta s_1 c_2 + s_2 \\ 0 & c_\psi s_1 - s_\psi c_1 & c_\psi c_1 c_2 + s_\psi s_1 c_2 \\ 0 & s_\psi / s_\theta s_1 + c_\psi / s_\theta c_1 & s_\psi / s_\theta c_{12} - c_\psi / s_\theta s_1 c_2 \end{bmatrix} \tag{13}$$

If we place centers of masses into joints in (9a), velocities of joints are obtained and it has been shown that these terms coincide from those obtained from $\mathbf{J}_I$.

Determination of singular positions is of great importance in the design of control system. From $\det(\mathbf{J}_{II}) = c_2$ singular position of manipulator $q_2 = \pm\pi/2$ is obtained. In this position for definitely small values of end-effector velocities, indefinitely large values of joint velocities are required. This position is avoided by control algorithm.

## 3. Inverse dynamics problem

The inverse dynamics problem is to find the actuator torques and/or forces required to generate a desired trajectory of the manipulator. In this paper, this problem is solved in joint space by applying covariant form of Lagrange's equation of motion. This method is based on knowledge of kinetic and potential energy of the robot or its links. Kinetic energy of link *i* is calculated from following equations[6]:

$$E_{ki} = E_{ki}^{tr} + E_{ki}^{rot} = \frac{1}{2} m_i \mathbf{v}_{ci}^2 + \frac{1}{2} \boldsymbol{\omega}_i^i \mathbf{J}_{ci}^i \boldsymbol{\omega}_i^i, i = n,...,2,1, \tag{14a, 14b}$$

Generalized force of $\alpha$ link from gravity is:

$$Q_\alpha^G = \sum_{i=1}^{n} m_i \mathbf{g} \cdot \vec{T}_{\alpha(i)}, \alpha = n,...,2,1 \tag{15}$$

From covariant form of Lagrange's equation of motion:

$$\sum_{\alpha=1}^{n} a_{\alpha\gamma} \ddot{q}_\alpha + \sum_{\alpha=1}^{n} \sum_{\beta=1}^{n} \Gamma_{\alpha\beta,\gamma} \dot{q}_\alpha \dot{q}_\beta = Q_{\gamma g} + Q_{\gamma a}, \gamma = 1,2,...,n \tag{16}$$

required actuator torque for $q_\gamma$ generalized coordinate, $Q_{\gamma a}$ is obtained. Here, $\Gamma_{\alpha\beta,\gamma}$ are Christoffel symbols:

$$\Gamma_{\alpha\beta,\gamma} = \frac{1}{2} \left( \frac{\partial a_{\beta\gamma}}{\partial q_\alpha} + \frac{\partial a_{\gamma\alpha}}{\partial q_\beta} - \frac{\partial a_{\alpha\beta}}{\partial q_\gamma} \right). \tag{17}$$

$a_{\alpha\beta}$ are metric tensor coefficients :

$$a_{\alpha\beta} = \frac{\partial^2 E_k}{\partial \dot{q}_\alpha \partial \dot{q}_\beta}, \; E_k = \sum_{i=1}^{n} E_{ki} = \frac{1}{2} \sum_{\alpha=1}^{n} \sum_{\beta=1}^{n} a_{\alpha\beta} \dot{q}_\alpha \dot{q}_\beta \tag{18}$$

## 4. Simulation in the off-line unit of control system

In robotics, during control design prior to the device realization, it is of great importance to test control algorithms for all possible conditions. The purpose of development of kinematic and dynamic models is possibility of analysis of controlled object behavior in simulated environment. As mentioned before in this paper, control system for this device is obtained by adding new functionalities into control unit for robot programming L-IRL (Lola Industrial Robot Language) and by implementing kinematic and dynamic model. This system has offline and online part. In the offline unit programming and testing of L-IRL code is done[7].

One of the possibilities for testing and analysis provided by offline system is an overview of all important kinematic and dynamic quantities obtained by implementing previously described model during different centrifuge operational scenarios. Graphs of some of these kinematic and dynamic quantities for planetary axis in the case of *open-loop* operational centrifuge mode produced by L-IRL offline unit are given *in Figs.* 4-8. Here, the predefined nonlinear profiles of the absolute acceleration in the center of gondola which is the input in inverse dynamics algorithm is given in Fig. 3. This profile is set by GMOVE instructions [8].

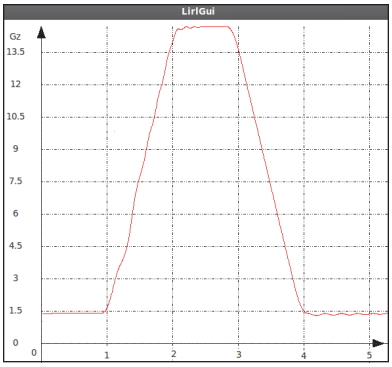


**Figure 3.** Abs. acceleration in the center of the gondola-input in inv. dyn. algorithm

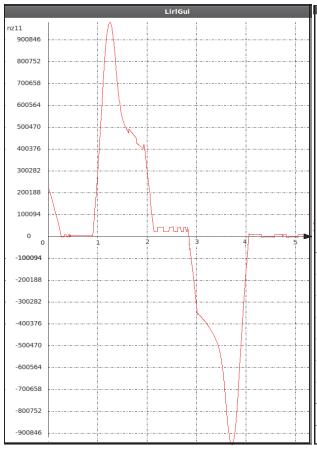


**Figure 4.** Actuator moment (Planetary axis)

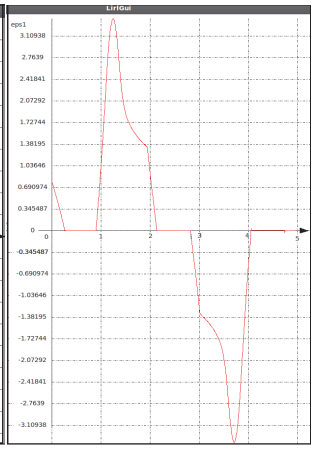


**Figure 5.** Angular acceleration of planetary axis

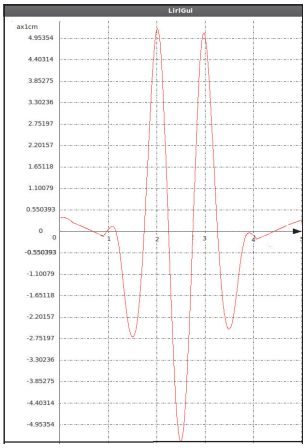


**Figure 6**. *x* component of linear acceleration of C w.r.t. based frame

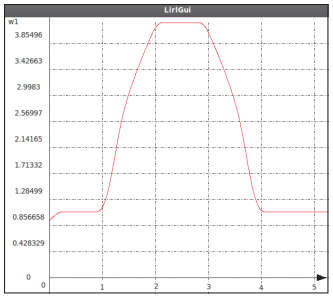


**Figure 7.** Angular velocity of first link

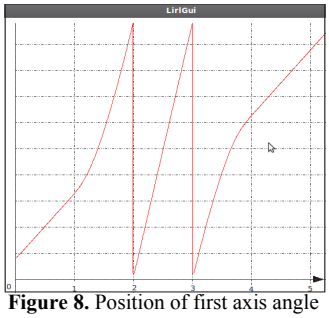


**Figure 8.** Position of first axis angle

## 5. Conclusion

In this paper modeling of human centrifuge as three DoF robot manipulator is presented. Algorithms of forward kinematics given by position of the pilot's seat w.r.t. to fixed frame and Euler angles, as well as the inverse kinematics algorithm are given. Velocities and accelerations of centers of masses as well of joints are determined. Development of manipulator Jacobian has shown that manipulator has singular position for $q_2 = \pm\pi/2$. Inverse dynamics algorithm based on covariant form of Lagrange equations of the second kind is given. These algorithms have been implemented into control unit and model has been simulated in offline part of the control unit. Simulation performed in offline system for open-loop centrifuge operational mode has given a fairly good insight of conduct of all important kinematical and dynamical quantities of this device.

*Acknowledgement.* This work was created within the research project that is supported by the Ministry of Education, Science And Technological Environment of Republic of Serbia: No (35023) and is partially supported by the Ministry of Education, Science And Technological Environment of Republic of Serbia, No (35006).

## References

[1] Levin B., Kiefer D. (2002) Dynamic Flight Simulator for Enhanced Pilot Training, *SAFE* Europe
[2] Chen Y. C., Repperger D. W. (1995) A study of the kinematics, dynamics and control algorithms for a centrifuge motion simulator, *Proceedings of the American Control Conference*, Seattle, Washington, June 21-23, 1995, pp. 1901-1905.
[3] Vidaković J., Kvrgić V., Ferenc G., Lutovac M., (2012 ) Kinematic model of human centrifuge, *Proceedings of 56th conference ETRAN,* Zlatibor, June 11-14, 2012, pp.
[4] Kvrgic V. (1998) Development of intelligent system for management and programming of industrial robots (in Serbian), PhD dissertation, University of Belgrade, Faculty of Mechanical Engineering
[5] Ferenc G., Dimić Z., Lutovac M.,Vidaković J., Kvrgić V., (2012) *Distributed Robot Control System Implemented on the Client and Server PCs Based on the CORBA Protocol*, Proceedings of the 1st Mediterranean Conference on Embedded Computing MECO, Bar, Montenegro, pp. 158-161
[6] Čović V., Lazarević M., (2009) Mechanics of Robots, University of Belgrade *Faculty of Mechanical Engineering*
[7] Lutovac M., Dimić Z., Ferenc G., Vidaković J., Bućan M., (2012) *Virtual robot in distributed control system*, *Proceedings of 20th Telecommunications forum TELFOR 2012*
[8] Vidaković J., Kvrgić V., Ferenc G., Dančuo Z., Lazerević M. (2012) Control of a human centrifuge, 29DA Symposium on Advances in Experimental Mechanics, 26-29 September, Belgrade, pp.186-189.

# THE INFLUENCE TERRAIN SLOPE ON IMPACT POINT OF ROCKETS BURST LAUNCHING FROM MLRS

**Milan Milošević [1], Vlado Đurković [2], Zoran Gajić [3]**

1 Military Technical Institute, Belgrade,
Ratka Resanovića. 1, Belgrade
e-mail: marija.m@beotel.net
2 Military Academy,Belgrade,
Pavla Jurišića Šturma 33, Belgrade
e-mail: vlado.djurkovic@va.mod.gov.rs
3 Military Technical Institute, Belgrade,
Ratka Resanovića. 1, Belgrade
e-mail: zoran.gajic52@gmail.com

**Abstract**: This paper analyzes the effect of the terrain slope to the firing elements and rocket impact point at burst launch of **M**ultiple **L**aunch **R**ocket **S**ystem (MLRS). Terrain slope were simulated over sensors of the slope in the longitudinal and transversal axis. Slope angle value is simulated by the random function. The influence of terrain slope through the mathematical expectation and standard deviation of the firing elements and rockets on the target dispersion using the Monte- Carlo method for a concrete rocket launcher is shown.

**Keywords:** terrain slope, inclinometers, rocket launcher, unguided rockets, the Monte-Carlo simulations and firing elements.

## 1. Introduction

The basic firing elements (elevation and azimuth angles) of artillery and rocket launchers are defined in the horizontal plane. All the deformation of vehicles and launcher mechanisms which are under a launching device affect the position of the sight lines in space. The values of these deformations for a particular system depend on many parameters. Certainly the parameters that have the largest effect are the number of rockets in the launching device and the position of a launching device for height and direction. The slope of cradle direction, measured with a device that would in itself has two inclination sensors. This device would be mounted to the moveable azimuth mechanism that is so called cradle direction. One sensor would measure the angle slope of the lower part in the direction of fire and the second perpendicular to it.
In addition to deformation cradle direction because by mass changes due to a decrease the number of rocket in launching device at burst firing, the device measures and any other deviation from the horizontal plane.
Automatic removal of terrain slope and other deformation cradle direction, means that the elements of fire from the horizontal plane are adjusted with the required software, based on the measured angles.

## 2. Mathematical model of the removal effects of terrein slope

Mechanical model of multi tubes rocket launcher system consists of: special purpose vehicles, launching device, the device for elastic system disconnection, the traversing mechanism and elevating mechanism and ammunition - missiles. The bearing or the lower

part of the vehicle and the vehicle frame have two longitudinal reinforced box profile fixed with the cross elements of great stiffness. The system for the elastic disconnection of the vehicle is detached to the frame of the vehicle and it consists of four legs supported on the ground [1].

On the movable part of the mechanism of traversing (the cradle direction) the absolute angular strain denoted $\varepsilon_L$ and $\varepsilon_T$ (relative to the horizontal plane) in the longitudinal and transverse axis ( $x, y$ ) of cradle directions are measured.

The basic model will be shown here, while a detailed mathematical model presented in [2].

The mathematical model is generalized by introducing a rectangular coordinate system moving in an inclined surface where the sensors that measure the angles of inclination of the cradle direction. The figure Fig. 1 shows the mutual position of the horizontal and inclined plane with the sensors on a moving cradle direction. The longitudinal axis of the vehicle was marked with the line $OL$, which is inclined by an angle to the horizontal $\varepsilon_{LV}$, transverse axis of the vehicle is marked $OT$ and is inclined to the horizontal by an angle $\varepsilon_{TV}$. Rightly $OP$ denoted by the intersection of horizontal and inclined plane whose mutual angle is denoted $\varepsilon_0$. With rollers $LL$ and $TL$ are marked with sensors that measure the angles of inclination to the horizon $\varepsilon_L$ and $\varepsilon_T$ (hatched triangles Fig. 1). The position of the longitudinal axis of the cradle direction of the inclined plane is denoted by an angle $\varphi_{KL}$ and its projection in the horizontal plane $\varphi_{HL}$.

Angular position of the moving coordinate system is defined by the longitudinal axis of the vehicle which is the angle the direction of a launching device ($\psi_{ENC}$). Since the azimuth angle is defined as the angle of the north to the longitudinal axis of the vehicle, you need to know the angle of inclination of the longitudinal and transverse axis of the vehicle in a stationary coordinate system.

From the spherical right-angled triangles $\Delta$ P_LL_LLH and $\Delta$ P_L_LH Fig. 1, based on the sine theorem follows the slope of the longitudinal axis of the vehicle $\varepsilon_{LV}$ as

$$\sin\varepsilon_{LV} = \sin\varepsilon_L \frac{\sin(\varphi_{KL} - \psi_{ENC})}{\sin\varphi_{KL}}. \tag{1}$$

Similarly for the transverse axis of the vehicle is obtained $\varepsilon_{TV}$ by using the expression

$$\sin\varepsilon_{TV} = \sin\varepsilon_T \frac{\cos(\varphi_{KL} - \psi_{ENC})}{\cos\varphi_{KL}}. \tag{2}$$

With equations (1) and (2) transfer goes to the stationary coordinate system whose mathematical model is given in [3].

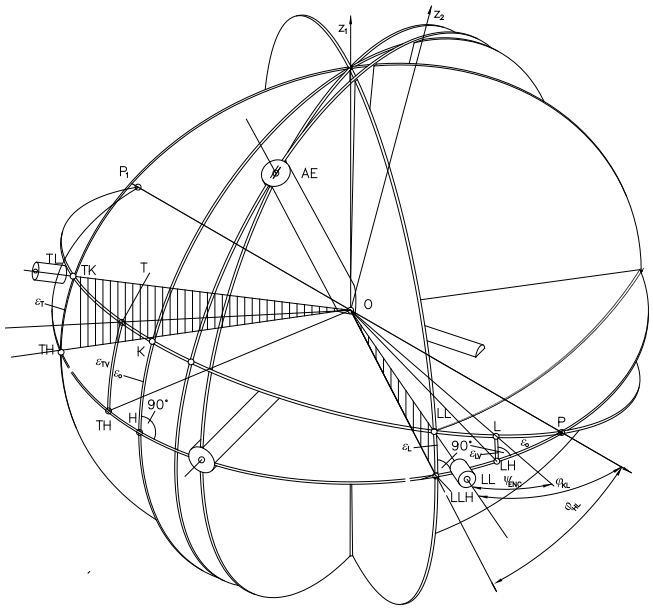


**Fig. 1:** *Interactions between a horizontal position and inclined plane with movable inclination sensors*

## 3. Firing elements from terrain slope

The elements of fire from the terrain slope are derived in details in [3] and can write the following expressions:

1. elevation angle is

$$\gamma_k = \arcsin\begin{pmatrix}\cos\gamma\sin(\psi+\alpha_0)\sin\theta_2 - \\ \cos\gamma\cos(\psi+\alpha_0)\cos\theta_2\sin\varepsilon_{LV} + \\ \sin\gamma\cos\theta_2\cos\varepsilon_{LV}\end{pmatrix} \tag{3}$$

2. azimuth angle is

$$\psi_k = \frac{\cos\gamma\sin(\psi+\alpha_0)\cos\theta_2}{\cos\gamma\cos(\psi+\alpha_0)\cos\varepsilon_{LV}+\sin\gamma\sin\varepsilon_{LV}} + \frac{\cos\gamma\cos(\psi+\alpha_0)\sin\theta_2\sin\varepsilon_{LV}-\sin\gamma\sin\theta_2\cos\varepsilon_{LV}}{\cos\gamma\cos(\psi+\alpha_0)\cos\varepsilon_{LV}+\sin\gamma\sin\varepsilon_{LV}} . \tag{4}$$

In the expressions (3) and (4) are:

$$\cos\theta_2 = \cos\varepsilon_{TV}\cos(\alpha_0+\alpha_1) \tag{5}$$

$$\alpha_0 = \left(\varphi_{KL}-\psi_{ENC}\right) - \cos^{-1}\left(\frac{\cos(\varphi_{KL}-\psi_{ENC})}{\cos\varepsilon_{LV}}\right) \tag{6}$$

$$\alpha_1 = \cos^{-1}\left(\frac{-\sin(\varphi_{KL} - \psi_{ENC})}{\cos\varepsilon_{TV}}\right) - \left(90^\circ + (\varphi_{KL} - \psi_{ENC})\right). \quad (7)$$

## 4. Numerical simulation of the terrein slope at burst launching

The simulation was performed for the elements of fire in the horizontal plane by an angle of elevation $\gamma = 30^\circ$, azimuth target $\psi_T = 190^\circ$ and azimuth vehicles $\psi_V = 100^\circ$. Readings of angles of the longitudinal and transverse slope of the numerical simulations obey the normal law of distribution with parameters:

- the mean slope of the longitudinal and transverse axis $\varepsilon_{Lsr} = 0.5^\circ$ and $\varepsilon_{Tsr} = 0.5^\circ$ and
- standard deviations of the slopes are $\sigma_L = 0.08^\circ$ and $\sigma_T = 0.08^\circ$.

The Fig. 2 shows 100 generated measurements of longitudinal and transverse terrain slope. Generation is performed by the following expressions:

$$\varepsilon_L = (\varepsilon_{Lsr} + \sigma_L \,\mathrm{rng}()) \text{ and } \varepsilon_T = (\varepsilon_{Tsr} + \sigma_T \,\mathrm{rng}()) \quad (8)$$

where is $\mathrm{rng}()$ a function that randomly generates numbers in the given limits.

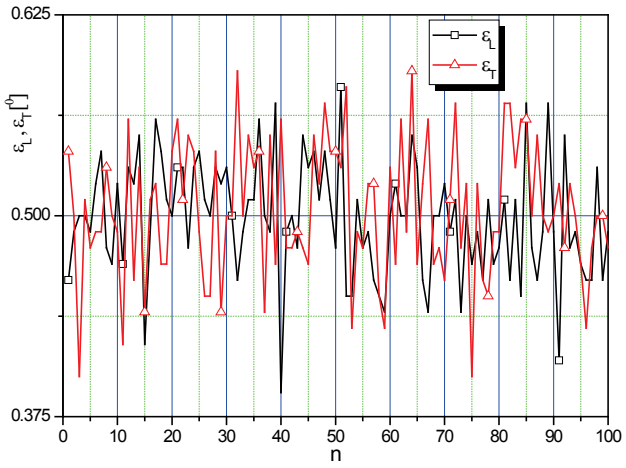


**Fig. 2:** *Simulation of terrain slope of the longitudinal and transverse axis measured by inclination sensors.*

Fig.3 The figure shows the firing elements, those are elevation angle $\gamma$ and azimuth angle $\psi$ of a launching device that are obtained based on the above mentioned mathematical model from the inclined i.e. inclined plane of the cradle direction.
The simulation is performed using Monte Carlo software package [4] with 100 simulations, where they obtained the mean elevation angle and the direction angle and their standard deviations. The mean value of the angle elevation is $\gamma_{sr} = 29.495^\circ$ and the standard deviation is $\sigma_\gamma = 0.043^\circ$.

The mean angle of direction is $\psi_{sr} = 89.716^\circ$ and the standard deviation is $\sigma_\psi = 0.021^\circ$.

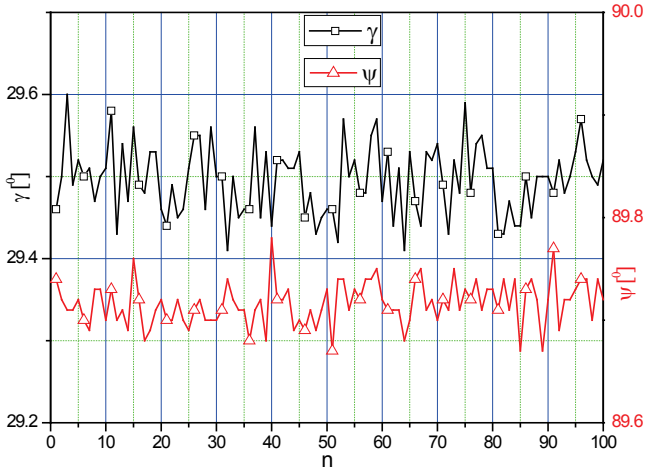


**Fig. 3**: *Firing elements elevation and azimuth angles*

## 5. The dispersion of rocket impact points on the target at burst launching

Launching system GRAD 122mm was taken for a numerical example. Based on 100 launches using the Monte Carlo method leads to the standard deviation of missiles impact point on the target:

- standard deviation of the range $\sigma_D = 12.913\,\text{m}$ and
- standard deviation of the direction is $\sigma_P = 6.198\,\text{m}$ .

Probably the range of deviation ($V_d$) and direction ($V_p$) are the axis of the ellipse and the unit can be calculated:

- $V_d = 0.6745\sigma_D = 8.7\,\text{m}$ and $V_p = 0.6745\sigma_P = 4.2\,\text{m}$

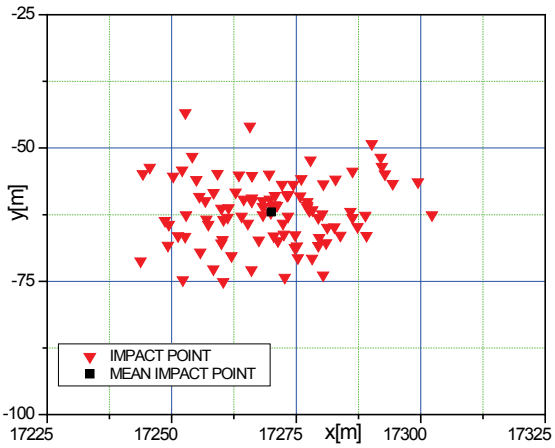


**Fig. 4:** *Simulation rocket impact point on target*

In Fig. 4 rocket impact point on target for the all 100 launches are shown. Calculation of trajectory was made on the basis of modeled rocket flight with 6 DOF [4]. The mean value is also shown with its coordinates $X_{mean} = 17269\,\mathrm{m}$ and $Y_{mean} = -62\,\mathrm{m}$.

## 6. Conclusion

Deformations of the cradle direction that arise due to different number of rockets to launch the device, the position of a launching device for height and direction is done by adjusting the set of basic elements of fire in the horizontal plane. This correction is calculated based on the measured slope cradle directions two directions perpendicular to the axis.
The paper is numerically simulated deformation of the cradle direction using data from two sensors located in the longitudinal and transverse axis of the cradle direction. The simulation is done with a normal distribution law for the mean angular deformation in the longitudinal and transverse axes cradle direction $\varepsilon_L = \varepsilon_T = 0.5^\circ$ and the mean square error or standard deviation $\sigma_L = \sigma_T = 0.08^\circ$. By using the numerical experiments and the random function 100 values of longitudinal and transverse inclination cradle direction are obtained.
Firing elements with strain planes were calculated on the basis of these simulated measurements of angles of strain the cradle direction using equations (3) and (4).
The mean elevation angle and the mean azimuth angle and their standard deviations were obtained by using Monte Carlo methods.
Also by using the Monte Carlo method for the rocket system "GRAD" the standard deviation and probable deviations of the rocket impact point on the target are obtained.
The results of numerical simulations of terrain slope by using the inclination sensors in the longitudinal and transverse axis of the cradle direction show that the probable deviations of rocket of the impact points $V_d = 8.7\,\mathrm{m}$ and $V_p = 4.2\,\mathrm{m}$ are significant. When they are compared to the tablet probable deviations for this range it visible that they are $\frac{V_d}{V_{dTAB}} = 0.10$ and $\frac{V_p}{V_{pTAB}} = 0.04$.

From presented, we can see that due to the terrain slope the correction of the firing elements have to be done in advance according to the given model.

## Reference

[1] Živanić D., Milošević B.M., *"Design and Basic Calculation of the Multiple Rocket Launcher Subsystem"*- Examples notes, ВТИ –03-01-0524, 1998.

[2] Милошевић Б.М., *"Математички модел отклањања утицаја косине терена на самоходним вишецевним ракетним лансерима"*, ВТИ–02-01-0056, 2010.

[3] Милошевић Б.М., *"Допринос истраживању параметара интеракције ракета- лансирни уређај на рад система управљања ватром вишецевних ракетних система"*- докторска дисертација, Универзитет одбране, Војна академија, Београд 2012.

[4] Ћук Д., Мандић С., Милошевић Б.М., "*Софтверски пакет GMTC_6D – M1*", ВТИ, Београд, 2012.

# ASSESSMENT OF THE FATIGUE LIFE REDUCTION OF MACHINE PARTS WITH CORROSION PIT

**Dejan B. Momčilović[1], Ivana Atanasovska[2], Ljubica Milović[3], Zorica Đorđević[4]**

[1] Institute for Testing of Materials IMS,
Bulevar vojvode Mišića 43, 11000 Belgrade,
e-mail: dejanmomcilovic@yahoo.com
[2] Institute Kirilo Savić,
Vojvode Stepe 51, 11010 Belgrade,
e-mail: iviatanasov@yahoo.com
[3] Faculty of Technology and Metallurgy, The University of Belgrade,
Karnegijeva 4, 11120 Belgrade,
e-mail: acibulj@tmf.bg.ac.rs
[4] Faculty of Engineering, The University of Kragujevac,
Sestre Janjic 6, 34000 Kragujevac,
e-mail: zoricadj@kg.ac.rs

**Abstract.** This paper describes the assessment methodology for quantifying the influence of corrosion pit on reduction of fatigue life of machine parts. The real case study is used as a basis for the research. The Finite Element Analysis was completed to calculate the stress concentration factor increase as a result of corrosion pit occurrence. The corrosion pits are modelled at a zone with maximum stresses i.e. shaft-flange transition section. The modelled corrosion pit was dimensioned to comply with real in-situ measured dimension of pits.
The presented research points to new trends in quantification of corrosion pit stress concentration by application of Theory of Critical Distances. The TCD represents a major extension of linear elastic fracture mechanics (LEFM), allowing it to be used for short cracks as well as for stress concentrations of arbitrary geometry, using the results of finite element analysis (FEA) or other computer-based numerical methods. This paper illustrates the application and potentials of the TCD on a case study on the failure analysis of a turbine shaft from a hydro power plant.

## 1. Introduction

Pitting corrosion represents an important limitation to the safe and reliable use of many alloys in various industries. Pitting is a form of serious damage in metal such as high-strength aluminium alloys and various grades of steels, which are susceptible to pitting when exposed to a corrosive attack in aggressive environments [1]. Numerous studies on corrosion fatigue on test specimens with artificially induced pits and failure analyses on real components, shows that pits are usually found at the origin of fracture surface [2–4]. It is well-known that machine components and structure such as super-heaters, propeller shafts, turbine and pump elements, offshore structure severely suffer from corrosion attack and c cyclic loading [5,6]. Pit formed on the surface of the structure or component tends to

intensify the local stress field and hence reduce the load carrying capacity of the component. Recent works achieved quantification of this influence of corrosion pits by numerical simulation and calculation of stress concentration factors [7, 8].

Micro-mechanic model presented by De Los Rios [9] and numerical investigation [10] pave the path to the phenomenology approach of fatigue macro crack initiation near stress concentration [11]. At the same time group of the Taylor start to formulate his work [12] into what is known as Theory of Critical Distances – TCD [13]. The major question, still valid, is how to improve present design procedures [14] and reconstruct chain of events that cause the failure. The significant improvement of calculation of influence of stress concentration features was presented [15] and that was the basis of this paper. This paper uses the TCD and knowledge about geometry of corrosion pits on assessment of fatigue life of failure analysis of real engineering component

## 2. Background

The bulb turbine generator's horizontal shaft, Fig. 1, is made by joining the forged and cast parts by slag welding. The shaft is manufactured as hollow, housing a servomotor inside it, for shifting the runner blades. The flange, on which the crack occurred, is made of steel casting of 20GSL designation, according to GOST 977-88 [16]. The equivalent material quality designation of cracked flange is G20Mn5 according to EN 10293 : 2005, [17]. The operating speed of turbine shaft was 62.5 rpm. Between 2007 and 2008 the cracks were found on seven turbine shafts, Fig 2. The detail results of the failure analysis was published and described in reference [6].

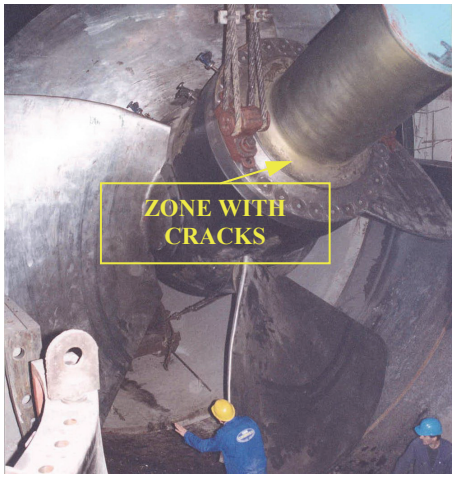


**Fig 1.** Turbine shaft with runner during assembling in the bulb

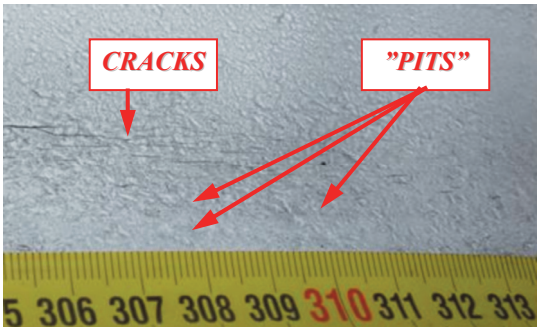


**Fig. 2.** Actual size of corrosion pits on transition radius

## 3. Description of applied methodology

One of the key points in failure analysis is the ability to make accurate predictions of the strength and fracture of materials in complex load-bearing structures in vicinity of stress

concentration raiser. This task, the strength calculation of failed part like turbine shaft in this case, is also linked with the review of original designer approach in order to check hidden design errors. The majority of failures could be addressed to high-cycle fatigue [15,18], and due to the fact that real engineering structures contain stress concentrations from which fatigue cracks frequently initiate, the prediction of the effect of stress concentrations on fatigue life and fatigue strength is of great importance.

The common point in all theories related to notch fatigue the assumption that the relevant parameter is the stress averaged over some critical volume, but for convenience of calculation this has usually been simplified to the stress at one point (a given distance from the hot spot) or to the stress averaged over a line of given length. The origin of above stated is in work of Peterson and Neuber. Peterson considered that fatigue failure occurs when the stress at a constant distance beneath the surface equals the fatigue strength of the material [19] while Neuber related the stress concentration factor at the root of a sharp notch to the average stress over a certain critical distance [20].

Summary of the materials response under fatigue is presented by Suresh [21] where is clearly demonstrated that process of fatigue starts with the first cycle. The local regions of high stress promote the basic process of crack nucleation during high cycle fatigue. The damage progresses through mechanisms starting with crack nucleation, and the growth of micro structurally small cracks. Each mechanism is associated with a characteristic size or scale of magnitude, and each characteristic size has its own geometric complexity, constitutive law, and heterogeneity. Fatigue behavior cannot be fully understood and predicted without obtaining information about each of the characteristic sizes. According to the observations of Kitagawa and Takahashi [22], fatigue crack growth behavior of short cracks differs in a non-conservative manner from expectations based upon long crack behavior. Further contribution in understanding was done by El Haddad [23] who introduced an effective crack length to predict the propagation behavior of short cracks. In this formulation the effective crack length is equal to the crack length plus an amount "$l_0$", which is related to the critical distance. This value "$l_0$" was stated by the authors as a characteristic of the material and the material condition accounting for the non-continuum behavior of very small cracks.

The theory of critical distances (TCD) as named by Taylor [13] attempts to predict the effect of notches and other stress concentration features by considering the stress field in the region close to the notch tip. This theory requires two parameters, a characteristic distance and a critical stress or strain characterizing failure. In one version of the critical distance theory, termed as the Point Method, the failure occurs when the stress becomes equal to the failure stress at a given distance from the notch root. In the other version of the critical distance theory, termed as the Line Method, the failure is assumed to occur when the stress becomes equal to the failure stress when computed as an average value over a line of given length. The background philosophy lying behind the TCD is described as wish to observe engineering components rather than to test specimens. In practice this meant that we only considered predictive methods which could be applied to bodies of arbitrary shape and size, subjected to arbitrary loadings, containing stress concentration features of arbitrary geometry. This is achieved by measuring material behavior using test specimens containing notches rather than cracks (fatigue threshold $\Delta K_{th}$ and toughness $K_c$ using sharp notches rather than pre-cracks) which avoids the difficulties and uncertainties of carrying out standard fracture mechanics tests. The second presumption of successful application of TCD is the existence of an accurate stress analysis of the machine part. Methodology of application of TCD for this case is presented at [24].

The corrosion pit with diameter of 600 $\mu m$ was first incorporated into transition radius of the model presented by [8, 24], fig 3. This size of corrosion pit was determined as a result of in-situ measurement on turbine transition radius, Fig. 2.

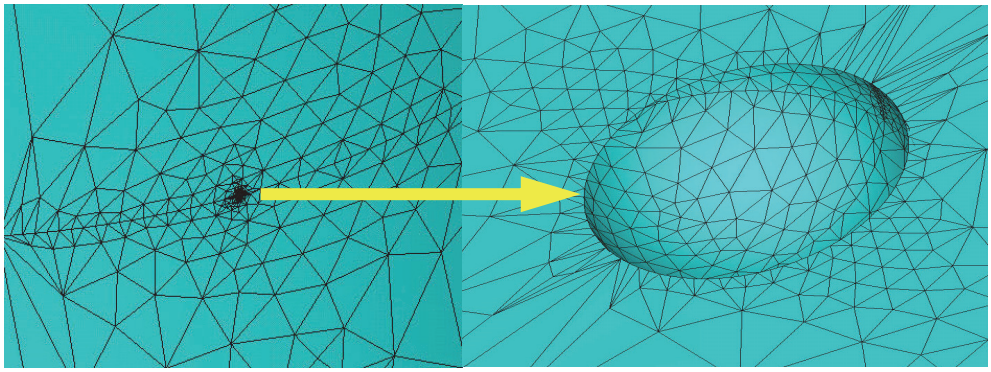

**Fig. 3.** Model of corrosion pit with 600 µm diameter on transition radius

Effect of corrosion pit on crack initiation was described in detail by Hoeppner [25]. This analysis is based on aircraft corrosion analysis and on non-ferrous metals. However, Hoeppner'a analysis and conclusions and analysis made by Chattopadhyay [26] points out that the TCD based analysis will be very convenient for our case.
On Fig 4 the stress gradients for two load cases without (LC1-turbine start and LC2-turbine stationary operation) and one load case with corrosion pit $LC1_{pit}$ are drawn on diagram. Change of the pit size and shift of stresses are shown at Fig. 5 and 6. It can be seen on figures 5 and 6, that the change in stresses caused by tension loading only doesn't changes stresses significantly at the bottom of the pit. The increase of the stresses is observed by increase of corrosion pit but on the edges of corrosion pits. The highest stress value is found, as expected, on pit with the diameter size of 1500µm, at the edge of corrosion pit. The fact that the stress level shown on Fig 4a) is higher of the value of corrosion strength of material in fresh water [24] is also another solid evidence toward pointing on corrosion fatigue as a main cause of premature failure of turbine shaft. The stresses at the bottom of the pit [27] shows that they are more critical on smaller pits, such as 600 µm diameter pit, due to influence of relevant material feature such as grain size and orientation. Calculation of critical length as described by TCD and compared with stress gradient undoubtely demonstrate conditions for corrosion fatigue crack initiation, at the bottom or on the edge, as a function of external loading.

## 4. Discussion and conclusions

From above presented, it is again confirmed that TCD methodology has significant potential in quantification and assessment of influence of any type of stress raiser on machine parts fatigue life decrease.
The practical aspect of the TCD use should be in better calculation of the stress raiser influence of structures under fatigue loading. Results of presented analysis also shows the TCD has ability to assess a magnitude of influence of corrosion pits from mechanistic point of view, without taking into account a chemistry kinetic aspects of corrosion fatigue. The further application of TCD in electric power industry should prevent failure of mechine parts and systems in design phase.

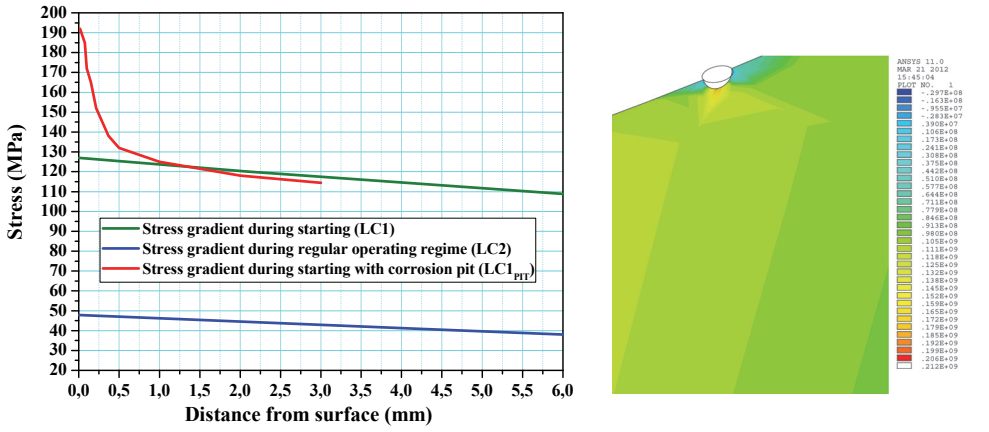


a) b)

**Fig 4.** a) Stress gradients from surface of transition radius for all load cases, b) Position of simulated corrosion pit on transition radius

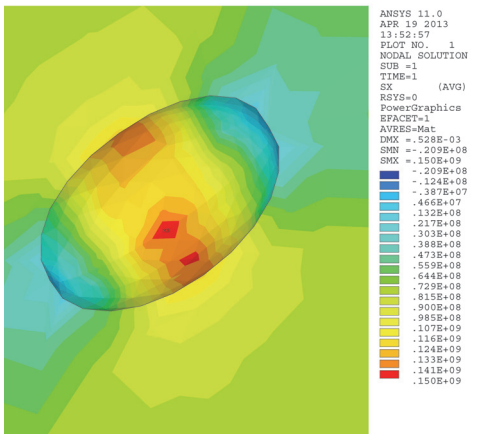

Fig 5. The stress distribution arrond simulated corrosion pit of the diameter of 1100μm

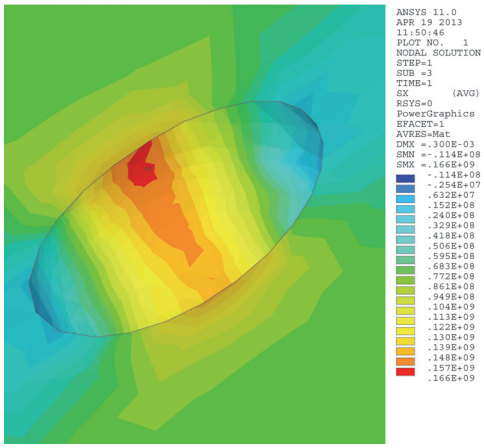

Fig 6. The stress distribution arrond simulated corrosion pit of the diameter of 1500μm

The very next step and further extension of TCD will be the calculation the number of cycles when a crack will occur on stress raiser under variable amplitude fatigue loading. The recent results strongly supports the idea that the TCD is a powerful engineering tool which can safely be used in situations of practical interest also to design notched components experiencing in-service variable amplitude fatigue loadings [28, 29]. This further work required for extension and validation of TCD in above mentioned directions, as damonstrated in this paper, emphasize the value of TCD as a tool for better estimating of fatigue lifetime of notched components.

*Acknowledgement.* This work is a contribution to the Ministry of Education, Science and Technological Development of the Republic of Serbia funded Project TR 35011.

## 5. References

[1] Winston R, Uhlig H, (2008) *Corrosion and corrosion control*. John Wiley & Sons, Inc, pp 149 – 180.
[2] Kondo Y. (1989) Prediction of fatigue crack initiation life based on pit growth. *Corrosion* Vol 45, No. 1, pp7–11.
[3] Genel K, Demirkol M, Gulmez T. (2000) Corrosion fatigue behaviour of ion nitrided AISI 4140 steel. *Mater Sci Eng A,* Vol.288, pp 91–100.
[4] *ASM Metals handbook. Failure analysis and prevention*, (1995) Fatigue failure, vol. 11. Ohio: ASM Int Metals Park.
[5] Ebara,R. (2006) Corrosion fatigue phenomena learned from failure analysis, *Engineering Failure Analysis* Vol. 13, pp. 516–525
[6] Momčilović D, Odanović Z, Mitrović R, Atanasovska I, Vuherer T, (2012) Failure Analysis of hydraulic turbine shaft, *Engineering Failure Analysis*, Vol. 20, pp. 54-66.
[7] Cerit M, Genel K, Eksi S, (2009) Numerical investigation on stress concentration of corrosion pit, *Engineering Failure Analysis*, Vol.16, pp 2467–2472
[8] Momčilović D, Mitrović R, Atanasovska I, Vuherer T, (2012) Methodology of determination the influence of corrosion pit on decrease of hydro turbine shaft fatigue life, *Machine Design - The Journal of Faculty of Technical Sciences*, ISSN 1821-1259, Vol. 4.No.4. pp 231 – 236
[9] De Los Rios E.R, Wu X.D, Miller K.J, (1996) A Micro-Mehanics Model of Corrosion-Fatigue Crack Growth in Steels, *Fatigue Frac. Engng Material. Structur.* Vol. 19. No. 11. pp. 1383-1400
[10] Rokhlin S.I, Kim J.-Y, Nagy H, Zoofan B,(1999) Effect of pitting corrosion on fatigue crack initiation and fatigue life, *Engineering Fracture Mechanics* 62 pp 425-444
[11] Ostash, O.P, Panasyuk V.V, Kostyuk E.M, (1999) A phenomenological model of fatigue macrocrack initiation near stress concentrators, *Fatigue Frac. Engng Material. Structur.* Vol. 22. pp. 161-172
[12] Taylor D., (1999) Geometrical effects in fatigue: a unifying theoretical model. *Int. J. Fatigue,* Vol 21, (1999), pp 413–20
[13] Taylor, D, (2007) *Theory of Critical Distances: A New Perspective in Fracture Mechanics,* ISBN 978-0-08-044478-9, Elsevier Science
[14] Ghidini T, Dalle Donne C, (2009) Fatigue life predictions using fracture mechanics method, *Engineering Fracture Mechanics* Vol. 76, pp 134–148
[15] Taylor, D, (2011) Applications of the theory of critical distances in failure analysis, *Engineering Failure Analysis* Vol. 18, pp543–549
[16] GOST 977-88, Steel Catings. General Specification, (1988).
[17] EN 10293, Steel castings for general engineering uses, (2005)
[18] Brooks, R,C., (1993) Metallurgical failure analysis. New York: McGraw-Hill, pp 6-11
[19] Peterson, R. E. (1959), Notch Sensitivity, Metal Fatigue, Edited by G. Sines, J. L. Waismas, McGraw - Hill, pp. 293-306.
[20] Neuber, H., (1958) Theory of Notch Stresses, translation of 1957 Edition in German, Springer, Berlin.
[21] Suresh, S.(1998), *Fatigue of Materials,* Cambridge University Press. ISBN 9780521578479, pp 30 -94
[22] Kitagawa, H., Takahashi, S. (1976) *Proc. of the 2nd Int. Conf on Mech. Behaviour of Materials*., ASM, 627–631.
[23] El Haddad M. H., Dowling, N.E., Topper, T. H., and Smith. K. N., (1980) J Integral Applications for Sort Fatigue Crack at Notches, International Journal of Fracture, Vol 16, pp 15 - 30.
[24] R. Mitrović, D. Momčilović, I. Atanasovska, (2013) Assessment of the effect of pitting corrosion on fatigue crack initiation on hydro turbine shaft, *Advanced Materials Research, ISSN: 1022-6680, Vol. 633 (2013): Advances in Engineering Materials, Product and Systems Design (Special topic volume with invited peer reviewed papers only), Editor: Aleksandar Subić, ISBN-13: 978-3-03785-585-0, Trans Tech Publications, Switzerland*
[25] Hoeppner, D.W., Arriscorreta C.A, (2012) Exfoliation Corrosion and Pitting Corrosion and Their Role in Fatigue Predictive Modeling: State-of-the-Art Review, *International Journal of Aerospace Engineering* Volume 2012, doi:10.1155/2012/191879
[26] Chattopadhyay, S, (2010) High Cycle Fatigue of Structural Components Using Critical Distance Methods, Proceedings of the SEM Annual Conference June 7-10, 2010, ISBN 978-1-4419-9497-4, *The Society for Experimental Mechanics,* Indianapolis, Indiana USA, pp 463 – 468
[27] Momčilović D, Mitrović R, Atanasovska I, (2012) Quantification of stress raiser influence on decrease of machine parts fatigue life, *KOD2012, Proceedings – the Seventh International Symposium KOD 2012*, 24-26.05.2012., Balatanfured, Hungary, ISBN 978-86-7892-399-9, COBISS.SR-ID 271298311, Published by Faculty of Technical Science – Novi Sad, Serbia, pp.215-218.
[28] Taylor, D (2005), Analysis of fatigue failures in components using the theory of critical distances, *Engineering Failure Analysis*, Vol.12, Issue 6, pp 906 - 914
[29] Susmel L, Taylor D, (2011), The Theory of Critical Distances to estimate lifetime of notched components subjected to variable amplitude uniaxial fatigue loading, *International Journal of Fatigue*, Vol. 33, Issue 7, *pp 900-911*

# FRAGMENT SHAPE DISTRIBUTION IN EXPLOSIVELY DRIVEN FRAGMENTATION

**Predrag Elek, Slobodan Jaramaz, Dejan Micković**

Faculty of Mechanical Engineering, University of Belgrade
Kraljice Marije 16, 11120 Belgrade 35
E-mail: pelek@mas.bg.ac.rs, sjaramaz@mas.bg.ac.rs, dmickovic@mas.bg.ac.rs

**Abstract.** The paper considers the shape distribution of fragments generated by detonation of a fragmentation warhead. Determination of the fragment shape distribution is very important for analysis of fragment ballistics and then for treatment of fragment interaction with a target. Morphology of metal fragments originating from casings of high-explosive projectiles is examined. Subsequently, the idealized fragment geometry and shape parameters are defined. Two theoretical models of fragment shape distribution are presented: (a) the model based on Mott's two-dimensional fragmentation approach, and (b) the Curran's "slot machine" model. The results of both models are transformed into previously defined shape parameters. Theoretical results are shown to be in good agreement with available experimental data.

## 1. Introduction

Dynamic fragmentation is a common phenomenon in nature and engineering systems that takes place in different size and time scales (asteroid impacts, explosively driven fragmentation, fragmentation induced by impact of nuclei, etc.).
The present research is focused on fragmentation of a metal cylinder caused by internal detonation of an explosive charge. Modeling of fragmentation process implies determination of following fragments' properties: (i) size (or mass) distribution of fragments, (ii) velocity of fragments, (iii) spatial distribution of fragments, and (iv) distribution of shape of generated fragments. In contrast to the first three problems, for which there are numerous models (e.g. [1-6]), significantly smaller number of studies is related to the problem of distribution of fragment shapes. Determination of fragment shape distribution is important for analysis of fragments' flight (fragment ballistics), as well as for modeling of interaction of a fragment and a target (penetration mechanics of fragments).

## 2. Morphology and shape parameters of fragments

The first study of the shape of fragments generated by explosive fragmentation of a metal cylinder was Mott's report [7]. Mott observed two dominant processes that lead to the fracture of the cylinder: (i) tension of the external part of the cylinder that causes a brittle or ductile fracture, and (ii) adiabatic shear bands at the internal part of the cylinder. A few characteristic shapes of large fragments, which have both the inner and outer surfaces of the

cylinder, are shown in Fig. 1a (fragments 1–4). Small fragments (fragment 5) are result of the adiabatic shearing. More complex classification of fragments originating from a thick-wall cylinder fragmented by internal explosive detonation was proposed by Mock and Holt [8, 9]. According to this approach, there are four types of fragments (Fig 1b): (i) type 1 – has both the inner and outer surfaces of the original cylinder, (ii) type 2 – has only the outer cylindrical surface; further subdivision (2A, 2B) is related to the character of the other surfaces of the fragment, (iii) type 3 – has only the inner cylindrical surface, and (iv) type 4 – does not contain either the inner or outer original cylindrical surface.
Figures 1c and 1d show actual appearance of fragments originating from metal rings, as reported in experimental investigations [10, 11].
As previously mentioned, determination of the particle shape is relevant for modeling of the further motion of a fragment after the separation. An important parameter of the model is the reference fragment area $A$ – the orthographic projection of the fragment on a plane perpendicular to direction of motion. The fragment has complex motion along the trajectory and the reference area $A$ is continuously changed. Given that virtually all positions of the fragment during the flight are equally likely, the relevant value of reference area can be considered as the average area of fragment projection on an arbitrary plane. It can be proved that $A=S/4$. This relation which shows that the average projection area $A$ of a convex body is equal to a quarter of its total surface area $S$ is known as the Cauchy theorem [12].
Similar argument regarding the reference area can be applied to the penetration mechanics of the fragment. The comprehensive study of non-ideal penetration by Goldsmith [13], and the review of the relevant models of fragment penetration mechanics [14] suggest a possible way to treatment of the problem.

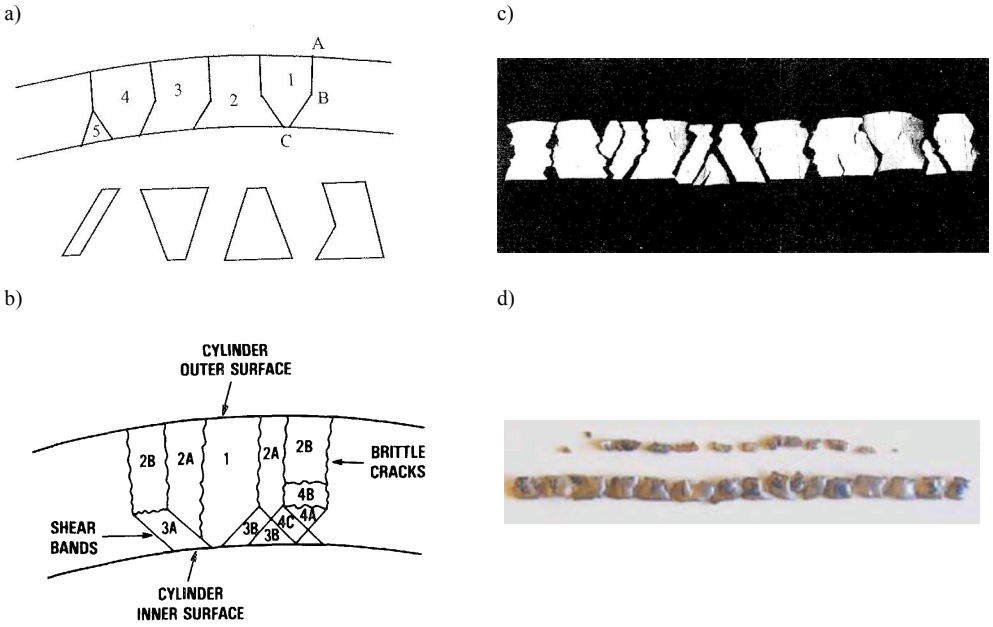


**Figure 1.** Morphology of fragments generated by internally detonated metal cylinder: a) Mott's classification of fragments from thin cylinder [7], b) complex classification of fragments originating from thick cylinders [8, 9], c) appearance of fragments from experiment [10], d) fragments from ring fragmentation [11]

Observing the diversity of possible fragment geometry, it is impossible to define a "universal" shape of the fragment. However, a triaxial ellipsoid has been adopted as a general approximation of fragment's shape, i.e. an idealization of the fragment convex envelope. An ellipsoid is defined by the length of semi-principal axes $a$, $b$ and $c$ ($a \geq b \geq c$), while its shape is determined by two parameters representing aspect ratios:

$$p = \frac{b}{a}, \quad q = \frac{c}{a}, \quad q \leq p \leq 1 . \tag{1}$$

An experimental approach to the fragment shape characterization implies measurement of fragment dimensions $a$, $b$ and $c$, and calculation of corresponding shape parameters using Eq. (1). It should be noted that there is not a unique approach to determination of the characteristic dimensions of a fragment [15].

## 3. Models of fragment shape distribution

There are several analytical models that handle the shape distribution of fragments. Two of these basically two-dimensional (2D) models will be briefly analyzed.

*2D model of fragment shape distribution*. Investigation of biaxial 2D fragmentation, based on analytical treatment of Mott's model [16], leads to the distribution of area and aspect ratio of rectangular fragments in the form:

$$g(a,r) = \frac{n^2}{a_0}\left(\frac{a}{a_0}\right)^{n-1} \frac{1}{2r} \exp\left[-\left(\frac{a}{a_0}\right)^{n/2}\left[\left(\frac{r}{r_0}\right)^{n/2} + \left(\frac{r_0}{r}\right)^{n/2}\right]\right]. \tag{2}$$

In Eq. (2) $a$ is the fragment area, $r=x/y$ is the aspect ratio of a fragment, $n$ is the optimized shape parameter of the Weibull distribution, $a_0=x_0y_0$ where $x_0$ and $y_0$ are the scale parameters of the corresponding Weibull distributions. The nominal value of aspect ratio $r_0$ depends only on strain rates in two orthogonal directions:

$$r_0 = \frac{x_0}{y_0} = \left(\frac{\dot{\varepsilon}_y}{\dot{\varepsilon}_x}\right)^{2/3} . \tag{3}$$

Distribution of the aspect ratio of fragments is calculated by integration of eq. (2) over the whole domain of fragment area $a$:

$$h(r) = \int_0^\infty g(a,r)\mathrm{d}a = \frac{n}{r_0}\frac{\rho^{n-1}}{\left(1+\rho^n\right)^2}, \tag{4}$$

where $\rho=r/r_0$. The aspect ratio $r=x/y$, whose values are in the interval $(0,\infty)$, differs from previously defined shape parameter $p=b/a$, whose values belongs to the interval (0, 1]. Taking into account that $p=\min(r, 1/r)$, the probability density function of shape parameter $p$ can be expressed in the form:

$$f_{2\mathrm{D}}(p) = \frac{2np^{n-1}(mp^{2n} + 2p^n + m)}{(p^{2n} + 2mp^n + 1)^2} \tag{5}$$

where the parameter $m$ is defined by

$$m = \frac{r_0^{2n} + 1}{2r_0^n}. \tag{6}$$

An analogous probability density function can also be derived for the shape parameter $q$.

*"Slot machine" model*. The second approach postulates that formation, growth and coalescence of thermoplastic shear instabilities (shear bands) is the main mechanism of fragmentation of the cylinder [17]. Various geometries and orientations of shear bands are possible, but experimental findings imply that half-penny shaped shear bands formed on internal surface of the cylinder are dominant. Consideration of overlapping of the crack's process zones and assumption of equal average fragment size in axial and circular direction yields the final form of the cumulative distribution of fragment shape:

$$F(n) = \frac{N(n)}{N_0} = \beta^{n-1}, \quad n \geq 1,\ \beta < 1. \tag{7}$$

In Eq. (7) $N(n)$ is the number of fragments whose length-to-width ratio is greater than $n$, $N_0$ is the total number of fragments and $\beta$ is the parameter primarily dependent on the cylinder material properties and should be optimized for each experiment.
The shape parameter $p$ is the reciprocal value of the fragment length-to-width ratio, $p=1/n$, which leads to the probability density function of the form:

$$f_{\mathrm{sm}}(p) = \ln\left(\frac{1}{\beta}\right)\frac{\beta^{\frac{1}{p}-1}}{p^2}. \tag{8}$$

## 4. Comparison with experimental results

Validation of analyzed theoretical models is performed by comparison with experimental results, which are very scarce. Marchand et al. [18] reported detailed test results for scaled models of two bombs: Mk 82 GP 500 lightly cased bomb and AN-Mk1 AP 1600 heavily cased bomb. Figures 2 and 3 show comparison of experimentally determined distribution of shape parameters $p$ and $q$ with results of two models considered. The model parameters $m$ and $\beta$ are optimized by the least squares method. As can be seen from the diagrams, probability density functions obtained by both models qualitatively follow the experimentally determined histograms for shape parameters $p$ and $q$.
Results of fragmentation experiment of scaled BLU-109 munitions are presented in [17]. In this experiment with very thin cylinder wall (0.6 mm) only the fragment aspect ratio, and corresponding shape parameter $p$ is determined. Theoretical distributions are in satisfactory agreement with the histogram obtained from the experiment (Fig. 4).
It is important to conclude that the 2D fragmentation model provides systematically better compatibility with the observation data than the "slot machine" model. Having in mind relative simplicity of the model and the fact that it involves only one adjustable parameter, the results of comparison can be considered promising. In order to fully validate, and possibly improve the model, it is necessary to use significantly larger experimental database.

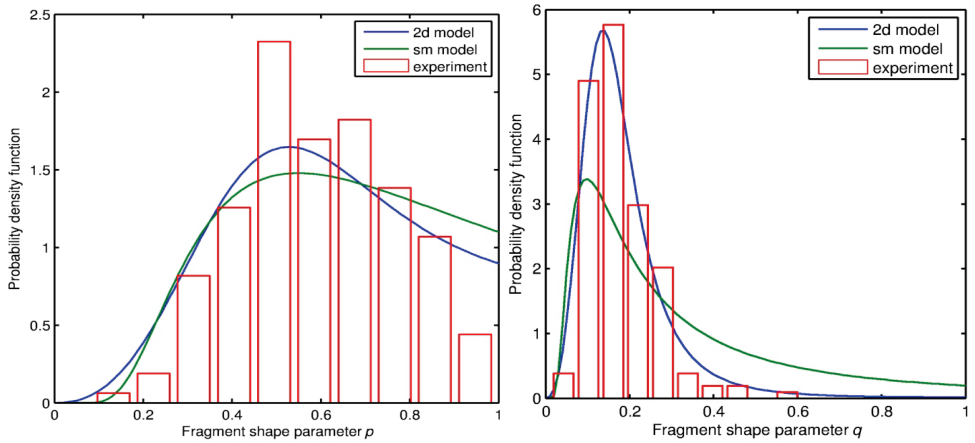


**Figure 2**. Comparison of experimentally determined histograms of shape parameters for a thin walled bomb [18] with probability density functions based on 2D fragmentation model and the "slot machine" model

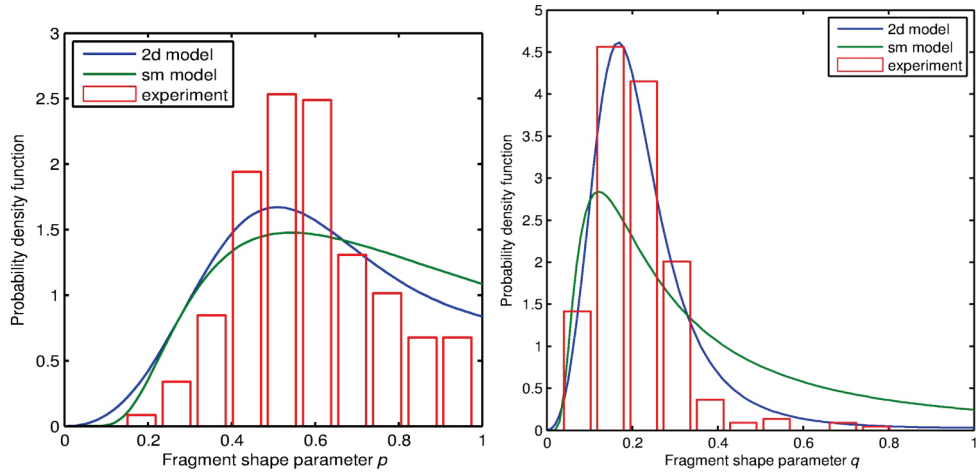


**Figure 3**. Comparison of experimentally determined histograms of shape parameters for a thick walled bomb [18] with probability density functions based on 2D fragmentation model and the "slot machine" model

## 4. Conclusion

The paper considers the shape distribution of fragments generated by detonation of a fragmentation warhead. Morphology of metal fragments originating from casings of high-explosive projectiles is examined and the fragment shape parameters are defined. Two theoretical models of fragment shape distribution are outlined: (a) the model based on Mott's two-dimensional fragmentation approach, and (b) the Curran's "slot machine" model. Theoretical results of 2D fragmentation model are shown to be in good agreement with limited experimental data.

*Acknowledgement.* This research has been supported by the Ministry of Education, Science and Technological Development, Republic of Serbia, through the project III-47029, which is gratefully acknowledged.

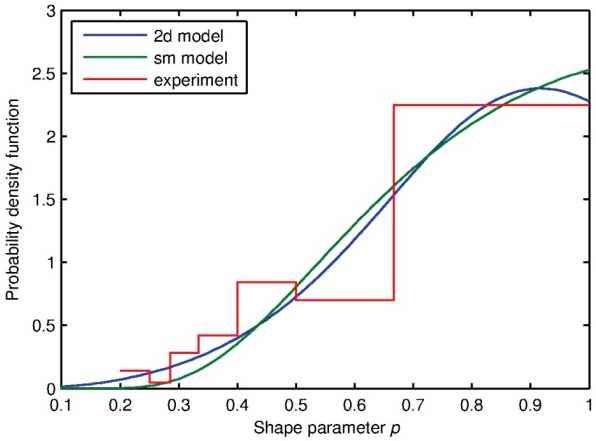


**Figure 4**. Comparison of experimental data for BLU-109 bomb [17] with probability density functions of 2D fragmentation model and "slot machine" model

## References

[1] Mott, N.F. (1947) Fragmentation of shell cases, *Proceedings of the Royal Society of London*, Series A (Mathematical and Physical Sciences), 189, pp. 300-308.
[2] Grady, D.E., Kipp, M.E. (1985) Geometric statistics and dynamic fragmentation, *Journal of Applied Physics*, **58** (3), pp. 1210-1222.
[3] Gurney, R.W. (1943) The initial velocities of fragments from bombs, shells and grenades, *US Army Ballistic Research Lab, BRL report 405*.
[4] Vukašinović, M. (2000) *Contribution to the theory and practice of experimental investigation of HE projectiles fragmentation effect*, PhD dissertation, Military Technical Academy, Belgrade (in Serbian).
[5] Elek, P., Jaramaz, S. (2009) Fragment mass distribution of naturally fragmenting warheads, FME Transactions, **37** (3), pp. 129-135.
[6] Elek, P., Jaramaz, S., Micković, D. (2012) Two-stage model of explosive propulsion of metal cylinder, 5th International Scientific Conference on Defensive Technologies – OTEH 2012, pp. 294-300.
[7] Mott, N.F. (1943) A theory of the fragmentation of shells and bombs. British Ministry of Supply, AC 4035.
[8] Mock, W, Holt, W.H. (1983) Fragmentation behavior of Armco iron and HF-1 steel explosive filled cylinders. *Journal of Applied Physics*, **54**, pp. 2344-2351.
[9] Mock, W, Holt, W.H. (1985) Computation of fragment mass distribution of HF-1 steel explosive-filled cylinders, *Journal of Applied Physics*, **58** (3), pp. 1223-1228.
[10] Weisenberg, D.L., Sagartz, M.J. (1977) Dynamic fracture of 6061-T6 aluminum cylinders. *Journal of Applied Mechanics*, **44** (4), pp. 643-646.
[11] Diep Q.B., Moxnes J.F., Nevstad G. (2004) Fragmentation of projectiles and steel rings using numerical 3D simulations, *21st International Symposium of Ballistics*, Adelaide, Australia.
[12] Cauchy, A. (1908) *Oevres Complétes d'Augustin Cauchy* II. Gauthier-Villars. Paris.
[13] Goldsmith, W. (1999) Non-ideal projectile impact on targets, *International Journal of Impact Engineering*, **22**, (2–3), pp. 95-395.
[14] Elek, P., Jaramaz, S., Micković, D. (2005) Modeling of perforation of plates and multi-layered metallic targets, *International Journal of Solids and Structures*, **42** (3-4). pp. 1209-1224.
[15] La Spina, A., Paolicchi, P. (1996) Catastrophic fragmentation as a stochastic process: sizes and shapes of fragments, *Planetary and Space Science*, **44** (12), pp. 1563-1578.
[16] Grady, D. (2006) *Fragmentation of Rings and Shells: The Legacy of N.F. Mott*, Ch. 6: Application to the Biaxial Fragmentation of Shells, Springer.
[17] Curran, D.R. (1997) Simple fragment size and shape distribution formulae for explosively fragmenting munition, *International Journal of Impact Engineering*, **20**, pp. 197-208.
[18] Marchand, K.A., Vargas, M.M., Nixon, J.D. (1992) The synergistic effects of combined blast and fragment loadings, Southwest Research Institute, Final Report No. ESL-TR-91-18, Florida.

# INFLUENCE OF IMPROVED STATOR CURVE ON THE CHARACTERISTIC OF VANE PUMP

**Radovan Petrović[1], Radovan Slavković[2], Nenad Todić[3]**

[1]College of Applied Engineering,
Center for power control hydraulics (CPCH),Trstenik,Serbia
e-mail: radovan4700@yahoo.com
[2] Faculty of Engineering Kragujevac,
The University of Kragujevac,Kragujevac,Serbia
[3] Faculty for Mechanical and Civil Engineering in Kraljevo,
University of Kragujevac, Dositejeva 19,Kraljevo, Serbia
e-mail: ntodic@gmail.com

**Abstract.** The main role of arc in stator curve of vane pump is forming sealed working room and making the equal force on the bottom and top of the vane. But when working pressure of vane pump is raised to 21MPa, the research will have important significance because the influence of compression of oil became enlarged.
In the article, the arc area of stator curve in a vane pump is replaced by an equal velocity curve whose radius is changed according to rotating angle. And advance rising pressure of oil in working room, dynamics characteristic of vane and flow characteristic of pump are studied for vane pump in the article. It is found the gradients of advance rising pressure of oil in working room is decreased, and the dynamics characteristic of vane can be improved, which can reduce the abrasion of vane and noise of pump when the arc area of stator curve is replaced by an equal velocity curve. And have little influence on rat of flow characteristic

## 1. Introduction

The stator curve is constituted of arcs and transition curves in early period double acting vane pump. In the article, the arc area of stator curve in a vane pump is replaced by an equal velocity curve whose radius is changed according to rotating angle. And advance rising pressure of oil in working room, dynamics characteristic of vane and flow characteristic of pump are studiedfor vane pump in the article. It is found the gradientsof advance rising pressure of oil in working room is decreased, and the dynamics characteristic of vane can be improved, which can reduce the abrasion of vane and noise of pump when the arc area of stator curve is replaced by an equal velocity curve. And have little influence on rat of flow characteristic. The curve called improved stator curve whose arc is replaced by equal velocity curve is studied in the article. Advance rising pressure of oil in working room, dynamics characteristic of vane and flow characteristic of pump are studied for vane pump whose research object is vane pump with double effect type 641–4300, by PPT Trstenik company Figure 1.

Technical data:

- Speed :*1500 min*$^{-1}$
- Presssure:*210 ·10*$^{5}$ *Pa*
- Flow:*62 l/min*
- Number of vanes:*10*

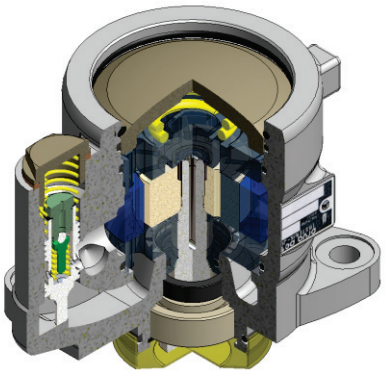

**Figure 1a.** Section Vane pump with double effect

**Figure 1b.** Rotor with vanes

## 2. Influence of improved stator curve on the characteristic of vane pump

Outlet area is the main working area so many researches of transition curve and arc are one outlet area. And arc area of stator curve is replaced by an equal velocity curve for the study of characteristic of vane pump.

### *2.1 Force*

Total force between the vane and profiled stator originates from: pressure forces acting above and beneath the vane, the centrifugal force of rotating vane mass (during radial movement of the vane), from accelerating force and friction. The resultant force $F_R$ will have a normal direction at the point of contact. Its component makes the radial force between the vane and profiled stator at the contact point in the normal direction.

#### *2.1.1. Force above the vane*

The forces acting above the vane are identified by the pressure acting in front of and behind the contact point. Figure 2. shows geometrical relations at the vane top.

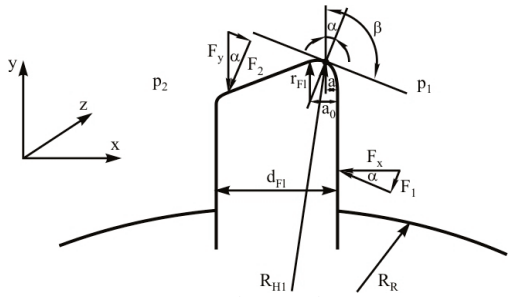


**Figure 3.** Pressure forces acting on vane top

Vertical pressure force of the vane whose length is LVat direction of axis zis:

$$F_y = L_{Va}\left(t \cdot p_1 + \left(d_{Va} - t\right) \cdot p_2\right) \tag{1}$$

Horizontal pressure force is:

$$F_x = L_{Va}\left(p_1 - p_2\right) \cdot \left(R_{S1} - R_R\right) \tag{2}$$

Following pressure forces are obtained by projecting at normal direction:

$$F_1 = F_x \cdot \sin\alpha = L_{Va} \cdot \left(R_{S1} - R_R\right) \cdot \left(p_1 - p_2\right) \cdot \sin\alpha \tag{3}$$

$$F_2 = F_y \cdot \cos\alpha = L_{Va} \cdot \left(p_2 \cdot d_{Va} + t \cdot \left(p_1 - p_2\right)\right) \cdot \cos\alpha \tag{4}$$

The force at the vane top (above the vane) is:

$$F_G = F_1 + F_2 \tag{5}$$

### *2.1.2. Force beneath the vane*

Counter-vane is designed so that delivery pressure pw constantly acts on vane lifting and during that process compressive force $F_S$ is provided between the stator and vane. The remaining part of the vane is connected, through the port, with pressure zone above the vane, so the force Fwalways depends on the pressure state above the vane.

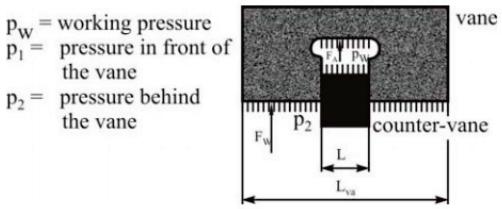


**Figure 4.** Pressure forces acting on vane bottom

The figure clearly shows the following:

$$F_S = p_w \cdot L \cdot d_{va} \qquad F_W = p_2 \cdot \left(L_{Va} - L\right) \cdot d_{Va} \tag{6}$$

Pressure force beneath the vane FDuis projected perpendicularly at contact point

$$F_{Du} = \left(F_S + F_W\right) \cdot \cos\alpha \tag{7}$$

2.1.3. Centrifugal force

Centrifugal force is caused by rotation of vane mass around centre point C. Its form at normal direction of contact point is:

$$F_I = m_{Va} \cdot (R_S - R_T) \cdot (2 \cdot \pi \cdot n)^2 \cdot \cos\alpha \tag{8}$$

where $R_T$ is the distance from vane centre to vane top.

2.1.4. *Acceleration force*

Acceleration force is proportional to radial acceleration of the vane which has a forced motion through the contour of profiled stator. There is a mutual dependence between stator radius and radial acceleration $a_R$, Figure 5.

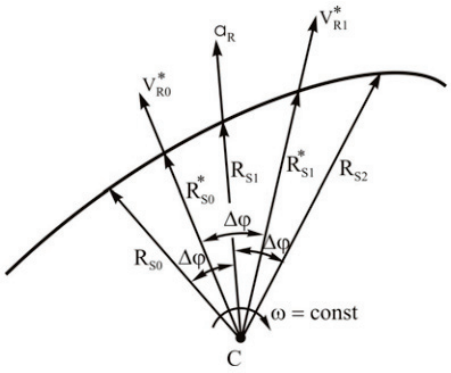


**Figure 5.** Calculation of radial acceleration

$$\Delta t = \frac{\Delta\varphi}{\omega} \qquad vR_0^* = \frac{R_{S1} - R_{S0}}{\Delta\varphi} \cdot \omega \qquad vR_1^* = \frac{R_{S2} - R_{S1}}{\Delta\varphi} \cdot \omega \tag{9}$$

It follows:

$$a_R = \frac{vR_1^* - vR_0^*}{\Delta\varphi} \cdot \omega = \frac{(R_{S2} - 2 \cdot R_{S1} + R_{S0})}{\Delta\varphi^2} \cdot \omega^2 \tag{10}$$

Thus, acceleration force projected at normal direction at the contact point is:

$$F_a = (R_{S2} - 2 \cdot R_{S1} - R_{S0}) \cdot \frac{\omega^2}{\Delta\varphi^2} \cdot \cos\alpha \tag{11}$$

2.1.5. *Frictional force*

At the contact point of the vane and stator there is friction which causes cross-force at the vane. Friction is the result of abovedescribed components which make radial force acting on the point of contact. Horizontal force acts due to various pressures in front of and behind the vane. Both forces simultaneously act on the vane, Figure 6. Therefore, two reaction

forces are caused due to the vane which rests on rotor orifice. When the vane radially moves upward or downward, there is a frictional force between the vane and rotor appearing at two positions. The following expression is obtained from equilibrium of moments

$$F_{TR} = \mu \cdot \left( \frac{\mu \cdot F_R \cdot (h_{Va} + (R_{S1} - R_R)) + F_X h_{Va}}{h_{Va} - (R_{S1} - R_R)} \right) \cdot \cos\alpha \tag{12}$$

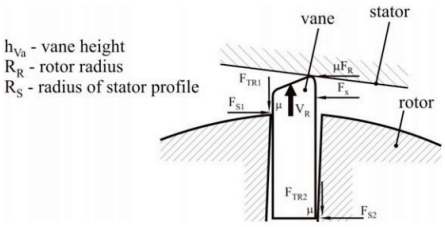


**Figure 6.** Frictional forces

2.1.6. *Velocity of contact point*

Relative velocity $V_{REL}$ of the contact point consists of two components. The first part of the velocity is sliding while the second part results from vane radius rolling along the stator profile.

$$V_{rel} = V_S + V_R \tag{13}$$

Velocity $V_S$ is obtained by multiplying angular velocity and stator radius. Figure7 shows that the velocity of moving point $V_R$ of the rolling part is the result of changing the rotation angle α.

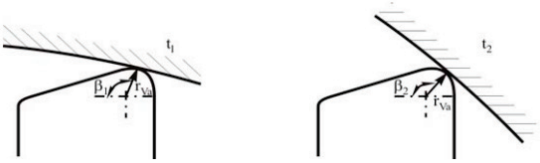

**Figure 7.** Velocity of the contact point of rolling par

Velocity $V_S$ for sliding part is $V_s = R_s \cdot \frac{\Delta\varphi}{\Delta t}$

Velocity $V_R$ for rolling part is $V_R = r_{FVa} \cdot \frac{\Delta\beta}{\Delta t}$

Thus, the relative velocity of the contact point is

$$V_{rel} = R_S \cdot \frac{\Delta\varphi}{\Delta t} + r_{FVa} \cdot \frac{\Delta\beta}{\Delta t} \tag{14}$$

### 2.2. *Influence of improved stator curve on force of vane*

The dynamics characteristic has many differences between low-pressure vane pump and high-pressure vane pump when compressibility of oil is considered, and the value of contact reaction force $F_G$ is high because of vane's moving and friction when vane moves from equal velocity curve to the point of transition curve in outlet area. The dynamics characteristic of vane became well and the max value of force became low with the increasing of k when arc is replaced with equal velocity curve, which can reduce the abrasion of vane, noise of pump and prolong the life of pump. The curve of contact reaction force between vane and stator is obtained during one action by computer simulation as shown in Figure 8 when a series of value of k ($k=R_{S2}-R_{S0}$) are taken into equations.

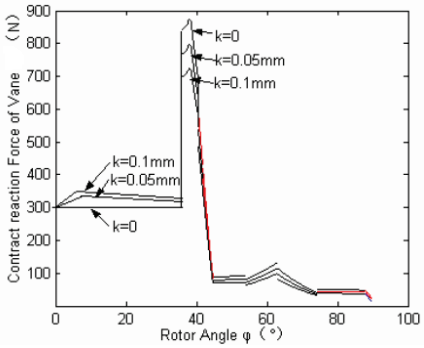


**Figure 8** Variation curves of reaction force between vane and stator when k is given different values

## 3. Conclusion

The gradients of pressure of oil in chamber is became little in the range of $0\text{-}2^0$ in advance rising pressure area, and effect of advance rising pressure became well. Uneven coefficient of flow will be a little augmented,but a little affect. The value of contact reaction force of vane between vane and stator can be decreased in the beginning of transition curve, which can reduce the abrasion of vane, noise of pump and prolong the life of pump. In a word, the arc of stator curve is replaced with equal velocity curve has positive action for improving vane pump's characteristic which has important reference for vane pump's design.

## References

[1] Petrovic,R. Mathematical modeling and identification of multicylindrical axial piston pump parameters, *PhD Thesis, Faculty of Mechanical Engineering,* Belgrade, 1999.
[2] Petrović,R. Mathematical Modeling and Experimental Verification of Operating Parameters of Vane Pump With Double Effect,*Strojniški vestnik - Journal of Mechanical Engineering 55(2009)1UDC 621.9.04*
[3] Petrović,R. Mathematical Modeling and ExperimentalResearch of Characteristic Parameters Hydrodinamic Processes of a Piston Axial Pump,*Strojniški vestnik - Journal of Mech. Eng. 55(2009)4, UDK 621.785.4*
[4] Ortwig, H. Analytische und experimentelle Untersuchung hochbelasteter linienförmiger Gleitkontakte in einer Flügelzellenpumpe,1990, Aachen.
[5] Axel,F. Theoretische und experimentelle Untersuchungen saugseitiger Widerstandssteurungen bei Verdrängerpumpen,1991, Aachen
[6] Shaonian Li, Liejiang Wei, Research on stator curve of double acting vane pump, *International Conference on Fluid Power Transmission and Control,2009.Hangzou*

# WEAK AND STRONG COUPLED STOCHASTIC OSCILLATORS WITH DELAYS IN COUPLING

**Ines Grozdanović[1], Nikola Burić[2],Kristina Todorović[3] , Nebojša Vasović[1]**

[1] Faculty of Mining and geology, Department of Applied Mathematics,
The University of Belgrade, Đušina 7, 11000 Belgrade
e-mail: ines@rgf.bg.ac.rs
[2] Institute of Physics
University of Belgrade P. O. Box 68 11080 Beograd-Zemun, Serbia
e-mail: buric@phy.bg.ac.rs
[3] Faculty of Pharmacy,Department of Physics and Mathematics
The University of Belgrade Vojvode Stepe 450
e-mail: kisi@pharmacy.bg.ac.rs

**Abstract.** Stochastic coherence (SC) and self-induced stochastic resonance (SISR) are two distinct mechanisms of noise-induced coherent motion. Infuence of small time delays on the coherence resonance in weak and strong coupled, stochastic,type II excitable pairs of SC and SISR systems is studied. It is shown that the transition between diferent phenomena when the coupling strength is gradually changed from weak to strong coupling is quite homogenous with some diferences between SC and SISR neurons, and that small time-delays can have interesting efect on the noise induced coherent oscillations.

## 1. Introduction

Excitability is a common property of many physical and biological systems. Although there is no unique definition [2] the intuitive meaning is clear: A small perturbation from the single stable stationary state can result in a large and long lasting excursion away from the stationary state before the system is returned back asymptotically to equilibrium. Furthermore, in the framework of the bifurcation theory, as an external parameter is changed, the global attractor in the form of the stationary point bifurcates into a stable periodic orbit, and the excitability is replaced by the oscillatory dynamics.

Typical example of excitable behavior is provided by the dynamics of neurons. However, realistic models of coupled neurons, must include the following two phenomena:

(a) influence of different types of noise and (b) different time scales of the creation of impulses on one hand and their transmission between neurons on the other. It is well known that neurons *in vivo* function under influences of many sources of noise [6]. It is also well known that the noise of an appropriate small intensity can change the systems dynamics by turning the quiescent state of the neuron into the state of periodic firing [5]. There are different types of noise induced coherent oscillations that could occur in examples of excitable systems [4], as will be discussed later. Our aim here is to investigate the influence of coupling delay, on different types of coherent oscillations that have been induced solely by the noise, when the neurons are both weak and strong coupled. Such a detailed and extensive analyzes would supply information complementary to the research on the effects of noise on the properties of oscillations and synchrony introduced by sufficient time-lag in the delayed coupling. We would like to emphasis, that our goal in this paper, is to study the effects of interplay between the time-delay, coupling strength and noise, on different types of noise induced coherent oscillations in each pair of the coupled units.

**2. The model**

Excitable behavior of a single neuron could be of two qualitatively different types [2]. They are distinguished phenomenologically by different properties of the frequencies and the amplitudes of the oscillatory dynamics in each of the two types, and the corresponding qualitative mathematical models are characterized by different bifurcation mechanisms. In this paper we shall consider typical type II excitable systems, modeled by the FitzHugh-Nagumo differential equations [2], where the excitable behavior bifurcates into the oscillatory regime via the Hopf bifurcation. Each of the excitable neurons in the model is subjected to white noise that could appear in the model equations in two qualitatively different ways. Thus each neuron is described by the following stochastic differential equations:

$$\begin{aligned} \varepsilon dx &= f(x,y) = (x - x^3/3 - y)dt + \sqrt{\varepsilon}\sqrt{2D_1}dW_1 \\ dy &= g(x,y) = (x + a)dt + \sqrt{\varepsilon}\sqrt{2D_2}dW_2 \end{aligned} \tag{1}$$

where $dW_{xy}$ are independent increment of normalized Winer processes, i.e. $E(dW_i) = 0$; $E(dW_i dW_j) = \delta_{ij}$, $i, j = 1, 2$ and $E(\ldots)$ denotes expectation with respect to the stochastic process. The small parameter $\varepsilon$, which is in our paper fixed as $\varepsilon = 0.01$, takes care of the different time scales in the dynamics of the excitatory variable $x$ (membrane potential) and the recovery variable $y$. The parameter $a$ is the bifurcation parameter. For $|a| > 1$ the deterministic system (1) is excitable and for $|a| < 1$ the stationary state is unstable and there exists a stable limit cycle. In this paper $a$ is fixed to $a = 1{,}05$. The two noise terms can produces series of spikes in the $x$ variable which for certain values of the parameters $D_1$ or $D_2$ occur regularly so that the dynamics appears simply periodic i.e. coherent with quite well defined frequency. However the coherent oscillations induced by $D_1 = 0$; $D_2 \neq 0$ are qualitatively different from those that occur due to $D_1 \neq 0$; $D_2 = 0$. The first case, i.e. $D_1 = 0$; $D_2 \neq 0$ has been extensively studied, since it was reported in [8]. The effect is traditionally called coherence resonance [5], but we shall use the term stochastic coherence (SC) [7] in order to emphasize the noisy origin of the coherent oscillations. SC occurs only when the parameter $a$ is close to its bifurcation value, the properties of the ensuing oscillations resemble the Hopf limit cycle of the deterministic system, and the properties of SC follow from this fact. The oscillations in the other case, $D_1 \neq 0$; $D_2 = 0$ are induced by quite different mechanism from that of the SC. It has been studied in details for example in [4], where it has been called self-induced stochastic resonance (SISR). The main properties of SISR (and the name) follow from the fact that the system (1) asymptotically resembles a particle in a double well potential [4]. In particular SISR happens even when $a$ is far from the bifurcation value, and the resulting stochastic limit cycle does not resemble anything that could occur in the deterministic system. We shall study a pair of excitable FHN neurons (1) coupled by the electrical synapses. This type of synapse is modeled by delayed diffusive coupling between the membrane potentials of the coupled neurons. The model equations are as follows:

$$\begin{aligned} \varepsilon dx_i &= f(x_i, y_i) + c(x_j(t-\tau) - x_i)dt \\ dy &= g(x_i, y_i) \end{aligned} \tag{2}$$

where i,j=1,2 and $f(x_i\, y_i)$ and $g(x_i,\, y_i)$ are given by (1). The coupling constant $c$ in this paper always assumes positive values, c = 0,01 for weak and c = 0,1 for strong coupling, which

ensures that the system (2) with $a$ = 1,05 and for $D_1;D_2$ all equal to zero, has the stable stationary state as the only attractor *for any value of the time-lag* . Thus, possible oscillatory behavior of (2) can occur only because of the noise, and not because of strong coupling or time-delay. However, as we shall see, once the noise has produced spike trains that look coherent, quite small time delay for sufficiently strong coupling can induce important qualitative changes in the SC and SISR as well as in the properties of synchronization between the two units.

**3. Numerical results**

Each of the isolated noisy FHN neurons can display a train of spikes due to the noise even when the only attractor of the deterministic system is the stable stationary solution. Time distribution of the spikes can be regular with almost constant inter-spike interval. Occurrence of coherent series of spikes for particular values of the noise intensity is the common manifestation of both SC and SISR. However, the two cases occur via quite different mechanisms and have different properties, like dependence of the inter-spike period and on the noise intensity. Mechanisms of SC and SISR, and their properties, have been compared in [4]. Coupling between the neurons which are in the state of SC or SISR could preserve the coherence of each of the units and furthermore lead to synchronization of noise induced oscillations. This effects have been studied in the case of instantaneous coupling (no time-delay) for example in [1] for the case of equal units, and in [7] for the case of one unit in the state of SC and the other in the state of SISR. In this section we illustrate the main effects of the time-delay in the weak and strong coupling between the neurons on the properties of SC and SISR, for both units either in the SC or in the SISR state.

The coherence of noise induced series of spikes in each of the neurons is commonly characterized by a kind of signal to noise ratio defined by:

$$SNR = \frac{\overline{T_k}}{[Var(T_k)]^{1/2}} \tag{3}$$

$T_k$, denotes time averaging. Large *SNR* corresponds to high coherence of the noise induced spike trains.

There are different types of synchronization between the two coherently spiking neurons that could be of interest. For example, the strongest kind is the exact synchronization, i.e. $x_1(t) = x_2(t)$ for all $t > t_0$, and another commonly studied is the synchronization between the phases of the two oscillators. We shall analyze the kind of synchronization such that each spike of one of the neurons occurs within the duration of some spike of the other neuron. This notion of synchrony is motivated by neurological considerations [3], and is quantified by the so called coincidence function (CF). This is defied as the time average of the ratio between the numbers of spikes of one of the neurons, which are coincident with some of the spikes of the other neuron, and the average number of spikes per neuron. Two spikes are considered coincident whenever the sum of $x_1(t)+x_2(t)$ is larger then some threshold, say the hight of spikes $\max\{x_i\}$. This type of synchrony does not assume coherent spiking and is weaker than either exact or phase synchronization.

In our numerical integration we have used the Runge-Kutta 4-th order routine for the deterministic part of (2) and the Euler method for the stochastic part. Many sample paths for each value of the variable parameters $_{D1,2}$ and $\tau$ have been calculated. Values of *SNR*

that are presented in what follows represent values that have been obtained with single typical sample paths.

Results of our numerical calculations are illustrated in figures 1, 2, 3, 4 and 5 where on each figure a), b), c), d) corresponds to two SC and e), f), g), h) to two SISR neurons. We fix the noise intensity of one of the neurons, say $D_2$ to the maximal coherence of SC type (a, b, c, d on all the figures) or $D_1$ to the maximal coherence of SISR type (e, f, g, h on all the figures) and study the dependence of firing coherence of both neurons on the noise intensity $D_1$ or $D_2$ of the adjustable unit, on the time-lag $\tau$ and on coupling strength: $c$ = 0:01(fig.1); 0.03(fig.2); 0.05(fig.3); 0.07(fig.4); 0.1(fig.5). We consider only relatively small time-lags up to the refractory period of a single spike of an isolated excitable FHN neuron, which is about $\tau \leq 1.3$. On each of the figures 1-5 values of time-lags are: $\tau = 0$ and $\tau = 0.4$ (on the a, e); $\tau = 0$ and $\tau = 0.7$ (on the b, f); $\tau = 0$ and $\tau = 1$ (on the c, g); $\tau = 0$ and $\tau = 1.3$(on the d, h).

From fig.1 and fig.2 we can see that the coherence of noise induced spiking for both SC and SISR type neurons is not qualitatively affected by weak coupling ($c = 0.01$ and $c = 0.03$) for time-delay $\tau \leq 1$, but for $\tau = 1.3$ even for still weak coupling value $c = 0.03$ we can see first "reaction on the coupling strength" in both SC and SISR cases, which is shown in fig.2d and 2h respectively. Stronger coupling introduces significant modifications which very much depend on the time-lag and is illustrated in fig.3,4 and 5.

Figures 3a,b,c,d ($c = 0.05$) and fig.2a,b,c,d (c=0.03) (SC type) are qualitatively the same, but the qualitative and quantitative changes in curves $SNR_1(\log 10\ D_1)$ and $SNR_2(\log 10\ D_1)$ for SISR type in fig.3h (for $\tau = 1.3$) are obvious which means significant improvement in coherence comparing with the previous fig.2h (for same value of the time-delay).

Figure 4 presents improvement in coherence for lower intensity of the noise $-4 < \log_{10} D_2 < -2.5$ of the curves $SNR_1(\log_{10} D_2)$ and $SNR_2(\log_{10} D_2)$ for coupled neurons of SC type in the fig.4d for $\tau = 1.3$, while the other diagrams are qualitatively the same as in previous figure 3.

Typical effects of the influence of small time lag are shown in fig.5b and illustrated with $\tau = 0.7$, when both neurons are of the SC type and the noise intensity of one of them is held fixed at the SC maximum for single neuron. Other values of the time-lag less then $\tau < 1$ cause similar small modifications of the dependencies $SNR_1(\log_{10} D_2)$ and $SNR_2(\log_{10} D_2)$. However, large influence of the time-delay on $SNR_1(\log_{10} D_2)$ and $SNR_2(\log_{10} D_2)$ is demonstrated for all $\tau \geq 1$, as is illustrated in fig. 5c,d for $\tau = 1$ and $\tau = 1.3$ respectively. The curves $SNR_1(\log_{10} D_2)$ and $SNR_2(\log_{10} D_2)$ with $\tau \geq 1$ are qualitatively and quantitatively different from those with $\tau < 1$. Let us stress that deterministic systems with delayed coupling of the same coupling strength $c = 0.1$ show no bifurcations or other qualitative changes for any $\tau \geq 0$. Thus, qualitative change in the properties of noise induced spiking coherence achieved with $\tau \geq 1$ should be attributed to the simultaneous action of noise and time-delay. Figures 5e, f, g, h illustrate the same effects in the case when the two neurons are of the SISR type with fixed noise intensity in one of them. The situation is qualitatively similar to the previous case: small $\tau < 1$ introduces only small quantitative changes, but $\tau \geq 1$ changes the curves $SNR_1(\log 10\ D_1)$ and $SNR_2(\log 10\ D_1)$ drastically. Observe that the influence of time-delay for $\tau = 1$ in the SC-SC case is quite different from the SISR-SISR case.

## 4. Summary

We have studied a pair of FitzHugh-Nagumo neurons with noise coupled by time-delayed diffusive coupling. The bifurcation parameters of each of the neurons and the coupling strength were such that the only attractor of the system without the noise terms is the stable

stationary state for any value of the time-lag. Thus, the deterministic system is excitable with no oscillatory dynamics for any value of the time-lag. Addition of white noise in two different ways produces spiking that appears periodic for particular values of the noise strength. We have studied the influence of coupling strength and time-delay in the coupling on the coherent spiking induced by noise in the slow variable, called stochastic coherence (SC), and on that induced by the noise in the fast variable which is called self-induced stochastic resonance (SISR). Then we numerically studied changes in the signal to noise ratio introduced by small time-delay for each of the neurons in the pairs like SC-SC, SISR-SISR varying the coupling strength from weak ($c = 0.01$) to strong ($c = 0.1$). Our main results can be summarized as follows: Weak coupling with any time-lag does not introduce any qualitative change of the signal to noise ratio. Transition toward strong coupling is quite uniform, with remark that pair of SISR neurons are more sensitive to the intensity of the coupling strength, than SC pair of neurons. Even strong coupling with the time-lag $\tau < 1$ induces only small changes of the signal to noise ratio. However, time-lag $\tau \geq 1$ and sufficiently strong coupling drastically change signal to noise ratio in the quantitative and qualitative manner. New local minima and maxima of the signal to noise ratio as a function of the noise intensity are created by the time-lag $\tau > 1$, and the coherence of spiking measured by (3) can be greatly enhanced. In this paper we have used the "homogeneous pair" of FitzHugh-Nagumo neurons (SC-SC and SISR-SISR) as the typical example of an excitable type II system, and the diffusive coupling as the model of an electrical synapse.

*Acknowledgement.* This work is partly supported by the Serbian Ministry of Science contract No.174010, and No.171017.

FIGURE CAPTIONS

Figure 1-5: Illustrates coherence in the (a,b,c,d) SC-SC case, and (e,f,g,h) in the SISR-SISR case, for: $c = 0.01$ (weak) on fig.1; $c = 0.03$ on fig.2; $c = 0.05$ on fig.3; $c = 0.07$ on fig.4 and $c = 0.1$ (strong) on fig.5, coupled pair of neurons. $SNR_1$(circles) and $SNR2$ (triangles) full for $\tau = 0$ and hollow for $\tau = 0.4$ (a,e), $\tau = 0.7$ (b,f), $\tau = 1$ (c,g) and $\tau = 1.3$ (d,h). Calculated values of $SNR_{1,2}$ are indicated by symbols and the lines (dotted fot $\tau = 0$, and full for $\tau = 0.4 - 1.3$) serve only to connect the values corresponding to the same $\tau$ and different $\log_{10} D_{1,2}$.

## References

[1] S. K. Han, T. G. Yin, D. E. Postnov and O. V. Sosnovceva, *Interacting coherence resonance oscillators* Phys.Rev.Lett. 83, 1771 (1999).
[2] E. M. Izhikevich, *Dynamical Systems in Neuroscience: The Geometry of Excitability and Bursting*, (The MIT Press, 2005).
[3] W. Kistler, W. Gesrner and J. Van Hemmen, *Neural computation*, 9, 1015 (1997).
[4] R. E. Lee DeVille, E. Vanden-Eijnden and C. B. Muratov, *Two distinct mechanisms of coherence in randomly perturbed dynamical systems* Phys.Rev.E, 72, 031105 (2005).
[5] B. Linder, J. Garcia-Ojalvo, A. Neiman and L. Schimansky-Geier, *Effects of Noise in Excitable Systems* Phys. Rep. 392, 321, (2004).
[6] Z. F. Mainen and T. J. Sejnowski, *Reliability of spike timing in neocortical neurons* Science 268,1503, (1995).
[7] J. Zhang, Z. Yuan, J. Wang and T. Zhou, *Controlling the onset of Hopf bifurcation in the Hodgkin-Huxley model* Phys.Rev. E, 77, 021101, (2008).

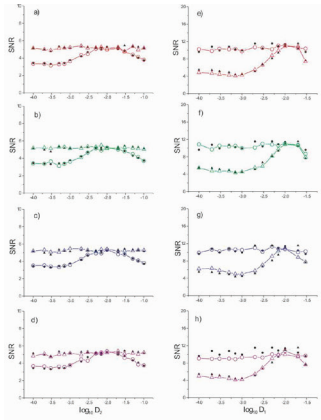

fig.1

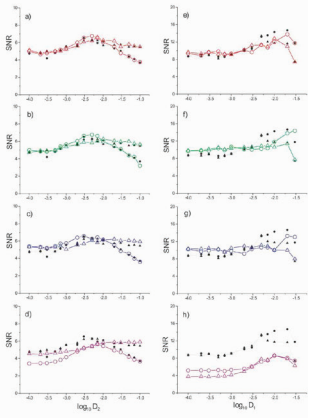

fig.2

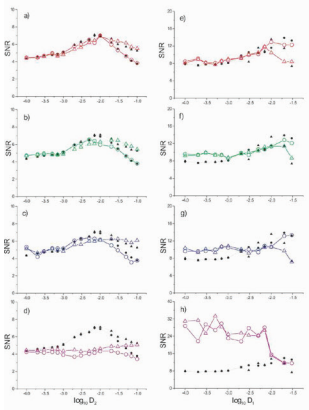

fig.3

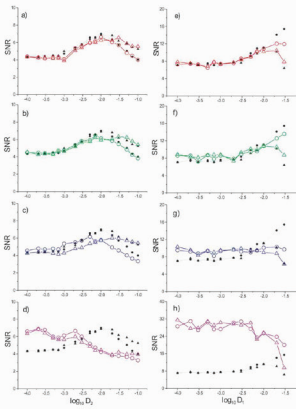

fig.4

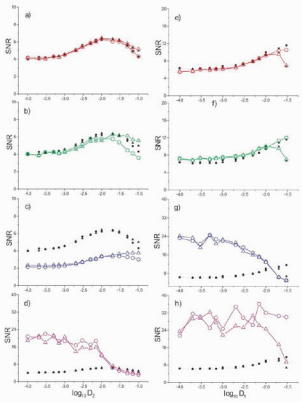

fig.5

# RANDOM SOIL PARAMETERS EFFECT TO THE ACCURACY ON ROCKET IMPACT POINTS OF MULTIPLE LAUNCHER ROCKET SYSTEMS

**Siniša Jovančić[1], Dragoslav Živanić[2], Milan Milošević[3]**

[1] Military Technical Institute, Belgrade
Ratka Resanovića 1, Belgrade
e-mail: jovancicsinisa@gmail.com
[2] Military Technical Institute, Belgrade
Ratka Resanovića 1, Belgrade
e-mail: dragoslav@ptt.rs
[3] Military Technical Institute, Belgrade
Ratka Resanovića 1, Belgrade
e-mail: marija.m@beotel.net

**Abstract.** This paper analyzes a sandy ground with the random values of the mechanical properties and their influence on the reduced coefficients of stiffness and damping from multiple launcher rocket support system. Simulation of stiffness and damping elements of support system was carried out using the Monte Carlo method. Interaction launcher - rocket was observed through the important effects on the initial disturbance of launching: the change of angular velocity of rocket in the vertical plane, the change of the initial launch angle and the change of initial angle of attack, for the full and empty launching device. The probability of hitting rocket is presented in dependence on the deviation from the midpoint of target.

**Keywords**: stiffness and damping of soil, rocket launcher, unguided rockets, the Monte - Carlo simulations, probability of hitting.

## Nomenclature:

| | |
|---|---|
| $E$, | modulus of elasticity of soil |
| $\nu$, | Poisson ratio of soil |
| $\rho$, | density of the soil |
| $C$, | reduced coefficients of stiffness |
| $\beta$, | reduced coefficients of damping |
| $l_2$, | distance of the center of mass of the rear of the vehicle to the front outrigger |
| $z$, | vertical movement of the vehicle frame |
| $\varepsilon$, | rotation of the vehicle frame around the transverse axis |
| $\theta$, | rotation of the launching device around the elevation rotating axis |
| $\varphi_z$, | rotation of the vehicle rear frame around the longitudinal axis |
| $\psi_c$, | angular movement of the tip of launching tube due to bending |
| $\xi$, | motion of the rocket into launching tube during firing |
| $d, l_R, m_R$, | diameter, length and mass of rocket |
| $x_{CG}$, | rocket center of gravity |
| $\gamma, \psi$, | angle of elevation and azimuth |
| $U_K, \tilde{v}_K, \tilde{w}_K$, | velocity of rocket along the axis of aeroballistic frame |
| $m, \sigma$, | mathematical expectation and standard deviation of random variables |
| $V_d, V_p$, | probable deviation of the range and direction (ballistic tabular value) |

## 1. Introduction

The support system influences on dynamic behavior and stability of the multitube rocket launcher is very important, and that is shown in reference [3] and [4]. The support system consists of several stiffness - damping elements (soil, outrigger, leaf spring, pneumatic wheel, etc.) inter connected in series - parallel connections. With higher accuracy is assumed that the full support system is described by the mechanical properties of the soil. Since the soil which carries out combat missions of multi-barrel rocket launchers is usually different for each mission, we will examine more closely the impact of the physical - mechanical characteristics of the soil and their random selection of the initial disturbance of launching.

The firing simulation, for the launcher supported on the ground with random characteristics, results in random value of initial disturbances of launching. As the initial conditions for the ideal rocket flight are random disturbances of launching, the impact points on target are also random, and they depend directly on the physical - mechanical properties of the soil.

## 2. Dynamic properties of soil

In many cases, the supports of the launching devices suffer the short, oscillatory dynamic loads, which results in soil deforming, and the soil is adopted as the linear - deformable environment. The elastic deformation of the leaf spring, pneumatic wheel and outrigger, will be ignored. All possible movement except displacement in vertical direction will be ignored, too. With this assumption the entire deformation of the support system is reduced to the deformation of the soil, so all further considerations of the support system will only refer to the reduced dynamic properties of soil (reduced coefficients of stiffness and reduced coefficients of damping). In the case of outrigger, with the support plate of circular cross-section, with radius $R$, according to the reference [1] and [2], stiffness and damping of the soil are as follows in the next form:

$$C = \frac{2E}{1-\nu^2} \cdot R \tag{1}$$

$$\beta = \frac{3,4}{1-\nu}\sqrt{\frac{\rho E}{2(1+\nu)}} \cdot R^2 \tag{2}$$

It is assumed that the modulus of elasticity, Poisson's ratio and density of the soil have a normal Gaussian distribution, defined on the basis of the mean and standard deviation:

$$\begin{aligned} E &\sim N\left(m_E, \sigma_E^2\right) \\ \nu &\sim N\left(m_\nu, \sigma_\nu^2\right) \\ \rho &\sim N\left(m_\rho, \sigma_\rho^2\right) \end{aligned} \tag{3}$$

Using the Monte Carlo simulation to determine the system (3), according to (1) and (2), the stiffness and damping of the soil are obtained as a random function of physical properties. The figure 1 presents the randomly obtained values of the stiffness and damping for 200 realizations of random variables for sandy soil.

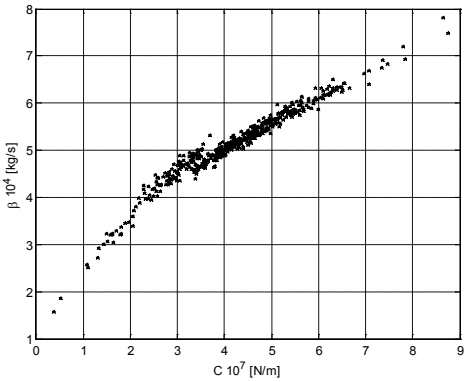


**Figure 1.** Graphs of random realization stiffnes – damping coefficients for sand

## 3. Mathematical model of interaction launcher - rocket

According to reference [3] и [4], for accepted mechanical model of multitube rocket launcher during the rocket motion through the tube and after its leaving the tube, we define the displacement from eight generalized coordinates. The system of eight inhomogeneous, nonlinear differential equations in matrix form can be presented:

$$\mathbf{A}\cdot\ddot{q}+\mathbf{B}\cdot\dot{q}+\mathbf{C}\cdot q=\mathbf{D} \tag{4}$$

where the corresponding matrices of: inertia $\mathbf{A}$, damping $\mathbf{B}$, stiffness $\mathbf{C}$ and excitation $\mathbf{D}$, are functions of generalized coordinates and generalized velocity, ref. [4]. This system of differential equations is solved by the usage the software package LANS-M [7].

All disturbances that launcher delivers to the rocket at the moment of its separation from the launching tube are the initial conditions for the rocket's flight. The equations of rocket flight will be used, assuming that the rocket is absolutely rigid with 6 degrees of freedom in aeroballistic coordinate frame, neglecting the influence of the Earth's rotation, ref. [4], [10].

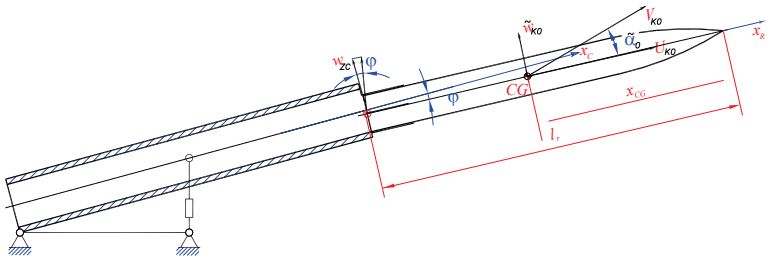


**Figure 2**. Moment when the rocket leaves the launcher

The angle between the rocket's axis and the launching tube's axis, at the moment when the rocket leaves the launcher $\varphi$, represents the numerical solution to the following differential equation:

$$\ddot{\varphi}-\frac{F_x\left(\xi+\left(l_R-x_{CG}\right)-l\right)}{m_R\left[r_y^2+\left(\xi+\left(l_R-x_{CG}\right)-l\right)^2\right]}\varphi=-\frac{g\left(\xi+\left(l_R-x_{CG}\right)-l\right)\cos\left(\gamma_o-\varphi\right)}{r_y^2+\left(\xi+\left(l_R-x_{CG}\right)-l\right)^2} \tag{5}$$

The velocity of the tube tip here $w_{zc}$, is the result of the oscillation of launcher, described by equation in form (5), as follows:

$$w_{zc} = \dot{z}_1 \cos\gamma + \dot{\varphi}_z \left(l\cos\gamma\sin\psi - b\sin\psi\right) - \theta\dot{\varphi}_z l\sin\gamma\sin\psi - \varphi_z\dot{\theta}l\sin\gamma\sin\psi \\ - \dot{\theta}l\cos\gamma + \left(\varepsilon\dot{\theta} + \dot{\varepsilon}\theta\right)\left(l\sin\gamma\cos\psi\right) + \dot{\varepsilon}\left(b\cos\psi - l\cos\gamma\cos\psi\right) - \dot{\psi}_c l_2\cos\gamma \tag{6}$$

The initial angle of the rocket's axis to the horizon $\theta_0$, presents the difference between the elevation angle and changes of the initial launching angle during the rocket's motion throughout the launching tube. That will be calculated by the following equation:

$$\theta_0 = \gamma_0 + \varphi + \varphi_z\sin\psi - \theta - \psi_c \tag{7}$$

The initial angular velocity of the rocket in the vertical plane $\tilde{q}_0$, is presented by equation:

$$\tilde{q}_0 = \frac{d\theta_0}{dt} = \dot{\varphi} + \dot{\varphi}_z\sin\psi - \dot{\theta} - \dot{\psi}_c \tag{8}$$

The initial attacking angle of the rocket $\tilde{\alpha}_0$ is determined by the transcendental equation in form:

$$\sin\tilde{\alpha}_0 = \frac{w_{zc}\cos\varphi + \tilde{q}_0(l_R - x_{CG})}{\sqrt{U_{K0}^2 + \left(w_{zc}\cos\varphi + \tilde{q}_0(l_R - x_{CG})\right)^2}} \tag{9}$$

## 6. Analysis of results

For a numerical example, the multitube missile launcher BM-21 will be considered, during the launching with elevation of 45° and angle of azimuth 90°. Two cases are examined: launcher loaded with 40 rockets (full launcher) and launcher loaded with one rocket (empty launcher). The simulation of the firing is performed in a single rocket launching, where the system of differential equations is solved using the software package PUTNPV3-M [8].

Figure 3 shows the initial disturbances which launcher delivers to rocket due to oscillating in function of stiffness changes, while a few characteristic values of stiffness are chosen, which shows the character of changes of the initial launching disturbances. From the diagram can be noted that the initial launching disturbances of the last missile in launcher (empty launcher, n=1) are practically insensitive to to the randomly selected ground from which the launching was performed. During the firing of the first rocket (loaded launcher, n=40), it can be observed that for small values of soil stiffness, launching tube makes a considerable change in initial launching angle and initial angular velocity. For ranges of stiffness around the mean - expected values of stiffness and damping, these disturbances for full and for empty launcher are approximately equal. For the ranges of stiffness that are larger than the mean value, the initial angular velocity changes the direction and delivers a positive attacking angle to the rocket.

Figure 4 show the impact points of rockets, as the result of the ideal rocket flight simulation (without its own disturbances) with initial disturbances that are defined as previously described. It is clear that the last rocket firing out of launcher (n=1) causes a small deviations in both the distance and the direction regarding to the nominal (table) path, at the whole range of possible soil from which the launching was performed. When firing from a fully loaded launcher the deviations in the direction are particularly noticeable.

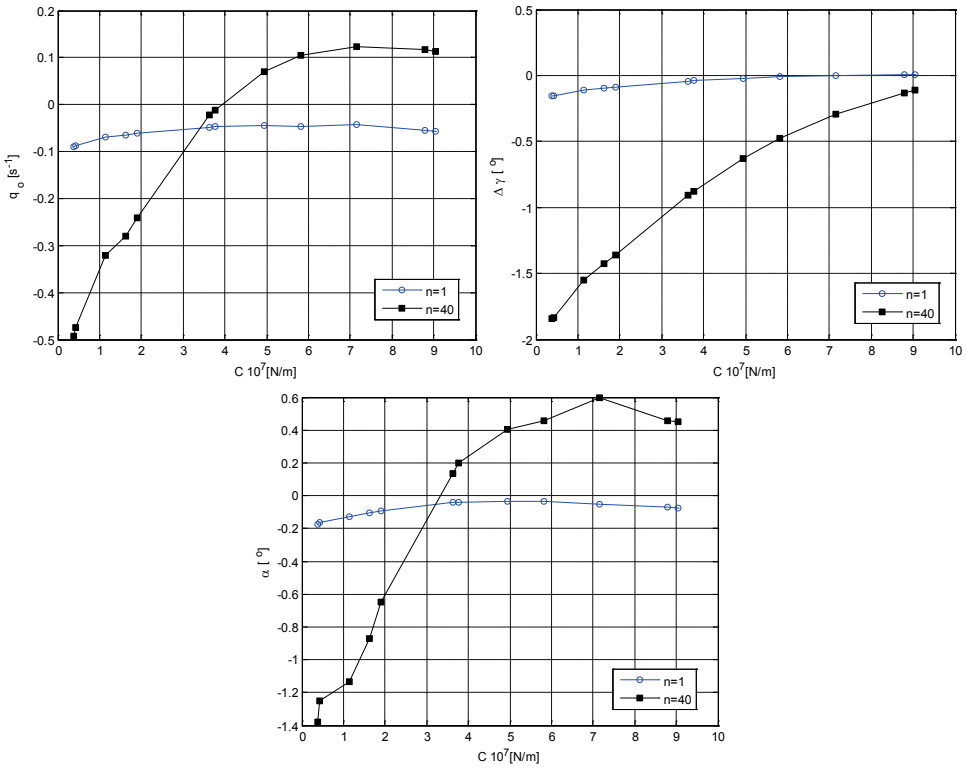


**Figure 3.** Graphs of initial flight disturbances

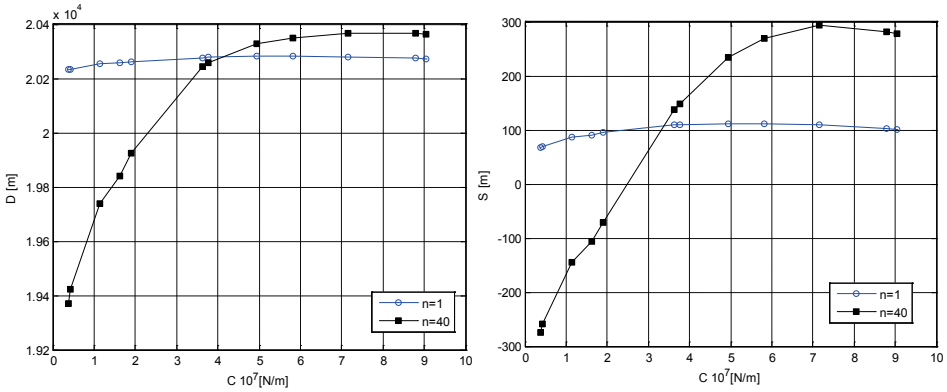


**Figure 4.** Range and direction functions of soil stiffness

Figure 5 shows the joint presentation of the impact points. It should be noted that the impact points are shown only for a few characteristic values of the entire range of stiffness and damping. In reality the most of the impact points will be in the range of most probable values of stiffness and damping (see the figure 1) and will fall into the marked rectangular area. Based on 200 realizations of random variables, rocket impact points for full and empty launcher, are obtained. The probability that impact points will be inside the rectangle with sides $2V_p$ *x* $2V_d$ is determined according to [9], and presented in figure 5.

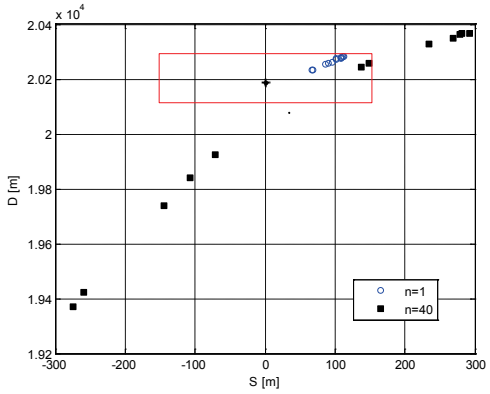


| Probabilistic values | | n=40 | n=1 |
|---|---|---|---|
| Range $D$ [m] | $m_x$ | 20197,1 | 20265,5 |
| | $\sigma_x$ | 28,59 | 6,22 |
| Direction $S$ [m] | $m_y$ | 178,9 | 97,09 |
| | $\sigma_y$ | 26,76 | 7,78 |
| Probability $p[\%]$ | | 55,331 | 99,974 |

**Figure 5.** Graphs of rocket impact points and table of probabilistic values

## 7. Conclusion

For any random value of soil parameters, during the last rocket firing (empty launcher) it can be noticed that the soil does not significantly affect to the direction, but the range is slightly higher than the ballistic tabular value for the ideal rocket flight. At the firing of the first rocket (loaded launcher), the initial launching disturbances are sensitive to changes in the physical-mechanical properties of the soil.

In the area around the mean values stiffness and damping, the total deviation on the target does not depend on the number of missiles in the launcher, but the deviation at the distance is slightly higher for the first rocket launching (fully loaded launcher). It is presented that for an ideal rocket, accuracy of impact points for the launching from random soil depends on the number of missiles in the launcher.

## References

[1] Das B. M., Ramana G. V., (2010) *Principels of Soil Dynamics*, Thomson Engineering, Alabama.

[2] Gunaratne M., (2006) *The Foundation Engineering Handbook*, Taylor & Francis Group, New York.

[3] Živanić, D., (1991) *Effect of Oscillation of Self-Propelled Multiple Rocket Launchers on Rocket Dispersion and Rate of Fire*, MSc thesis, Faculty of Mechanical Engineering, University of Belgrade, Belgrade, (in Serbian).

[4] Milošević M., (2012) *Contribution to the investigation parameters of interaction between rocket and launching device to the fire control system of multiple launchers rocket system*, PhD thesis, Military Academy, University of Defence, Belgrade, (in Serbian).

[5] Newland D. E., (1993) *An Introduction To Random Vibrations Spectral & Wavelet Analysis*, by Dover Publications, Inc, New York.

[6] Lalanne C., (2002) *Random Vibration (Mechanical Vibration and Shock)*, by HermesPenton Ltd., London.

[7] Milošević M., (2010) *Computer Software LANS-M,* Military Technical Institute, Belgrade

[8] Ćurčin M., Milošević M., (2010) *Computer Software PUTNPV3-M,* Military Technical Institute, Belgrade

[9] Вентцель Е. С., Овчаров Л. А., (2000) *Теория вероятностей и её инженерные приложения*, Высшая школа, Москва

[10] Дмитриевский А. А., Лысенко Л. Н., Богодистов С. С., (1991) *Внешняя баллистика*, Машиностроение, Москва

# NONLINEAR DYNAMICS OF SPRING-BLOCK EARTHQUAKE MODELS

**Srđan Kostić[1], Igor Franović[2], Kristina Todorović[3], Nebojša Vasović[4]**

[1] Faculty of Mining and Geology
University of Belgrade , Djusina 7, 11000 Belgrade, Serbia
e-mail: srdjan.kostic@rgf.bg.ac.rs
[2] Faculty of Physics
University of Belgrade , Studentski trg 12, 11000 Belgrade, Serbia
e-mail: igor.franovic@gmail.com
[1] Faculty of Pharmacy
University of Belgrade , Vojvode Stepe 450, 11221 Belgrade, Serbia
e-mail: kisi@pharmacy.bg.ac.rs
[4]Faculty of Mining and Geology
University of Belgrade, Djusina 7, 11000 Belgrade, Serbia
e-mail: nvasovic@rgf.bg.ac.rs

**Abstract.** The dynamical behavior of three variants of the Burridge-Knopoff single-block model of earthquake nucleation [1] is studied. In the first case, we use the model proposed by by Carlson and Langer [2] and modified by Vieira [3] with friction force dependent only on the velocity of the block. By increasing the introduced time delay $\tau$ in friction term and by changing the friction strength with included parameter $c$, the system under study shows a transition from equilibrium state to periodic and quasiperiodic motion with transient deterministic chaos. In the second case, we consider the model suggested by Madariaga [3], with Dieterich-Ruina rate-and state- dependent friction law. By introducing the time delay $\tau$ in the friction term, model exhibits a transition from equilibrium state to periodic, quasiperiodic motion and deterministic chaos. The third model, initially suggested by Becker [4] is modified by assuming periodic perturbations of two control parameters. In this case, also, deterministic chaos is observed. The obtained results indicate that the onset of deterministic chaos for certain values of control parameters represents typical property of the presented spring-block models of earthquake nucleation.

## 1. Introduction

The Burridge-Knopoff model [1] is today recognized as a common model for earthquake nucleation mechanism. In our case, presented here, it consists of one block of a certain rock type, connected through harmonic spring to a moving plate and driven along the rough surface, which causes the whole system to move in a stick-slip fashion (Fig. 1). Stick-slip motion as a possible mechanism of earthquake nucleation was firstly proposed by Brace and Byerlee [5]. According to their research, the earthquake is the ''slip'', and the ''stick'' is the interseismic period of the elastic strain accumulation. The main nonlinearity in this system comes from the friction law at the contact of moving block and the rough surface of the lower plate. Usually, two different friction laws are considered – one, where friction depends only on the velocity of block [2], and the other, where rate-and state-dependent friction is assumed [6,7]. Each of these friction laws, when coupled with governing equation of the motion, generate more or less complex behavior.

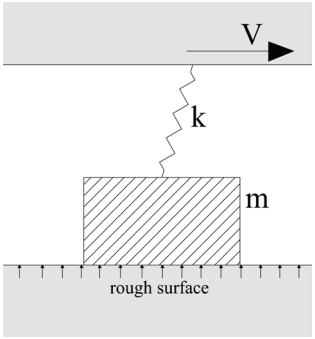


**Figure 1.** The Burridge-Knopoff block and spring model, represented by a slider coupled through a spring to a loader plate.

In this paper, we study three different variants of Burridge-Knopoff single-block model. In the first, so called Carslon-Langer model, friction depends only on the velocity of the block. In other two models (Madariaga and Becker), Dieterich-Ruina rate-and state-dependent friction law is assumed, with two state variables in the third (Becker) model. The first two models (Carslon-Langer and Madariaga) are further extended by introducing time delay parameter $\tau$, which is considered to be inherent property not only for the spring-block model, but also for the earthquake cycle itself. Apparently, upon cessation of motion, there is an initial ,,steady'' period of surface adjustment, where no frictional restrengthening is observed. It is this retarted, delayed interval that we model in this case, by including the parameter $\tau$. Also, Carlson-Langer model is further modified by including friction strength parameter, which could be related to fault zone properties (e.g. width of zone). The third, Becker, model is modified by assuming periodic perturbations of stress and spring stiffness parameters, which could describe the external dynamical triggering effects (e.g. impact of another earthquake, tide or reservoir effects). In all the cases, the analysis is performed numerically, using the fourth-order Runge-Kutta method.

## 2. Carslon-Langer model

As it was already stated, the dynamics of the first model, originally proposed by Carlson and Langer [2] and modified by Vieira [3], is analyzed by introducing time delay $\tau$ and friction strength parameter $c$, in the following way:

$$\ddot{U} = -U - \frac{c}{1 + \frac{\dot{U}(t-\tau)}{v^c}} + vt \tag{1}$$

where $U$ represents block displacement, $v$ – dimensionless pulling speed, as the ratio of slipping time to the loading time and $v^c$ represents dimensionless characteristic velocity. In present paper, in contrast to Vieira [3], we allow backwards motion. The analysis was done by varying the control parameters ($c$, $\tau$), for the constant value of parameter $v^c$=1, as already suggested by Vieira [3]. The results of the analysis indicate two well defined regions of different dynamical behavior, namely equilibrium state and periodic motion (Fig. 2). However, except for these two distinct states of the studied system, namely equilibrium state and periodic motion, which could be considered as typical features, we captured relatively weak chaotic behavior, but only as a transient feature (Fig. 3).

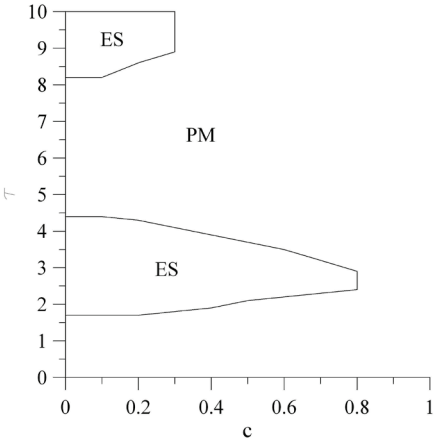


**Figure 2**. Bifurcation diagram of the one-block model in the parameter plane $(c,\tau)$, for the fixed value $v^c$=1. ES and PM are abbreviations for equilibrium state and periodic motion, respectively.

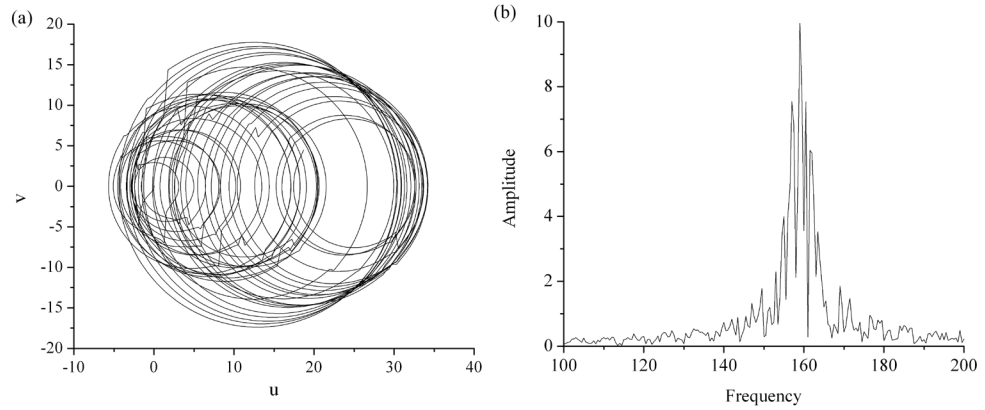


**Figure 3.** Phase portrait of the system (1) for the following parameter values: c=1.0, τ=0.7 and $v^c$=1.0 (chaos). The continuous broadband noise in the Fourier power spectrum indicates relatively weak chaotic behavior of the system

## 3. Madariaga model

The second analysis is conducted for the model originally proposed by Madariaga [3], modified by introducing time delay parameter τ in the following way

$$\begin{aligned} \dot{\theta} &= -v\left(\theta\left(1+\varepsilon\right)log\left(v-\tau\right)\right) \\ \dot{u} &= v-1 \\ \dot{v} &= -\gamma^2\left[u+\left(1/\xi\right)\left(\theta+log\left(v\right)\right)\right] \end{aligned} \tag{2}$$

where ε=(B−A)/A measures the sensitivity of the velocity relaxation, ξ =(kL)/A is the nondimensional spring constant, and γ = $(k/M)^{1/2}(L/v_0)$ is the nondimensional frequency [3].

Parameter M is the mass of the block, *k* corresponds to the spring stiffness, L is the critical sliding distance necessary to replace the population of asperity contacts [8]. Parameters A

and B are empirical constants, which depend on material properties [9]. Parameter θ represents the state variable, which is a function of history of sliding. The numerical analysis has shown that only by increasing the time-lag, the system under study exhibits chaotic behavior, via the quasiperiodic (Ruelle-Takens-Newhouse) route to chaos, which means that after two supercritical Hopf bifurcations, regular motion become highly unstable and replaced by a strange attractor (Fig. 4). Broadband continuous noise in power spectrum (Fig. 5a) and positive value of maximal Lyapunov exponent (Fig. 5b) confirm the onset of deterministic chaos.

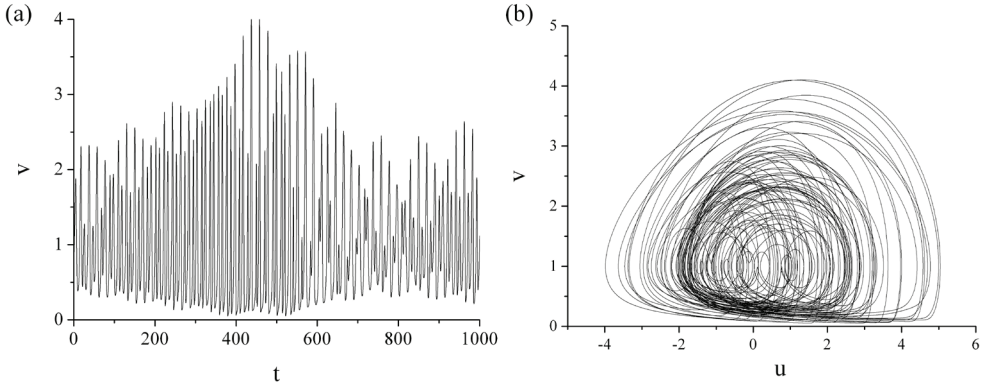


**Figure 4.** Temporal evolution of variable $v$ and the appropriate phase portraits for $\tau$=20, $\varepsilon$=0.5, $\xi$ = 0.5 and $\gamma$ = 0.8 (chaos).

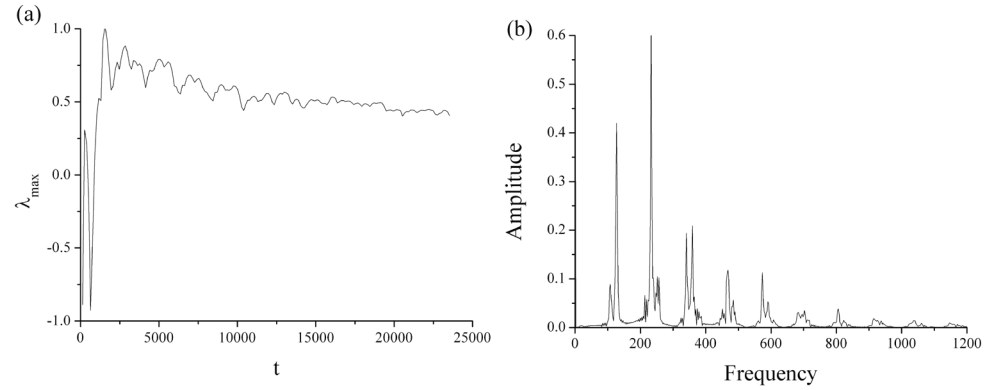


**Figure 5.** a. Maximum Lyapunov exponent converges well to 0.41; b. The broadband noise in the Fourier power spectrum indicate the chaotic behavior of the system.

## 4. Becker model

The third analyzed model is based on the system of equations suggested by Becker [4], which are given in the non-dimensionalized form in the following way:

$$\begin{aligned}\dot{x} &= e^x\left(\left(\beta_1(t)-1\right)x+y-z\right)+\dot{y}-\dot{z}\\ \dot{y} &= \left(1-e^x\right)\kappa(t)\\ \dot{z} &= -e^x\rho\left(\beta_2 x+z\right)\end{aligned} \tag{3}$$

where parameters are:

$$\begin{aligned} x &= \ln\left(\frac{V}{V_*}\right) \qquad \beta_i = \frac{B_i}{A} \qquad y = \frac{\tau-\tau_*}{A} \qquad \kappa = \frac{KL_1}{A}\\ z &= \beta_2 \ln\left(\frac{V_*\theta_2}{L_2}\right) \qquad \rho = \frac{L_1}{L_2} \qquad T = \frac{V^*}{L_1}t\end{aligned} \tag{4}$$

with $x$ as nondimensionaly velocity of the block, $y$ field stress and $z$ – state variable. Other parameters are the same as in the equation (2). The main difference between this and Madariaga model is that two state variables are introduced in the Becker model. Previous analyses have shown that only by perturbing the spring stiffness parameter $\kappa$, and for constant values of other parameters ($\beta_1$=1, $\beta_2$=0,84 and $\rho$=0,048), system exhibits the period-doubling route to chaos ($\kappa$=0.8525). In this case, we observe the dynamics of the model by assuming that parameters $\beta_1$ and κ are the positive periodic functions of time:

$$\begin{aligned}\beta_1(t) &= \beta_1 + \delta_\beta \sin(\omega_\beta t)\\ \kappa(t) &= \kappa + \delta_\kappa \sin(\omega_\kappa t)\end{aligned} \tag{5}$$

such that $\delta_\beta$, $\delta_\kappa$, $\omega_\beta$, and $\omega_\kappa$ present the constant oscillation amplitudes and the angular frequencies, respectively. The former satisfy the constraint $\delta_\beta \leq \beta_1$, $\delta_\kappa \leq \kappa$, which ensures the model's consistency as it confines each perturbation term to an appropriate range of values. Angular frequency is set to correspond the natural frequency of the periodic oscillation of the system in the unperturbed state. If these two parameters $\beta_1$ and $\kappa$ are perturbed, while the remaining ones are held fixed at previously proposed values, it turns out that the fully developed chaos emerges, with an instance of the typical phase portrait shown in Fig. 6(a). It is necessary to emphasize that in this case the onset of chaos is obsrved for higher value of κ (1.0) than in the unperturbed case (0.85). The conclusions on the character of the observed behavior rely on the power spectrum for the time series *v(t)*, provided in Fig. 6(b).

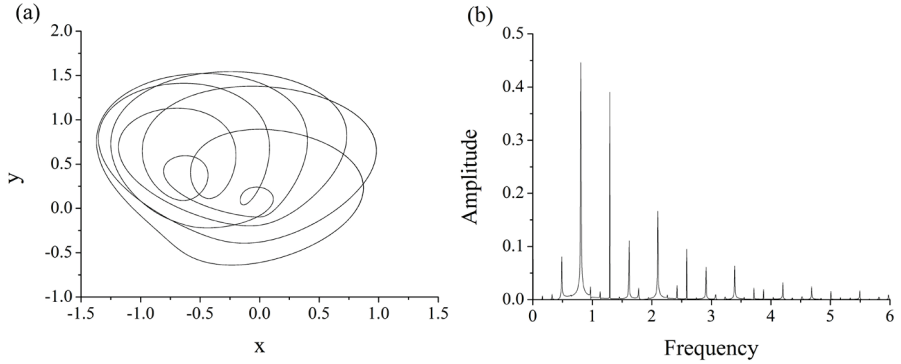


**Figure 6.** (a) Projection on the *(x,y)* plane of the typical chaotic orbit of the system (3). The results are obtained for the perturbation amplitudes $\delta_\beta$=0.9 and $\delta_\kappa$=0.5, while the other parameters are set so that the unperturbed system would exhibit periodic behavior: $\beta 1$=1, $\kappa$=1.5, $\beta_2$=0.84, $r$=0.048, $\omega_\beta$=0.8, $\omega_\kappa$=0.5 (b) The power spectrum for the time series *x(t)*.

## 5. Conclusion

In present paper, we analyzed three variants of single-block Burridge-Knopoff model. In the first case, we started from system with velocity dependent friction law, which we modified by introducing frictional strength parameter $c$, and tine delay $\tau$. In this case, we captured chaotic behavior, but only as a transient feature. In the second case, we started from the model with rate-and state-dependent friction law, which we also modified by introducing time delay parameter. However, in this case, we observed the Ruelle-Takens-Newhouse route to chaos, where the dynamics of block changes from equilibrium state, through periodic and quasiperiodic motion to deterministic chaos. In the third model, we assumed periodic perturbations of two control parameters, which has also yield the onset of deterministic chaos. Even though we examined the models with only one block, which could be considered as the simplest case of Burridge-Knopoff model, we were able to capture the complex behavior, already observed in the models with larger number of blocks. In that way, our research shows that the onset of deterministic chaos is not size-dependent.

The main assumption, made in present paper, and, in general, in adopted friction laws, is that the normal stress is constant during the motion. However, in real conditions in Earth's crust, it is this variable change that is considered to have significant effect on the nucleation of earthquakes. This is why our further research will be directed towards the inclusion of normal stress variable $\sigma$ in the presented models.

*Acknowledgement.* This research has been supported by the Ministry of Education, Science and Technological development, Contracts No. 176016, 171015 and 171017.

## References

[1] Burridge R and Knopoff L (1967) Model and theoretical seismicity, *Bulletin of the Seismological Society of America*, **57**, pp. 341-371.
[2] Carlson J M, Langer, J S (1989) Mechanical model of an earthquake fault, *Physical Review A* **40**, pp. 6470–6484.
[3] Erickson B, Birnir B and Lavallee D (2008) A model for aperiodicity in earthquakes, *Nonlinear processes in geophysics*, **15**, pp. 1-12.
[4] Becker T W (2000) Deterministic chaos in two state-variable friction sliders and the effect of elastic interactions, *Geocomplexity and the physics of earthquakes*, Rundle, J B Turcotte and D L Klein (eds.) pp. 5-26, American Geophysical Union.
[5] Brace W and Byerlee J (1966) Stick-slip as a mechanisms for earthquakes, *Science*, **153**, pp. 3739, 990-992.
[6] Dieterich J H (1997). Modeling of rock friction, 1. Experimental results and constitutive equations. *Journal of Geophysical Research*. **84**, 2161-2168.
[7] Ruina A L (1983) Slip instability and state variable friction laws. *Journal of geophysical research*, **88**, pp. 10359-10370
[8] Dieterich J H and Kilgore B D (1994) Direct observation of frictional contacts: new insights for state dependent properties, *Pure and Applied Geophysics,* **143**, pp. 283–302.
[9] Rice J R and Ruina A L (1983) Stability of steady frictional slipping. *Journal of Applied Mechanics*, **50**, pp. 343-349.

# VISUAL CONTROL OF A MOBILE ROBOT USING HOMOGRAPHY AND LEARNING FROM DEMONSTRATION METHODOLOGY

**Marko Mitić[1], Zoran Miljković[2], Najdan Vuković[3], Ivan B. Lazarević[4]**

[1] University of Belgrade – Faculty of Mechanical Engineering
Production Engineering Department, Kraljice Marije 16, 11120 Belgrade 35
e-mail: mmitic@mas.bg.ac.rs
[2] University of Belgrade – Faculty of Mechanical Engineering
Production Engineering Department, Kraljice Marije 16, 11120 Belgrade 35
e-mail: zmiljkovic@mas.bg.ac.rs
[3] University of Belgrade – Faculty of Mechanical Engineering
Innovation Center, Kraljice Marije 16, 11120 Belgrade 35
e-mail: nvukovic@mas.bg.ac.rs
[4] "Ecolab Hygiene", Milana Tankosića 8, 11000 Belgrade
e-mail: ivan.lazarevic@ecolab.com

**Abstract.** This paper presents novel intelligent approach for visual servoing of differential drive mobile robots. A hybrid control scheme that switches between vision-based control and intelligent control based on learning from demonstration (LfD) methodology is presented and evaluated on a mobile robot in a laboratory model of a manufacturing environment. Linear velocity of a nonholonomic vehicle is obtained using homography calculated from images in current and desired robot pose. Integrated visual homing strategy enables the guidance to the desired pose by calculating the error in matched features between the aforementioned images. The desired area for visual features is defined in the image plane in order to ensure the visibility of an object of interest in each control loop. LfD framework and neural network (NN) are utilized to learn angular velocity in current pose depending on the position of the selected image feature. Empirical data consisting of numerous feature positions in target and current robot poses is gathered for learning a direct mapping from image space to the actuator command. Moreover, different learning algorithms and NN architectures are implemented and tested on a robot platform. The experiments are conducted on a *KheperaII* mobile robot with compatible camera *KheCMUCam* in order to prove the effectiveness of the proposed approach. The convergence of the intelligent control system is ensured in every task, with the very good resulting performance considering the challenging real world conditions.

## 1. Introduction

In the last decade, a large number of mobile robot applications use machine vision in order to acquire rich information from the known/unknown and indoor/outdoor environment. Complex tasks in practice such as inspection of hazardous surroundings, surveillance and/or rescue missions can be addressed and successfully solved using robot vision. Likewise, the navigation capabilities of the robotic systems are significantly improved with the feedback information from monocular and/or stereo vision system. This information is used within the control loop in order to ensure the robot desired pose (i.e. position and

orientation) as required by a task in hand. Excellent surveys on the topic of mobile robot vision based navigation are [1] and [2].

Control approaches based on homography have become very popular techniques recently [3, 4, 5, 6, 7, 8]. One of the first papers addressed the asymptotic regulation of the mobile robot pose using the decomposed homography [3]. This decomposition is bypassed in [4], where the robot control is based on the input-output linearization of the system considering the nonholonomic constraints of the platform. The same authors next developed the shortest path homography based visual control algorithm for differential drive mobile robots [5]. The significant improvement was reported in this study, since the three novel methods for calculating the robot velocities are introduced. By invoking the homography based control law in the hybrid scheme in [6], the drawback of homography approach for planar scenes is eliminated. Likewise, the field of view constrained is treated in [7], which gives the individual control laws for the three path classes that define the language of optimal paths: rotations, straight-line segments and logarithmic spirals. In [8] multi robot systems are controlled in indoor environment using homography. However, none of these approaches incorporates learning methods able to respond to the unpredictable environmental conditions.

Learning from Demonstration (LfD) methodology represents a subset of supervised learning in which behavior is represented as pairs of states and actions [9]. In order to develop a successful mapping from world observations to the robot actions, the teacher robot and/or human demonstrates the correct actions in accordance with the determined state. In mobile robotics, LfD is used in behavior based control architecture where experiments for learning reactive and history dependent tasks proved usefulness of this paradigm [10]. Likewise, a certain number of studies incorporate neural networks (NN) [11] in order to speed up the learning process. In [12] echo state neural network and LfD paradigm are used for mobile robot behavior acquisition. In [13] LfD is utilized to learn the demonstrated trajectories as a mapping between the visual features computed with respect to a panoramic view onto a corresponding robot motion. However, despite the various studies described here, the similar research on homography and LfD for mobile robot control has not been reported in the literature so far.

This paper is organized as follows. Section 2 presents the homography based on visual servoing for mobile robots. Neural network Learning from Demonstration controller and the description of the hybrid switching scheme are given in Section 3. Experimental results on a mobile robot platform in real world conditions are provided in Section 4, followed by the conclusion part at the end of this paper.

## 2. Homography based visual servoing

Two images obtained with the same camera have the projection matrixes in a common reference system defined as [14]:

$$\mathbf{P_1} = \mathbf{K}\left[\mathbf{I} \mid 0\right], \tag{1}$$

$$\mathbf{P_2} = \mathbf{K}\left[\mathbf{R} \mid -\mathbf{Rc}\right], \tag{2}$$

where: $\mathbf{K}$ represents calibration matrix; $\mathbf{R}$ is the camera rotation and $\mathbf{c}$ is the translation between the optical centres of the two cameras. It is known that homography H can be related to camera motion using the following relation:

$$\mathbf{H}=\mathbf{K}\left(\mathbf{R}-\mathbf{t}\frac{\mathbf{n}^{\mathbf{T}}}{d}\right)\mathbf{K}^{-1}=\mathbf{K}\left(\mathbf{R}+\mathbf{R}\mathbf{c}\frac{\mathbf{n}^{\mathbf{T}}}{d}\right)\mathbf{K}^{-1}=\mathbf{K}\mathbf{R}\left(\mathbf{I}+\mathbf{c}\frac{\mathbf{n}^{\mathbf{T}}}{d}\right)\mathbf{K}^{-1}, \tag{3}$$

where: $\mathbf{n}=\left[nx\ ny\ nz\right]^{\mathrm{T}}$ is the *normal* to the homography plane, and $d$ is the distance between the camera origin and the point (i.e. object of interest) P in that plane. Replacing the well known equations for $\mathbf{R}$ and $\mathbf{c}$ into Eq. (3), and after normalizing the $\mathbf{H}$ matrix, we obtain:

$$h_{11}=\cos\phi+\left(x\cos\phi+y\sin\phi\right)\frac{n_x}{d}, \tag{4}$$

$$h_{12}=\frac{\alpha_x}{\alpha_y}+\left(x\cos\phi+y\sin\phi\right)\frac{n_y}{d}, \tag{5}$$

$$h_{13}=\alpha_x\left(\sin\phi+\left(x\cos\phi+y\sin\phi\right)\frac{n_z}{d}\right), \tag{6}$$

$$h_{31}=\frac{1}{\alpha_x}\left(-\sin\phi+\left(-x\sin\phi+y\cos\phi\right)\frac{n_x}{d}\right), \tag{7}$$

$$h_{32}=\frac{1}{\alpha_y}\left(-x\sin\phi+y\cos\phi\right)\frac{n_y}{d}, \tag{8}$$

$$h_{33}=\cos\phi+\left(-x\sin\phi+y\cos\phi\right)\frac{n_z}{d}, \tag{9}$$

where: $x$, $y$, $\phi$ are robot position and orientation in the motion plane (i.e. pose), and $\alpha_x$ and $\alpha_y$ are focal lengths in calibration matrix Finally, the mobile robot linear velocity can be obtained from homography matrix as [5]:

$$v=-k_v\left(h_{11}-h_{33}\right). \tag{10}$$

with $k_v$ as the control gain. In this paper, the hybrid system involves switching between homography based linear controller and NN-LfD based angular controller. Therefore, the angular controller as well as intelligent switching hybrid control scheme is described in the next section.

### 3. Neural network LfD and switching based control scheme

The aim of the LfD employment is to develop a successful mapping from world observations to the robot actions using behavior demonstrated by the human or robot teacher. LfD experiment consists of three different steps: demonstration, learning and drive phase. In the first mode, the demonstrations representing desired actions are executed by the teacher robot. The sensor values and corresponding wheel commands are memorized in the demonstration log. In this study, the learning pair consists of coordinate difference between the selected feature position in the current and the target image (i.e. distance in the

$u$ value), and time-wise corresponding actuator command that moves the selected feature towards its desired image position [15]. In the learning mode, the data from the demonstration log is used for the NN training. In this study, several learning algorithms and various network architectures are experimentally tested. The networks with the best behaviors are recorded and used in the next step. Driving mode presents the final part of the LfD experiment, which is used to test the data trained in the previous stage. After the testing conditions are set and the learner robot is placed in the environment, the input sensor values are transformed into the actuator commands using the NN-LfD controller. The testing pairs (sensor value-actuator command) for different experimental conditions are recorded into the drive log. It is important to mention that the actual robot performance is evaluated through the calculated MSE between the corresponding learning pairs in the demonstration and drive mode.

After the selection of optimal network, the online phase of the intelligent controller is active. Starting from an arbitrarily pose in the structured indoor environment, the mobile robot is to navigate to the desired pose defined with the pre-recorded target image. After the current image is acquired, the feature detection and matching is done next. If the selected feature is outside the image desired area, then the correction in the robot orientation is carried out; otherwise, the forward homography based robot motion is performed. The control method is determined by calculating the difference between the positions of current and target feature. Finally, the robot motion finishes when the control goal is achieved, i.e. when the norm of the image features is smaller then an error tolerance set by the designer.

## 4. Experimental results and discussion

The developed intelligent controller is evaluated through the experiments carried out on a real mobile robot in an indoor structured environment. The robotic system used for experimental validation consists of *KheperaII* mobile robot and a low resolution camera. The AMD Athlon™ X2 Dual-Core QL-64 2.1GHz processor laptop computer with 4GBs RAM on Windows Vista is employed for robot control and data manipulation. The chessboard-like pattern is used in the experiment, so as to ease the signal and image processing.

In an experimental offline phase several learning algorithms are employed in order to investigate the best possible NN behavior. All the main algorithms that have the best performance over the function approximation, classification or pattern recognition problems were tested in *Matlab* so as to discover the most suitable one. These 6 algorithms with corresponding acronyms and 18 NN architectures are listed in Table 1.

**Table 1.** Learning algorithms and NN architectures used in the experiment.

| No. | Learning algorithm | Acronym | No. | NN architecture | No. | NN architecture |
|---|---|---|---|---|---|---|
| 1 | Levenberg–Marquardt | LM | 1 | 1 | 10 | 5-2 |
| 2 | Bayesian Regularisation | BR | 2 | 2 | 11 | 8-4 |
| 3 | Resilient Backpropagation | RP | 3 | 3 | 12 | 10-4 |
| 4 | Scaled Conjugate Gradient | SCG | 4 | 5 | 13 | 2-2-2 |
| 5 | BFGS Quassi-Newton | BFG | 5 | 8 | 14 | 3-2-2 |
| 6 | Variable Learning Rate Backpropagation | GDX | 6 | 10 | 15 | 4-3-2 |
| | | | 7 | 1-1 | 16 | 5-3-2 |
| | | | 8 | 2-2 | 17 | 8-3-2 |
| | | | 9 | 3-2 | 18 | 8-4-2 |

Following the NN training with MSE goal of $10^{-5}$ using 75% of data, the optimal network (trained with each learning algorithm) is implemented and tested on a robot platform in an experimental environment. The NN-LfD controller is tested on the remaining amount (25%) of data several times for each NN and learning algorithm. The best results are obtained and presented in Fig. 1. Next, the mobile robot is to move from the pose indicated by the acquired initial image to the pose defined by the pre-recorded target image, as in Fig. 2. The orientation of the mobile robot in every pose is denoted with the short black line. It is noticeable that the final robot pose is obtained using the NN-LfD controller. The change of mobile robot, linear and angular velocity during its motion is given in Fig. 3 and Fig. 4, respectively. It is obvious that the velocities match the robot's evolution given in Fig. 2. The final error in the robot position and orientation is minimal, which evidence the potential and applicability of the novel intelligent controller in the real world conditions.

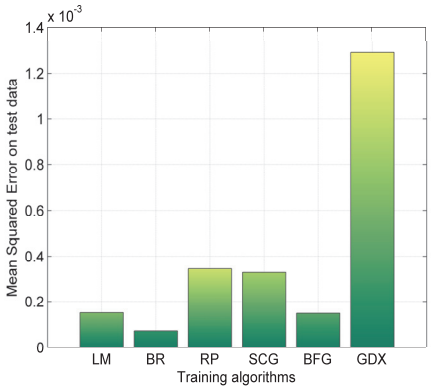


**Figure 1.** Results of NN training.

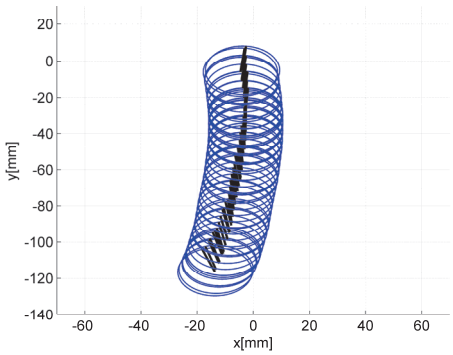


**Figure 2.** Mobile robot path in x-y plane.

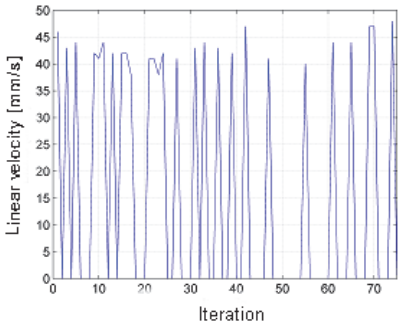


**Figure 3.** Linear velocity during robot motion.

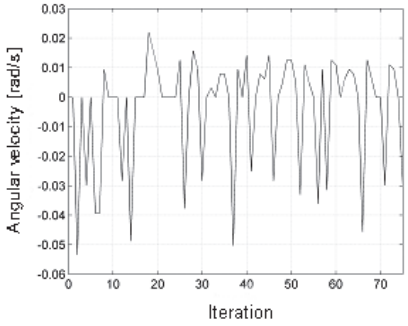


**Figure 4.** Angular velocity during robot motion.

The feature detection and matching during robot navigation is presented in Fig 5. The outcome of the employed image processing system is a robust visual control able to deal with the real world conditions imposed in the real environment. Fig. 6 depicts the switching parameter which is equal to 1 when the NN-LfD controller is active or 0 if the homography based controller is employed. During the experiment, the NN-LfD controller and the homography based controller are active in accordance with the feature position in the image, as seen in the Fig. 6. Evidently, the preferred robot path is ensured in each control iteration which proves the effectiveness of the developed system.

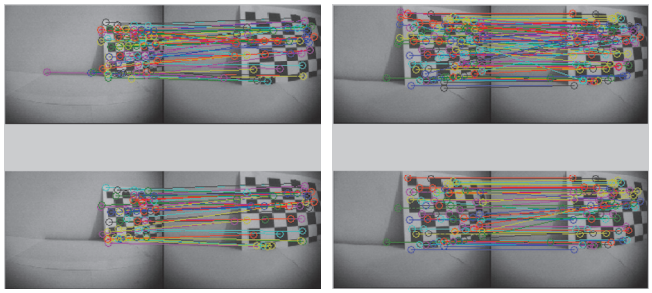

a) b)

**Figure 5.** Matched and detected features at: a) first and b) final iteration.

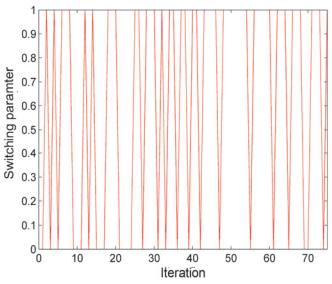


**Figure 6.** Switching parameter.

## 5. Conclusion

In this paper, the development and performance evaluation of a novel intelligent visual control approach for a nonholonomic mobile robot is presented. A successful mapping from the image space to the robot actions is conducted using offline and online phase. Depending on the feature position in the image plane, the neural network learning from demonstration controller for lateral motion correction or the homography based controller for robot forward motion is employed. The results show robustness, effectiveness and applicability of the developed hybrid switching scheme regarding unpredictable conditions in real time.

*Acknowledgment.* This research is supported by the Serbian Government – the Ministry of Education, Science and Technological Development under grant TR35004 (2011–2014).

## References

[1] Bonin-Font F, Ortiz A, Oliver G (2008) Visual Navigation for Mobile Robots: A Survey, *Journal of Intelligent and Robotic Systems*, **53(3)**, pp. 263–296.
[2] DeSouza G N and Kak A C (2002) Vision for Mobile Robot Navigation: A Survey, *IEEE Transactions on Pattern Analysis and Machine Intelligence*, **24(2)**, pp. 237–267.
[3] Fang Y, Dixon W E, Dawson D M, Chawda P (2005) Homography-Based Visual Servo Regulation of Mobile Robots, *IEEE Transaction on Systems, Man and Cybernetics, Part B: Cybernetics*, **35(5)**, pp. 1041–1050.
[4] López-Nicolás G, Sagüés C, Guerrero J J (2007) Homography-Based Visual Control of Nonholonomic Vehicles, In: *IEEE International Conference on Robotics and Automation*, pp. 1703–1708.
[5] López-Nicolás G, Sagüés C, Guerrero J J (2007) Shortest Path Homography-Based Visual Control for Differential Drive Robots, In: *Vision systems (I-Tech.)*, G Obinata and A Dutta (Eds.), pp. 583–596
[6] López-Nicolás G, Guerrero J J, Sagüés C (2010) Visual Control of Vehicles using Two-View Geometry, *Mechatronics*, **20(2)**, pp. 315–325.
[7] López-Nicolás G, Gans N R, Bhattacharya S, Guerrero J J, Sagüés C, Hutchinson S (2010) Homography-Based Control Scheme for Mobile Robots with Nonholonomic and Field-of-View Constraints, *IEEE Transaction on Systems, Man and Cybernetics, Part B: Cybernetics*, **40(4)**, pp. 1115–1127.
[8] López-Nicolás G, Aranda M, Mezouar Y, Sagüés C (2012) Visual Control for Multi-Robot Organized Rendezvous, *IEEE Transaction on Systems, Man and Cybernetics, Part B:Cybernetics*, **42(4)**, pp. 1155–1168.
[9] Argall B D, Chernova S, Veloso M, Browning B (2009) A Survey of Robot Learning from Demonstration, *Robotics and Autonomous Systems*, **57(5)**, pp. 469–483.
[10] Kasper M, Fricke G, Steuernagel K, Puttkamer E V (2001) A Behavior-Based Mobile Robot Architecture for Learning from Demonstration, *Robotics and Autonomous Systems*, **34(2–3)**, pp. 153–164.
[11] Miljković Z and Aleksendrić D (2009) *Artificial Neural Networks – Solved Examples with Theoretical Background (in Serbian)*, University of Belgrade – Faculty of Mechanical Engineering, Belgrade.
[12] Hartland C, Bredeche N (2007) Using Echo State Networks for Robot Navigation Behavior Acquisition, In: *IEEE international conference on robotics and biomimetics*, pp 201–206.
[13] Narayanan K K, Posada L F, Hoffmann F, Bertram T (2009) Imitation Learning for Visual Robotic Behaviors, In: *Proceedings of the19th Workshop on Computational Intelligence*, pp 221–236.
[14] Hartley R I, Zisserman A (2004) *Multiple View Geometry in Computer Vision*, University Press, Cambridge.
[15] Miljković Z, Mitić M, Lazarević M, Babić B (2013) Neural Network Reinforcement Learning for Visual Control of Robot Manipulators, *Expert Systems with Applications*, **40(5)**, pp. 1721–1736.

# ON DYNAMICS OF A SPATIAL DISORIENTATION TRAINER FOR PILOT TRAINING

**Zorana Dančuo[1], Vladimir Kvrgić[1], Boško Rašuo[2], Jelena Vidaković[1]**

[1] Lola Institute
Kneza Višeslava 70a, Belgrade
e-mail: zorana.dancuo@li.rs
[2] Faculty of Mechanical Engineering,
University of Belgrade, Kraljice Marije 16, 11120 Belgrade 35
e-mail: brasuo@mas.bg.ac.rs

**Abstract.** Spatial disorientation represents one of the major physiological threats for pilots of modern combat aircraft. The Spatial Disorientation Trainer (SDT) enhances the situational awareness of pilots, and provides an effective training to avoid the phenomenon of Spatial Disorientation (SD) [1]. In this paper the dynamic analysis of the SDT is presented. The SDT is modelled as a four-joint revolute robotic manipulator. The four axes intersect at the pilot's head, which is treated as the end-effector. In order to calculate the end-effector's position, velocity, acceleration, and forces, coordinate frames are set according to the Denavit-Hartenberg convention. The homogenous transformation matrices and equations that constitute the dynamics of the disorientator are presented. The forces necessary for the robot motion are determined [2]. Total forces and moments for each axis are determined by the Newton-Euler method. The SDT dynamic analysis represents an essential part of the robotic mechanism, the drive and control system design.

***Keywords:*** *Spatial Disorientation, Robot, Denavit-Hartenberg, Forces, Moments*

## 1. Introduction

The highest death rates of fighter pilots during peace time are result of G-LOC, and Spatial Disorientation (SD). Common illusions that occur in-flight are autokinesis, false horizon, leans, Coriolis, blackhole approach, etc. [3]. Beside human centrifuges [4], which are in essence "G-Machines", Spatial Disorientation Trainer (SDT) play a significant role in aircrew training. In human centrifuge training, the emphasis is put on the determination of individual G-tolerances, whilst in SDT training on proprioceptive illusions. Spatial orientation defines the natural ability to maintain the body orientation and/or posture in relation to the surrounding environment at rest and in motion. The environment of flight is unfamiliar to the human body, creating sensory conflicts and illusions [5]. Spatial disorientation (SD) can be defined as "a failure to sense correctly the position, motion, or attitude of the aircraft or of him/herself within the fixed coordinate system provided by the surface of the earth and the gravitational vertical." (Benson, 1998). An integral part of successful flight is proper visual orientation, perception of motion and position (vestibular function), and auditory cues from sound sources. SD is categorized into three types: Type I (unrecognized), Type II (recognized), and Type III (incapacitating). Most mishaps are related to Type I, and insignificantly to Type III [6]. In-flight awareness and training of

various illusions is ideal, but it is not safely to simulate all disorientating effects that occur in flight. Air forces worldwide use high-fidelity devices capable of simulating specific flight profiles [6]. All aircrew members, regardless of flight experience, are vulnerable to SD. Despite academic training and new technologies, SD accident rates are not improving [7]. A study by Cheung et al. confirmed that SD is a significant factor in about 23% of all category A accidents between 1982.-1992. Category A accident is defined as an accident when the aircraft is destroyed, declared missing, or damaged beyond economical repair. SD training may be performed in-flight, or on ground. SD demonstration in-flight consists of reinforcement of the orientation senses in flight, and the enhancement of aircrew awareness to potential SD situations. On the other hand, SD training on ground consists of a series of flight procedures to cope with disorientating circumstances and illusions [8].

## 2. Spatial Disorientation Trainer

Various SD Trainer are known in the art. The SDT is a highly reliable system with a single-seat, which provides 360 degrees of continuous motion in the planetary axis, with four axes (4DoF). The planetary, roll, pitch and yaw are independently controlled, and rotated around the main planetary axis. The planetary arm rotates to achieve a centripetal acceleration of 2.5G [1].

### *2.1. Coordinate systems and Kinematics*

The SDT is a robotic 4DoF system with revolute joints. The pilot's head is treated as the end-effector, and lies in the intersection of the yaw (2), roll (3), and pitch (4) axis, Fig. 1. The coordinate systems are set in accordance with the Denavit-Hartenberg convention (DH). Coordinate systems {2}, {3} and {4} in Fig. 1. are for clarity relocated outside the point of the intersection of the (2), (3) and (4) axis. Once the coordinate frames are determined, inter-link transformations are uniquely described by the following four parameters, Table 1. [1]:

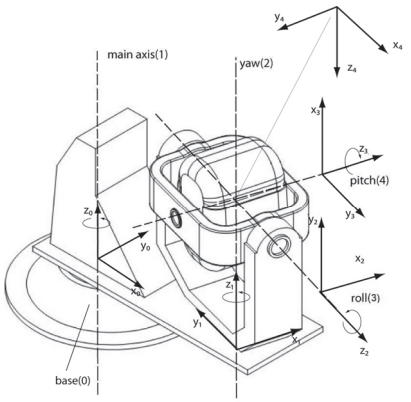


**Figure 1.** Coordinate systems according to DH

| Joint *i* | $q_i$ | $\alpha_i$ [°] | $a_i$[mm] | $\theta_i$[°] | $d_i$[mm] |
|---|---|---|---|---|---|
| **1** | $q_1$ | 0 | $a_1$ | $\theta_1$ | 0 |
| **2** | $q_2$ | 90 | 0 | $\theta_2$ | $d_2$ |
| **3** | $q_3$ | 90 | 0 | $\theta_3+90$ | 0 |
| **4** | $q_4$ | -90 | 0 | $\theta_4+90$ | 0 |

**Table 1**. DH SDT parameters [1]

*Kinematics:* In order to determine forces and torques needed for the SDT motion, kinematic values have to be determined first.

$$\mathbf{T}_4=\begin{bmatrix} c_{1+2}s_3s_4+s_{1+2}c_4 & -c_{1+2}c_3 & c_{1+2}s_3c_4-s_{1+2}s_4 & a_1c_1 \\ s_{1+2}s_3s_4-c_{1+2}c_4 & -s_{1+2}c_3 & s_{1+2}s_3c_4+c_{1+2}s_4 & a_1s_1 \\ -c_3s_4 & -s_3 & -c_3c_4 & d_2 \\ 0 & 0 & 0 & 1 \end{bmatrix}=\begin{bmatrix} n_{x4} & o_{x4} & a_{x4} & X_4 \\ n_{y4} & o_{y4} & a_{y4} & Y_4 \\ n_{z4} & o_{z4} & a_{z4} & Z_4 \\ 0 & 0 & 0 & 1 \end{bmatrix}=\begin{bmatrix} n_{xe} & o_{xe} & a_{xe} & p_{xe} \\ n_{ye} & o_{ye} & a_{ye} & p_{ye} \\ n_{ze} & o_{ze} & a_{ze} & p_{ze} \\ 0 & 0 & 0 & 1 \end{bmatrix} \tag{1}$$

$T_4$ in Eq. (1) represents the homogenous transformation matrix for the last robot member. This matrix is equated with the end-effector matrix, because the end-effector lies in the intersection of the roll, pitch and yaw axes. Notations $c_i$ and $s_i$ represent the sine, and cosine of the angle $\theta_i$ The angular velocities $\boldsymbol{\omega}_{i+1}=\boldsymbol{\omega}_i+\mathbf{z}_i\,\dot{q}_{i+1}$, of the SDT links ($i$=1, 2, 3, 4) Eq.(2) are:

$$\boldsymbol{\omega}_1=\begin{bmatrix}0\\0\\\dot{q}_1\end{bmatrix},\boldsymbol{\omega}_2=\begin{bmatrix}0\\0\\\dot{q}_1+\dot{q}_2\end{bmatrix},\boldsymbol{\omega}_3=\begin{bmatrix}s_{1+2}\dot{q}_3\\-c_{1+2}\dot{q}_3\\\dot{q}_1+\dot{q}_2\end{bmatrix},\boldsymbol{\omega}_4=\begin{bmatrix}s_{1+2}\dot{q}_3+c_3c_{1+2}\dot{q}_4\\-c_{1+2}\dot{q}_3+c_3s_{1+2}\dot{q}_4\\\dot{q}_1+\dot{q}_2+s_3\dot{q}_4\end{bmatrix} \tag{2}$$

The angular accelerations $\dot{\boldsymbol{\omega}}_{i+1}=\dot{\boldsymbol{\omega}}_i+\mathbf{z}_i\,\ddot{q}_{i+1}+\boldsymbol{\omega}_i\times\mathbf{z}_i\,\dot{q}_{i+1}$ of the SDT links ($i$=1, 2, 3, 4) Eq.(3) are:

$$\begin{aligned}\dot{\boldsymbol{\omega}}_1&=\begin{bmatrix}0\\0\\1\end{bmatrix}\ddot{q}_1,\dot{\boldsymbol{\omega}}_2=\begin{bmatrix}0\\0\\1\end{bmatrix}(\ddot{q}_1+\ddot{q}_2),\dot{\boldsymbol{\omega}}_3=\begin{bmatrix}0\\0\\1\end{bmatrix}(\ddot{q}_1+\ddot{q}_2)+\begin{bmatrix}s_{1+2}\\-c_{1+2}\\0\end{bmatrix}\ddot{q}_3+\begin{bmatrix}(\dot{q}_1+\dot{q}_2)\dot{q}_3c_{1+2}\\(\dot{q}_1+\dot{q}_2)\dot{q}_3s_{1+2}\\0\end{bmatrix},\\ \dot{\boldsymbol{\omega}}_4&=\begin{bmatrix}0\\0\\1\end{bmatrix}(\ddot{q}_1+\ddot{q}_2)+\begin{bmatrix}s_{1+2}\\-c_{1+2}\\0\end{bmatrix}\ddot{q}_3+\begin{bmatrix}(\dot{q}_1+\dot{q}_2)c_{1+2}\\(\dot{q}_1+\dot{q}_2)s_{1+2}\\0\end{bmatrix}\dot{q}_3+\begin{bmatrix}c_3c_{1+2}\\c_3s_{1+2}\\s_3\end{bmatrix}\ddot{q}_4+\begin{bmatrix}-c_{1+2}\dot{q}_3\dot{q}_4s_3-c_3\dot{q}_1\dot{q}_4s_{1+2}-c_3\dot{q}_2\dot{q}_4s_{1+2}\\c_3c_{1+2}\dot{q}_4(\dot{q}_1+\dot{q}_2)-s_3s_{1+2}\dot{q}_3\dot{q}_4\\c_3\dot{q}_3\dot{q}_4\end{bmatrix}\end{aligned} \tag{3}$$

The linear velocities $\mathbf{v}_{i+1}=\mathbf{v}_i+\boldsymbol{\omega}_{i+1}\times\mathbf{p}^*_{i+1}$ of the SDT links ($i$=1, 2, 3, 4) Eq.(4) are:

$$\mathbf{v}_1=\mathbf{v}_2=\mathbf{v}_3=\mathbf{v}_4=\begin{bmatrix}-a_1s_1\\a_1c_1\\0\end{bmatrix}\dot{q}_1 \tag{4}$$

The homogeneous transformation matrix 4x4, between the coordinate system of the last robot member and the fixed robot base coordinate system, consists of the first three

columns, which constitute the rotational matrix. The fourth column represents the positional vector of the last robot unit ($p^*$) relative to the base of the robot [1].

The linear accelerations $\dot{\mathbf{v}}_{i+1} = \dot{\mathbf{v}}_i + \dot{\boldsymbol{\omega}}_{i+1} \times \mathbf{p}^*_{i+1} + \boldsymbol{\omega}_{i+1} \times (\boldsymbol{\omega}_{i+1} \times \mathbf{p}^*_{i+1})$, $i$=1,2,3,4 of the SDT links are Eq.(5):

$$\dot{\mathbf{v}}_1 = \dot{\mathbf{v}}_2 = \dot{\mathbf{v}}_3 = \dot{\mathbf{v}}_4 = \begin{bmatrix} -a_1 s_1 \\ a_1 c_1 \\ 0 \end{bmatrix} \ddot{q}_1 + \begin{bmatrix} -a_1 c_1 \\ -a_1 s_1 \\ 0 \end{bmatrix} \dot{q}_1^{\,2} \tag{5}$$

## 3. Spatial Disorientation Trainer Dynamics

As the position, velocity and accelerations of joints are known, with the knowledge of the mass distribution, forces and torques required to cause motion, can be calculated. Based on Newton-Euler equations, total forces and torques acting on each member are determined. The position vector of the center of mass of the $i$-member relative to the coordinates of the $i$-member are expressed with $\hat{\boldsymbol{r}}_i^{cm} = \begin{bmatrix} \hat{r}_{xi} & \hat{r}_{yi} & \hat{r}_{zi} \end{bmatrix}^T$ Linear accelerations of the center of mass of the SDT links are expressed with: $\dot{\mathbf{v}}_i^{cm} = \begin{bmatrix} \dot{v}_{xi}^{cm} & \dot{v}_{yi}^{cm} & \dot{v}_{zi}^{cm} \end{bmatrix}^T = \dot{\mathbf{v}}_i + \dot{\boldsymbol{\omega}}_i \times \mathbf{r}_i^{cm} + \boldsymbol{\omega}_i \times (\boldsymbol{\omega}_i \times \mathbf{r}_i^{cm})$. The moment of inertia matrix for the center of mass for link (member) 1, relative to the coordinate system {1} is given in Eq. (6):

$$\mathbf{I}_1^{cm} = \begin{bmatrix} \hat{I}_{x1} c_1^2 + \hat{I}_{y1} s_1^2 & c_1 s_1 (\hat{I}_{x1} - \hat{I}_{y1}) & 0 \\ c_1 s_1 (\hat{I}_{x1} - \hat{I}_{y1}) & \hat{I}_{x1} s_1^{\,2} + \hat{I}_{y1} c_1^{\,2} & 0 \\ 0 & 0 & \hat{I}_{z1} \end{bmatrix} \tag{6}$$

where $I_1^{cm}$ represents the center of mass matrix of inertia for the fixed coordinate system, depending on the moments of inertia $\hat{I}$ for the moving coordinate system. For easier calculations, the moving coordinate system $O\hat{x}\hat{y}\hat{z}$ is placed in the center of mass of each link. Based on this, total forces acting on the member *i=1,2,3,4* are given in Eqs. (7-14):

<u>*i*=1</u>:

$$\mathbf{F}_1 = m_1 \dot{\mathbf{v}}_1^{cm} = m_1 \left( \begin{bmatrix} -a_1 s_1 - r_{y1} \\ a_1 c_1 + r_{x1} \\ 0 \end{bmatrix} \ddot{q}_1 + \begin{bmatrix} -a_1 c_1 - r_{x1} \\ -a_1 s_1 - r_{y1} \\ 0 \end{bmatrix} \dot{q}_1^{\,2} + \begin{bmatrix} 0 \\ 0 \\ -g \end{bmatrix} \right) \tag{7}$$

$$\mathbf{N}_1 = \mathbf{I}_1^{cm} \cdot \dot{\boldsymbol{\omega}}_1 + \boldsymbol{\omega}_1 \times (\mathbf{I}_1^{cm} \cdot \boldsymbol{\omega}_1) = \begin{bmatrix} 0 \\ 0 \\ \hat{I}_{z1} \end{bmatrix} \ddot{q}_1 \tag{8}$$

<u>*i*=2:</u>

$$\mathbf{F}_2 = m_2\left(\begin{bmatrix} -a_1 s_1 - r_{y2} \\ a_1 c_1 + r_{x2} \\ 0 \end{bmatrix}\ddot{q}_1 + \begin{bmatrix} -r_{y2} \\ r_{x2} \\ 0 \end{bmatrix}\ddot{q}_2 + \begin{bmatrix} -a_1 c_1 - r_{x2} \\ -a_1 s_1 - r_{y2} \\ 0 \end{bmatrix}\dot{q}_1^{\,2} + \begin{bmatrix} -r_{x2} \\ -r_{y2} \\ 0 \end{bmatrix}\dot{q}_2^{\,2} + 2\begin{bmatrix} -r_{x2} \\ -r_{y2} \\ 0 \end{bmatrix}\dot{q}_1\dot{q}_2 + \begin{bmatrix} 0 \\ 0 \\ -g \end{bmatrix}\right) \tag{9}$$

$$\mathbf{N}_2 = \mathbf{I}_2^{cm}\,\dot{\boldsymbol{\omega}}_2 + \boldsymbol{\omega}_2 \times (\mathbf{I}_2^{cm}\ \boldsymbol{\omega}_2) = \begin{bmatrix} 0 \\ 0 \\ \hat{I}_{z2} \end{bmatrix}(\ddot{q}_1 + \ddot{q}_2)\,. \tag{10}$$

<u>*i*=3:</u>

$$\begin{aligned}\mathbf{F}_3 = m_3\Bigg(&\begin{bmatrix} -a_1 s_1 - r_{y3} \\ a_1 c_1 - r_{x3} \\ 0 \end{bmatrix}\ddot{q}_1 + \begin{bmatrix} -r_{y3} \\ -r_{x3} \\ 0 \end{bmatrix}\ddot{q}_2 + \begin{bmatrix} -c_{1+2} r_{z3} \\ -s_{1+2} r_{z3} \\ c_{1+2} r_{x3} + s_{1+2} r_{y3} \end{bmatrix}\ddot{q}_3 + \begin{bmatrix} -a_1 c_1 \\ -a_1 s_1 \\ 0 \end{bmatrix}\dot{q}_1^{\,2} \\ &+2\begin{bmatrix} s_{1+2} r_{z3} \\ -c_{1+2} r_{z3} \\ c_{1+2} r_{y3} - s_{1+2} r_{x3} \end{bmatrix}(\dot{q}_1 + \dot{q}_2)\dot{q}_3 + \Bigg(\begin{bmatrix} -r_{x3} \\ -r_{y3} \\ 0 \end{bmatrix}(\dot{q}_1 + \dot{q}_2)^2 + \begin{bmatrix} -c_{1+2}(c_{1+2} r_{x3} + s_{1+2} r_{y3}) \\ -s_{1+2}(c_{1+2} r_{x3} + s_{1+2} r_{y3}) \\ -r_{z3} \end{bmatrix}\dot{q}_3^{\,2} + \begin{bmatrix} 0 \\ 0 \\ -g \end{bmatrix}\Bigg)\end{aligned} \tag{11}$$

$$\begin{aligned}\mathbf{N}_3 = &\begin{bmatrix} -I_{xz3} \\ -I_{yz3} \\ I_{z3} \end{bmatrix}(\ddot{q}_1 + \ddot{q}_2) + \begin{bmatrix} I_{xy3} c_{1+2} + I_{x3} s_{1+2} \\ -I_{y3} c_{1+2} - I_{yx3} s_{1+2} \\ I_{zy3} c_{1+2} - I_{zx3} s_{1+2} \end{bmatrix}\ddot{q}_3 + \begin{bmatrix} c_{1+2}(I_{x3} + I_{y3} - I_{z3}) \\ s_{1+2}(I_{x3} + I_{y3} - I_{z3}) \\ -2(I_{zx3} c_{1+2} - I_{zy3} s_{1+2}) \end{bmatrix}(\dot{q}_1 + \dot{q}_2)\dot{q}_3 + \begin{bmatrix} I_{zy3} \\ -I_{xz3} \\ 0 \end{bmatrix}(\dot{q}_1 + \dot{q}_2)^2 \\ &+\begin{bmatrix} c_{1+2}(I_{zx3} s_{1+2} - I_{zy3} c_{1+2}) \\ s_{1+2}(-I_{zy3} c_{1+2} - I_{zx3} s_{1+2}) \\ I_{xy3} + c_{1+2} s_{1+2}(I_{x3} - I_{y3}) \end{bmatrix}\dot{q}_3^{\,2}\end{aligned} \tag{12}$$

<u>*i*=4:</u>

$$\begin{aligned}\mathbf{F}_4 = m_4\dot{\mathbf{v}}_4^{cm} = &\begin{bmatrix} 0 \\ 0 \\ -g \end{bmatrix} + \begin{bmatrix} -a_1 s_1 - r_{y4} \\ a_1 c_1 + r_{x4} \\ 0 \end{bmatrix}\ddot{q}_1 + \begin{bmatrix} -r_{y4} \\ r_{x4} \\ 0 \end{bmatrix}\ddot{q}_2 + \begin{bmatrix} -c_{1+2} r_{z4} \\ -s_{1+2} r_{z4} \\ (c_{1+2} r_{x4} + s_{1+2} r_{y4}) \end{bmatrix}\ddot{q}_3 + \begin{bmatrix} -s_3 r_{y4} + s_{1+2} c_3 r_{z4} \\ -c_3 c_{1+2} r_{z4} + s_3 r_{x4} \\ c_3(c_{1+2} r_{y4} - s_{1+2} r_{x4}) \end{bmatrix}\ddot{q}_4 \\ &+\begin{bmatrix} -a_1 c_1 - r_{x4} \\ -a_1 s_1 - r_{y4} \\ 0 \end{bmatrix}\dot{q}_1^{\,2} + \begin{bmatrix} -r_{x4} \\ -r_{y4} \\ 0 \end{bmatrix}\dot{q}_2^{\,2} + \begin{bmatrix} -c_{1+2}(c_{1+2} r_{x4} + s_{1+2} r_{y4}) \\ -c_{1+2} s_3 r_{z4} - c_{1+2} s_{1+2} r_{x4} - s_{1+2}^2 r_{y4} \\ -r_{z4} \end{bmatrix}\dot{q}_3^{\,2} + 2\begin{bmatrix} -r_{x4} \\ -r_{y4} \\ 0 \end{bmatrix}\dot{q}_1\dot{q}_2 + 2\begin{bmatrix} -c_{1+2} c_3(s_{1+2} r_{x4} - c_{1+2} r_{y4}) \\ s_{1+2} c_3(s_{1+2} r_{x4} - c_{1+2} r_{y4}) \\ s_3(s_{1+2} r_{x4} - c_{1+2} r_{y4}) \end{bmatrix}\dot{q}_1\dot{q}_3 \\ &+2\begin{bmatrix} s_{1+2} r_{z4} \\ -c_{1+2} r_{z4} \\ 0 \end{bmatrix}(\dot{q}_1 + \dot{q}_2)\dot{q}_3 + 2\begin{bmatrix} c_3 c_{1+2} r_{z4} - s_3 r_{x4} \\ -s_3 r_{y4} \\ 0 \end{bmatrix}(\dot{q}_1 + \dot{q}_2)\dot{q}_4 + \begin{bmatrix} c_3 c_{1+2} s_3 r_{z4} - s_3^2 r_{x4} + c_3^2 c_{1+2} s_{1+2} r_{y4} - c_3^2 s_{1+2}^2 r_{x4} \\ -c_3^2 c_{1+2}^2 r_{y4} - s_3^2 r_{y4} + c_3^2 c_{1+2} s_{1+2} r_{x4} \\ -c_3^2 c_{1+2}^2 r_{z4} + c_3 c_{1+2} s_3 r_{x4} + c_3 s_3 s_{1+2} r_{y4} \end{bmatrix}\dot{q}_4\dot{q}_4]\end{aligned} \tag{13}$$

$$\mathbf{N}_4 = \begin{bmatrix} -I_{zz4} \\ -I_{yz4} \\ I_{z4} \end{bmatrix} \ddot{q}_1 + \begin{bmatrix} -I_{xz4} \\ -I_{yz4} \\ I_{z4} \end{bmatrix} \ddot{q}_2 + \begin{bmatrix} (I_{xy4}c_{1+2} + I_{x4}s_{1+2}) \\ (-I_{y4}c_{1+2} - I_{xy4}s_{1+2}) \\ (I_{yz4}c_{1+2} - I_{xz4}s_{1+2}) \end{bmatrix} \ddot{q}_3 + \begin{bmatrix} c_3(I_{x4}c_{1+2} - I_{xy4}s_{1+2}) - I_{xz4}s_3 \\ c_3(-I_{xy4}c_{1+2} + I_{y4}s_{1+2}) - I_{yz4}s_3 \\ c_3(-I_{xz4}c_{1+2} - I_{yz4}s_{1+2}) + I_{z4}s_3 \end{bmatrix} \ddot{q}_4 + \begin{bmatrix} c_{1+2}(I_{x4} - I_{z4} + I_{y4}) \\ s_{1+2}(I_{y4} - I_{z4} + I_{x4}) \\ -2I_{xz4}c_{1+2} - 2I_{yz4}s_{1+2} \end{bmatrix} (\dot{q}_1 + \dot{q}_2)\dot{q}_3$$

$$+ \begin{bmatrix} -c_3 s_{1+2}(I_{x4} - I_{z4} + I_{y4}) + 2I_{yz4}s_3 \\ c_3 c_{1+2}(I_{y4} - I_{z4} + I_{x4}) - 2I_{xz4}s_3 \\ 2c_3(s_{1+2}I_{xz4} - c_{1+2}I_{yz4}) \end{bmatrix} (\dot{q}_1 + \dot{q}_2)\dot{q}_4 + \begin{bmatrix} c_{1+2}s_3((-I_{x4} + I_{y4} - I_{z4}) + 2I_{xy4}s_3 s_{1+2} - I_{xz4}c_3((s_{1+2}^2 - c_{1+2}^2) + 1) + 2I_{yz4}c_3 s_{1+2}c_{1+2} \\ -s_3 s_{1+2}(I_{y4} + I_{z4} - I_{x4}) + 2I_{xy4}s_3 c_{1+2} - I_{yz4}c_3(-(c_{1+2}^2 - s_{1+2}^2) + 1) + 2I_{xz4}c_3 s_{1+2}c_{1+2} \\ c_3(I_{z4} - (c_{1+2}^2 - s_{1+2}^2)(I_{y4} - I_{x4})) - 4I_{xy4}c_3 s_{1+2}c_{1+2} \end{bmatrix} \dot{q}_3\dot{q}_4 \quad (14)$$

$$+ \begin{bmatrix} I_{yz4} \\ -I_{xz4} \\ 0 \end{bmatrix} (\dot{q}_1 + \dot{q}_2)^2 + \begin{bmatrix} -c_{1+2}(I_{yz4}c_{1+2} - I_{xz4}s_{1+2}) \\ -s_{1+2}(I_{yz4}c_{1+2} - I_{xz4}s_{1+2}) \\ I_{xy4}(c_{1+2}^2 - s_{1+2}^2) + s_{1+2}c_{1+2}(I_{x4} - I_{y4}) \end{bmatrix} \dot{q}_3^2 + \begin{bmatrix} c_3 s_3(s_{1+2}(-I_{y4} + I_{z4}) + I_{xy4}c_{1+2}) - I_{xz4}c_3^2 s_{1+2}c_{1+2} + I_{yz4}(s_3^2 - s_{1+2}^2 c_3^2) \\ c_3 s_3(c_{1+2}(I_{x4} - I_{z4}) - I_{xy4}s_{1+2}) + I_{xz4}(c_3^2 c_{1+2}^2 - s_3^2) + I_{yz4}c_3^2 s_{1+2}c_{1+2} \\ -c_3^2(I_{xy4}(c_{1+2}^2 - s_{1+2}^2) - c_{1+2}s_{1+2}(I_{x4} - I_{y4})) - s_3 c_3(I_{yz4}c_{1+2} - I_{xz4}s_{1+2}) \end{bmatrix} \dot{q}_4^2$$

## 4. Conclusion

In this paper the dynamic analysis of the SDT is presented. The SDT is modelled as a four-joint revolute robotic manipulator. A recursive Newton-Euler algorithm was used for the determination of forces and moments. The recursive NE method appears more efficient than the Lagrange method, by referring forces and moments to local link coordinates for real-time control. The associated equations and matrices have been given using a common, concise notation. Total forces and moments for each axis are determined. Direct dynamics is used for robot simulations, whereas inverse dynamics is used for solving problems considering robot control. The inertia matrix is used in analysis, in feedback control to linearize the dynamics. The SDT dynamics is very important for the SDT robot design, and the selection of the drive and control system.

*Acknowledgement.* This research is supported by the Ministry of Education, Science and Technological Development of Serbia "Development of devices for pilot training and flight simulation of modern combat aircraft, 3DoF Human Centrifuge and 4DoF Spatial Disorientation Trainer".

## 5. References

[1] Dančuo Z., Rašuo B., Kvrgić V., Vidaković J., Džinić Nj., (2013) Kinematska analiza uređaja za prostornu dezorijentaciju pilota, *Tehnika Mašinstvo*, 2/2013
[2] Craig, J.J., (1986) *Introduction to Robotics*, *Mechanics and Control*, Addison-Wesley Publishing Company
[3] Duda, K., (2002) Spatial Disorientation, Humans and Automation Journal Club (internet source) http://web.mit.edu/16.459/www/AvTrain2.pdf
[4] Dančuo, Z., Rašuo, B., Zeljković, V., Kvrgić, V.,(2012) Methodology of the Main Drive Selection for a Human Centrifuge, FME Transactions vol. 40. No 2, pp.
[5] Antunano, M., Medical facts for pilots Spatial Disorientation, Publication: AM-400-03/1, FAA
[6] Rajat Baijal, Jha, VN, Sinha, Simulator based Spatial Disorientation training in the Indian Air Force,
[7] Estrada, A., Adam, G., Leduc, P.,(2002) Use of Simulator Spatial Disorientation Awareness Training Scenarios by the U.S. Army and National Guard, Symposium "Spatial Disorientation in military vehicles: Causes, consequences and cures", La Coruna, Spain.
[8] Cheung, B., (1998) Recommendations to enhance Spatial *Disorientation Training for the Canadian Forces,* Defence and Civil Institute of Environmental Medicine, Canada
[9] Stepanenko, Y., Vukobratović, M., (1976) Dynamics of Articulated Open-chain Active Mechanisms, *Mathematical Biosciences*, vol. 28.

# INTEGRITY ASSESSMENT FOR TANK WITH CRACKS IN WELDED JOINTS

**Katarina Jovičić[1], Radomir Jovičić[2], Milan Prokolab[1], Bore Jegdić[1]**

[1] Institute Goša d.o.o.
Milana Rakića 35, Belgrade, Serbia
e-mail: katarina.jovicic@institutgosa.rs

[2] Innovation Centre of the Faculty of Mechanical Engineering,University of Belgrade,
Kraljice Marije 16, Belgrade,
e-mail: rjovicic@mas.bg.ac.rs

**Abstract.** During the exploitation of the tank for liquid carbon dioxide the need for installation of two new connections on the head of the vessel appeared. In the heat-affected zone of welded joints, micro cracks were found by using nondestructive testing. These micro cracks can lead to tank failure during its further exploitation
In this paper, the influence of micro cracks on the integrity of welds, therefore on the integrity of the tank, was estimated using the standard BSI PD 6493. Nondestructive testing for data dimensions of micro cracks, were used. In addition, the data of material properties, obtained examinations of samples in which welding thermal cycle was simulated in certain parts of the heat-affected zone, were utilized. It was concluded that the detected micro cracks do not put at risk further tank's safe operation.

**Keywords**: micro cracks, integrity, weld, tank

## 1. Introduction

There was a need for installation of the two new connections, in it's upper of the reservoir head, during the exploitation. The reservoir is in form of the vertical tank for storage the liquefied carbon dioxide. The connectors are designed to connect the external unit of freon and internal heat exchanger.

## 2. Installation Of The Connections

The tank is cylindrical, thermally insulated, pressure vessel by volume of 25m$^3$ and 12 mm thick. It is made of microalloyed steel P460 NL1. Other basic reservoir data are: maximum working pressure is 25 bar, test pressure is 32.5 bar, the lowest operating temperature is -50°C, the outer diameter is 2000 mm, overall height is 10080 mm and class of the pressure vessel is II [1]. There were used the same materials and welding technology as manufacturer to made the new connections [1]. The high alloyed austenitic stainless steel X6CrNiTi 18 10 was used. According to the calculation [2], for the exploatation pressure in the tank and heat exchanger, fitting diameters of the connections are 26.9 mm and wall thicknesses are 2.6 mm. Groove shape and dimensions are shown in figure 1.

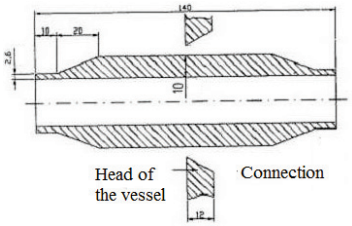


**Figure 1.** Shape and dimensions of reinforcement connection and groove of welded joint

It was adopted, that reinforced connections will be welded at the head of the vessel with approximate thickness as a head of the vessel, figure 1, and then, the pipes will be welded to the connections. The new connections are welded by E procedure, with rutile coated electrode E 29 9 R 12 (standard EN 1600). The chemical composition and mechanical properties of the basic and filler material are given in [3,4] and tables 1 and 2.

**Table 1.** Chemical composition of basic and filler material (%)

| | C | Si | Mn | P | S | Cr | Ni | Al | Ti |
|---|---|---|---|---|---|---|---|---|---|
| P460NL1 | ≤ 0,20 | 0,40 | 1,45 | ≤0,02 | ≤0,02 | - | - | ≥0,02 | - |
| X6CrNiTi 18 10 | ≤ 0,08 | ≤ 1,0 | ≤ 2,0 | ≤0,035 | ≤0,025 | 17,0-19,0 | 9,0 - 11,0 | - | 5x% C |
| E29 9 R 12 | 0,15 | ≤0,9 | 0,9 | - | - | 29 | 9 | - | - |

**Table 2**. Mechanical properties of basic and filler material

| | Yield stress $R_{p0,2\%}$ MPa min. | Tensile strength $R_m$ MPa | Elongation $A_5$ % min. | Toughness ISO – V min. |
|---|---|---|---|---|
| P460NL1 | 470 | 540 - 740 | 19 | 27 J na - 40°C |
| X6CrNiTi 18 10 | 205 | 490 - 740 | 40 | 27 J na - 40°C |
| E29 9 R 12 | 500 | 740 – 840 | 20 | 27 J on - 40°C |

## 3. Testing results of the welded joints

Regulations [5,6] provide that, after welding, the welded joints of new connections must be examine by the non-destructive methods (NDT). The required quality level of the welded joints is C class [7]. Significantly errors are not detected, except the minor edge cuts of an acceptable size, by above metods [8]. The prescribed NDT method, in the case of welded joints between micro-alloyed and high-alloyed steels, does not always give a confidential results [9] and replica method and hardness test are included. At each of the connections, one replica was made, so that implied the basic material (BM) of the vessel head, its heat affected zone (HAZ) and weld (W). Microstructural testing [8] was found that:

- Material of the head has nonhomogeneous arrangement of micro constituents, much larger grain than is typical for microalloyed steels, the proportion of pearlite is higher than expected for this type of steel and alignment of inclusions in the rolling direction was observed. This suggest that the production process of this steel was not carried out with optimal parameters.
- HAZ microstructures of both connections are bainitic structure, with relatively fine grain. There was no appearance of martensite structure.
- In abrasive grain part of the HAZ microcracks are detected, in both connections. Figure 2. shows three microcracks, close to each other, so it could be assumed, that these are remnants of a larger microcrack, which was partially removed by grinding the surface, during the preparation for metallographic examination.

- The both welds have austenite structure with about 25% of δ - ferrite. White surface, Figure 2., represents nonetched austenitic weld. Line, that separates the white area and surface with microcracks, represents the fusion line between the weld and microalloyed steel.

The hardness of material were measured by portable Vickers method, on tested microstructure, polished and etched surface [8]. There were determinated precisely defined mesurement locations, based on differences in coloration of the BM, HAZ and W. Hardness of 184 HV on the BM, and 215 to 345 HV on the HAZ were measured.

**Figure 2**. Microcracks in the HAZ of the connections welded joints

## 4. Microcracks evaluation of acceptability

Replica method was discovered a number of microcracks. Removal of microcracks, by cutting and re-welding the connections, do not guarantee that these will not appear again. Therefore, it is estimated the impact of existing microcracks on the integrity of welds connections. For this estimate procedure, the literature [9] was used. Based on the description of microcracks and Figure 2., it can be concluded, that it is a superficial cracks that lie in the plane, upright to the direction of main stress. The all three microcracks, due to the small mutual distances, will be treated as a semielliptical superficial cracks. Figure 2. shows somewhat modify shape and dimensions of microcracks, in relation to the situation right away after welding, because of the removal of the surface layer, thickness of about 0.5 mm, during the preparation of the surface for metallographic examination. The deepness was estimated based on the results of NDT, which were made before preparation of the surface for metallographic testing. Microcracks were not uncovered by ultrasonic testing. It can be concluded, that the deepness of microcracks is less than 1 mm. The results by penetrant confirm, that there are no cracks of larger deepness. Based on these findings, for the calculation was adopted, the deepness of cracks a = 1 mm, although, it is probably less in reality. Estimation of fracture risk with slightly larger than the actual deepness of the cracks, gives more reliable end result. Estimate of crack length is equal to the total crack length of the microcracks and the space between them, increased per shortening the length of microcracks in metallographic preparation, figure 2. Figure 2. shows that the total length of microcracks and space between them is 1.6 mm. It can be estimated, by figure 3., that the shortening of the metallographic preparation per about 0.5 mm at both ends of the crack.

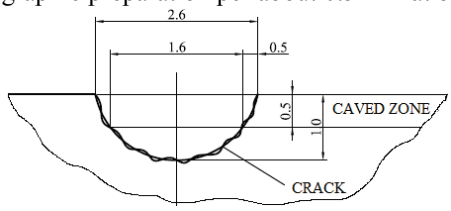


**Figure 3**. Dimensions of cracks in HAZ of joint connection by calculation

Based on the above, adopted crack length is 2c = 2.6 mm by calculation. Can be distinguish two regimes where the tank may be exposed. One is in the internal pressure test

and the other is in working conditions. In testing by internal pressure, the test medium is water, on temperature 10-20°C and test pressure is 32.5 bar. The working conditions of the tank are the temperature from -20°C to -30°C, and the pressure from 20 to 14 bar. In more critical terms of measurement is examination on internal pressure, taking into account that the temperature drop decreases stress in the wall of the tank, decreases toughness of the material, but not below the minimum guaranteed value (27J) and that, to some extent, grows strength of the material. Document PD 6493 [10] provides the three levels of risk assessment of fracture, depending on the capabilities and accuracy of stresses measurement acting near the crack tip. In this case, the risk of fracture will be assessed on the basis of the level II. For the application of level II, it is necessary to know the values of the parameters $S_r$ and $K_r$ or $\delta_r$. $S_r$ parameter was calculated from the expression:

$$S_r = \sigma_n/\sigma_f \quad (1)$$

where $\sigma_n$ is effective stress in the net range, and $\sigma_f$ is stress hardening of material, i.e. half of the sum the yield strength $\sigma_y$ and tensile strength $\sigma_m$, and for the rating level II takes up 1.2 $\sigma_y$. Effective stress in the cross section was calculated from the expression:

$$\sigma_n = 1{,}2\ M_s\ P_m \quad (2)$$

where $P_m$ is stress membrane due to the pressure in the tank, and $M_s$ is coefficient of shape. Stress of the membrane was determined by the expression:

$$P_m = p\ D/4\ B \quad (3)$$

where p = 32.5 bar is test pressure; D = 2000 mm is outer head diameter of the vessel; and B = 12 mm is wall thickness of the vessel head; so the Pm = 135 MPa. $M_s$ coefficient of shape was calculated from the expression:

$$M_s = 1 - (a/BM_t)/1 - (a/B)$$

where B = 12 mm, a = 1 mm was estimated deepness of crack; c = 1.3 mm half length of crack and the factor

$$M_t = [1 + 3{,}2\ (c^2/DB)]^{0,5}$$

It was calculated the following values: $P_m$ = 135 MPa; $M_t$ = 1,00; $M_s$ = 1,00; $\sigma_n$ = 162 MPa. It was not possible to determine precisely, by the replica method, where in the temperature zone of the HAZ the crack tip is located. Therefore, the integrity of the welded joints will be evaluated for two cases, the first zone of maximum strength and the lowest toughness (A) and the second zone of the lowest strength and maximum toughness (B). The important results, obtained by examinations, of samples where the simulated welding thermal cycle in certain parts of the HAZ of steel P460 NL1, are given in the literature [11] and in table 3.

**Table 3.** Crack opening of each zone HAZ of steel P460NL1

| Temperature of simulation,°C | 1350 | 1100 | 950 | 850 |
|---|---|---|---|---|
| Yield stress $\sigma_y$, MPa | 1101 | 943 | 818 | 660 |
| Tensile strength $\sigma_m$, MPa | 1101 | 1189 | 1036 | 936 |
| Crack opening $\delta_c$ (20°C), mm | 0,007 | 0,002 | 0,164 | 0,130 |

Regulation [10] provides that, in cases when the fracture are moderate, the stress, that is in any case estimated, is multiplied by the safety factor 1.2, and the stress that is measured, is multiplied by safety factor 1.1. For:

- Case A, the temperature zone 1350°C, $\sigma_f = (\sigma_y + \sigma_m)/2$ = 1101 MPa, where $\sigma_y$ = 1101MPa, $\sigma_m$ = 1101 MPa; substituting in (1) $S_{rA} = 1{,}2 \cdot 162/1{,}1 \cdot 1101 = 0{,}161$
- Case B, the temperature zone 850°C, $\sigma_f = (\sigma_y + \sigma_m)/2$ = 798 MPa, where $\sigma_y$ = 660MPa, $\sigma_m$ = 936 MPa; substituting in (1) $S_{rB} = 1{,}2 \cdot 162/1{,}1 \cdot 798 = 0{,}221$

The value of the crack opening $\delta_r$ for level II, was calculated from the expression:

$$\sqrt{\delta_r} = \sqrt{(\delta_I/\delta_{mat})} + \rho \quad (4)$$

where $\delta_I$-acting opening of crack, which was calculated from the expression

$$\delta_I = K_I^2/\sigma_y E \quad (5)$$

$K_I$ - stress intensity factor, $\delta_{mat}$ - critical crack opening of material ($\delta_c$), $\rho$ - the correction factor due to the interaction of the primary and secondary stress and E - modul of elasticity of steel. Stress intensity factor of the superficial cracks was calculated by expression:

$$K_I = (M_m/\Phi)\sigma_I\sqrt{(\pi a)} \quad (6)$$

where $M_m$ is enlargement factor of stress, which takes into account the shape of the crack, [10], $\Phi$ is elliptic integral, [10]. For the crack of length 2c = 2.6 mm and a depth = 1mm, which is located in the wall thicknesses B = 12 mm is $M_m = 1.03$, $\Phi = 1.40$. The maximum tensile stress $\sigma_I$ is equal to the sum ($P_m + P_b + Q + F$), where $P_m$ is membrane stress, due to the pressure in the tank, $P_b$ - bending stress, as a consequence of the removal of the groove edges, Q - secondary stresses, which include residual stresses in the welded joints and thermal stresses, F - peaks stresses, that occur due to stress concentration at the sites of local discontinuity. Visual inspection was determined that no removal and sharp transition from the face of the weld to the base metal, so that Pb and F will be ignored. Examination of the test specimens WM [12], which is welded in the same manner as reviewed welded joints, the yield strength of 550 MPa was obtained. Yield strength of the components of the vessel head in which the connections are fitted, is 490 MPa [1]. The total tensile stress $\sigma_I$ in this case, is equal to the sum of membrane stress $P_m$ = 135 MPa and residual stress Q = 490 MPa, ie. equal to 625 MPa. Substituting the expression (6), it was obtained:

$$K_I = (1{,}03/1{,}40)\ 625\sqrt{(\pi \cdot 1{,}0)} = 814 \text{ MPa } \sqrt{\text{mm}}$$

Substituting the expression (5), it was obtained for the case:

- A, temperature zone 1350°C, $\delta_{IA} = 814^2/1101 \cdot 207000 = 0{,}003$; where $K_I$ = 814 MPa$\sqrt{\text{mm}}$, $\sigma_{yA}$ = 1101 MPa, E = 207 GPa,
- B, temperature zone 850°C, $\delta_{IB} = 814^2/660 \cdot 207000 = 0{,}005$; where $K_I$ = 814 MPa$\sqrt{\text{mm}}$, $\sigma_{yB}$ = 660 MPa, E = 207 GPa.

Critical values of $\delta c$ for considered temperature zones are given in Table 3. The correction factor $\rho$, according to [10], has a value close to zero. From equation (4) follows:

- For zone A, $\sqrt{\delta_{rA}} = (0{,}003/0{,}007)^{0,5} = 0{,}655$; where $\delta_{IA} = 0{,}003$ i $\delta_{mat} = \delta_c = 0{,}007$ mm,
- For zone B, $\sqrt{\delta_{rB}} = (0{,}005/0{,}130)^{0,5} = 0{,}196$; where $\delta_{IB} = 0{,}005$ i $\delta_{mat} = \delta_c = 0{,}130$ mm,

Entering values of $S_r$ and $\sqrt{\delta_r}$, for both cases, in the diagram for the assessment of fracture, figure 4., get the points that are in the zone where the risk of failure do not exists.

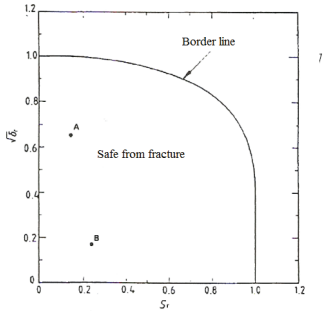


**Figure 4**. Diagram of fracture assessment for Level II

The presence of other microcracks near the fusion line, increases the probability of the growth of considered microcracks in the lateral direction. Increasing the crack length,

increases the value of the stress intensity factor, crack opening, and the parameter, which moving the points A and B towards the borderline risk of fracture, figure. 4. The growth of microcracks, in direction perpendicular to the plate of surface, is less likely. If the crack propagates in the direction perpendicular to the plate surface, its tip moves from the roughly-grain structure to the structure of fine grain of HAZ and then, in the fine grain structure of the BM. If crack grows in the HAZ plane of propagation, then the angle, between the plane of crack propagation and the direction of main stress decreases and the applied stresses also reduces. Figure 5. shows the distribution of residual stress according to the thickness of sheet metal in the case of double-sided welds with full penetration of the welding. The figure shows that the largest residual stresses are on the sheet surface and at a depth of about 20% of the thickness becomes approximately zero [10]. Because, possibility of the cracks growth in the lateral direction can not be excluded, periodically control by NDT methods of the welded joints on new connections is necessary.

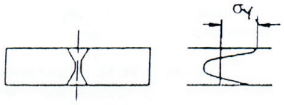


**Figure 5**. The distribution of residual stress that acting in the direction of plate thickness

## 5. Conclusions

1. Using the procedure for assessing the acceptability of defects in welded joints given in BSI PD 6493 was estimated that microcracks, detected in the HAZ of connections the tank for storage of liquid carbon dioxide, does not endanger its safe work, the reservoir is released into the further exploitation with these microcracks.
2. A certain insecurity in assessing the acceptability of microcracks, brings a limitations in NDT of the welded joints between the micro-alloyed and stainless steels.
3. The risk of fracture, strongly depends in which part of the HAZ is located the crack tip. High-temperature parts of the HAZ, steel P 460 NL1, have low values of the critical crack opening $\delta_c$, when could be expected growth of microcracks in the lateral direction.
4. It is anticipated, that during the operation of the tank, the welded joints must be periodically examined by NDT methods, because of the potential growth of microcracks.

## References

[1] Tehnička dokumentacija rezervoara, tip SRU V25, f.b. 1503, proizvođač TPO Goražde, 1983.
[2] Projekat ugradnje freonske jedinice u rezervoar za skladištenje tečnog ugljendioksida, Messer Tehnogas AD Inženjering, Beograd, 2001.
[3] Toplo valjani limovi, Katalog proizvoda, Železarna Jesenice, 1990
[4] Dodatni materijali za zavarivanje, Katalog proizvoda, Železarna Jesenice, 1990
[5] Pravilnik o tehničkim noramtivima za stabilne posude pod pritiskom, Službeni list SFRJ 16/83
[6] Standard SRPS M.E2.159 Posude pod pritiskom, Kontrola i ispitivanje zavarenih spojeva
[7] Tehnologija ugradnje priključaka za freonsku jedinicu u rezervoar za skladištenje tečnog ugljedioksida f.b. 1503, Mašinski fakultet u Beogardu, 2001.
[8] Elaborat o zavarivanju i ispitivanju priključaka za freonsku jedinicu na rezervoaru za skladištenje tečnog ugljedioksida f.b. 1503, Mašinski fakultet u Beogardu, 2003.
[9] R. Jovičić, R. Prokić Cvetković, O. Popović: Ograničenja u primeni metoda IBR na feritno austenitne zavarene spojeve na posudi pod pritiskom, Structural Integrity and Life, Vol. 5, No 3 (2005), pp 119 - 128
[10] S. Sedmak: Uputstvo za ocenu prihvatljivosti grešaka u zavarenim konstrukcijama PD 6493, Seminar za specijaliste za posude pod pritiskom, Tehnološko metalurški fakultet u Beogradu, Beograd, 1996.
[11] K. Gerić: Pojava i rast prslina u zavarenim spojevima čelika povišene čvrstoće, Doktorska disertacija, Tehnološko metalurški fakultet Univerziteta u Beogradu, Beograd, 1997.
[12] R. Jovičić: Analiza uticaja prslina na integritet feritno austenitnih zavarenih spojeva, Doktorska disertacija, Mašinski fakultet Univerziteta u Beogradu, Beograd, 2007.

# MOLECULAR DYNAMICS SIMULATION OF NANOSCALE TAYLOR TEST

**Sreten Mastilović**

Union – Nikola Tesla University, Faculty of Construction Management
Cara Dusana 62-64, Beograd, Serbia
e-mail: smastilovic@fgm.edu.rs

**Abstract.** A series of molecular dynamics simulations of the classical Taylor test is performed by using a monocrystalline nanoscale projectile made of the Lennard-Jones 2D solid. These atomistic simulations offer insight into nature of fragment distributions. According to simulation results, cumulative distribution of fragment sizes in the course of this non-homogeneous fragmentation process for hypervelocity impacts appears to be well represented by the bimodal-exponential distribution commonly observed during uniform fragmentation events. For lower impact velocities, the cumulative distribution of fragment sizes, in addition to the bimodal-exponential part, exhibits a large-fragment tail. Details of the cumulative fragment distribution, including the onset of the bimodal-exponential distribution "breakdown," are naturally highly dependent upon the impact energy. The breakdown threshold increases with increase of the impact velocity until it apparently disappears at hypervelocity level, which results in the bimodal-exponential distribution of fragments of a completely comminuted nano-projectile. The instantaneous kinetic temperature field and its temporal evolution are visualized for two impact velocities. It is observed that the disturbance propagation velocity for the plate-like impacts departs from a linear form of the equation of state in the hypervelocity impact region.

## 1. Introduction

This is a work in progress aiming at, perhaps elusive, goal to investigate temperature-related aspects of constitutive modeling to be used in the high-strain-rate mesoscale discrete simulations. A series of two-dimensional (2D) molecular dynamics simulations of the Taylor test is performed by using nanoscale projectiles made of the Lennard-Jones 6-12 (L-J) monocrystalline solid, matching, as close as possible, physical properties of tungsten ($_{74}$W). The three L-J model parameters used are the atomic mass $3.1\times10^{-25}$ kg (183.85 u), the atomic radius 1.4 Å, and the depth of the potential well (the strength of the attraction) $7.5\times10^{-20}$ J estimated based on the sublimation energy [1].

## 2. Simulation model

Molecular dynamics is a numerical simulation technique frequently used to study evolution of discrete systems at spatial and temporal scales that go beyond the current experimental limits. The present investigation is limited to the traditional molecular dynamics in which atomic interactions are defined by empirical potentials and atomic motions obey laws of

classical mechanics [2]. Specifically, a monoatomic, monocrystalline system (a flat-nosed projectile) is comprised of atoms of known masses $m$ that interact with their first-nearest neighbors according to the L-J potential. This approximation is based on the primacy of the short-range order and motivated by tremendous computational savings, but it cannot capture either surface energy (due to imperfect coordination of surface atoms) or effects of the background electron density of surrounding atoms. The system of Newton's differential equations of motion is solved by using the Verlet algorithm [2].

The estimate of temperature evolution during extreme dynamic events, which is of crucial analytical importance, gives rise to some basic questions related to fundamental thermostatic concepts such as entropy and absolute temperature of a system that is far from equilibrium. As pointed out by Callen [3], the nonequilibrium entropy definitions are dependent on uncertain premises. Thus, a consensus appears to be established over the last few decades that the most prudent approach is to use the Gibbs' temperature definition, familiar from the kinetic theory, $3k_B T/2 = \langle mv^2 \rangle / 2$, which has the firm statistical-mechanics foundations since it follows from the canonical ensemble maximum-probability distribution [4]. Hoover and coworkers [5] argued that this standard temperature definition can be extended and applied to any stable configuration, even far from equilibrium. Indeed, it is claimed that "in nonequilibrium situations, the instantaneous kinetic temperature is the only meaningful definition" [6]. Therefore, the term "*temperature*," whenever used henceforth, implies the "*instantaneous kinetic temperature*." Nonetheless, it should be kept in mind that "thermodynamic temperature ≡ long-time average of the instantaneous kinetic temperature at equilibrium" are the only rigorously defined equivalencies. Be it as it may, the temperature within an averaging area centered around $i$-th atom is defined as

$$T_i = \frac{m}{dN_i k_B} \sum_{j=1}^{N_i} \left( v_{xj}^2 + v_{yj}^2 \right), \quad \left( i = 1,..., N_{at} \right) \tag{1}$$

where $d$ is the dimensionality of the system (e.g., $d = 2$ in 2D), $N_i$ is the number of atoms of mass $m$ belonging to the averaging area, and $k_B$ is the Boltzmann's constant. Also, $v_x$ and $v_y$ are the vibrational velocity components obtained by subtracting the velocity of correlative motion from the total particle velocity. The velocity of correlative motion is obtained as the spatial average of total velocities of all atoms belonging to the averaging area. Thus defined quantity (1) is than averaged over a small time period in the usual manner.

## 3. Observations and discussion

The dynamic response of materials at high loading rates is inherently related to evolution of their microstructure. Defects at various scales, phase transformations, and their interplay govern the macroscopic behavior [7]. Some observations of dynamic response of the 2D L-J solid are presented below.

### *3.1. Distribution of fragment sizes*

Substantial literature exists in which the fundamental principles of dynamic fragmentation process were investigated both experimentally and theoretically [8][9]. Because of inherent

experimental complexity, laboratory fragmentation tests are not able to "differentiate unambiguously among the various competing geometric statistical theories" [9]. Holian and Grady [9] were first to use molecular dynamics to explore the fragmentation phenomena by simulating a homogeneous adiabatic expansion of condensed matter (dubbed the microscopic "big bang"). According to their results, the cumulative distribution of fragment masses is well represented by a bimodal-exponential (B-E) distribution and the average fragment mass can be explained by an energy balance between the kinetic energy of expansion and the potential energy of broken surface bonds.

One objective of the present set of simulations is to determine to what extent these results remain valid for a non-homogeneous fragmentation process caused by application of a highly *non-uniform* transient strain-rate field. The distribution of fragment sizes is studied, therefore, during the impact of a slender (35 × 411 atoms ≈ 10×100 nm), deformable L-J projectile with a rigid target. The results are presented in Table 1 and Figs. 1 and 2.

Table 1. Cumulative frequency of fragment size N (in number of atoms constituting a fragment) at the end state for seven impact velocities. (Note that the largest cluster corresponding to the arrested nano-projectile is not included in the statistics hereinafter.)

| | | $v_i$ [km/s] | | | | | | |
|---|---|---|---|---|---|---|---|---|
| | | **0.5** | **0.7** | **0.85** | **1.0** | **2.0** | **3.0** | **4.0** |
| **lnN=0** | N=1 | 167 | 547 | 939 | 1375 | 2542 | 3468 | 3147 |
| **0<lnN≤1** | N=2 | 21 | 86 | 114 | 193 | 580 | 767 | 814 |
| **1<lnN≤2** | 2<N≤7 | 12 | 53 | 97 | 131 | 450 | 661 | 653 |
| **2<lnN≤3** | 7<N≤20 | 1 | 6 | 16 | 31 | 144 | 207 | 182 |
| **3<lnN≤4** | 20<N≤55 | 0 | 2 | 6 | 16 | 50 | 70 | 38 |
| **4<lnN≤5** | 55<N≤148 | 0 | 0 | 9 | 11 | 20 | 12 | 10 |
| **5<lnN≤6** | 148<N≤403 | 0 | 4 | 6 | 10 | 10 | 1 | 6 |
| **6<lnN≤7** | 403<N≤1097 | 2 | 5 | 3 | 4 | 1 | 0 | 0 |

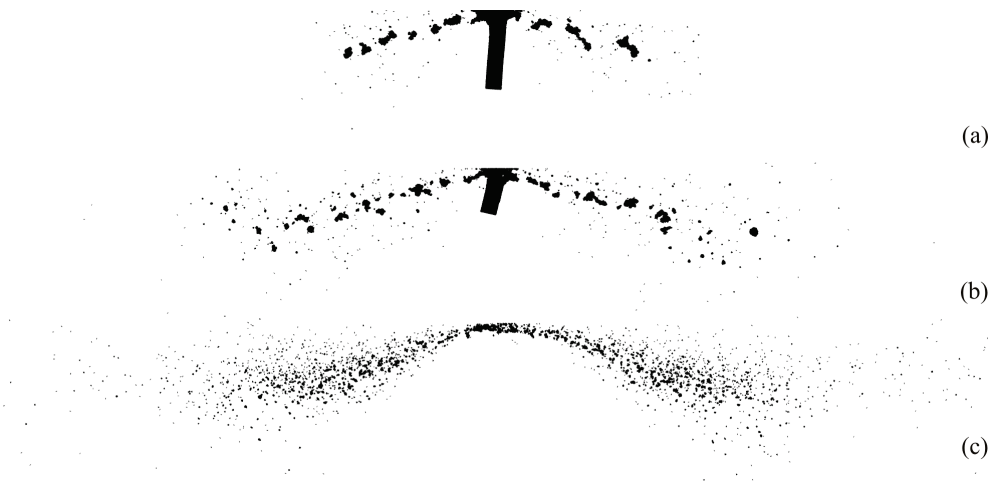


**Fig. 1.** Fragmentation snapshots of the simulation end state (defined by the stop of the projectile) for three impact velocities: (a) 0.7 km/s, (b) 1 km/s, and (c) 3 km/s.

In short, the simulation results suggest that the B-E distribution emerges in the smaller-clusters region for every impact velocity. For example, for $v_i = 0.7$ km/s the fragment size apparently obeys the B-E distribution up to the range of 25-30 atoms (Fig. 2), which implies that all larger fragments visible in Fig. 1(a) are outside of it. This is not surprising bearing in mind that the B-E distribution is obtained under the "big bang" simulation framework that largely precludes existence of the exceptionally large fragments. The onset of B-E distribution breakdown increases with the impact-velocity increase since more energy becomes available for creation of new surfaces. Simulation results for $v_i = 2$ km/s indicate the B-E-breakdown fragment size of approximately 50 atoms while for $v_i = 3$ km/s the breakdown seems to disappear, which might reflect the projectile annihilation illustrated by Fig. 1(c). The later may be caused by the projectile's kinetic energy sufficient to leads to adiabatic pulverization, similar to the Holian and Grady's "big bang" conditions [9].

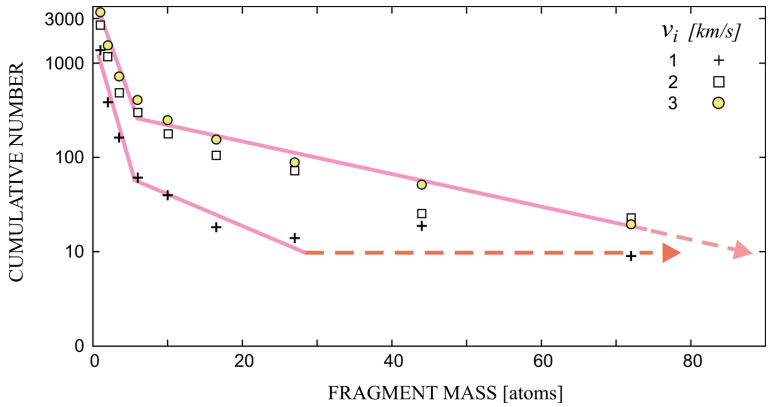


**Fig. 2.** Cluster statistics at the end state of 2D Taylor test for three impact velocities.

### *3.2. Temperature field*

The high-strain-rate deformation is often adiabatic, and the deformation work is transformed into heat with the attendant rise of temperature. As outlined by Meyers [8], this temperature increase has "a profound affect on the constitutive behaviour of the material because of the thermal softening, which may lead to shear instability."

The snapshots of temperature field evolution during the Taylor test at 0.7 km/s and 1.5 km/s are presented in Fig. 3 (53×429 atoms ≈ 15×120 nm). These illustrations demonstrate vividly the extreme temperature localization within a very narrow region of the contact zone. More detailed picture can be obtained from the corresponding isothermal maps. The time histories of temperature are also available at three selected measurement areas ("measurement gages"). The illustrations in Fig. 3 indicate that the melting temperature of 3695 K [1] is reached in the contact zone even for relatively modest impact velocities such as 0.7 km/s (albeit into the rigid target), which is consistent with experimental evidence pointing to melting in the contact zone. The implication of this result on the computational terminal ballistics is far reaching from the standpoint of hydrodynamic theory and selection of the appropriate friction coefficient in the contact zone for high-velocity impacts.

Examination of Fig. 3 reveals existence of vacancies, pores, and dislocations. The change of crystalline structure (suggesting, perhaps, phase transformations) can be noted as well, with the complete breakdown of crystalline regularity in the contact zone expected to accompany melting. Other fragment snapshots indicate a nonequilibrium state since most clusters are far from spherical. It should be recalled that if a material undergoes a phase transformation, the linear equation of state (EOS) is no longer applicable [8]. The present simulation results indeed suggest a departure from linearity at the high impact velocities.

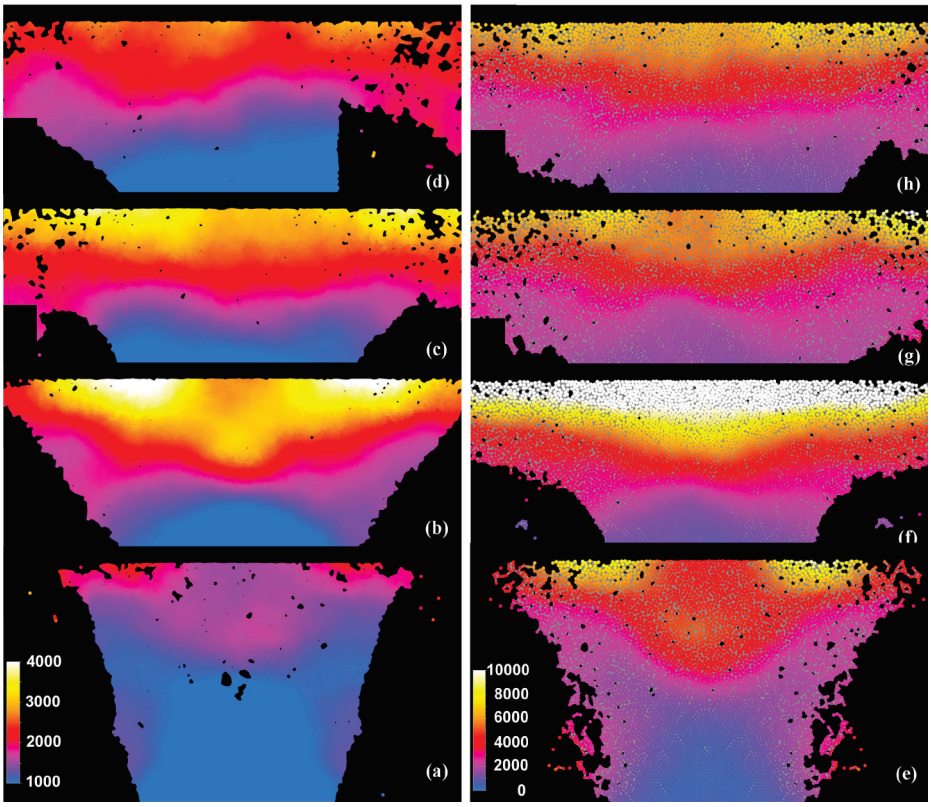


**Fig. 3.** Absolute temperature evolution during Taylor tests with $v_i = 0.7$ m/s (the left side; individual atoms blurred) and $v_i = 1.5$ km/s (the right side; individual atoms distinct). The snapshots correspond to the following time instances and number of fragments: (a) 10 ps and 10, (b) 20 ps and 11, (c) 50 ps and 84, (d) 100 ps and 397; (e) 5 ps and 23, (f) 15 ps and 168, (g) 20 ps and 258, (h) 50 ps and 1318. The end state is defined by the projectile stop at 172 ps and 114 ps, respectively.

### *3.3. Disturbance propagation velocity*

Three measurement areas are defined along the projectile's centreline close to the proximal end to mimic the stress and temperature measurement gages. The average velocity of disturbance propagation is defined herein as the ratio between the distance separating the first two measurement areas and the time lag between *compressive* stress pulse occurrences at the two locations. Simulations are performed for 10 impact velocities depicted in Fig. 4. The dimensions of the plate-like projectile are 69×9 nm (247×59 atoms).

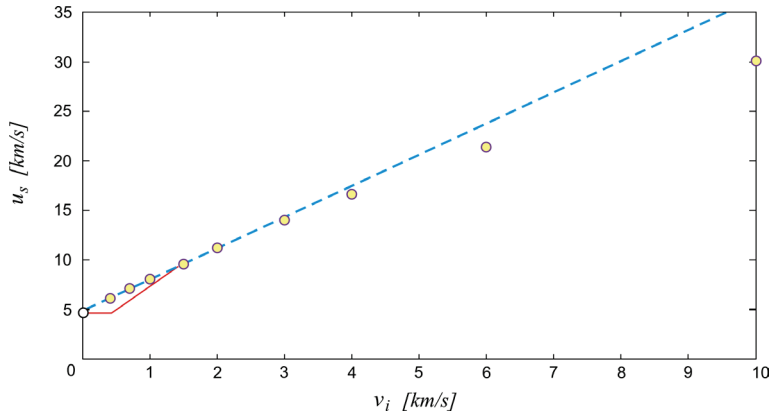


**Fig. 4.** Disturbance propagation velocity vs. impact velocity.

The simulation data plotted in Fig. 4 suggest that the disturbance propagation velocity follows initially the linear form of EOS, $u_s = C_0 + S\,u_p$, which is common for most metals [8]. Here, $u_s$ is the velocity of the shock front, $u_p$ is the particle velocity, $C_0$ is the sound velocity at zero pressure, and $S$ is the empirical parameter. The velocity of longitudinal elastic wave propagation is within 5-10% of the reported values [1][8]. A steadily increasing departure from linearity is observed in the hypervelocity range, which is consistent with the shock-induced phase transitions. Note the red solid line that shows schematically a peculiar small-scale phenomenon that occurs if the (minuscule) tensile ("pre-pull") stress pulse is account for at the smaller impact velocities. The simulations are repeated for three projectiles of the same mass (thus, the same impact energy at a given $v_i$) but different aspect ratios (10, 4, 1) to explore effects of the lateral inertial confinement.

*Acknowledgement.* Funding for this research was provided through the Serbian Ministry of Education and Science, under the grant OI 174010.

## References

[1] Weast R C (1976) *Handbook of Chemistry and Physics*, CRC Press, Cleveland.
[2] Allen M P and Tildesley D J (1987) *Computer Simulation of Liquids*, Oxford University Press, Oxford.
[3] Callen H B (1961) *Thermodynamics*, John Wiley & Sons, New York.
[4] Hoover W G (1985) Canonical dynamics: Equilibrium phase space distributions, *Physical Review A*, **31**, pp. 1695-1697.
[5] Hoover W G, Holian B L, Posch H A (1993) Comment on "Possible experiment to check the reality of a nonequilibrium temperature," *Physical Review E*, **48**: 3196-3198.
[6] Holian B L, Voter A F, Ravelo R (1995) Thermostatted molecular dynamics: how to avoid the Tada demon hidden in Nose-Hoover dynamics, *Physical Review E*, **52**, pp. 2338-2347.
[7] Bourne N K (2011) Materials' Physics in Extremes: Akrology, Metallurgical and Materials Transactions A, **42A**, pp. 2975-2984.
[8] Meyers M A (1994) *Dynamic Behavior of Materials*, John Wiley & Sons, New York.
[9] Holian B L and Grady D E (1988) Fragmentation by molecular dynamics: the micro-scopic "big bang". *Physical Review Lett*ers, **60**, pp. 1355-1358.

# DEFINITION AND INVESTIGATION OF OPERATION AND NONLINEAR STIFFNESS OF PULLING AND BUFFER DEVICES FOR LOAD AND RELAXATION PROCESS

**Drago Blagojević[1], Mladen Todić[2], Ostoja Miletić[3], Valentina Golubović-Bugarski[4]**

[1] University of BanjaLuka, Faculty of Mechanical Engineering,
e-mail: drago.blagojevic@unibl.rs
[2] University of BanjaLuka, Faculty of Mechanical Engineering,
e-mail: mladentodic@unibl.rs
[3] University of BanjaLuka, Faculty of Mechanical Engineering,
e-mail: ostoja.miletic@unibl.rs
[4] University of BanjaLuka, Faculty of Mechanical Engineering,
e-mail: valentina.gb@ unibl.rs

**Abstract.** Stiffness and operation of pulling and buffer elastic devices (bumpers) during load and relaxation processes are standardized values, depending on service conditions of technical system in which they are installed. This paper shows results of investigation and testing of the nonlinear stiffness and actual work of bumpers type A, capacity of 30 kJ and stroke of $105^{-5}$ mm. The bumper is mounted with 7 elastomer rings and 6 spacing steel rings. Pulling device has capacity of 20 kJ, stroke of 60 mm, with built-in 3 elastomer rings and two spacing steel rings. Intensity of accumulated and absorbed energy is the function of operating stroke. Stiffness under load has progressive character, but during relaxation has digressive character. Results are presented and compared for three successive tests, which provides overview of the energy dissipation of elastomer sets.

**Keywords:** bumper, pulling device, elastomer, nonlinear stiffness

## 1. Introduction

Stiffness and operation of pulling and buffer elastic devices (bumpers) during load and relaxation process are standardized values, depending on service conditions of technical system in which they are installed. Appropriate dynamic characteristics of these systems such as pulling and buffer elastic devices of different vehicles, must be held through longer period. Elastic steel elements (springs) embedded in these devices are recently replaced with sets of elastomer rings, which fulfill standardized dynamic requirements (pre-load force, load force, absorbed energy, accumulated energy, load speed). Very often, there is no audit or test of new-established static and dynamic characteristics of elastic device, which can cause the whole system operates in irregular regime. This work presents methodology and results of investigation of pulling and buffer devices having standardized characteristics for cargo wagons.

## 2. Design and investigation of bumpers (buffering devices)

Bumper has a built-in elastomer set „TecsPack" type 30, with 7 rings and 6 steel spacing rings forming compact assembly. Recommended mounting length of elastomer set is 302 mm. Table 1 shows standardized characteristics of elastomer set built in bumper, [1].

**Tabela 1.** Standarized characteristics of elastomer with 7 rings and 6 steel spacing rings

| Nominal value | 1. operating cycle | 3. operating cycle |
|---|---|---|
| Mounting force | 15 kN | 9 kN |
| Acumulated energy, We | 21,8 kJ | 17,7 kJ |
| Ratio between absorbed and acumulated energy, Wa/We | 0,55 | 0.47 |

Figure 1 shows operating elastomer assembly and bumper on the test table of laboratory presses.

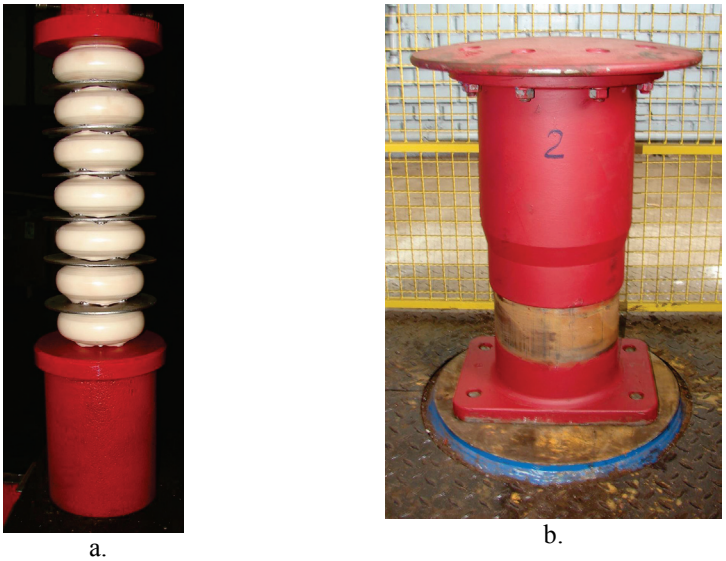


a. b.

**Figure 1.** Bumper assembly: a. Operating elastomer assmebly, b. Bumper on the test table

The investigation procedure of static characteristics of bumper with elastomer, stroke of 105 mm, for cargo wagons, has been done for 4 specimens and 3 measurements per specimen, at 0.016 m/s load speed. Diagram of the achieved work for the 1st measurement

is given in figure 2. A Comparative review of nominal physical values according to standard UIC 526-1 and measured values for 4 investigated bumpers are presented in table 2.

**Tabela 2** A Comparative review of nominal values according to standard UIC 526-1 and measured values for 4 investigated bumpers

| Nominal value | Values accord. to UIC 526-1 | Measured values | | | | | | | | | | | |
|---|---|---|---|---|---|---|---|---|---|---|---|---|---|
| | | Specimen 1 | | | Specimen 2 | | | Specimen 3 | | | Specimen 4 | | |
| | | 1. mea. | 2. mea. | 3. mea. | 1. mea. | 2. mea. | 3. mea. | 1. mea. | 2. mea. | 3. mea. | 1. mea. | 2. mea. | 3. mea. |
| Pre-load force stroke 0 mm | 10-50 kN | 42,3 | 19,9 | 17,9 | 40,1 | 19,5 | 15,4 | 45,1 | 17,4 | 15,7 | 41,1 | 18,5 | 17,4 |
| Force for stroke 25 mm | 30-130 kN | 130 | 60 | 56,0 | 130 | 60 | 42 | 130 | 50 | 50 | 130 | 60 | 50 |
| Force for stroke 60 mm | 100-400 kN | 348 | 210 | 200 | 325 | 210 | 175 | 340 | 200 | 185 | 330 | 200 | 180 |
| Force for stroke 100 mm | 350-1000 kN | 900 | 820 | 780 | 880 | 820 | 750 | 900 | 820 | 770 | 880 | 810 | 780 |
| Force for stroke 105 mm | $\geq$ 750N | 961 | 960 | 790 | 960 | 950 | 760 | 977 | 960 | 800 | 953 | 950 | 795 |
| Acumulated energy, We | $\geq$ 12,5 kJ (nom. 30 kJ) | 39,1 | 27,9 | 21,4 | 37,2 | 27,8 | 19,8 | 38,8 | 26,8 | 21,3 | 37 | 27,1 | 20,8 |
| Absorbed energy, Wa | $\geq$ 0,5 We | 26,1 | 15,2 | 9,7 | 24,3 | 15,1 | 9,5 | 25,5 | 13,7 | 10,5 | 23,3 | 14,5 | 8,8 |

Results of investigation of bumpers show:

- Force of the elastomer set pre-load in the 2nd cycle of load is decreased for about 55%, while in th 3th cycle this decrese is about 60% regarding the default value.
- Force at stroke of 25 mm in the 2nd cycle is decresed for about 54%, while in th 3th cycle this decrese is about 57% regarding the default value.
- Force at stroke of 60 mm in the 2nd cycle is decresed for about 40%, while in th 3th cycle this decrese is about 57% regarding the default value.
- Force at stroke of 100 mm in the 2nd cycle is decresed for about 1%, while in th 3th cycle this decrese is about 18% regarding the default value.
- Acumulated energy in the 2nd cycle of load is decresed for about 28%, while in th 3th cycle this decrese is about 45% regarding the default state.
- Absorbed energy in the 2nd cycle of load is decresed for about 38%, while in th 3th cycle this decrese is about 60% regarding the default state.
- Curve of relaxation in the operating diagram has not been changed for repeated load cycles, while curve of load has been collapsed down.

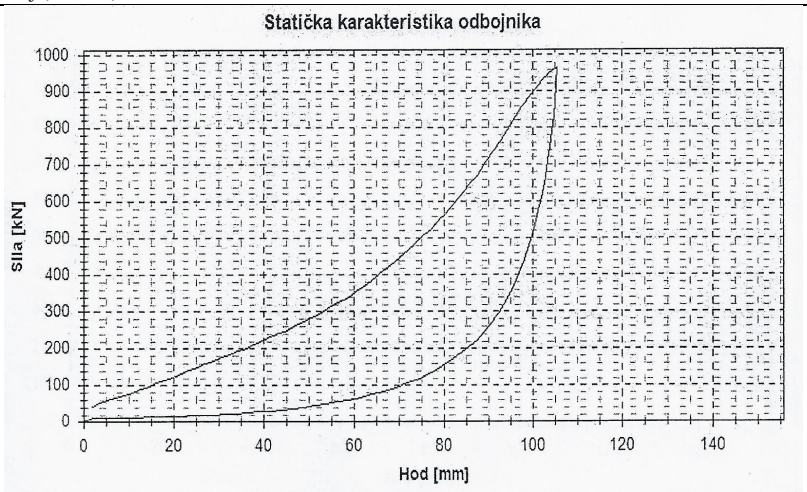


**Figure 2.** Working diagram of bumper for the 1. measurement

## 3. Design and investigation of a pulling device

A pulling device has a built-in elastomer set „TecsPack ST-9-2" with 3 rings and 2 steel spacing rings. Figure 3 shows elastomer set and pulling device on the test table of laboratory presses. Recommended mounting length of elastomer set is 160 mm. Table 3 shows standardized characteristics of pulling device with 3 elastic rings and 2 steel spacing rings, [2].

a. b.

**Figure 3.** Pulling device assembly: a. Operating elastomer assmebly, b. pulling device on the test table

**Tabela 3** Standardized characteristics of elastomer,,TecsPack Springs ST-9-2'' with 3 rings and 2 steel spacing rings

| Nominal value | 2. operating cycle | 3. operating cycle |
|---|---|---|
| Mounting force | 51 kN | 46 kN |
| Acumulated energy, We | 24 kJ | 21 kJ |
| Ratio between absorbed and acumulated energy, Wa/We | 0,51 | 0.43 |

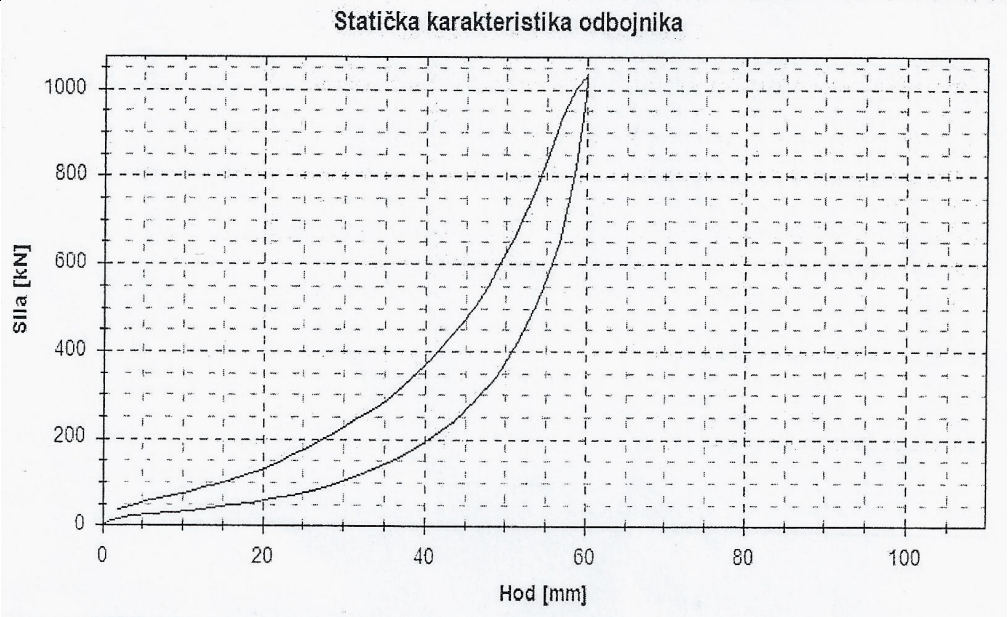


**Figure 4.** Work diagram of pulling device for the 1st measurement

A Comparative review of nominal physical values according to standard UIC 520 and measured values for 2 investigated pulling devices are presented in table 4.

**Tabela 4.** Comparative review of nominal values according to standard UIC 520 and measured values for 2 investigated pulling devices

| Nominal value | Values accord. UIC 520 | Measured values | | | | | |
|---|---|---|---|---|---|---|---|
| | | Specimen 1 | | | Specimen 2 | | |
| | | 1. Meas. | 2. Meas. | 3. Meas. | 1. Meas. | 2. Meas. | 3. Meas. |
| Pre-load force (stroke= 0) | 10-20 kN | 36.6 | 39,1 | 37,6 | 39.3 | 36,8 | 35,8 |
| Force for stroke 20 mm | | 130 | 140 | 140 | 128 | 125 | 150 |
| Force for stroke 40 mm | | 375 | 390 | 380 | 370 | 355 | 350 |
| Force for stroke 50 mm | | 630 | 640 | 640 | 615 | 580 | 580 |
| Force for stroke 50-60 mm | 400-550 kN | 1026 | 1025 | 1025 | 1001 | 1001 | 1001 |
| Acumulated energy, We | 8-10 (nom. 20kJ) | 19.3 | 19,9 | 19,4 | 19.1 | 18,7 | 18,3 |
| Absorbed energy, Wa | $\geq$ 0,3 We | 7.7 | 8,1 | 7,4 | 7.5 | 6,9 | 6,5 |

Results of investigation of pulling device show:

- The pre-load force of the elastomer set in higher cycles of load is slightly changed, which account for forces in different operating strokes, up to maximal stroke of 60 mm
- Absorbed and acumulated energy are insignificantly changed for all 3 cycles of load.
- Curve of relaxation in work diagram has not been changed for repeated load cycles, while curve of load collapsed down, as with bumper device.

## 4. Conclusion

Results of investigation of static characteristics of pulling and buffering devices with built-in elastomers show that devices fulfill requirements of standards and can successfully replace steel spring elements. For higher load cycles of a bumper, force of elastomer set for each stroke is significantly reduced, as well as values of accumulated and absorbed energy. When it comes to pulling devices, these parameters are slightly changed. Curve of relaxation in the work diagram, both for pulling and buffer devices, has not been changed for repeated cycles of investigation, while curve of load collapsed down. For installation of devices, special attention should be paid to the choice of optimal value of pre-load force of elastomer set.

## References

[1] Blagojevic M., Todić M., Miletić O., Verification of investigation of bushing bumper for cargo wagons (Verifikacina ispitivanja čaurastog odbojnika za teretne vagone), Faculty of Mechanical Engineering Banja Luka, 2012.

[2] Blagojevic M., Todic M., Miletic O., Verification of investigation of pulling device for cargo wagons (Verifikacina ispitivanja vučnog uredjaja za teretne vagone), Faculty of Mechanical Engineering Banja Luka, 2012.

# ELASTOPLASTIC ANALYSIS OF TRUSSES SUBJECTED TO CYCLIC LOADING

**Zoran Perović[1], Dragoslav Šumarac[2]**

1 Faculty of Civil Engineering
The University of Belgrade, Bulevar kralja Aleksandra 73, 11000 Belgrade
e-mail: zperovic@grf.bg.ac.rs
2 Faculty of Civil Engineering
The University of Belgrade, Bulevar kralja Aleksandra 73, 11000 Belgrade
e-mail: sumi@eunet.rs

**Abstract.**Nonlinear analysis of structures that includes material nonlinearity is very important and complex task, especially when applied to cyclic loading. In the present paper, Preisach model of hysteresis which was already successfully implemented for solving problems of cyclic plasticity of axially loaded bar and cyclic bending of elastoplastic beam, will be extended to structural analysis of trusses subjected to cyclic loading. Using finite element method, equilibrium equations will be obtained and algorithm for numerical solution will be defined In C++ code. As a result, various numerical examples will be presented and finally, conclusions and remarks for future research will be given.

## 1.Introduction

Since there are numerous examples of hysteresis phenomena occurring in physical processes (hysteresis in continuum mechanics, in ferromagnetism, in filtration through porous media etc.), appropriate modeling of hysteresis is of great interest to engineers and physicists. One of the most powerful scalar model of hysteresis among those that are known so far was proposed by the physicist F. Preisach in 1935 [1] to represent scalar ferromagnetism. Application of the Preisach model to cyclic behavior of elasto-plastic material was introduced in 1993 by (Lubarda, Sumarac, Krajcinovic) [2],[3].One of the most important properties of the Preisach operator is the so-called memory map but it is shown in [3] that suggested (Preisach) model also possesses congruency and wiping out property and it is obvious from [2],[3] that this model is appropriate to describe hysteretic behavior of elasto-plastic material. It was also shown that Preisach model can be defined in purely geometric terms, without any reference to analytical definition, which is less attractive approach for engineers. First part of this paper contains basic outline to Preisach model used in [3] and [4], and in second part, finite element equations for static and dynamic nonlinear analysis of trusses subjected to cyclic loading are obtained. In third part, numerical examples were presented and results were analyzed and compared.

## 2.Preisach model

According to [3], the Preisach model implies the mapping of an input of strain $\varepsilon(t)$ on the output stress $\sigma(t)$ in the integral form as shown in Eq. (1). $G_{\alpha,\beta}$ is an elementary hysteresis operator. Parameters $\alpha$ and $\beta$ are up and down switching values of the input and two

possible outputs for expression $G_{\alpha,\beta}\cdot\varepsilon(t)$ are +1 and -1 [3]. $P(\alpha,\beta)$ is the Preisach function, i.e. a weight (Green's) function of the hysteresis nonlinearity to be represented by the Preisach model.

$$\sigma(t) = \iint_{\alpha\geq\beta} P(\alpha,\beta) G_{\alpha,\beta} \times \varepsilon(t) \times d\alpha d\beta \tag{1}$$

The domain of integration of integral in Eq. (1) is right triangle in the $\alpha,\beta$ plane, with $\alpha=\beta$ being the hypotenuse and $(\alpha_0,\beta_0=-\alpha_0)$ being the triangular vertex (Fig.1.(b)). History of loading corresponds to staircase line $L(t)$ which divides triangle into two parts [3]. Elastic-linearly hardening material behavior characterized by the stress-strain curve shown in Fig.1.(a) can be replicated with three element unit [2],[3]. For the system consisting of infinitely many of three-element units, connected in parallel (or in series) with uniform yield strength distribution within the range $Y_{min} \leq Y \leq Y_{max}$, total stress can be calculated when strain is used as input load, using the Preisach model for axially loaded bars as it shown in Eq.(2). Since in this paper, displacement-based finite element method is used, model consisting of infinitely many of three-element units connected in parallel, where strain is used as input function, was adopted for analysis.

$$\sigma(t) = \frac{E}{2}\int_{-\varepsilon_0}^{\varepsilon_0} G_{\alpha,\alpha} \times \varepsilon(t) \times d\alpha - \frac{E(E-E_h)}{4(Y_{\max}-Y_{\min})} \iint_A G_{\alpha,\beta} \times \varepsilon(t) \times d\alpha d\beta \tag{2}$$

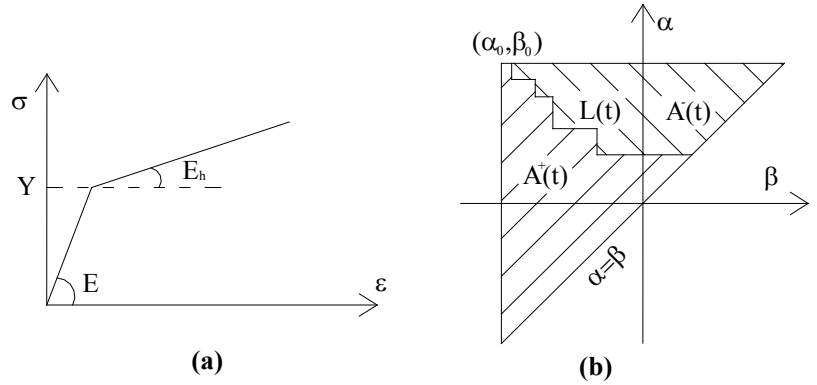


**Figure 1.**(a) Elastic linearly hardening stress–strain behavior with elastic modulus $E$, initial yield stress $Y$ and hardening modulus $E_h$.;(b) Preisach triangle divided by staircase line $L(t)$.

## 3. Finite element equations for trusses

Using principle of virtual displacements, equations for finite element procedures can be obtained. If only truss elements are considered, (body forces and surface forces are zero), there are only concentrated loads as externally applied load possible. In the finite element analysis we approximate the structure (in this case truss) as the assemblage of the discrete finite elements interconnected at the nodal points on the element boundaries. The expression for principle of virtual displacements then becomes:

$$\sum_m \int_{V^{(m)}} \bar{\varepsilon}^{(m)T} \sigma^{(m)} dV^{(m)} = \sum_i \bar{u}^{iT} R_C^i \tag{3}$$

Where σ represents stresses in equilibrium with applied loads, $R_C^i$ denotes concentrated

forces on point *i* of applied loads, $\bar{U}^i$ denotes virtual displacements, $\bar{\varepsilon}$ corresponding virtual strains and *m= 1,2…k,* where *k* is the number of elements. It is shown in [2] and [3] that first part of the expression in Eq.(2) represents elastic stress of axially loaded bars [5] and if we introduce strain displacement matrix *B*, elastic stiffness matrix will be obtained as shown later in Eq.(6). It is considered that this problem would not require large displacement and large strain analysis, so that only possible nonzero strain could be $\varepsilon_{11} = \Delta u/L$.

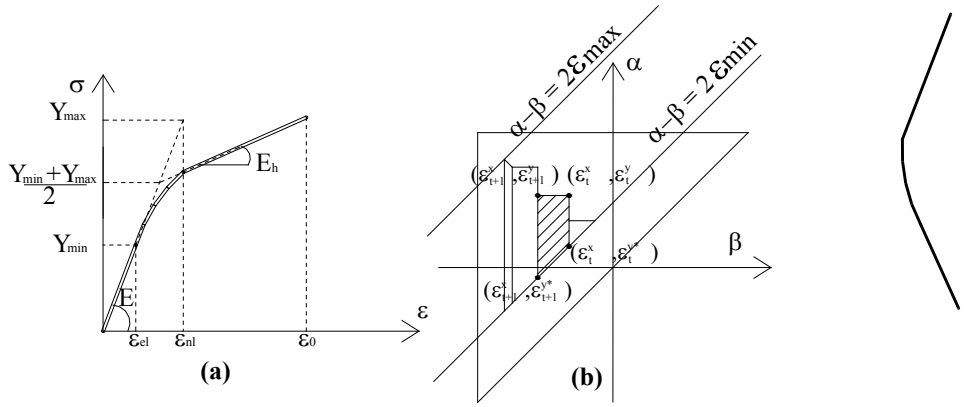


**Figure 2.**(a) Stress-strain behavior of material modeled by parallel connection of infinite number of three element units (b) Set $A^+(t)$of Preisach triangle reduced to sum of trapezes.

It was demonstrated in [3] and [4] that for corresponding minimum and maximum strain limit $\varepsilon_{min}$ and $\varepsilon_{max}$, Preisach triangle is formed as presented on Fig.2.(b). Second part of the expression in Eq.(2) determines plastic behavior when stress in material exceeds elastic limit $(\sigma > \sigma_{el})$ and by geometric interpretation it is shown in [2] and [3], that it actually represents difference of positive and negative sets $A^+(t)$ and $A^-(t)$ in Preisach triangle. At any instant of time, integral in Eq.(1) can be subdivided into two integrals $A^+(t)$ and $A^-(t)$, determined by particular shape of interface line *L(t)*. It is obvious that area $A^+(t)$ will be consisted of sum of trapezes whose vertices have coordinates equal to past input extrema [2], and therefore it will represent function of predominant input strain data values $(\varepsilon_t^x, \varepsilon_t^y)$:

$$A^+(t) = \sum_{t=1}^{N} \left[ \left( \varepsilon_{t+1}^x - \varepsilon_t^x \right) \left( \varepsilon_{t+1}^y - \varepsilon_{t+1}^{y*} + \varepsilon_t^y - \varepsilon_t^{y*} \right) / 2 \right] \tag{4}$$

Where positive set of Preisach triangle $A^+(t)$ is divided to *N* trapezes (Fig.2.(b)). Considering that displacement-based finite element method is used, it is necessary to exchange strain variable $\varepsilon$ with $\Delta u$, and because of Eq.(4), $A^+(t)$ will therefore represent function of predominant input bar length change data values $(\Delta u_t^x, \Delta u_t^y)$. As a result Preisach triangle where bar length change is used as input function is obtained. Second part of the expression in Eq.(2) becomes:

$$\iint_A G_{\alpha,\beta} \times \varepsilon(t) \times d\alpha d\beta = A^+(t) - A^-(t) = \frac{1}{L^2} \times u_{pl} \tag{5}$$

Where $u_{pl}$ represents difference of positive and negative sets in Preisach triangle where bar length change $\Delta u$ is used as input function $(\Delta u_t^x, \Delta u_t^y)$.If we analyze only one element *m* of finite element assemblage, and substitute Eq.(5) in (3):

$$\overline{u}^{(m)T}\left[\int_{V^{(m)}} B^{(m)T} E B^{(m)} dV^{(m)}\right]\overline{u}^{(m)} - \overline{u}^{(m)T}\left[\int_{V^{(m)}} B^{(m)T} \frac{E\left(E-E_h\right)}{4\left(Y_{\max}-Y_{\min}\right)} \frac{1}{\left(L^{(m)}\right)^2} dV^{(m)}\right]\cdot u_{pl}^{(m)}$$

$$= \overline{u}^{(m)T} R_C^i \tag{6}$$

These expressions can be written as:

$$K_{el}^{(m)}\overline{u}^{(m)} - K_{pl}^{(m)}\cdot u_{pl}^{(m)} = R_C^i \tag{7}$$

For the finite element assemblage, expression in Eq.(7) becomes

$$K_{el}U - K_{pl}\cdot U_{pl} = R \tag{8}$$

And elements of vectors $U$ and $U_{pl}$ are $u^{(m)}$ and $u^{(m)}{}_{pl}$. It is important to emphasize that elements $u^{(m)}{}_{pl}$ are not displacements, but function of predominant input bar length changes $\Delta u^{(m)}$,that actually represent difference of positive and negative sets $A^+(t)$ and $A^-(t)$ in corresponding Preisach triangle. For solving problem of nonlinear static analysis, iterative procedure using Newton-Raphson initial stress method can be applied. Procedure for iteration $i$ in Eqs.(9) is repeated until convergence is achieved.

$$\begin{aligned} K_{el}\Delta U^{(i)} &= {}^{t+\Delta t}R - {}^{t+\Delta t}F^{(i-1)} \\ {}^{t+\Delta t}U^{(i)} &= {}^{t+\Delta t}U^{(i-1)} + \Delta U^{(i)} \\ {}^{t+\Delta t}F^{(i-1)} &= K_{el}\,{}^{t+\Delta t}U^{(i-1)} + K_{pl}\,{}^{t+\Delta t}U_{pl}^{(i-1)} \end{aligned} \tag{9}$$

## 4. Numerical examples

According to defined procedures for numerical analysis from Eqs.(6) to (9), algorithm for elastoplastic analysis of trusses subjected to cyclic loading was defined in C++ code. During every step and iteration in expressions from Eqs.(6) to (9), in every bar of truss structure, plastic part from Eq.(6) is being calculated according to current state of corresponding bar and then assembled in global matrix in Eq.(8). For assigned material properties, corresponding stress-strain behavior obtained by Preisach model can be presented as shown on Fig.2.(a), where $\varepsilon_{el}$ is elastic strain limit of material, $\varepsilon_{nl}$ is plastic strain limit of nonlinear behavior and $\varepsilon_0$ is maximum strain limit of material. In static analysis if material has very small or no strain hardening ($E_h \approx 0$), in order to provide some indication of when both the displacements and the forces are near their equilibrium values, it is recommended [5] that convergence criteria be based on energy tolerance condition as shown in Eq.(10). Increment in internal energy during each iteration is compared to initial internal energy increment.

$$\Delta U^{(i)T}\left({}^{t+\Delta t}R - {}^{t+\Delta t}F^{(i-1)}\right) \le \in_E \left(\Delta U^{(1)T}\left({}^{t+\Delta t}R - {}^{t}F\right)\right) \tag{10}$$

In dynamic analysis, since Newmark method with coefficients $\delta = 0.5$ and $\alpha = 0.25$ is used for direct integration, convergence criteria should satisfy both energy and force tolerance condition [5]. For all numerical examples, truss structure from Fig.3. is analyzed and three load cases are presented. Structure consists of two types of bars. Horizontal bars have length of $6m$, and cross section areas $A_{hor} = 0.04m^2$; and diagonal bars have cross section areas $A_{dia} = 0.03m^2$. Modulus of elasticity for whole structure is $E = 200\ GPa$, hardening moduli is $E_h = 40\ GPa$ and maximum input strain is $\varepsilon_0 = 0.4\%$. It is considered that yield strength of every three element unit is within the range $160Mpa \le Y \le 320Mpa$.

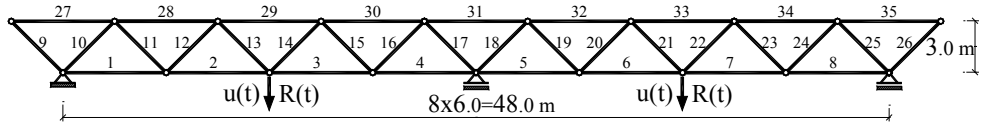


**Figure 3.**Truss structure and disposition of load applied in first( *R(t)* ) and in second( *u(t)* ) numerical example

In first example, truss structure was subjected to cyclic loading which was applied as system of concentrated forces on two nodes, and in second example cyclic loading was applied as system of nodal displacements on same nodes (Fig.3.). Input functions of concentrated forces *R(t)* and nodal displacements *u(t)* are shown on Fig.4.(left). It is obvious from symmetrical load on structure, that corresponding symmetrical bars will have identical response, therefore four characteristic bars are analyzed and compared with corresponding linear elastic analysis for both cases. It can be seen that in every incremental step, stress-strain relation of each bar is gained as defined for material property shown on Fig.2.(a).

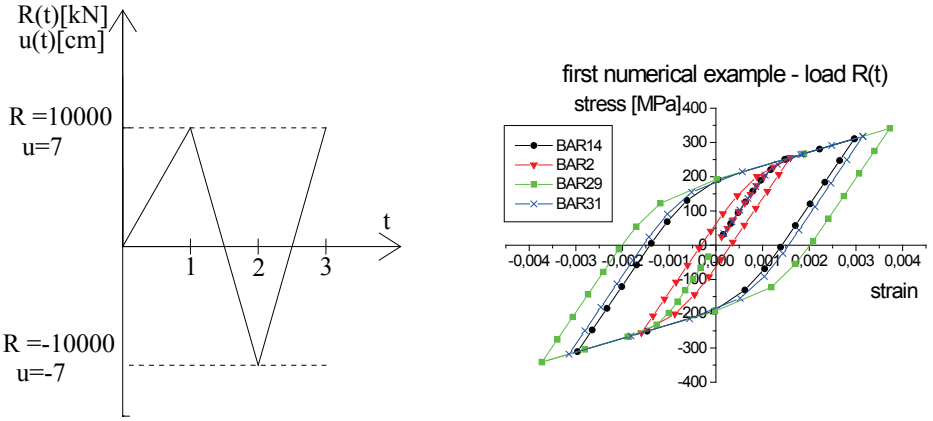


**Figure.4.**(left) Input function of loads *R(t)* and *u(t)* applied on truss structure; (right) Stress-strain hysteresis curves for first numerical example

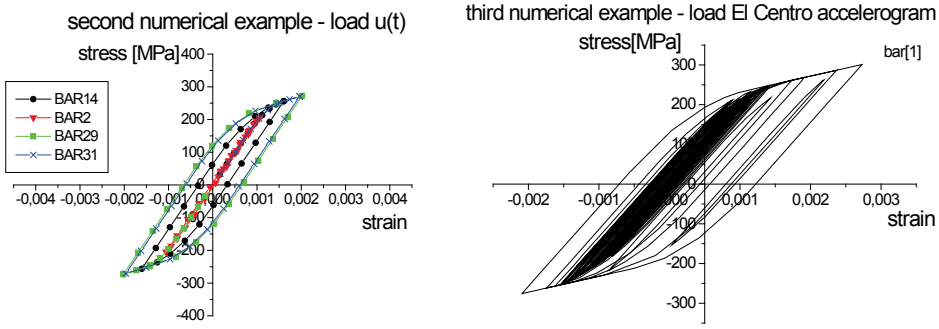


**Figure 5.** Stress-strain hysteresis curves for second and third numerical example

While results from corresponding linear elastic analysis are almost identical, in elastoplastic analysis redistribution of load results in significantly different output. In third example, structure was subjected to ground acceleration in horizontal direction. For input function of acceleration, time history record of ground acceleration from El Centro earthquake was

used. Mass density of material was neglected, but additional mass of $100kN \cdot s^2/m$ and $20kN \cdot s^2/m$ was appended to each bar in upper and lower zone of truss respectively.

## 5.Conclusion

In previous papers that concerned Preisach model in continuum mechanics [2],[3], it is shown that this model for hysteresis poses adequate properties for modeling of material cyclic plasticity. The most powerful advantage of Preisach model in comparing to other hysteresis models used in continuum mechanics is memory mapping and analytical solution that can be geometrically interpreted with ease. In this paper, it is shown that equations for nonlinear finite element procedures for trusses subjected to cyclic loading can be derived by introducing Preisach triangle where bar length change is used as input function enabling static and dynamic nonlinear analysis of trusses. Although proposed model have numerous advantages in modeling, for more complex analysis, modifications and more advanced algorithm in finite element procedure is needed. Considering all possibilities that Preisach model poses, this type of analysis in finite element procedures is yet to be applied.

*Acknowledgement*: The work reported in this paper is a part of the investigation within the research project financed by the Ministry of education and science, Republic of Serbia. This support is gratefully acknowledged.

## References

[1] Preisach F., 1935, Über die magnetische Nachwirkung, *Z . Phys*.,94, 277- 302
[2] Lubarda A. V., Sumarac D., Krajcinovic D., 1992, Hysteretic Response of Ductile Materials Subjected to Cycling loads, *Recent Advantages in Damage Mechanics and Plasticity* (Edited by J. Wu. Ju, ASME Pub. AMD, 123), 145-147.
[3] Lubarda A. V., Sumarac D., Krajcinovic D., 1993, The Preisach model and hysteretic behavior of ductile materials, *Eur. J., Mech, A/Solids*, 12, n° 4, 445-470.
[4] Sumarac D., Stosic S., 1996, The Preisach model for the cyclic bending of elasto-plastic beams, *Eur. J., Mech, A/Solids*, 15, n° 1, 155-172.
[5] Bathe K J., 1996, Finite Element Procedures, Prentice Hall
[6] Erlicher S., 2003, Hysteretic degrading models for the low-cycle fatigue behavior of structural elements, Theory, Numerical aspects and Applications, Dottorato di ricerca in Modellazione, Conservazione e Controllo dei Materiali e delle Strutture, Universita Degli studi di Trento
[7] Visintin A., 2005, Mathematical Models of Hysteresis, Dipartimento di Matematica dell'Universitŕ degli Studi di Trento, Italia.
[8] Mayergoyz I. D.,1991, Mathematical Models of Hysteresis, Springer, New York.
[9] Asaro, R.J., 1975, Elastic-plastic memory and kinematic type hardening, *Acta Metall*., 23, 1255-1265.
[10] Iwan W. D., 1967, On a class of models for the yielding behavior of continuous and composite systems, *J. Appl. Mech*., 34, 612-617.

# INFLUENCE OF WELDED JOINT GEOMETRY ON FRACTURE BEHAVIOUR - MICROMECHANICAL ASSESSMENT

**Bojan Medjo[1,*], Marko Rakin[1], Nenad Gubeljak[2], Dražan Kozak[3], Ivana Cvijović-Alagić[4], Aleksandar Sedmak[5]**

[1] University of Belgrade, Faculty of Technology and Metallurgy,
Karnegijeva 4, 11120 Belgrade, Serbia
[2] University of Maribor, Faculty of Mechanical Engineering,
Smetanova 17, 2000 Maribor, Slovenia
[3] University of J.J. Strossmeyer, Osijek, Mechanical Engineering Faculty,
Trg Ivane Brlić-Mažuranić 2, HR-35000 Slavonski Brod, Croatia
[4] Institute of Nuclear Sciences "Vinča",
P.O. Box 522, 11001 Belgrade, Serbia
[5] University of Belgrade, Faculty of Mechanical Engineering,
Kraljice Marije 16, 11120 Belgrade, Serbia

* corresponding author: e-mail: bmedjo@tmf.bg.ac.rs

**Abstract.** Ductile fracture of high-strength low-alloyed (HSLA) steel welded joints is analysed in this work using the micromechanical approach. The examined joints are double mismatched, i.e. they consist of overmatched (OM) and undermatched (UM) weld metal portion. The constraint effect caused by the different joint geometries is examined on two types of double mismatched welded specimens: in the first type, the crack front passes through both weld metals, while in the second type it is located in OM. Therefore, the crack front either passes through the interface between the two weld metals or is located in the vicinity of the interface. Three point bending tests are conducted, and fracture mechanics parameter CTOD, crack tip opening displacement, is determined using the δ5 concept. The complete Gurson model (CGM) is applied for determining the conditions for damage initiation and modelling the crack growth.

## 1. Introduction

Understanding the fracture behaviour of welded structures is very important, especially having in mind that welded joints typically contain some initial defects. In fracture of welded joints, the influence of material heterogeneity (mismatch) is present in addition to the geometry constraints. The mechanical heterogeneity is a key factor for predicting the failure conditions of such structures under various exploitation conditions [1-4]. Influence of heterogeneity on fracture of steel welded joints was analysed by micromechanical approach in [5-10]. In this work, overmatched and undermatched joints are examined, as well as joints with two different weld metals (double mismatched or DM joints), Fig. 1. The latter contain overmatched and undermatched portion [11,12]. The fatigue pre-crack is in the middle of the weld metal in all cases. This fact enabled the modelling of the joints without taking into account the properties of (HAZ); it was shown in [2,5,7,10] that such approach is justified for the cracks in the middle of the weld metal. Micromechanical

analysis is performed to assess the fracture behaviour of the joints. The Gurson yield criterion is applied, through the complete Gurson model (CGM). Crack growth simulation is performed by tracking the deterioration of finite elements (FE) in front of the crack tip.

## 2. Micromechanical modelling

The GTN model [14-16] extends von Mises plasticity theory to cover the effects of porosity $f$ (damage parameter) and mean stress $\sigma_m$. The expression for plastic potential is than:

$$\phi = \frac{3S_{ij}S_{ij}}{2\sigma^2} + 2q_1 f^* \cosh\left(\frac{3q_2\sigma_m}{2\sigma}\right) - \left[1 + \left(q_1 f^*\right)^2\right] = 0 \tag{1}$$

where $\sigma$ denotes the flow stress of the material matrix and $S_{ij}$ is the stress deviator. Constitutive parameters $q_1 = 1.5$ and $q_2 = 1$ were introduced by Tvergaard [15] to improve the fracture prediction of the Gurson model and $f^*$ is the damage function [16]. The critical value of $f$, at the moment when the void coalescence begins, is denoted by $f_c$. Zhang et al. [17] applied the Thomason's plastic limit load criterion [13] to the GTN model, obtaining the complete Gurson Model (CGM). In CGM, criterion for the onset of void coalescence is:

$$\frac{\sigma_1}{\sigma} > \left(\alpha\left(\frac{1}{r} - 1\right) + \frac{\beta}{\sqrt{r}}\right)\left(1 - \pi r^2\right), \qquad r = \sqrt[3]{\frac{3f}{4\pi}e^{\varepsilon_1+\varepsilon_2+\varepsilon_3}} \Bigg/ \left(\frac{\sqrt{e^{\varepsilon_2+\varepsilon_3}}}{2}\right) \tag{2}$$

where $\sigma_1$ is the maximum principal stress, $\varepsilon_i$ are principal strains and $\alpha/\beta$ are constants fitted by Thomason [13]. Therefore, $f_c$ can be calculated during the FE analysis, i.e. it is not a material constant in the CGM.

## 3. Experimental testing

The base metal (BM) is high-strength low-alloyed (HSLA) steel NIOMOL 490. True stress - true strain curves, along with the material properties, of BM and both weld metals, are given in Fig. 1.

Microstructural parameters, volume fraction of non-metallic inclusions $f_v$ and mean free path between them $\lambda$ are determined by quantitative microstructural analysis (UM: $f_v$ = 0.7057%, $\lambda$ = 126 mm; OM: $f_v$ = 0.6342%, $\lambda$ = 157 mm). During the early phase of ductile fracture of steel, the locations for void nucleation are primarily around non-metallic inclusions. Therefore, the initial porosity $f_0$ is set as equal to $f_v$, [9,10,18,19].

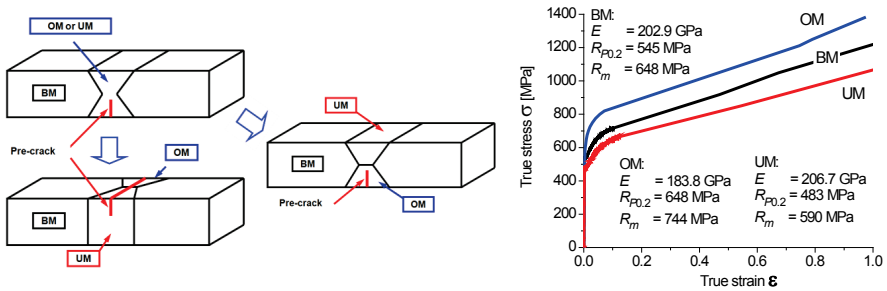


Fig. 1: Schematic view of the examined joints and stress - strain curves

Firstly, welded OM and UM SENB specimens with three different widths (6, 12 and 18 mm) are examined. CTOD values are measured using a $\delta_5$ clip gauge, developed by GKSS. Details about the welding process and preparation of the plates are given in [20]. measures of the specimens are 25x25x130 mm, with the distance between the supports 100 mm and pre-crack length 8 mm.
In addition to the mismatched joints, double mismatched joints with the crack in through-thickness direction (through both weld metals - TT DM, first two drawings in Fig. 2) and in OM weld metal (ODM, right-hand side of Fig. 2) are also examined. Main dimensions of the specimen are given in the same figure, except the pre-crack length in the specimens with the crack located in OM (this dimension is varied: 10.4-12.3 mm).

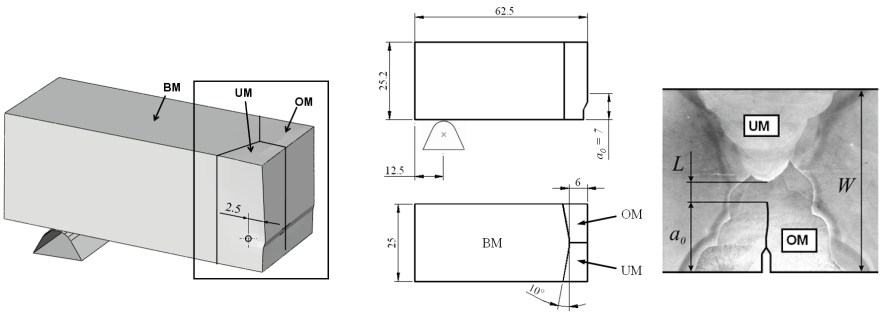


Fig. 2: Double mismatched TT DM SENB specimen (one half, due to the symmetry) and ODM joint

## 4. Numerical analysis

Finite element software package Abaqus (www.simulia.com) is used for numerical analysis, with the CGM applied through user subroutine created by Z.L. Zhang, based on [17]. Specimens with OM or UM joints are analysed under plane strain conditions, using 4-noded isoparametric reduced integration elements. The FE mesh is given in Fig. 3, including the magnified detail around the crack tip. External loading and supports are modelled by contact with rigid bodies, Fig. 3.
Crack growth is modelled by tracking the damage development ahead of the crack tip; complete loss of load-carrying capacity is defined through the micromechanical model (CGM). 3D model is used for TT DM joints, due to the changes in material properties and geometry along the crack front. Linear 8-noded elements with full integration are used.

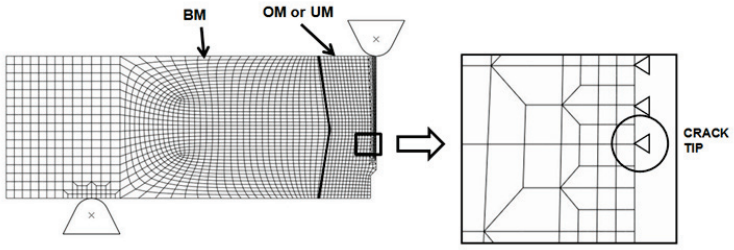


Fig. 3: FE mesh of the OM/UM SENB specimen

## 5. Results and Discussion

CTOD - $\Delta a$ diagrams (Fig. 4) exhibit opposite trends for OM and UM weld metals - increase of OM joint width causes lower crack growth resistance, while increase of UM joint width causes higher resistance. Similar conclusion can be drawn from the measured values of CTOD at final fracture, also given in Fig. 4. UM joints with 18 and 12 mm width exhibit almost the same behaviour - therefore, increase of width above 12 mm does not further increase the fracture resistance.

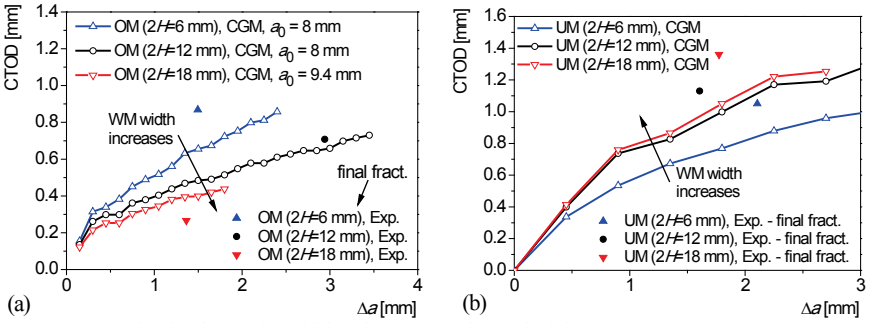


Fig. 4: CTOD - $\Delta a$ curves for the three joint widths of OM (a) and UM (b) joint

It is important to emphasize that the local approach to fracture requires determination of the appropriate FE size in the ligament, which can be regarded as its drawback. A significant difference between OM and UM is obtained in [21]; FE size in OM approximates the mean free path between the inclusions (0.15 x 0.15 mm), while the size 0.45 x 0.45 mm is appropriate for UM. FE size in the ligament of DM joints is adopted based on the examination of OM and UM joints - this size is a parameter which is transferred.
The increase of the damage parameter (porosity $f$) in TT DM joint is given in Fig. 5. Due to high stress triaxiality, $f$ increases more prominently in the middle of the specimen. Also, the damage develops more rapidly in the OM portion in comparison with the UM.

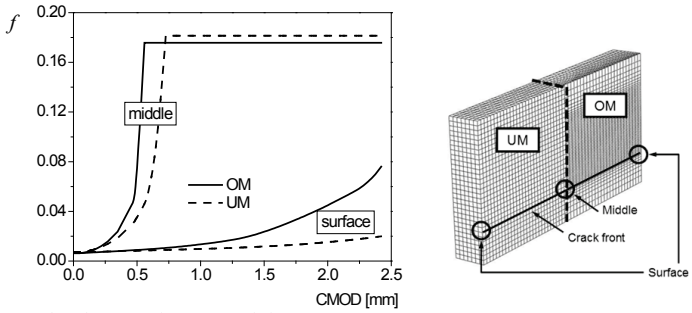


Fig. 5: Damage development in TT DM joints

Distribution of damage parameter $f$ is given in Fig. 6. Red colour represents the areas with elements that have lost the load carrying capacity. Micromechanical criterion (CGM) successfully predicts that the crack growth resistance is much lower in the OM weld metal. This is obtained by transferring the micromechanical parameters, initial porosity and FE size, from single mismatched (OM and UM) to double mismatched (OM + UM) joints.

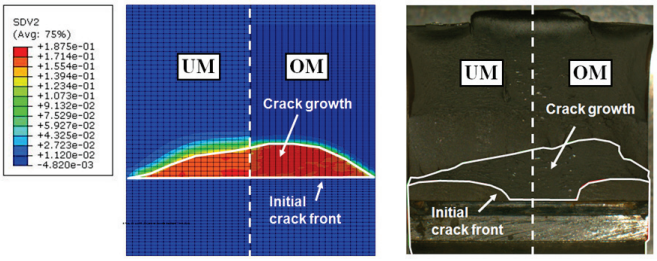


Fig. 6: Fracture plane - damage parameter field (porosity *f*) and photo of the fracture surface - TT DM joints

In the case of DM joints with a crack in OM weld metal (ODM joints), length of the pre-crack (along with distance from OM/UM interface) is varied. *F*-CTOD and CTOD-Δ*a* curves are shown in Fig. 7. It can be seen that there is significant difference in load carrying capacity between the specimens, caused by the joint geometry (pre-crack position and length). These differences are predicted using the CGM. On the other hand, analysed crack lengths did not cause a significant difference in CTOD-Δ*a* curves, which is shown in the same figure.

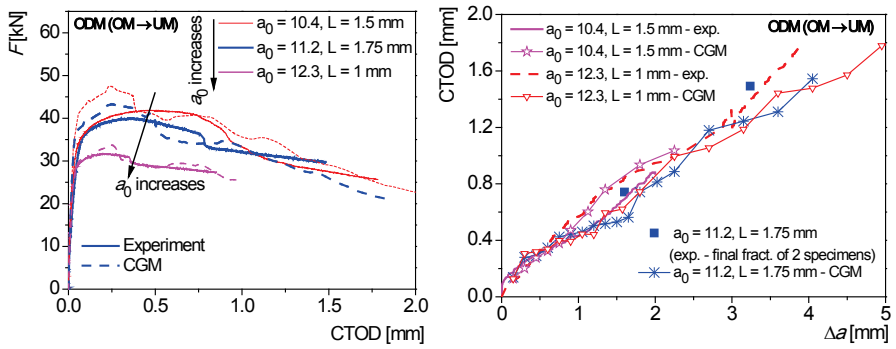


Fig. 7 *F*-CTOD and CTOD- Δ*a* curves for DM specimens with a pre-crack in OM weld metal - ODM joints

## 6. Conclusions

- Complete Gurson model can capture the mismatch/constraint effects in analysed joints.
- In overmatched joints, resistance to ductile fracture increases with the decrease of weld metal width; vice versa is true for undermatched joints.
- For undermatched joints, the mismatch effect almost vanishes with increase of the joint width above 12 mm.
- The influence of material inhomogeneity along the crack front for double mismatched joints is determined by transferring of the fracture parameters from single mismatched joints.
- Dependence of fracture resistance on the initial crack length and distance from the UM/OM interface for double mismatched joints is established.

*Acknowledgement.* The authors acknowledge the financial support of the Serbian Ministry of Science under the project ON 174004. The authors would also like to thank Z.L. Zhang for the CGM user subroutine.

## References

[1] Dexter R (1997) Significance of Strength Undermatching of Welds in Structural Behaviour, *Mis-matching of interfaces and welds*, KH Schwalbe and M Koçak (Eds.). Geesthacht: GKSS Research Center, pp. 55-74.
[2] Schwalbe KH, Ainsworth RA, Eripret C, Franco C, Gilles P, Koçak M (1997) Common Views on The Effects of Yield Strength Mis-Match on Testing and Structural Assessment, *Mis-matching of interfaces and welds*, KH Schwalbe and M Koçak (Eds.). Geesthacht: GKSS Research Center, pp. 99-132.
[3] Koçak M (Ed.) (1998) *Weld Mis-match Effect*. International Institute of Welding (IIW), IIW Doc. X-1419-98
[4] Ravi S, Balasubramanian V, Babu S, Nemat Nasser S (2004) Assessment of Some Factors Influencing the Fatigue Life of Strength Mis-Matched HSLA Steel Weldments, *Materials and Design*, **25**, pp. 125-135.
[5] Rakin M, Gubeljak N, Dobrojević M, Sedmak A (2008) Modelling of Ductile Fracture Initiation in Strength Mismatched Welded Joint, *Engineering Fracture Mechanics*, **75**, pp. 3499-3510.
[6] Burstow MC and Howard IC (2000) Damage Mechanics Models of Ductile Crack Growth in Welded Specimens, *Fatigue and Fracture of Engineering Materials and Structures*, **23**, pp. 691-708.
[7] Chhibber R, Biswas P, Arora N, Gupta SR, Dutta BK (2011) Micromechanical Modelling of Weldments Using GTN Model. *International Journal of Fracture*, **167**, pp. 71-82.
[8] Younise B, Sedmak A, Rakin M, Gubeljak N, Medjo B, Burzić M, Zrilić M (2012) Micromechanical Analysis of Mechanical Heterogeneity Effect on the Ductile Tearing of Weldments, *Materials and Design*, **37**, pp. 193-201.
[9] Nonn A, Dahl W, Bleck W (2008) Numerical Modelling of Damage Behaviour of Laser-Hybrid Welds, *Engineering Fracture Mechanics*, **75**, pp. 3251-3263.
[10] Penuelas I, Betegon C, Rodriguez C (2006) A Ductile Failure Model Applied to the Determination of the Fracture Toughness of Welded Joints. Numerical Simulation and Experimental Validation, *Engineering Fracture Mechanics*, **73**, pp. 2756-2773.
[11] Predan J, Gubeljak N, Kolednik O (2007) On the Local Variation of the Crack Driving Force in a Double Mismatched Weld, *Engineering Fracture Mechanics*, **74**, pp. 1739-1757.
[12] Medjo B, Rakin M, Gubeljak N, Predan J, Arsić M, Sedmak A (2011) Influence of Crack Length on Ductile Fracture Initiation in Welded Joints with One and Two Weld Metals, *Key Engineering Materials*, **465**, pp. 578-581.
[13] Thomason PF (1990) *Ductile Fracture of Metals*, Pergamon Press, Oxford.
[14] Gurson AL (1977) Continuum Theory of Ductile Rupture by Void Nucleation and Growth: Part I - Yield Criteria and Flow Rules for Porous Ductile Media, *Journal of Engineering Materials - Transactions of ASME*, **99**, pp. 2-15.
[15] Tvergaard V (1981) Influence of Voids on Shear Band Instabilities under Plane Strain Conditions, *International Journal of Fracture*, **17**, pp. 389-407.
[16] Tvergaard V and Needleman A (1984) Analysis of Cup–Cone Fracture in a Round Tensile Bar, *Acta Metallurgica*, **32**, pp. 157-169.
[17] Zhang ZL, Thaulow C, Ødegård J (2000) A Complete Gurson Model Approach for Ductile Fracture, *Engineering Fracture Mechanics*, **67**, pp. 155-168.
[18] Besson J, Steglich D, Brocks W (2003) Modeling of Plane Strain Ductile Rupture, *International Journal of Plasticity*, **19**, pp. 1517-1541.
[19] Rakin M, Cvijović Z, Grabulov V, Putić S, Sedmak A (2004) Prediction of ductile Fracture Initiation using Micromechanical Analysis, *Engineering Fracture Mechanics*, **71**, pp. 813-827.
[20] Gubeljak N, Scheider I, Kocak M, Oblak M, Predan J (2002) Constraint Effect on Fracture Behaviour of Strength Mis-Matched Weld Joint, *Proceedings of the 14th European Conference on Fracture*, A. Neimitz, I.V. Rokach, D. Kocanda, K. Golos (Eds.), pp. 647-655, ISBN 1-901537-35-8
[21] Rakin M, Medjo B, Gubeljak N, Sedmak A (2013) Micromechanical Assessment of Mismatch Effects on Fracture of High-Strength Low Alloyed Steel Welded Joints, *Engineering Fracture Mechanics*, revised manuscript sent to the Journal Editorial Board.

# INFLUENCE FORM FUNCTION NETWORK CONSTRUCRION PIPELINE IN THE OPTIMAL PARAMETERS IN DISTRICT HEATING AND COOLING

**Sefik M.Bajmak**

Faculty of Mechanical Engineering,
The University of Pristina, Kneza Miloša 7, Kosovska Mitrovica
e-mail: bajmak@yahoo.com

**Abstract**. Disposition of thermal network and the size of the impact on the optimal speed, specific pressure drop and optimum depth of laying the pipeline. Based on the so far derived hot water can be determined that the costs of construction of hot water can be represented as a linear or quadratic dependence depending on the diameter of the pipeline. As you know, the same heating system can, depending on the season, we transported hot water for heating (district heating) and cold water for cooling (district cooling).In this context, the paper gives the optimization parameters for the most widespread anger and channel distribution channel, depending on the temperature of heat carrier.

## 1.Introduction

It is calculated that the cost of building a distribution network without house connections and transit highway, reaching 30 ÷ 60% of the construction cost heat source (heating). High investment costs are due to two main causes: an expensive way of building the network, not the used capacity of the network in the first years of district heating and in the course of operation. Apart from the method of construction, lowering investment costs can be achieved by increasing the temperature difference between the water and the increasing speed of the water flow in the pipe system. Increasing the temperature of the water at flow by 10% to reduce investment costs by 4%, transit routes for 8 ÷ 12%, and drive energy for circulator pumps for 7 ~ 8%.

## 2. Defining a cost function shape and distribution network optimization criterion

Analysis of more hot water system construction, in Figure 1, is shown as a function of the flow cost of distribution network, depending on the nominal diameter [1,4,5], in table T1 linear and quadratic dependence on the costs of nominal diameter. Keeping this in mind, the paper gives the optimization of flow velocity of water $W(m/s)$, $R_l(Pa/m)$ specific pressure drop and pipeline installation depths $H_{op}(m)$. Optimization is done when the total cost of the network that is linearly dependent on the square diameter pipelines. Ordinary least squares coefficients have been determined:

$A_{li} = -35.25, B_{li} = 3887.0, A_{kv} = 12, B_{kv} = 3069, C_{kv} = 2206$

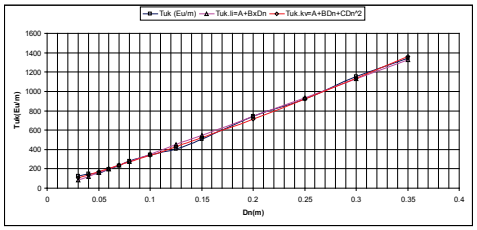


**Figure 1**.The dependence of the diameter of the cost of piping network

Using the minimum annual cost of the system is determined by the specific optimal parameters of the system. From the condition of $\partial T_{sis}/\partial X_i = 0$ are optimum values of the required size, and from the condition of $\partial^2 \overline{T}_{sis}/\partial X^2 > 0$ we come to the conclusion that the function has the optimal parameters.

**Table 1**

| Dn(m) | 0.03 | 0.04 | 0.05 | 0.06 | 0.07 | 0.08 | 0.1 | 0.125 | 0.15 | 0.200 | 0.250 | 0.300 | 0.350 |
|---|---|---|---|---|---|---|---|---|---|---|---|---|---|
| Ttot(Eu/m) | 126 | 150 | 153 | 195 | 234 | 278 | 345 | 407 | 505 | 743 | 924 | 1151 | 1347 |
| Ttot.lin (Eu/m) | 81 | 120 | 159 | 198 | 237 | 276 | 353 | 451 | 548 | 742 | 937 | 1131 | 1325 |
| Tuk.squ(Eu/m) | 106 | 138 | 171 | 204 | 238 | 272 | 341 | 431 | 523 | 716 | 920 | 1136 | 1363 |

## 3.Determine the optimum parameters of a branching pipeline

While designing the centralized supply of heat and cooling energy, should adopt such optimal parameters of carrier heating and cooling energy, at which the project will cost the system $T_{sis}(Eu/yearly)$ to be minimal.

### *3.1. Determination of the optimum speed of the water flow in an extensive pipeline*

Since the cost of the generator energy costs consumers of energy and other costs do not depend on the rate, specific pressure drop and fluid depth laying pipelines, them during the budget can be omitted to consider them is constant. On this basis, the costs of the system are:

$$T_{sis} = con + T_{ps} + T_{mc} \tag{1}$$

The total cost of the system as a function of speed $W(m/s)$ equal expression:

$$\overline{T}_{sis} = con + P_1 + P_2P_3 + (P_2P_7 + P_4)\sum \frac{Q_i^{0.5} l_i}{\Delta\tau_i^{0.5} W_i^{0.5}} + P_5 \sum \frac{Q_i l_i}{\Delta\tau_i W_i} + P_6 \left(\frac{Q}{\Delta\tau_w}\right)^{0.375} W_i^{2.375} \tag{2}$$

Optimal speed fluid flow bolted according to the expression (3) (costs of the system are linearly dependent) or by the expression (4) (costs of the system are dependent quadratic) function in the intersection Y1 and Y2, Figure 2:

$$W_{op} = \left\{ \left[ 0.5(P_2P_7 + P_4)\sum (Q_i l_i/\Delta\tau_w)^{0.5} \right] / \left[ 2.375 P_6 (Q_6/\Delta\tau_w) \right]^{0.375} \right\}^{0.348} \tag{3}$$

$$Y_1 = 2.375 P_6 \left(\frac{Q_{uk}}{\Delta\tau_w}\right)^{0.375} W^{2.875} - 0.5(P_2P_7 + P_4)\sum \frac{Q_i^{0.5}}{\Delta\tau_w^{0.5}};\ Y_2 = P_5 \sum \frac{Q_i l_i}{\Delta\tau_w} \frac{1}{W^{0.5}} \tag{4}$$

### *3.2.Determining the optimum specific pressure drop in the pipeline branched*

Taking into account that $G = Q^{'}/c_w \Delta\tau_w$, $G_i = Q_i/c_w \Delta\tau_w$ $Q_{god} = Q^{'} N_b$, after ordering expression (1) we have that specific costs are equal to the formula:

$$\overline{T}_{sis} = R_1 \frac{Q^{'} R_l}{Q_{\max} N_b c_w \Delta\tau_w} + \frac{R_2}{Q_{\max} N_b} + R_3 \frac{\sum Q_i^{0.38} l_i}{(c_w \Delta\tau_w)^{0.38} Q_{\max} N_b R_l^{0.19}} + \\ + R_4 \frac{\sum Q_i^{0.76} l_i}{(c_w \Delta_w)^{0.76} Q_{\max} N_b R_l^{0.38}} + \frac{R_5}{Q_{\max} N_b} \left[ R_7 + R_6 \frac{\sum Q_i^{0.38} l_i}{(c_w \Delta\tau_w)^{0.38} R_l^{0.19}} \right] \quad (5)$$

Since there are two variables, $\Delta\tau_w$ and $R_l$ here, we'll take the $\Delta\tau_w = const$ that is, we will seek the optimal value for, in one of an accepted diff temperatures of the $\Delta\tau_w$ .Optimal Specified pressure drop according to the expression (7) (costs of the system are linearly dependent) and the expression (8) (costs of the system are dependent quadratic) in section functions Y3 and Y4, Figure 3:

$$R_{lop} = \left\{ \left[ 0.19 \Sigma Q_i^{0.38} l_i / Q \right] \cdot \left[ c_w \Delta\tau_w / (c_w \Delta\tau_w)^{0.38} \right] \cdot \left[ (R_3 + R_5 R_6) / R_1 \right] \right\}^{0.84} \quad (6)$$

$$Y_3 = 5.26 R_1 \frac{Q_{uk}}{c_w \Delta\tau_w} R_l^{1.19}, \quad Y_4 = (R_3 + R_5 R_6) \frac{\sum Q_i^{0.38} l_i}{(c_w \Delta\tau_w)^{0.38}} + 2 R_4 \frac{\sum Q_i^{0.76} l_i}{(c_w \Delta\tau_w)^{0.76}} \frac{1}{R_l^{0.19}} \quad (7)$$

*3.3. Determination of optimal depth in the soil deposit branched pipelines*

Total (investment and exploitation) costs consist of the costs of construction (excavation, leveling and filling of channels) and mechanical (delivery, installation and finishing work on laying pipelines) works as a function of pipeline diameter, can be represented by equation:

$$T_{sis} = S_1 + H S_2 + S_3 \frac{t_{ze}^{sr} + \theta_F^{\max} \exp(-SH) - t_{hw}^{sr}}{R_{iz} + S_4 \ln\left(1 + 4H^2 / b^2\right)^{0.5}} \quad (8)$$

In section functions Y5 and Y6 (12):

$$Y_5 = R_{iz} + S_4 \ln\left(1 + S_5 H^2\right)^{0.5}, \quad Y_6 = \frac{S_3}{S_4} \left[ \frac{S \theta_F^{\max}}{\exp(SH)} + S_4 S_5 \frac{H}{1 + S_5 H^2} \frac{t_{ze}^{sr} - \tau_{hw}^{sr} + \theta_F^{\max} / \exp(SH)}{R_{iz} + S_4 \ln\left(1 + S_5 H^5\right)} \right] \quad (9)$$

there is an optimum depth of laying pipelines cold water, Figure 6 .

## 4.Analysis of the result of calculation and analysis

In order to perform an analysis of the optimal speed, optimal specific pressure drop and optimum depth of laying pipelines cold water adopt conditional scheme tubing system whose characteristics are shown in Table T2. To analyze and determine the optimal parameters we adopt the following values of the parameters, constants and physical properties of water and soil, expression (10).Based on the data acquired on the basis of characteristics usvojnih heat and cooling source and network configuration, performed the analyzes and calculations. The result of analysis and calculations are shown in Thee T3 and Figures 2,3,4 and 5.

**Tabela 2.**

| variant | Qmax(KW) | ΣLi(m) | ΣQiLi | ΣQi^0.5*Li | ΣQi^0.38*Li | ΣQi^0.76* Li |
|---|---|---|---|---|---|---|
| 1 | 2000 | 800 | 877500 | 26063 | 11362 | 160448 |
| 2 | 10000 | 4800 | 20040000 | 294222 | 108527 | 2607869 |
| 3 | 14000 | 8735 | 43655000 | 593064 | 214052 | 5484475 |

$$A_d = 0.4359; A_{li} = -35(Eu/m); B_{li} = 3887(Eu/m^2); A_{kv} = 12(Eu/m); B_{kv} = 3069(Eu/m^2);$$
$$C_{kv} = 2206(Eu/m^3); m = 0{,}15; \beta_m = 0{,}25; \eta_{ps} = 0.75; \alpha = 0{,}20; r_{pmw} = 0{,}12(1/god);$$
$$r_{ps} = 0{,}10(1/yearly); r_{const} = 0.08(1/yearly); C_{cons} = 12(Eu/m^3); C_{ps} = 500(Eu/KW);$$
$$Z_{ps}^{cw} = 1650(h/god); Z_{ps}^{hw} = 3000(h/yearly); K_{cm} = 0.80(W/m^2K); N_{hl} = 2201(h/yearly); \quad (10)$$
$$N_{hy} = 4570(h/yearly); \Delta\tau_{cow} = 8^0 C; c_{cow} = 4{,}205(KJ/kgK); \rho_{cow} = 1000(kg/m^3);$$
$$\mu_{cow} = 1547 \cdot 10^{-6}(Pa \cdot s); \Delta\tau_{hw} = 20^0 C; c_{hw} = 4{,}183(KJ/kgK); \rho_{hw} = 998(kg/m^3);$$
$$\mu_{hw} = 1004 \cdot 10^{-6}(Pa \cdot s); C_{hen} = 40(Eu/GJ); C_{coen} = 20(Eu/GJ) C_{een} = 0.15(Eu/KWh);$$
$$t_{env} = 13.1^0 C; \tau_{cow,me} = 7^0 C; \lambda_{gro} = 1.75(W/mK); \rho_{gro} = 1600(kg/m^3); c_{gro} = 1.44(KJ/kgK);$$
$$\lambda_{insu} = 0.035(W/mK); S = 0.3623(1/m); \theta_F = t_{a,gro} - t_{gro}^{sr} = 22.4 - 13.1 = 9.3^0 C; \tau_{cow.}^{sr} = 10^0 C;$$

## 5. Conclusion

Based on the above it can be said that the shape of the flow cost function pipeline network has an impact on the optimal size of the tubing system parameters, namely the size of the optimal speed and optimal specific pressure drop flow cold and hot water, Figure 4 and 5
Expressions are put in such a mathematical form that can easily determine the influence of many variables. Among others see the effect of heat (cooling) loads and network configuration table T2. the size of the optimal parameters. The analysis shows that the optimal current velocity does not depend on the type of functions mighty annual cost of piping network. Dependence on temperature distribution of water and depending on the price of electricity velocity range between the following limits: the cold water of 2.2 (m / s) to 4.0 (m / s), the hot water of 1.33 (m / s) to 3.3 (m / s), as seen in Figure 4.
Optimum specific pressure drop depends on the type of the function of the annual cost of piping network. Dependence on temperature distribution of water and depending on the price of electricity optimum specific pressure drop ranges between the following limits: **the cold water** from the 130 (Pa / m) to 400 (Pa / m), the lower values relate to higher thermal loads and greater length of piping network, **for hot water**, increasing water temperature optimum specific pressure drop increases, with increasing heat load and the length of the pipeline network, specifically the pressure drop decreases, Figure 5. The optimum flow velocity and specific pressure drop depends on the size of the heat (cooling) load for transport, temperature differences of water, ambient temperature, time of heating or cooling season, network characteristics, cost of heat, cooling and electricity prices gas stations and duration of pump operation. Increasing heat (cooling) loads, the temperature difference at the same, and the optimum flow velocity of the fluid increases. At the same heat or cooling load and the temperature difference at the same, increasing the length of the route optimal rate of fluid flow tends to slow decline. Increasing the price of electricity, the same network parameters, the optimal rate of fluid flow decreases significantly. By increasing the temperature difference, the same network parameters, the optimal rate of fluid flow is reduced. Price of thermal energy at optimal speed no significant impact. By increasing the temperature difference supply and return water, the same cooling loads and the same network parameters, optimum specific pressure drop increases. Increasing the length of the cooling load and the network, at the same price of heat and electricity, the optimum specific pressure drop decreases. Under the same network parameters with decreasing price of

thermal energy we reduce the optimal specific pressure drop. With the increasing cost of electricity we reduce specific pressure drop.

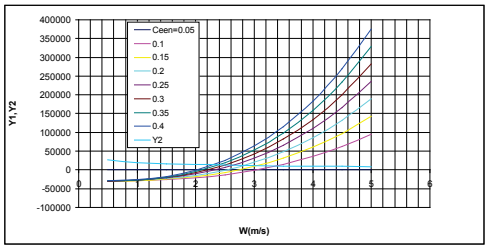


**Figure 2** . Stream function Y1 and Y2

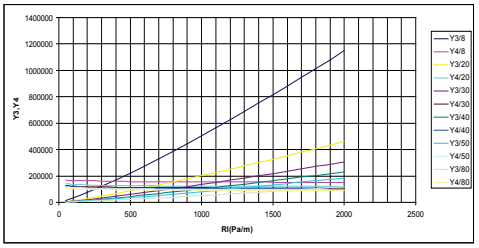


**Figure 3.** Stream function Y3 and Y4

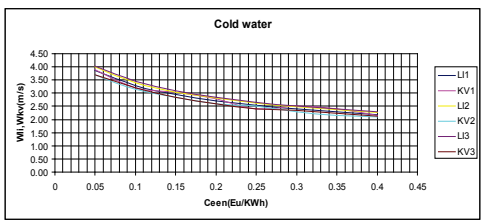


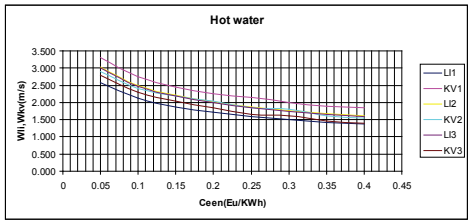


**Figure 4.** The dependence of the optimum velocity for hot and cold water, depending on the variant of the system of supply, the cost of pipeline characteristics (linear or quadratic) and electricity prices synergy.

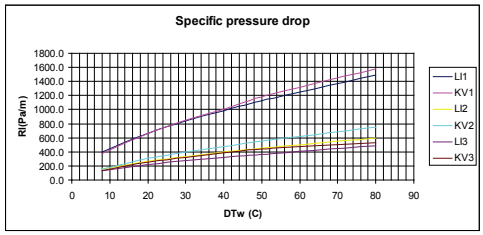


**Figure 5.** The dependence of the optimal specific pressure drop of hot and cold water, depending on the variant of the system of supply, cost attributes pipelines (linear or quadratic) and the cost of electricity.

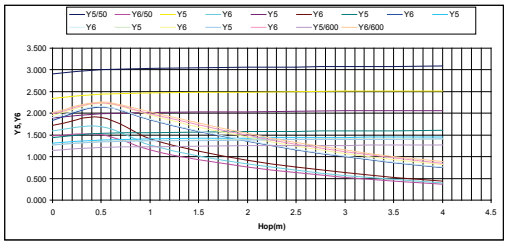


**Figure 6** Dependence Y5 and Y6 depth of laying pipelines and the diameter of the pipeline


**Figure 7**. The optimum depth of laying pipelines cold water, depending on the diameter of the pipeline

**Tabela 3.**

| DN | 65 | 80 | 100 | 125 | 150 | 200 | 250 | 300 | 350 | 400 | 450 | 500 | 550 | 600 |
|---|---|---|---|---|---|---|---|---|---|---|---|---|---|---|
| DS(mm | 76.1 | 88.9 | 114.3 | 139.7 | 168.3 | 219.1 | 273 | 323.9 | 355.6 | 406.4 | 457.2 | 408 | 558 | 600 |
| Diz(m | 140 | 160 | 200 | 225 | 255 | 315 | 400 | 450 | 500 | 560 | 630 | 700 | 750 | 800 |
| Δiz(mm | 32 | 36 | 43 | 43 | 43 | 48 | 64 | 63 | 72 | 77 | 86 | 96 | 96 | 100 |
| Hop(m) | 0.9 | 0.9 | 0.9 | 0.9 | 0.95 | 1.45 | 1.7 | 1.85 | 1.95 | 2.15 | 2.25 | 2.35 | 2.5 | 2.95 |

Under the same network parameters, increasing the number of pumps there is a reduction of the optimal specific pressure drop. This decrease was significantly with increasing cooling capacity. The presented method of determining the optimum depth of laying pipelines cold

water, Figure 6 and 7, and allows it to be, depending on the geographical regions (climatic conditions), ways of laying pipelines cooling water thermo physical properties of the country, the price of heating and cooling energy. Builder's works and network characteristics accurately determine the optimal pipeline depth of cooling water for cooling and air conditioning urban environment.

## 6. Nomenclature

$P_6 = 0.1354 \cdot 10^{-3} \mu^{0.25} \left[ r_{ps} C_{ps} (1+m) + Z_{ps} C_{een} \right] (1+\beta_m) (\rho_w / c_w)^{0.375} \left( \sum l_i / \eta_{ps} \right)$; $P_1 = A r_{pnw}$;
$P_2 = 11.34 \left( \tau_w^{me} - t_{env} \right) (1+\alpha) K_{pnw} N_{env} C_{hen}$; $P_3 = 2\delta_{insu}$; $P_4 = 1.129 r_{pnw} B / (c_w \rho_w)^{0.5}$; $T_{pu} = const$;
$P_5 = 1.275 r_{pnw} C / c_w \rho_w$; $P_7 = 1.158 / (c_w \rho_w)^{0.5}$; $R_1 = 10^{-3} (1+\beta) \left( \sum l_i / \rho_w \eta_{ps} \right) \left[ r_{ps} (1+m) C_{ps} + Z_{ps} C_{een} \right]$;
$R_2 = A r_{pnw} \sum l_i$; $R_7 = 2\delta_{insu} \sum l_i$; $R_3 = B r_{pnw} A_d / \rho^{0.19}$; $R_4 = C r_{pnw} A_d^2 / \rho^{0.38}$; $R_6 = A_d / \rho_w^{0.19}$;
$R_5 = 11.34 \left( \tau_w^{me} - t_{env} \right) (1+\alpha) K_{pnw} N_b C_{een}$; $S_3 = 3.6\pi 10^{-6} (1+\alpha) N_{co} D_{insu} C_{coen}$; $S_4 = 1/2\pi\lambda_{gro}$; $S_5 = 4/b^2$;
$S_1 = C_{cons} r_{cons} \left( 2m_1 b + b D_{insu} - 1.517 D_{iz}^2 \right) + r_{pnw} \left( A_1 + B_1 D_{insu} + C_1 D_{insu}^2 \right)$; $S_2 = 2b r_{consu} C_{consu}$; $S_5 = 4/b^2$;

$A_{li}, B_{li}, A_{sq}, B_{sq}, C_{sq}$ - coefficients which depend on the way of laying the pipeline network and meat requirements; $Eu/m; Eu/m^2; Eu/m^3$; $D$ - diameter of the pipeline, $m$; $D_{ins}$ - diameter piping insulation $m$; $C_{hen}$ - price of thermal energy $Eu/KWh$; $C_{coen}$ -, Prices cooling energy $Eu/KWh$; $C_{ps}$ - unit cost of installed power pumping station $Eu/KW$; $N_{col}, N_{he}$ - the duration of the period of cooling or heating, $h/yearly$; $K_{cm}$ - heat transfer coefficient of the pipeline supply network, $W/m^2K$; $r_{pnw}, r_{ps}, r_{gro}$ - Return on equity factor to pipe network, pumping stations and construction works, $1/yearly$; $t_{env}$ - mean ambient temperature during heating and cooling, $C$; $\tau_{w,me}$ - average lows in the distribution of water cooling-and heating period, $C$; $R_{iz}$ - thermal resistance layer $mK/W$; $S$ -designation, $1/m$; $T_{sis}$ - annual cost of the system, $Eu/yearly$; $Q_i$ - thermal power budget appropriate sections, $KW$; $Q_{\max}$ - , maximum thermal power of the heat budget (cooling) sources $KW$; $Z_{ps}$ - number of hours of pumping stations $h/yearly$; $\alpha$ - local coefficient of heat loss $\beta$ -; coefficient of local resistance network $\delta$ - Thin wall tubing system, $mm$; $\mu$ -dynamic viscosity, $Pas$; $\eta_{ps}$ -efficiency values pumping stations, $\Delta\tau_{w,me}$ - mean temperature difference energy carrier , $C$; $\rho_w$ - density of water, $kg/m^3$;

## 7.References

[1] Šefik M.B (1994) *Analysis and optimization of effectiveness and district heatingand district cooling systems using energy obtained from the combustion of municipal waste hard, Ph.D. thesis,* Pristina,
[2] Bordavkin L,Berezin L (1987) *Sooruženie magistralnjih truboprovodov,* Nedra, Moskva
[3] Zinger N.M, (1986) *Gidravaličesnie i toplovije režimi toplofikacionjih sistem*, Energoatomizdat, Moskva
[4] Sokolov E.J,(360) *Teplofikacija i teplovije seti,* Energoizdat, Moskva
[5] Šefik M.B, Zlatibor V, Blagoje N, Dejan L,(2007) *Studija o toplifikacije grada Leposavića*, Kosovska Mitrovica
[6] Isoplis YUGO.d.oo. *Tehničaka dokumentacija 2013*.Beograda .
[7] A.D.Izolir *Tehnička dokumentaciaj 2013*, Zrenjanin

# MECHANICAL PROPERTIES OF FIBER REINFORCED CONCRETE MADE WITH POLYPROPYLENE FIBERS

**Dragica Jevtić[1], Aleksandar Savić[2]**

[1] Professor, University of Belgrade, Faculty of Civil Engineering, Belgrade, Serbia, Bulevar kralja Aleksandra 73
e-mail: dragica@imk.grf.bg.rs
[2] Teaching fellow, University of Belgrade, Faculty of Civil Engineering, Belgrade, Serbia, Bulevar kralja Aleksandra 73
e-mail: sasha@imk.grf.bg.rs

**Abstract.** Experimental research results of basic physical and mechanical properties of fiber reinforced concrete are presented in this paper. The concrete was made with two fractions of aggregate (0/4mm and 4/8mm). Fresh concrete consistency and density were monitored on fresh concrete. Compressive and splitting strength, as well as watertightness were monitored on hardened concrete. Also, dynamic properties (toughness) were also evaluated, according to "Drop-weight" test.

## 1. Introduction

Dispite the fact that it is the most commonly used building material, concrete has a number of shortcomings; its low values of tensile strength, large deformations of creep and shrinkage and low ductility seem to be the most notable of all. One of the ways to obtain concrete with improved physical, mechanical, rheological, and other properties is by adding fibers. Fiber reinforced concretes are composite materials obtained by reinforcing cement matrices by distributing the fibers more or less evenly. The simoultaneous use of short fibers and smaller aggregates (the so-called fine-grained concrete, with the grain sizes up to 8mm), reduces the tendency towards the grouping of the fibers and the creation of clusters (the "balling" effect).
Both loading and shrinkage lead to crack growth in concrete and should be controlled in various structures, for instance pavements, runways for airports, and continuous slab-type sleeper for high-speed trains. In these types of structures, effective prestressing for crack control purposes is usually very difficult, especially in the two principal directions. So, dispersed short fibre reinforcement seems to be the best solution in this case.
It has been shown by various researchers [1,2] that cracking resulting from shrinkage and differential settlements during the fresh state can be effectively inhibited by a monofilament type of polypropylene fibre reinforcement. Because of the large numbers involved, fibres can be properly distributed throughout the mortar matrix, around the coarse aggregate particles, and even in boundary layers of concrete elements. The polypropylene fibres (see Fig. 1) have a low Young's modulus (Table 1), so they can't prevent the formation and propagation of cracks at high stress level, nor provide an additional protection of concrete elements by bridging large cracks.

**Figure 1.** Polypropylene fibers

Fiber reinforced smaller aggregate grain sizes concretes (with grains of diameter $\leq$8mm) are characterized by higher tensile and flexural strength, lower shrinkage deformation, and increased resistance to impact and durability - as compared to conventional concrete of the same composition (but with grains of diameter $\leq$16mm or d$\leq$32mm). Besides the contribution to a more homogenous layout of fibers within the composites, the use of smaller aggregate grain sizes reduces the risk of concrete segregation - which affects the decrease in permeability and the increase in freeze-thaw resistance, reduced water absorption, etc. Leaving out larger grains of aggregates reduces the occurrence of stress concentration in matrix, which can lead to higher mechanical strength.

**Table 1.** The basic properties of monofilament polypropilene fibers

| **Fiber designation:** | **FIBERS** |
|---|---|
| Raw material | Polypropylene (100%) |
| Production method | Istezanjem i vučenjem |
| Fiber type | Monofilament, flat fibers |
| Cross section | Round |
| Diameter | 0.037mm |
| Length | 12mm |
| Aspect ratio (*l*/*d*) | 324 |
| No of fibers/kg | $240*10^6$ |
| Density | 0.91 kg/l |
| Tensile strength | 300-400 MPa |
| Modulus of elasticity | ~4000 MPa |
| Elongation at break | 22% |

In practice, some structural members are required to resist repeated impacts, such as concrete railroad ties, airport runways, beam-column joints under earthquake loading, and so on. Some experimental studies require the more or less adequate simulation of certain types of dynamic loading. Moreover, the total fracture energy of a beam under repeated impact loading is likely to be different than that obtained in tests that lead to failure of a specimen after a single strike. Dynamic properties (toughness) of polypropylene fibre reinforced concrete were evaluated according to "Drop-weight" test, in order to assess the amplitude and energy, with respect to the gradual deterioration of the member after each impact.

## 2. Experimental part

Polypropylene fiber reinforced concretes, with 8mm maximum aggregate grain and with the aid of 12 mm fibers (manufacturer: Sika, Switzerland) were made, with the aim of extensive appropriate experimental investigations, which were carried out in the Laboratory for Materials of the Institute for Materials and Structures, Civil Engineering Faculty, University of Belgrade. Three concrete mixtures were designed for this purpose: reference, with 0 g/m$^3$ (labeled "1"), concrete designated as "2" with 600 g/m$^3$, and concrete designated as "3" with 900 g/m$^3$ of polypropylene fibers. Table 1 shows the basic properties of monofilament polypropylene fibers used in this study.

The amount of cement in all concrete mixtures was constant (400 kg/m$^3$). Cement, with the label PC 20M(S-L) 42.5R"Lafarge" and with the specific mass of 3.00 g/cm$^3$ Beocin, was used as a binder. The w/c ratio was also the same for all four concrete mixtures (w/c = 0.5). The projected consistency in all mixtures corresponded to the usual conditions in practice, and was located within the limits of plastic consistency.

Aggregate with two fractions, I (0/4 mm) and II (4/8 mm), was used in all the mixtures. Contribution of the first fraction in the entire aggregate mass amounted to 55%, while the second amounted to 45%. The coresponding masses for 1 m$^3$ of concrete were 950 kg/m$^3$ and 777 kg/m$^3$ for fractions I (0/4 mm) and II (4/8 mm), respectively. The natural aggregate used in these studies was the river aggregate "Moravac". As stated before, only the quantity of fibers was changed in the mixtures.

Mixing process was conducted according to the following procedure in dosing the components (for concretes designated as "2" and "3"): cement and aggregates were dosed, and mixed for 30s; without any interruption of mixing, half of the amount of polypropylene fibers was added during the following 30s of mixing, after that, during the next 30s, the water was added, while mixing; then, without the interruption of mixing, the rest of polypropylene fibers were added to the mix during the next 30s; after the dosing of all components, the fresh concrete was mixed for additional 180s. During this phase the work of the mixer was sometimes shortly stopped, in order to clean the mixing shovel from fibers - which were then returned to the mix, and the mixing was continued.

Testing the consistency of fresh concrete was performed according to the standard SRPS EN 12350-2:2010 Testing fresh concrete - Part 2: Slump test. The values of slump, obtained in these tests, are shown in Table 2. Density of fresh concrete was determined according to the standard SRPS EN 12350-6:2010 - Testing fresh concrete - Part 6: Density. Fresh concrete density is also shown in Table 2. The entrained air content was also measured on fresh concrete (Table 2), according to SRPS EN 12350-7:2010 - Testing fresh concrete - Part 7: Air content - Pressure methods.

**Table 2.** The results of tests conducted on fresh concrete

| Concrete designation | Density | Slump | Entrained air |
|---|---|---|---|
| | ($kg/m^3$) | (mm) | (%) |
| "1" | 2363 | 40 | 2.5 |
| "2" | 2365 | 40 | 3.7 |
| "3" | 2348 | 35 | 4.1 |

Tests on hardened concrete included: determination of tensile strength by pull-off method ($f_{t,28}$) on 20cm cube samples, in accordance with SRPS 1542:2010, tensile shear strength ($f_{\tau s,28}$) on the 4x4x16cm prisms (according to disposition on Figure 2), water absorption (u) on 100mm cubes as well as shrinkage deformation ($\varepsilon_{sh}$) measured on the 40x40x160mm prisms, according to SRPS B.C8.029 - Cements - Dry shrinkage of cement mortars. All these tests were performed on the 28 days old samples.

**Figure 2.** Shear strength disposition, tests conducted on 4x4x16cm prisms

The obtained results of investigation made on hardened concretes are shown in the Table 3.

Ultrasound pulse velocity (v) (results shown in Table 3) was also recorded on 28 days old specimens, based on 8 measurments of time in μs, for each of concretes, on the same length of 20 cm, with the use of *Pundit ultrasonic* test equipment (Fig. 3).

**Table 3.** The results obtained on hardened concrete

| Concrete designation | $f_{t,28}$ | $f_{\tau s,28}$ | u | $\varepsilon_{sh}(28)$ | v |
|---|---|---|---|---|---|
| | [MPa] | [MPa] | [%] | [‰] | [m/s] |
| "1" | 3.7 | 13.7 | 3.68 | 0.55 | 4577 |
| "2" | 4.1 | 15.6 | 3.79 | 0.50 | 4561 |
| "3" | 4.3 | 13.9 | 3.52 | 0.46 | 4531 |

The response of these concretes to dinamic load was measured according to "Drop-weight" test, modified to be executed on 4x4x16cm specimens, three for each concrete. The total energy amount $E_N$ consumed after N impacts can be presented as:

$E_N = N \square * E = \square N * \square m * g * h$ , where the above mentioned symbols stand for:

E – energy consumed in one impact [N·m = J];
$E_N$ – total energy after N impacts [N·m = J];
N –number of impacts,
m – weight mass [kg];
v – impact mass velocity [m/s];
g – acceleration due to gravity [≈ 9,81 $m/s^2$];
h – initial height [m].

The results of this investigation are presented in Table 4.

**Table 4.** Drop weight test results

| Specimen | No. of impacts[n] | Energy [J] | Average energy [J] |
|---|---|---|---|
| 1-1 | 17 | 16,76 | **9,53** |
| 1-2 | 7 | 6,90 | |
| 1-3 | 5 | 4,93 | |
| 2-1 | 15 | 14,79 | **12,49** |
| 2-2 | 11 | 10,85 | |
| 2-3 | 12 | 11,83 | |
| 3-1 | 15 | 14,76 | **12,15** |
| 3-2 | 15 | 14,79 | |
| 3-3 | 7 | 6,90 | |


**Figure 3.** Ultrasound pulse velocity measurement equipment

## 3. Conclusion

Investigation on polypropylene fiber reinforced fine-grained concrete series was done on concrete series with (series "2" and "3") and without fiber reinforcement (series "1", regarded as reference concrete series). On the basis of conducted experiments, the conclusion can be drawn that the addition of polypropylene fibers influences the properties of concrete, both in fresh and hardened state [3,4]. Namely, the addition of fibers influences the fresh state properties; in the first instance it causes increase of entrained air. This increase is proportional to the content of fibers added to the mix. The content of polypropylene fibers influences the consistency of fine-grained concretes, changing their slump from 4cm (for reference concrete without fibers, designated as "1") to 3,5cm (for series "3" with the higher amount of fibers of 900 g/m$^3$).

Density of hardened concrete made with the fiber reinforcement changes insignificantly, similar to the compressive strength of such composites.The absorption reduction amounts

to 4,3% (when comparing series "3", with the highest amount of fibers, to reference). Shear strength increases in the presence of fiber reinforcement up to 14%, although it shown no linear connection with the increase of fiber content. Tensile strength, tested with the pull-off method, increased up to 16% with the fiber content increase. As for the shrinkage, this rheological property decreases with the fiber content, thus showing linear trend of decrease down to 14%.

Based on the "Drop-weight" test, such reinforcement of concrete can be made which can improve impact resistance [5,6] of concrete up to 30% in the case of composites presented in this paper. This increase doesn't seem to depend on the fiber content, as it results in similar impact resistance for both concretes II and III. Ultrasound pulse velocity tests conducted in this research show decrease of velocity, thus indicating the loss in compactness of concrete with the rise in amounts of fibers, in almost linear rate. The use of polypropylene fiber content between 600g/m$^3$ and 900g/m$^3$ is advised, depending of the specific properties we want to modify, and having in mind that higher amounts of fibers than this could lead to further loss of compactness due to incorporation of fibers.

*Acknowledgements.* The work reported in this paper is a part of the investigation within the research project TR 36017 "Utilization of by-products and recycled waste materials in concrete composites in the scope of sustainable construction development in Serbia: investigation and environmental assessment of possible applications", supported by the Ministry of Education, Science and Technological Development, Republic of Serbia. This support is gratefully acknowledged.

## References

[1] Wang N., Mindes S., Ko K. (1996) Fibre reinforced concrete beams under impact loading, *Cement and Concrete Research*, **26**, No. 3, pp. 363-376,

[2] Qian C.X., Stroeven P. (2000) Development of hybrid polypropylene-steel fibre-reinforced concrete, *Cement and Concrete Research*, **30**, Issue 1, pp. 63–69,

[3] Aćić M., Jevtić D. (2009) Mikroarmirani malteri i betoni - sastav, svojstva i primena, *Savremena teorija i praksa u graditeljstvu*, ZIBL, Banja Luka, str. 1-19, ISBN 978-99938-26-20-0,

[4] Jevtić D. (2010) Modifikovanje svojstava maltera i betona mikroarmiranjem, Predavanje po pozivu, *Teorijska i eksperimentalna istraživanja konstrukcija i njihova primena u građevinarstvu*, Zbornik radova, Knjiga 1, Niš,18.-19. mart., ISBN 978-86-80295-86-2, COBISS.SR-ID 173899532, str. 103-126.

[5] Jevtić D., Zakić D., Savić A. (2011) Relevant static and dynamic methods for toughness evaluation of fiber reinforced concrete, *Building materials and structures*, **LIV 1**, YU ISSN 0543-0798, UDK: 624.012.45;666.982.2; 620.178.2 = 861, originalni naučni rad, COBISS.SR-ID 6725890, pp. 3-27.,

[6] Jevtic D., Zakic D., Savic A., Radevic A. (2011) Properties of self compacting concrete reinforced with steel and synthetic fibers, *International Symposium about research and application of modern achievements in civil engineering in the field of materials and structures*, Society for materials and structures testing of Serbia, DIMK, Tara, COBISS.SR-ID 186877196, ISBN 978-86-87615-02-1, Proceedings, pp. 115-124.

# DEVELOPMENT OF SOFTWARE PAK-M FOR CALCULATION OF MAGNETOSTATIC FIELD

**Milan Blagojević[1], Miroslav Živković[2]**

[1] Faculty of Engineering,
University of Kragujevac, Sestre Janjić 6, 34000 Kragujevac, Serbia
e-mail: blagoje@kg.ac.rs
[2] Faculty of Engineering,
University of Kragujevac, Sestre Janjić 6, 34000 Kragujevac, Serbia
e-mail: zile@kg.ac.rs

**Abstract.** This paper presents the development of software PAK-M for calculation of magnetostatic field. For the low-frequency problems, a subset of Maxwell's equations (Biot-Savart law - divergence of magnetic flux density is null, and Ampère's law - the curl of the magnetic field is equal to the static electric current density) are invoked to compute the magnetic field and its related quantities due to electric currents and permanent magnets. Generally, the quantities of interest in magnetostatic analysis are field intensity, magnetic flux density, force, torque, inductance, and flux linkage. The program is based on a potential formulation. PAK-M can perform linear and nonlinear magnetostatic analysis over a user-defined domain for user-defined sources and boundary conditions. PAK-M can help study a large number of devices and address numerous magnetic and electromechanical phenomena. In example shown in this paper we consider a small solenoid, wound around iron and calculate the magnetic potential. Since the coil is very thin, it is assumed that sheet in which a current is flowing is thin and the potential of this sheet is a constant. The coil is sectioned along the axial plane. Solution calculated by in-house software PAK-M is compared by solutions of world leading software.

## 1. Introduction

Analysis of electromagnetic phenomenon provides insight into the response of structure, and thus represents a tool for regulating these fields to attain specific responses [1]. Many problems of practical engineering importance do not have an analytical solution. FEA can be used to analyze the linear or nonlinear electric or magnetic behavior of devices [2]. An analysis can be static, harmonic or transient state in nature [3]. Most of the physical issues in energy engineering can be described by quasistatic phenomena. Slowly varying and periodic fields up to 10 kHz are considered to be quasi-stationary [3].
Magnetic analysis is used to design or analyze a variety of devices such as solenoids, electric motors, actuators, induction furnaces, magnetic shields, permanent magnets, magnetic disk drives, high voltage transmission lines and so forth [4-6]. Generally the quantities of interest in magnetostatic analysis are magnetic flux density, field intensity, forces, torques, inductance, and flux linkage.
Due to the complexity of the practical applications of the technique, it is not unusual to have magnetic, dielectric and thermal couplings in a single model [7].

## 2. Mathematical model

The problem of electromagnetic analysis is a problem of solving a set of Maxwell's equations subject to given boundary conditions [3]. Maxwell's equations are fundamental equations that govern all macroscopic electromagnetic phenomena. Equations are valid in all circumstances regardless of the medium and the shape of the integration volume, surface, and contour. The field equations are expressed in terms of the derived field quantities, Equations (1)-(5)

$$\nabla \times \mathbf{E} = -\frac{\partial \mathbf{B}}{\partial t}, \tag{1}$$

$$\nabla \times \mathbf{H} = \mathbf{J} + \frac{\partial \mathbf{D}}{\partial t}, \tag{2}$$

$$\nabla \cdot \mathbf{D} = \rho, \tag{3}$$

$$\nabla \cdot \mathbf{B} = 0, \tag{4}$$

$$\nabla \cdot \mathbf{J} = -\frac{\partial \rho}{\partial t}. \tag{5}$$

where $\mathbf{E}$ is electric field, $\mathbf{D}$ is electric flux density, $\mathbf{H}$ is magnetic field, $\mathbf{B}$ is magnetic flux density, $\mathbf{J}$ is electric current density, and $\rho$ is electric charge density.

*Constitutive relations*. Among the five equations above, only three are independent for the case of time varying fields and thus are called independent equations. The other two equations can be derived from the independent equations and thus are called auxiliary or dependent equations. Maxwell's equations become definite when constitutive relations between the field quantities are specified. The constitutive relationships describe the macroscopic properties of medium being considered. In the most general case, these derived fields are complicated nonlocal, nonlinear functional of the primary fields $\mathbf{E}$ and $\mathbf{B}$.

$$\mathbf{D} = \mathbf{D}\left(t, \mathbf{x}, \mathbf{E}, \mathbf{B}\right), \tag{6}$$

$$\mathbf{H} = \mathbf{H}\left(t, \mathbf{x}, \mathbf{E}, \mathbf{B}\right). \tag{7}$$

Maxwell's equations do not make a distinction between low and high frequency applications, but for practical applications it is possible to adapt them to these two situations. PAK-M addresses limiting case of Maxwell's equations, magnetostatic problems, in which the fields are time-invariant. In this case, the fields $\mathbf{H}$ and $\mathbf{B}$ must satisfy:

$$\nabla \times \mathbf{H} = \mathbf{J}. \tag{8}$$

$$\nabla \cdot \mathbf{B} = 0. \tag{9}$$

For linear materials the fields and fluxes are simply related by a constitutive relationship between $\mathbf{H}$ and $\mathbf{B}$ for each material:

$$\mathbf{B} = \mu \mathbf{H}. \tag{10}$$

If a material is nonlinear, μ is actually a function of $\mathbf{B}$:

$$\mu = \frac{\mathbf{B}}{\mathbf{H}(\mathbf{B})} . \tag{11}$$

The constitutive parameter $\mu$ denotes permeability (henrys/meter) of the medium. The parameter is tensors for anisotropic media, and scalar for isotropic media. For inhomogeneous media, it is function of position, whereas for homogenous media is is not.
PAK-M goes about finding a field that satisfies (8)-(11) via a magnetic potential approach. Flux density is written in terms of the magnetic potential $\mathbf{A}$ , as:

$$\mathbf{B} = \nabla \times \mathbf{A} . \tag{12}$$

Now, this definition of $\mathbf{B}$ always satisfies (8). Then, (9) can be rewritten as:

$$\nabla \times \left( \frac{1}{\mu(\mathbf{B})} \nabla \times \mathbf{A} \right) = \mathbf{J} . \tag{13}$$

For a linear isotropic material, assuming the Coulomb gauge, $\nabla \cdot \mathbf{A} = 0$ , eq. (13) reduces to:

$$-\frac{1}{\mu(\mathbf{B})} \nabla^2 \mathbf{A} = \mathbf{J} . \tag{14}$$

PAK-M retains the form of (14), so that magnetostatic problems with a nonlinear $\mathbf{B}$ - $\mathbf{H}$ relationship can be solved.

### 3. Incremental finite element equations implemented in PAK-E software

The derivation of the finite element balance equations is based on equations given in the previous text. Galerkin method is then applied, for derivation of FE equations. Based on Poison differential equation (14), the following can be written

$$\int_{\mathrm{V}} \left[ h_{\mathrm{I}} \sum_{\mathrm{j}=1}^{3} \frac{\partial}{\partial \mathrm{x}_{\mathrm{j}}} \left( \varepsilon_{\mathrm{j}} \frac{\partial A}{\partial x_{\mathrm{j}}} \right) \right] \mathrm{d}V + \int_{\mathrm{V}} h_{\mathrm{I}} \rho \mathrm{d}V = 0 \qquad \mathrm{I} = 1, 2, \ldots, \mathrm{N} . \tag{15}$$

where $h_{\mathrm{I}}$ are interpolation functions and N is number of nodes per element, and $V$ is finite element volume. Three-dimensional (3D) isoparametric finite element is applied, as defined in [8,9]. Interpolation functions, geometry and number of nodes are also adopted. Magnetic potential $A$ in a point of element, defined in natural coordinates $r, s, t$ is given as:

$$A(r, s, t) = \sum_{\mathrm{I}=1}^{\mathrm{N}} h_{\mathrm{I}} \mathbf{A}^{\mathrm{I}} . \tag{16}$$

or in matrix form,

$$A = \mathbf{H}\mathbf{A} , \tag{17}$$

where $\mathbf{H}$ is row matrix of interpolation functions and $\mathbf{A}$ is column matrix of nodal potentials. Applying the partial integration and Gauss theorem on the first integral in (15), the following is obtained

$$\int_V \left[ h_I \sum_{j=1}^{3} \frac{\partial}{\partial x_j} \left( \varepsilon_j h_{J,j} \right) \right] dV \mathbf{A}^J = \\ = -\int_V \left( \sum_{j=1}^{3} \varepsilon_j h_{I,j} h_{J,j} \right) dV \mathbf{A}^J + \int_S \left[ h_I^s \sum_{j=1}^{3} \varepsilon_j \frac{\partial \mathbf{A}}{\partial x_j} n_j \right] dS \quad (18)$$

When element surface flux $q_n$ is given and based on, the following can be written

$$\int_S \left[ h_I^s \sum_{j=1}^{3} \varepsilon_j \frac{\partial A}{\partial x_j} n_j \right] dS = \int_S h_I^s \rho_s dS = Q_I^{\rho_s}, \quad (19)$$

where $Q_I^{q_n}$ are electric charge density column matrix components and $h_i^s$ are interpolation functions for nodes on surface.
Using (18), (19), (15) and (16), the system of equations of the following form is obtained

$$\mathbf{KA} = \mathbf{Q}, \quad (20)$$

where matrix components for $K$ and column matrix $Q$ are determined as

$$\mathbf{K}_{IJ} = \mathbf{K}_{IJ}^{\mu}, \quad (21)$$

$$\mathbf{Q}_I = \mathbf{Q}_I^{\rho} + \mathbf{Q}_I^{\rho_s}. \quad (22)$$

Coefficients of permeability matrix $K_{IJ}^{\mu}$ are given by

$$\mathbf{K}_{IJ}^{\mu} = \int_V \left( \sum_{j=1}^{3} \mu_j h_{I,j} h_{J,j} \right) dV = \int_V \left( \mu_x h_{I,x} h_{J,x} + \mu_y h_{I,y} h_{J,y} + \mu_z h_{I,z} h_{J,z} \right) dV. \quad (23)$$

By using interpolation matrix $H$, matrices in (20) can be written in the folowing form

$$\mathbf{K}^{\mu} = \int_V \mathbf{B}^T \mu \mathbf{B} dV, \quad (24)$$

$$\mathbf{K}^{\sigma} = \int_S \mathbf{H}^{sT} \mu \mathbf{H}^s dS, \quad (25)$$

$$\mathbf{Q}^{q} = \int_V \rho \mathbf{H}^T dV, \quad (26)$$

$$\mathbf{Q}^{q_n} = \int_S \sigma \mathbf{H}^{sT} dS. \quad (27)$$

Row matrices $H^s$ contain interpolation functions $h_i^s$ for the surfaces. The matrix **B** in (24) consist of derivatives of interpolation functions with respect to coordinates x, y and z.

In case of 2D, previous expressions remain unchanged, except that integrals over a volume $V$ are practically reduced to integrals over surface $S$ of the finite element, as shown in [8,9]. Interpolation functions $h_1$ have appropriate forms for 2D problem.

Nonlinear magnetostatic analysis is implemented with an implicit iterative method for solving nonlinear problems [8]:

$$\mathbf{K}^{(i-1)}\Delta\mathbf{A}^{(i)} = \mathbf{Q}^{(i-1)} - \mathbf{K}^{(i-1)}\mathbf{A}^{(i-1)}. \tag{28}$$

where matrix $\mathbf{K}^{(i-1)}$ and vector $\mathbf{Q}^{(i-1)}$ correspond to the last known magnetic potential $\mathbf{A}^{(i-1)}$ from the previous iteration. Iterative procedure is continued until potential increment at nodes is not sufficiently low, what can be expressed in the following form:

$$\frac{\left\|\Delta\mathbf{A}^{(i)}\right\|}{\left\|\Delta\mathbf{A}^{(1)}\right\|} \le \varepsilon_r . \tag{29}$$

where $\varepsilon_r$ is selected relative tolerance and $\left\|\Delta\mathbf{A}^{(i)}\right\|$ is magnetic potential increment norm.

## 4. Example: Solenoid

We consider a simple problem - small solenoid. A solenoid is a coil, wound around a metal like iron. When a current is passed through the coil the metal core acts as a magnet. We assume that sheet in which a current flowing is thin and the potential of this sheet is a constant. The coil is sectioned along the axial plane in the figure 2. The potentials of the top and bottom sheets will have equal magnitudes and opposite signs.

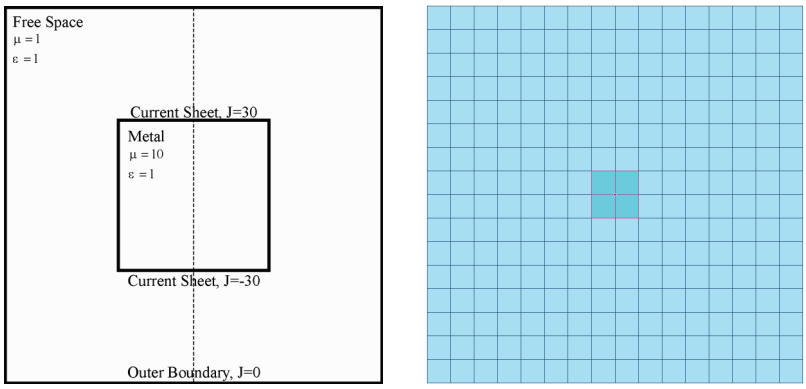


(a) (b)

**Figure 1.** Solenoid axial plane cross-section and computational mesh.

PAK-M numerical results of previously described example are compared with the results obtained by pdnMesh. pdnMesh is a 2 dimensional finite element analysis program, intended to solve Electrostatic, Magneto-static, Heat flow and Fluid dynamic problems.

Figure 4a and 4b shows the scalar field of magnetic potential numerically calculated by software pdnMesh and PAK-M, respectively. Comparison of the numerical analysis results was done by the potential values observation at the nodes marked in Figure 3. Developed software gives excellent results compared with pdnMesh's results.

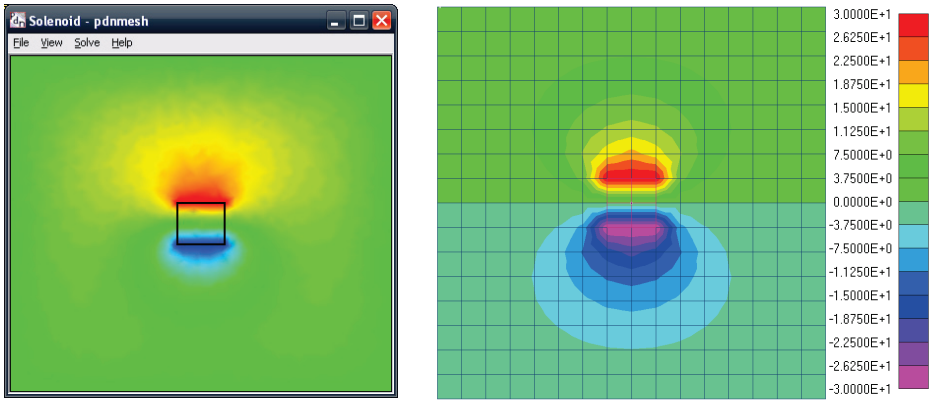


(a) (b)

**Figure 2.** Field of magnetic potential in Solenoid: (a) pdnMesh, (b) PAK-M.

## 5. Conclusions

PAK-M, the DC magnetic (magnetostatic) module of software PAK Multyphysics, can perform linear and nonlinear magnetostatic analysis for 2-D, axisymmetric and 3D models. Results obtained by PAK-M are magnetic flux density, field intensity, potential, permeability, energy, magnetic forces, torques, and other integral quantities. PAK – M, may be used for analysis of problems, which require calculation of static magnetic fields caused by combination of local and/or distributed direct currents, permanent magnets and also external fields defined by boundary conditions. The magnetic forces can be used for stress analysis in magneto-structural coupling.
Compared with most of academic software that solves these types of problems, program PAK-M has considerably more advanced features (3D elements, surface charges distribution as function of position, nonlinear analyses…). Solution calculated by in-house software PAK-M is equivalent to solutions of world leading software.

*Acknowledgement.* Part of this research has been supported by Ministry of Education, Science and Technological Development, Republic of Serbia, Grant TR32036.

## References

[1] Nedeljkovic M, Filipovic N (2006) Biomagnetic Flow in a Straight Tube Under the Influence of an Applied Magnetic Field, *Proceedings of the 1st South-East European Conference on Computational Mechanics, SEECCM-06*, Kragujevac, Serbia, 28-30 June 2006, M. Kojić, M. Papadrakakis (Eds.), pp.365-369.
[2] Hubing T, Su C, Zeng H, Ke H (2008) Survey of Current Computational Electromagnetics Techniques and Software, Technical report: CVEL-08-011.2, Clemson University.
[3] Rothwell J E, Cloud J M (2001) Electromagnetics, CRC Press.
[4] Meeker D (2010) Finite Element Method Magnetics, Version 4.2, User's Manual.
[5] QuickField™, Finite Element Analysis System, Version 5.8, User's Guide, Tera Analysis Ltd.
[6] http://www.comsol.com/
[7] Lewis W R, Nithiarasu P, Seetharamu N K (2005) Fundamentals of the Finite Element Method for Heat and Fluid Flow, John Wiley & Sons, Ltd.
[8] Kojić M, Slavković R, Živković M and Grujović N (1998) Finite element method I – Linear analysis, Faculty of Mechanical Engineering in Kragujevac, University of Kragujevac, Kragujevac.
[9] Bathe K J (1996) Finite Element Procedures, Prentice Hall

# PRACTICAL APPROACH TO INTEGRATED DESIGN OF AERONAUTICAL COMPOSITE CONSTRUCTIONS USING CATIA SOFTWARE

**Zoran Vasić[1], Vanja Stefanović[1], Perica Dragičević[2]**

[1] Military Technical Institute
Ratka Resanovića 1, 11133 Belgrade, Serbia
e-mail: vti@vti.vs.rs
[2] CAD CAM Data
Kneza Višeslava 70a, 11000 Belgrade
e-mail: drape@eunet.rs

**Abstract.** Modern approach to design of aeronautical structures implies effective resolving of different problems during design and stress analysis. In order to obtain optimal aeronautical construction with good weight, stress and stiffness in effective way it is necessary to solve a lot of designing problems. Aeronautical composite structures require careful approach and regard of different parameters that are not relevant in aeronautical metal constructions. Modern CATIA software offers broad capabilities for designing complex composite constructions using predefined laminated material catalogue. Once designed composite construction could be efficacy analyzed by integrated composite engineering module calculating appropriate stress and stiffness. Practical case study on part of realized unmanned aerial vehicle was chosen to show the process of design and stress analysis using adequate modules, and results analysis and discussion. Procedure of iterative design and analysis was chosen in order to obtain optimal aeronautical construction.

## 1. Introduction

Composites are not new materials in the aircraft industry, but it takes time for accepting and improving new technology and in the case of composites, it took several decades. From the first use of glass fiber reinforced composite aircraft structures, composite materials, as the main constructive element, have had rapid expansion of applications, from military aircraft to civil aircraft industry and in production of helicopter rotors and wind turbine blades. Special application of composites is for structure of the Unmanned Aerial Vehicle (UAV), from the beginning of their utilization [2].

High strength of composites comes from layers of fibers that are combined with matrix (resin), and fibers can be made by knitting, weaving, and can be in three – dimensional shape. Metals, as isotropic materials, have the same structural characteristics in any direction, but composites have significant anisotropic characteristics. Layers of fabrics placed in different direction, based upon functionality and load, make composites more efficient than metals, and its best use is when the position of the fibers and the main load are in the same direction [3].

Composite structures in respect to metal aircraft structures have better strength to weight aspect ratio, reduced producing time, simplified production of complicated shapes, use of fiber direction to accomplish special characteristics, reduced number of parts, assemblies and connection parts, reduced time of maintenance, etc.

In the Military Technical Insitute (MTI) aircraft made of composite structures have been designed, with thirty years of experience. With procurement of modern and sophisticated software in the MTI, designing of aircraft structure, development and analyzing of composites structure have been facilitated. CATIA is one of the software that is used for succesfull development of composite structures.

**Figure 1.** Tactical composite unmanned aerial vehicle layout

## 2. Designing of aircraft composite structures

Design of composite aircraft structures is not an easy task. Mechanical, thermical and production properties of the metal structure are well known for years, which is not the case for composite structures, because of the large number of influence factors. Strength and stiffness of composite structures depend on, for example, fibre type and partly on matrix, and modification of any basic material parameters (such as angle of fibre orientation) drastically changes characteristics of composite structures.

CAD software has special modules for creation of every layer in composite, including sandwich construction, which make designing much easier. Designer can use materials from catalog with all mechanical and physical characteristics. Laminate plies have to be connected with predefined 3D entites, such as solid or surface model [1].

### *2.1. Designing of UAV composite elevator*

The integrated approach of designing and analyzing composites structure of the realized medium range tactical unmanned aerial vehicle (UAV) was described, using CATIA software developed by *Dassault Systemes*. Mass estimation and optimization of basic airframe structure can be crucial for UAV performance, endurance and range [6], while iterative optimizing process can be accomplish using CATIA module *Composites Engineering Design* (CPE) and *Generative Structural Analysis*.

Several curent aeronautical projects in the MTI (aircraft *Lasta*, tactical UAVs) are realized using CAD/CAM/CAE programs. Effective designing and defining of complex composite structures are enabled in module *Composites Engineering Design* (CPE). (Fig. 1).

The success of a composite design is dependent upon establishing of material properties early in the process. Establishing an accurate and reliable material property database is one of the most important steps toward achieving a functional design. Experience indicates that the basic material allowables of a specific composite product should be determined utilizing the manufacturing facilities where production will take place prior to finalizing design. The prefered process should approximate the following: define environmental and performance requirements; review available materials against requirements to determine the family of material to be used; determine materials; determine material allowables using material processed at the intended manufacturer; proceed with design based on known material [5].

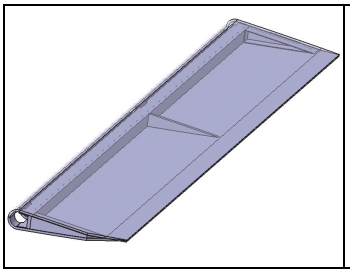

**Figure 2.** 3D computer model of elevator

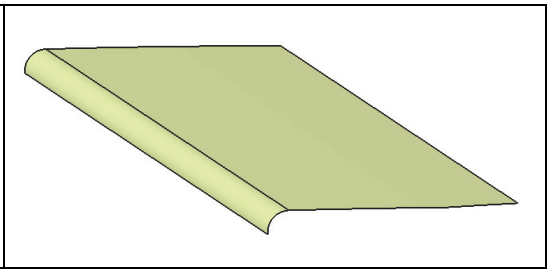

**Figure 3.** Outer surface of upper elevator skin

Several designing phases in module *Composites Engineering Design* (CPE) are described on example of elevator skin of tactical UAV. Bases for defining elevator composite structures are parametric surfaces which define outer surface of elevator skin (Fig. 2 and Fig. 3.).

During the conceptual phase of the composite part design, all of the critical design parameters are established. Maximum loads, both mechanical and thermal, are estimated. Weight, cost, and producibility concerns should be considered in the same time [4]. Preliminary design in the module *Composites Engineering Design* (CPE) comprises defining of material parameteres (*Composites Parameters*), after choosing optimal material that fulfil mentioned criteria. Selection was made of those materials from several composite materials catalogues that already exist in CATIA or were made by customer. This is the starting point for definition of material characteristics which enables designer to review material selection, when software calculates the sum of layer thickness or total material costs (Fig. 4).

Next activity is *Zone Groups* selection, which is defined by surface on which layers will be piled, with direction of piling and with axis system that represent the base for layers orientation. *Zone Groups* consist of diferent *Zones*, define discrete zones of composite elevator, that are physicaly constrained with other structural elements of elevator (in this case ribs and spar). Material is chosen for these zones, with specified plies and their orientation. *Zones* can contain *Transition Zones* where the thickness changings in a zone are defined. With *Zone Bridge Analyzer*, the first phase *Preliminary Design* is finished. *Stack Up File From Zones* option allows to create a stack up file based on predefined zones.

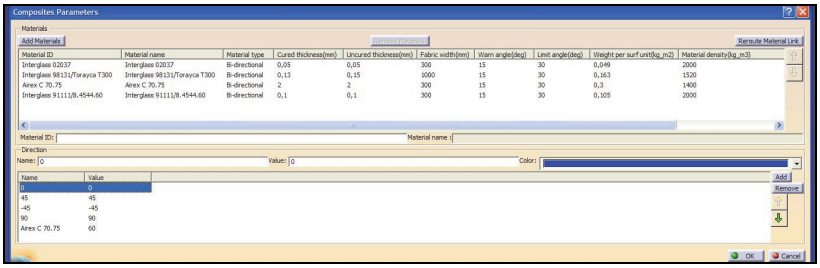

**Figure 4.** Characteristics of used material for elevator skin

The file contains the stacking order of the plies within the composite part. This provides a way to look at the way the plies would be created before actually creating them (Fig. 5).

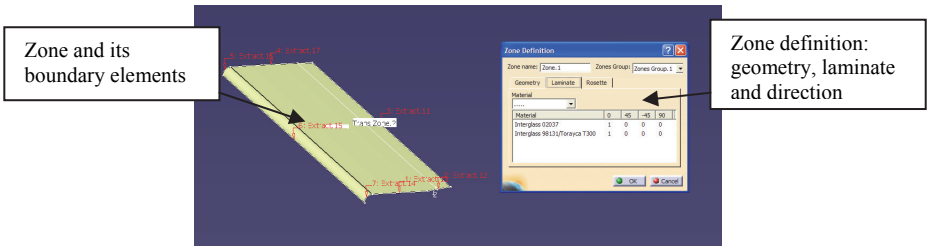


**Figure 5.** Zones and boundaries with window for zones definition

Phase *Detailed Design* includes *Plies Creation From Zones*, in which plies were automatically generated based on predefined zones. After creating plies, core was made with option *Creating a Core* along with choosed core characteristics. With tool *Solid generation from zones and plies*, the solid is created and the phase *Detailed Design* is terminated (Fig. 6). In order to compute the area, volume, center of gravity and mass it is necessary to do numerical analysis of composites skin. That can be done separately on a ply, a sequence, a plies group, or a stacking.

Similar procedure, from preparation of contour, detemination of materials, to gaining of solid is implemented to other structural parts of elevator (ribs and spar). The configuration is then subjected to stress analysis. Depending on complexity, the part may be subdivided into subcomponents for separate analysis. If required, a structural computer model may be generated.

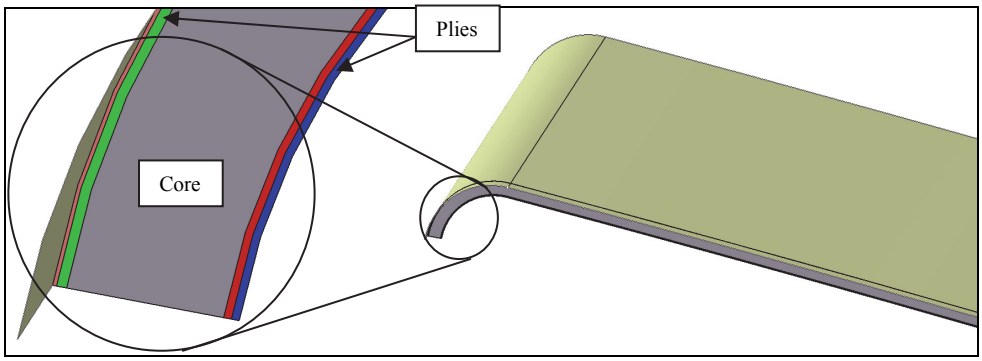


**Figure 6.** Configuration of elevator sandwich skin

## 3. Stress analysis of elevator composite structure

Module *Generative Structural Analysis* starts with three hipothesis: a) Small displacement (translation and rotation), b) Small strain , c) Linear constitutive law: linear elasticity.

Actual load for stress and strain analysis of the elevator are aerodynamic loads that act on surface skin during flight. Aerodynamic calculation shows that overall force is F = 96 N calculated for j = 1,0. This force is used during stress analysis in *Generative Structural Analysis* module as *Pressure field* applied to all surface of upper and lower elevator skin (the pressure direction is everywhere normal to the surface). Movement restraints were put at the places of elevator hinges at three cylindrical supports where the *surface slider pivot* type of supports were chosen. At the place of the middle support where the real command force from elevator actuator acts the *clamp* support was chosen and therefore the movements in three axis were restrained. Figure 7 shows FEM module for stress analysis.

Due to the fact that the elevator assembly is made of separate parts, the each part was assigned with set of composite plies from predefined catalogue. Next characteristics make contents of orthotropic material catalogue: Longitudinal Tensile Stress, Longitudinal Compressive Stress, Transverse Tensile Stress, Transverse Compressive Stress, Shear Stress Limit in XY Plane, Shear Stress Limit in YZ Plane, and Shear Stress Limit in XZ Plane.

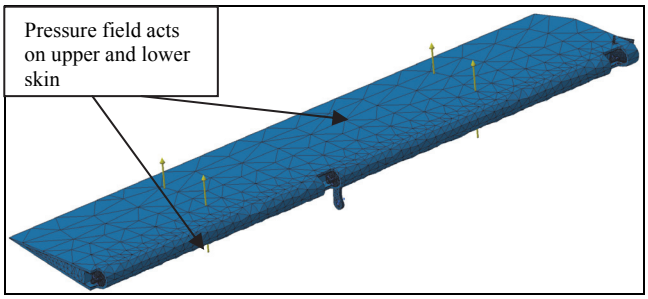


**Figure 7.** FEM model of elevator with three supports and pressure field

In *Generative Structural Analysis* module, using adequate options, such as *General Analysis Connection* and *Rigid Connection Property* the mutual movement restraints were accomplished for all assembly parts as it is in real assembly. After first stress and strain calculation the next calculation was accomplished. After three analysis iterations the satisfied assembly stress and strain was achieved.

There are four failure criteria for two and three dimensional orthotropic composite materials in *Generative Structural Analysis* module, as follows *Tsai-Hill, Tsai-Wu, Maximum Failure ili Hoffman*. According to our experience for such a type of structure assembly and elevator construction material the criterion *Tsai-Hill* (1) gives results that are closest to the test results. For each lamina the Tsai-Hill failure criterion requires that:

$$\left(\frac{\sigma_x}{S_1}\right)^2+\left(\frac{\sigma_y}{S_2}\right)^2+\left(\frac{\tau_{xy}}{S_{12}}\right)^2+\left(\frac{\tau_{xz}}{S_{13}}\right)^2+\left(\frac{\tau_{yz}}{S_{23}}\right)^2-\frac{\sigma_x\sigma_y}{S_1^2}\le 1 \qquad (1)$$

where:

- $S_1 = S_{1C}$ if $\sigma_x \leq 0$
- $S_1 = S_{1T}$ if $\sigma_x > 0$
- $S_2 = S_{2C}$ if $\sigma_y \leq 0$
- $S_2 = S_{2T}$ if $\sigma_y > 0$
- For the $\frac{\sigma_x \sigma_y}{S_1^2}$ term: if $\sigma_x \sigma_y \geq 0$, $S_1 = S_{1T}$; otherwise $S_1 = S_{1C}$

*Generative Structural Analysis* module enables post-processing simulation of stress analysis results showing: *Deformations, Principal Stresses*, and *Displacements*.

## 4. Conclusion

Experience of our design engineers in MTI, using CATIA software during design and analysis of aeronautical composite structures, is excellent. Efficiency during design is increased and issuing of appropriate documentation is made easier. Using iterative design consisted of simultaneous design and stress analysis, we achieved to obtain optimal composite airframe construction.

## References

[1] Dassault Systemes, CATIA V5.R21, Composites Engineering Design (CPE).
[2] Vasić, Z. Petrović, Savremeni kompozitni materijali u projektovanju i proizvodnji vazduhoplovnih konstrukcija, IIPP 2009, V7/4, str. 23-32, Beograd 2009.
[3] V. Stefanović, Primena kompozitnih materijala u vazduhoplovstvu, diplomski rad, Beograd, 2009.
[4] Z. Vasić, M. Blažić, V. Stefanović, (2012) Reconstruction of aircraft structure with the aim of optimizing and extending aircraft life cycle, 5th International Scientific conference on defensive technologies, OTEH 2012, Belgrade.
[5] Guideline No.GD-ED-2205, Design and Manufacturing Guideline for Aerospace Composites.
[6] V. Stefanovic, M. Marjanovic, M. Bajovic, Conceptual System Designs Civil Uav For Typical Aerial Work Applications, Oteh 2012, Belgrade

# ELASTO-PLASTIC BEHAVIOUR AND ULTIMATE LOAD OF PLATE GIRDERS SUBJECTED TO PATCH LOADING

**Nenad Marković[1], Dragana Turnić[2] , Tomislav Igić[3]**

[1] Civil Engineering Faculty, University of Belgrade,
Bulevar kralja Aleksandra 73, 11000 Belgrade, Serbia
e-mail: nenadgm@eunet.rs
[2] Faculty of Civil Engineering and Architecture,
University of Nis, Aleksandra Medvedeva 14, 18000 Niš, Serbia
e-mail: dragana.turnic@gaf.ni.ac.rs
[3] Faculty of Civil Engineering and Architecture,
University of Nis, Aleksandra Medvedeva 14, 18000 Niš, Serbia
e-mail: tomislav.igic@gaf.ni.ac.rs

**Abstract.** The paper deals with experimental research of the local buckling in the zone of load introduction for the plate girders (welded I girders) under the action of localized (patch) loading on a flange, in the plane of the web. Both, geometric and material non-linearity appear and influence the behaviour of the girder. Girders without vertical (transversal) stiffeners in this zone, but with and without horizontal (longitudinal) stiffeners are considered. Influence of the length of the patch loading and longitudinal stiffeners on the behaviour of the girders and their carrying capacities is analyzed. Longitudinal stiffeners in the vicinity of the loaded flange increase the ultimate load. An analysis is made of experimental results, especially strain gauge measurements that could give insight in to the stress state in the web during the loading. Obtained strains are compared for longitudinally stiffened and unstiffened girders. The development of the plastification is presented.

## 1. Introduction

The behaviour of plate girders subjected to patch load or partially distributed load on the flange in the plane of a web (Fig.1) represents a complex stability and elastoplastic problem. Both geometric and material non-linearity appear and influence the behaviour of the girder. Better knowledge of the behaviour of the girders is important in order to achieve more economic and safer design. The ultimate load is of special interest. The attainment of the ultimate load is manifested by local buckling out of the web plane in the zone of the load introduction.

Numerous investigations [1], [2], [3] during past 50 years indicated the main parameters that influence the behaviour of plate girders subjected to patch loading: thickness of the web, size of the flange, distance between vertical (transversal) stiffeners, position of longitudinal stiffeners, yield stresses of the web and flange, distribution length of the applied patch load, bending moment. Longitudinal stiffeners can significantly influence the behaviour of the girders if they are located near the zone of load introduction.

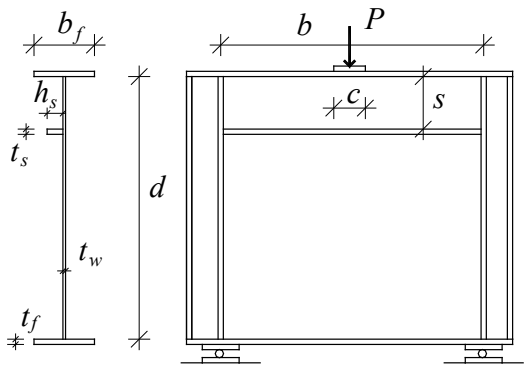


**Figure 1.** Girder - notation

Research presented in [1] dealt with the problem that needed additional studies: the influence of the patch load length for longitudinally stiffened girders. The investigation consisted of experimental and theoretical part. In order to support farther theoretical work the experimental investigation was carried out. There were two series of tested girders. The main one was with short and another with longer span, with varying loading length and with and without longitudinal stiffeners. During the tests different data were collected that enabled conclusions about the behaviour of the girders.

An analysis is presented in the paper dealing with the behaviour of the girder during the loading up to the ultimate load, regarding, first of all, development of the plastification in the web.

## 2. Strain gauge measurements

In order to follow development of the stresses and beginning and development of the plastification during the increase of the load and also in order to define more precise failure mechanism, strain measurements were taken for several test girders.

The experiments comprised two series of girders (with and without longitudinal stiffeners): the main series A, with span $b$ = 500 mm (web aspect ratio $\alpha$ = b/d = 1) and additional series B, with span $b$ = 1000 mm (web aspect ratio $\alpha$ = 2). Notation used is shown in Fig.1 and geometrical and material data for some of the girders are given in Table 1 for the girders that will be considered in this analysis. Only the length of the applied load c is varied by applying the load through either a half round bar or through rectangular stiff plates up to the length of 150 mm, all other dimensions being the same for all girders in each series. So, ratio $c/d$ was varied between 0 and 0.3 for shorter girders. Yield stresses (nominal values) of the web, flange and stiffener material are $\sigma w$, $\sigma f$ and $\sigma s$ respectively. Width and thickness of the stiffener are $hs$ and $ts$ . The width of plates for load application was equal to flange width.

Twenty tests were performed in the Laboratory of the Faculty of Civil Eengineering in Podgorica, Montenegro. In nine tests strain gauges were applied. Strains were measured with Hottinger strain gauges (LY11 3/120) on the web in the zone of load introduction and

on the loaded flange. After each load increment readings were taken with TML TDS-303 Data Logger and written in files on floppy disc.

Strain gauges were placed as individual vertical gauges and 0 - 45 - 90 rosettes made from individual strain gauges, or as ready-made rosettes. Strain gauges were positioned in pairs on both sides of the web or loaded flange to enable getting information about membrane and bending strains. The positions of the strain gauges were so chosen to enable comparison for the cases with different loading lengths. The location of the strain gauges was also influenced by the presence of longitudinal stiffeners.

| | *b* | *d* | *tw* | *bf* | *tf* | *c* | *hs* | *ts* | *s* | *Pexp* |
|---|---|---|---|---|---|---|---|---|---|---|
| | mm | mm | mm | mm | mm | mm | mm | mm | mm | kN |
| A1 | 500 | 500 | 4 | 120 | 8 | 50 | 0 | 0 | 0 | 165 |
| A2 | 500 | 500 | 4 | 120 | 8 | 150 | 0 | 0 | 0 | 215 |
| A3 | 500 | 500 | 4 | 120 | 8 | 50 | 30 | 8 | 100 | 183 |
| A7 | 500 | 500 | 4 | 120 | 8 | 150 | 30 | 8 | 100 | 255 |

**Table 1.** Strain Geometrical and material data

Characteristic locations of the strain gauges applied to girders A1 (without longitudinal stiffener) and A3 (with longitudinal stiffener near the loaded flange) are shown in Fig. 2. Strain gauges were positioned in the zone of the load introduction. For the first tests several rosettes were placed on one half of the web and on the other half of the web only vertical strain gauges were placed. They were placed symmetrically regarding the centre line of the web to corresponding vertical strain gauges in the rosetts (Fig. 2), in order to control whole behaviour of the system (symmetrical response). After first tests very good agreement was obtained. In other tests different dispositions of the strain gauges were applied to the left and right half of web in order to obtain more information.

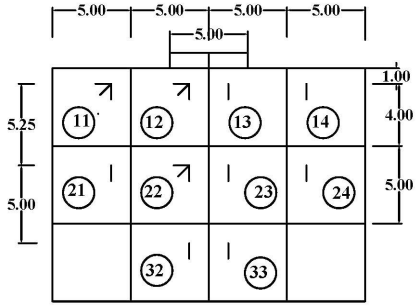


**Figure 2.** Strain gauges on the web of the girders A1 and A3 (front side)

Vertical strain gages on the web are marked in the Fig. 2 with numbers 11, 12 … to 32 according to their position.

A part of the analysis regarding influence of the presence of the longitudinal stiffeners for girders A1 and A3, with relatively short loading lengths $c$ = 50 mm ($c/b$=0.1) is presented.

Similar analysis can be done for girders A2 and A7 with longer loading lengths. In [1] more detailed analysis of the obtained stresses was made. In this paper simplified analysis using only measurements from the vertical strain gages, which gives quite good insight into the behaviour of the girders, is used to obtain given conclusions.

Due to the patch loading, basically in plane - membrane direct and shear stresses – constant across the thickness of the web - develop in the web in the vertical and horizontal direction. Also, due to the initial deformations of the web, additional bending stresses, variable across the thickness of the web, develop from the beginning of the loading, increasing with the increase of the out-of-plane deformations of the web. So, different values of the stresses are obtained in the corresponding points on front and rear surface of the web.

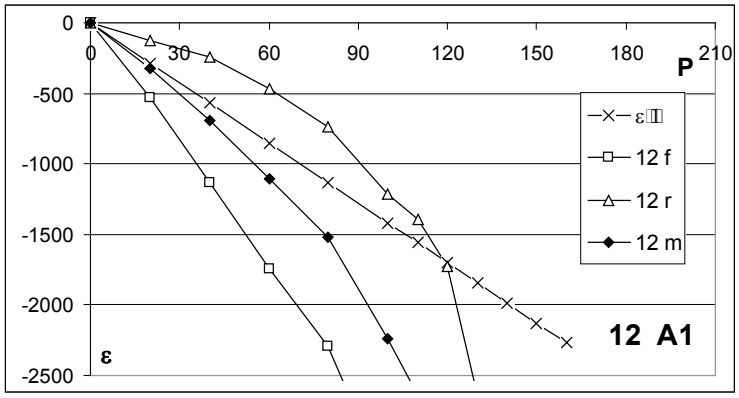


**Figure 3.** Strains for strain gages 12 on the girder A1 (Pexp=165 kN)

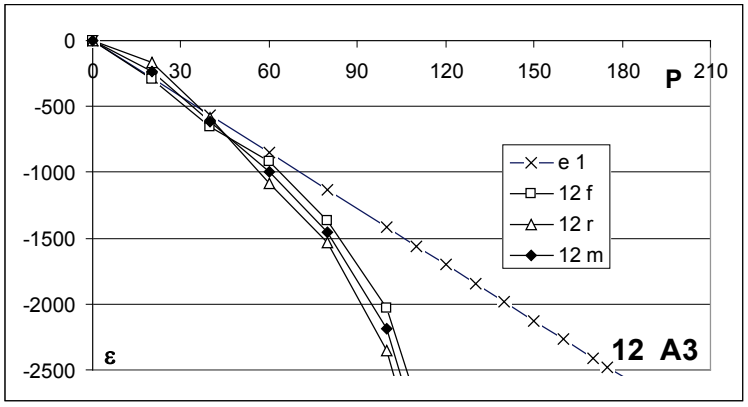


**Figure 4.** Strains for strain gages 12 on the girder A3 (Pexp=183 kN)

Due to limited space only some diagram will be shown that are representative for the behaviour of the investigated girders. Strain measurements multiplied by $10^6$ for the vertical strain gages 12 and 22 (that are directly under the load) for the girder A1 are given in Fig.3

and Fig. 5, and for the girder A3 are given in Fig.4 and Fig. 6. The given values are for the strain gages on the front side of the web (f) and on the rear side of the web (r) and for membrane strains – strains constant across the thickness of the web (m). (*P* is in kN)

In many codes of practice control of the vertical stresses in the web at certain distance from the loaded flange is asked for, not allowing to surpass yield stressis. It is there assumed that stresses spread from the loading length *c* under certain angle (usually 45°) into the web. In given figures lines (ε1) and (ε2) represent strains corresponding to so calculated stresses at the distance 10 mm (regarding strain gages 12), and at the distance 62.5 mm (regarding strain gages 22) from the loaded flange.

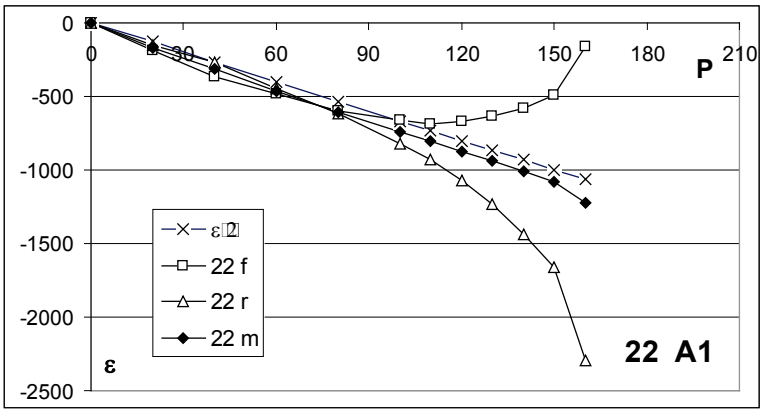


**Figure 5.** Strains for strain gages 22 on the girder A1 (Pexp=165 kN)

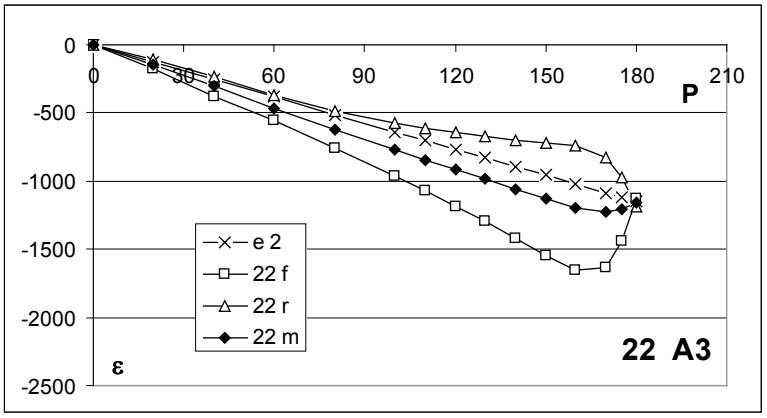


**Figure 6.** Strains for strain gages 22 on the girder A3 (Pexp=183 kN)

Strains that approximately correspond to the beginning of the plastification for steel used in tested girders ($\sigma w \cong 280$ MPa, E=205 GPa) are about 1370 x $10^{-6}$ .

After inspection of the diagrams given here and similar diagrams for other loading lengths and all other diagrams and measured values, and after detailed analysis, conclusions are obtained that will be summarized in the next part.

## 3. Conclusions

Behaviour of the plate girder under the action of the patch load is very complex and depends on various parameters. Already after 50% of the ultimate load plastification develop in the most stressed part of the web, firstly, only on the surface and spreading across the thickness. This plastification does not mean necessarily the attainment of the ultimate load, even it does not mean noticeable and significant deformations, but it indicates that care have to be taken about elasto-plastic behaviour. This behaviour depends on many parameters, and it can be rather complex due to variable stress field. That is, also, the reason for intensive research in many countries in the word nowadays. One of the procedure for determination of the ultimate load is given in [3].

Comparison of the Fig. 3 and Fig.4, or Fig.5 and Fig. 6, show that development of membrane stresses does not depend on the presence or absence of the longitudinal stiffeners, and that does not depend on the initial deformations and deformations out-of plane of the web in the course of the loading (although, development of the surface stresses depend on those facts). Presence of the longitudinal stiffener influences initial deformations, increase of the deformations and limits development of the final buckling to the space between loaded flange and stiffener and increase the ultimate load. The greater length of the applied load increase ultimate load, as greater part of the girder is engaged.

Assumption of spreading of stresses under certain angle down the web can be used for the assessment of the stresses in points with elastic behaviour, but shouldn't be used for the determination of the ultimate load.

This research is aimed to be used for planned further investigation of patch loading problem by the FEM, for checking the models that will be adopted. in process of the analysis of the influence of several important parameters that need further research.

*Acknowledgement.* The authors express their gratitude to Civil Engineering Faculty at Podgorica, Montenegro, for providing facilities and staff for carrying out the experimental part of the research in highly professional way and for obtaining reliable results.

## References

[1] Marković N (2003) *Buckling of the Plate Girders under the Action of Patch Loading* (in Serbian), Ph.D. Thesis, Civil Engineering Faculty, Belgrade, p136
[2] Janus K, Karnikova I, Škaloud M (1988) Experimental investigation into the ultimate load behaviour of longitudinally stiffened steel webs under partial edge loading, *Acta Technika ČSAV*, Prague, No.2, pp.158-195.
[3] Hajdin N., Marković N. (2012) Failure mechanism for longitudinally stiffened I girders subjected to patch loading, *Arch Appl Mech* **82**, pp.1377–1391. DOI 10.1007/s00419-012-0679-4.